Structural Characterisation of Ferrihaem in Solution: Insights into the Mechanism of Formation of Malaria Pigment and Its Inhibition by Aryl Methanol Antimalarial Drugs

This thesis is the work of

Katherine A. de Villiers (BSc. HONS)

of the

Department of Chemistry

It is presented for the degree of

Doctor of Philosophy (PhD)

to the

University of Cape Town

in

August 2008

DECLARATION

STRUCTURAL CHARACTERISATION OF FERRIHAEM IN SOLUTION: INSIGHTS INTO THE MECHANISM OF FORMATION OF MALARIA PIGMENT AND ITS INHIBITION BY ARYL METHANOL ANTIMALARIAL DRUGS

I, Katherine A. de Villiers, hereby declare the following:

1. That the above-titled thesis is my own work, both in concept and execution, apart from the normal guidance of my supervisor;
2. That in cases where others' work has been cited, this has been acknowledged and referenced;
3. That no part of this work has been, is being, or is to be submitted for another degree at this or any other university;
4. That I grant the University of Cape Town free license to reproduce this work, in whole or in part, for the purpose of research.

Having declared these things, I hereby present this thesis for examination for the degree of Doctor of Philosophy (PhD), Chemistry.

Signed at the UNIVERSITY OF CAPE TOWN, this 20th day of AUGUST, 2008.

Katherine A. de Villiers: Signed by candidate

Witness:

of the crystals, calculated from the full width at half maximum of Bragg peaks and their corresponding Bragg rods, is estimated to be 250 Å in the *bc* plane and 20 Å along *a*. The formation of β-haematin does not take place at a docosane/water interface and occurs in smaller yield at a methyl laurate/water interface. It is proposed that the –OH moieties on MMG molecules act as a nucleating site for β-haematin crystallisation and that they further orient the crystals based on epitaxial-type molecular complementarity.

The inhibition of β-haematin formation at the MMG/water interface by various antimalarial drugs was investigated. The IC_{50} values correlate reasonably well (r^2 = 0.80; P = 0.0162) with biological activity. Chloroquine (CQ) and quinine (QN) influence the Raman active A_{1g} modes of Fe(III)PPIX at approximately 679, 796, 1378 and 1569 cm^{-1} and the B_{1g} modes at approximately 795 and 1569 cm^{-1}, causing reductions in intensity of these bands relative to both Fe(III)PPIX and β-haematin as well as small wavenumber shifts. The crystal structure of the complex formed between Fe(III)PPIX and the antimalarial drug halofantrine has been determined by single crystal X-ray diffraction. Halofantrine is shown to coordinate to monomeric, five-coordinate Fe(III)PPIX through its alcohol (alkoxide) functionality, while π-stacking of the phenanthrene ring over the porphyrin and intermolecular hydrogen bonding between the terminal amine ($N–H^+$) of halofantrine and the porphyrin propionate group are also important. Almost identical changes in the UV-vis spectrum of Fe(III)PPIX upon addition of the free base forms of halofantrine and quinidine in acetonitrile suggest analogous binding. Molecular mechanics modelling of the Fe(III)PPIX complexes of QN and its stereoisomers according to this analogy suggests that antimalarial activity is based on the ability of complexes to adopt conformations in which it is possible to form charge-assisted intramolecular hydrogen bonds ($N–H^+_{quinuclidine}\cdots{}^-OOC_{Fe(III)PPIX}$). Conformations possess low energy in the case of the active isomers and high energy in the case of the inactive isomers. It is proposed that the formation of this intramolecular hydrogen bond blocks the formation of the haemozoin precursor dimer formed during Fe(III)PPIX detoxification, accounting for the strong antimalarial activity of the active isomers.

PUBLICATIONS AND CONFERENCE PROCEEDINGS

The following publications and conference proceedings have included aspects of this work:

Publications:

1. Egan, T. J., Chen, J. Y-J., de Villiers, K. A., Mabotha, T. E., Naidoo, K. J., Ncokazi, K. K., Langford, S. J., McNaughton, D., Pandiancherri, S. and Wood, B. R., Haemozoin (β-haematin) biomineralisation occurs by self-assembly near the lipid/water interface, *FEBS Lett.*, **2006**, 580(21), 5105 – 5110.
2. de Villiers, K. A., Kaschula, C. H., Egan, T. J. And Marques, H. M., Speciation and structure of ferriprotoporphyrin IX in aqueous solution: spectroscopic and diffusion measurements demonstrate dimerisation, but not mu-oxo dimer formation, *J. Biol. Inorg. Chem.*, **2007**, 12(1), 101 – 117.
3. de Villiers, K. A., Marques, H. M. and Egan, T. J., The crystal structure of halofantrine-ferriprotoporphyrin IX and the mechanism of action of arylmethanol antimalarials, *J. Inorg. Biochem.*, **2008**, 102(8), 1660 – 1667.

Conference Proceedings:

1. SACI Inorganic Chemistry Conference, **2005**, Pietermaritzberg, RSA
   Poster: Katherine A. de Villiers and Timothy J. Egan, The nature of haematin and its complexes with 4-aminoquinolines in aqueous solution.
2. SACI Young Chemists' Meeting, **2005**, Stellenbosch, RSA
   Oral: Katherine A. de Villiers and Timothy J. Egan, The nature of haematin in aqueous solution.
3. 37th International Conference on Coordination Chemistry, **2006**, Cape Town, RSA
   Poster: Katherine A. de Villiers and Timothy J. Egan, Spectroscopic and diffusion measurements demonstrate that the ferriprotoporphyrin (IX) dimer is not a μ-oxo dimer.
4. 3rd COST B22 Annual Congress "Drug Discovery and Development for Parasitic Diseases", **2006**, Athens, Greece
   Poster: Katherine A. de Villiers and Timothy J. Egan, 4-Aminoquinolines inhibit β haematin formation near the aqueous / lipid interface.
5. SACI Inorganic Chemistry Conference, **2007**, Mykanos, RSA
   Student Oral: Katherine A. de Villiers, Timothy J. Egan and Helder M. Marques, A crystallographic and computational investigation of the complexes of *Cinchona* alkaloids and related compounds with ferrihaem reveals new insights into their structure and activity.

ACKNOWLEDGEMENTS

Though the publication of this thesis is my own work, achieving what constitutes it would not have been possible without those who have contributed to the science, as well as to my spirit:

Professor Tim Egan: I truly could not have asked for a better supervisor. Without your guidance I would never have accomplished this feat. For your teaching, advice, direction, discussions, patience and above all, 100% dedication to all of your students 100% of the time, I thank you sincerely. The many good times we shared on the mountain were a bonus too.

Professor Helder Marques (University of the Witwatersrand, Johannesburg, South Africa): For invaluable discussions on several aspects of this work but primarily for providing answers to my numerous HYPERCHEM queries.

Professor Leslie Leiserowitz, **Dr Isabelle Weissbuch** and **Dr Inna Solomonov** (Weizmann Institute of Science, Rohovat, Israel): For the invitation to conduct experiments on the synchrotron at HASYLAB (Hamburg, Germany) and for helping every step of the way to collect and interpret the data.

Dr Bayden Wood, **Professor Don McNaughton**, **Grant Webster** and **Finlay Shanks** (Centre for Biospectroscopy, Monash University, Melbourne, Australia): For hosting me for 2 months in 2007 and introducing me to Raman spectroscopy.

Fellow students: **Dr Catherine Kaschula**, for leaving some stones unturned; **Dr Kanyile Ncokazi**, for providing mature leadership and invaluable experience in the lab; **Dr Tebogo Mabotha**, for support and friendship both in and out the lab; **David Kuter** and **Constance Asher**, for being like a breath of fresh air in the last days; **Ebrahim Mohammed**, for being a great friend throughout my time at UCT and for willingness to assist in anything Organic-related; **Chris B**, **Richard M**, **Meredith H** and **Claire L-N** for their individually special friendships.

Mr Pete Roberts, **Ms Miranda Waldon** and **Dr Andreas Lemmerer** (all UCT): For collection of NMR spectra, SEM images and assistance with the solution of my crystal structure respectively.

Dr Elizabeth Timme (CSIR): For providing access to the large-scale centrifuge.

Equity Development Program (Dept. Chemistry, UCT) and the **National Research Foundation**: For financial support throughout my post-graduate studies.

Department of Chemistry (UCT) including Professor Allen Rodgers (HOD), all academic staff, the ladies in the office, the DAs and even Sammy and Paula from Super-Care (for friendly smiles).

Finally, to my family: **Dad and Mom**, for sacrificing so much to provide me the opportunity to reach my full potential at UCT and for your unconditional love and support every step of the way. My brother **Pete**, you have flown the world time and again to be where it counts for me. Your being Fe(III)PPIX-ed out on my behalf is much appreciated too. My parents- and brother-in-law, **Eddie**, **Nancy** and **George Chen**, for loving me as a daughter and sister in so short a time and always taking an interest in my studies. A most special acknowledgement is owed to my dear husband **Jeff**, for your unfailing love and support throughout my PhD, for listening, encouraging and gently challenging me to take up a fresh outlook on occasion, and above all for being so proud of me.

TABLE OF CONTENTS

1. INTRODUCTION AND LITERATURE REVIEW

1.1 MALARIA: AN ACCOUNT OF THE DISEASE FROM DISCOVERY TO PRESENT

For more than four thousand years, written records have described symptoms of severe headaches, chills and periodic fevers that have plagued much of the world's population.[1] Today these symptoms are easily recognisable and attributable to malaria infection. Accounts in the medical literature dating back to the age of the Roman Empire are consistent with descriptions of malaria although the cause of the disease was not understood.[1] Historically, there was a connection between marshes and the contraction of disease.[2] The condition, referred to as "Roman fever", was thought to be contracted in "bad air" and in fact, the origin of the name malaria arises from the Italian translation of this phrase, "*mal'aria*".

In 1717 Giovanni Maria Lancisi, an Italian physician, was the first to describe the black pigment which is found in the brain and spleen of malaria victims.[3] The presence of malaria pigment remains a clear diagnostic of malaria infection even today. Though he connected the disease with marshes and stagnant waters, Lancisi remained convinced that malaria was the result of mosquitoes' "injurious juices [mixed] with the saliva" which they injected into humans with their bite. It was not until 1880 that the true cause of the disease was to be exposed. For the first time Charles Louis Alfonse Laveran, a French military surgeon working in Algeria, observed pigmented spherical bodies moving inside red cells of a fresh blood sample from a malaria sufferer.[4] He had discovered the malaria parasite. Through observation of the same pigment-filled parasites inside a mosquito's gut, Ronald Ross in 1897 proved that these insects transmit malaria.[5]

Today's research is directed toward understanding how malaria infection may be prevented and in cases of infection, how a patient may be cured. The antimalarial properties of the bark of the *Cinchona* tree were recognised in the 1630s and several precursors to chloroquine were developed between the World Wars. In the face of growing parasitic resistance to these drugs, new advances in drug discovery are critical.

1.2 EXTENT OF THE MALARIA PROBLEM

A comprehensive World Malaria Report[3] compiled by the World Health Organisation (WHO) in 2005 includes statistics of malaria transmission from 107 countries and territories across the globe. The highest prevalence of the disease occurs in sub-Saharan Africa although infections have also been reported in the tropical regions of Latin America, the Middle East and Asia (Figure 1.1). The climate in these regions favours the breeding of *Anopheles* mosquitoes, the vectors of the disease.[7] Malaria is a global burden, with an estimated 300 – 500 million cases occurring annually, resulting in 1.5 – 2.7 million deaths. Africa accounts for 90% of these cases, with mortality rates being highest in children under the age of five. The escalating resurgence of the disease has, in part, been attributed to population migration as a result of trade and tourism, agriculture and even war.[8] Fluctuating rainfall patterns, inadequate medical facilities and the appearance of resistant malaria parasites are also contributing factors.

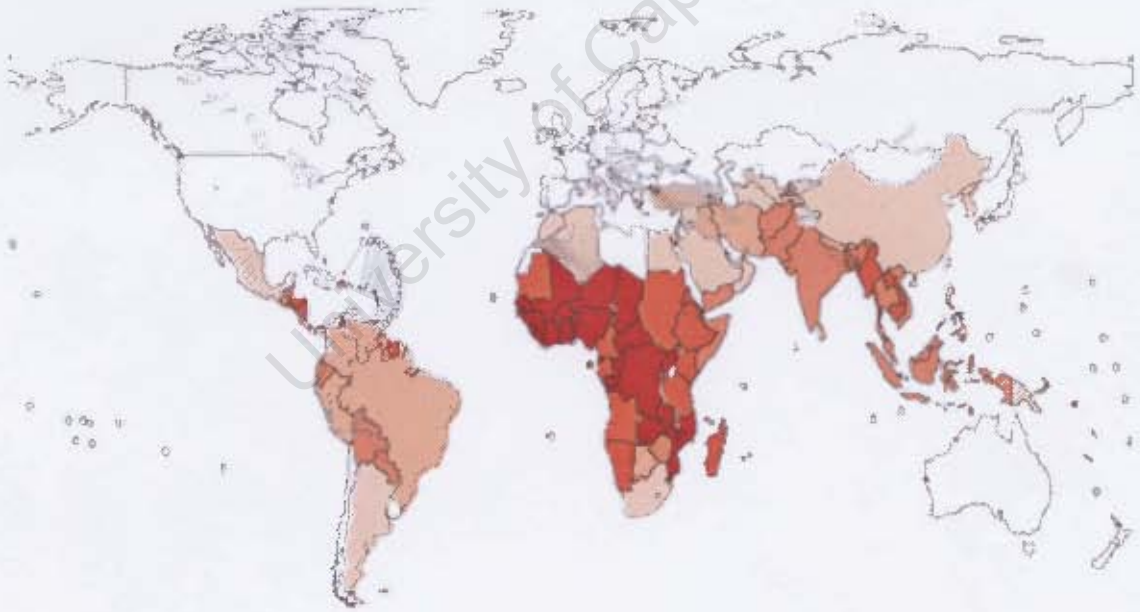

Figure 1.1 The global distribution of malaria. Areas of dark orange indicate the highest endemicity while light orange areas have the lowest statistics. Reproduced from reference 9.

1.3 LIFECYCLE OF THE MALARIA PARASITE

Malaria is caused by infection by one of four species of *Plasmodium*.[10] Of the four species, *P. falciparum* is the most widespread and the cause of the highest

morbidity and mortality in humans. While *P. vivax* is relatively common, it is less of a threat as it seldom causes fatality. *P. malariae* and *P. ovale* are not known to cause severe disease in humans.

The malaria parasite *P. falciparum* has a complex lifecycle involving both the mosquito vector and a human host (Figure 1.2).[11,12] Infectious parasites are transmitted to the human host in the saliva of a female mosquito of the genus *Anopheles*. Sporozoites introduced by the bite of the mosquito travel to the liver where they invade hepatocytes, develop as tissue schizonts and then divide and multiply asexually to form merozoites. This stage of infection is asymptomatic. Bursting out from the liver cells, merozoites are short lived and quickly enter erythrocytes (red blood cells). The symptoms of malaria infection are associated with the blood cycle, a recurring sequence of events every 48 hours in the case of *P. falciparum*. Merozoites develop into so-called rings, then trophozoites and finally into mature blood schizonts.[13] Upon schizont rupturing, merozoites that are released into the blood stream to complete one cycle go on to invade new red blood cells. Whilst in the red cells a number of merozoites develop into gametocytes, which later complete sexual reproduction inside the midgut of the mosquito after having been taken up during a blood meal.

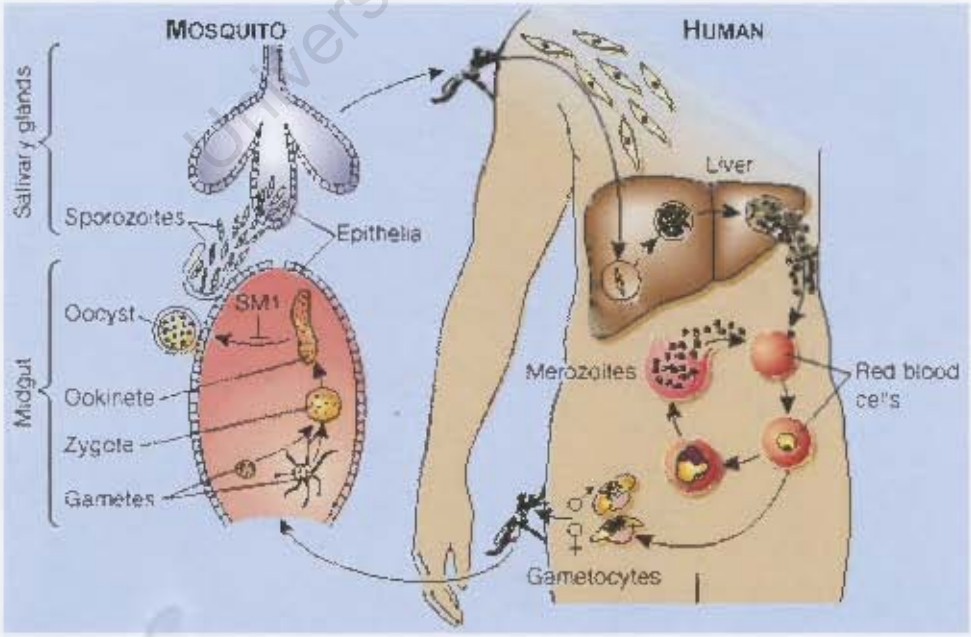

Figure 1.2 The lifecycle of the malarial parasite, *Plasmodium falciparum*. Reproduced from reference 11.

1.4 HAEMOGLOBIN DEGRADATION

During development inside the red blood cell (Figure 1.3 A), the malaria parasite *P. falciparum* digests between 60 and 80 % of the available haemoglobin,[14,15] mostly whilst in its trophozoite stage. Invagination of the parasite plasma membrane forms a cytostome from which endocytotic vesicles are pinched off and efficiently transport haemoglobin to a digestive compartment referred to as the food vacuole.[16] The local environment inside the food vacuole is acidic and several estimates of the pH have been put forward. Early studies using fluorescein reported values in the range 5 – 5.6,[17,18] while later work concluded that the pH in the case of a chloroquine-sensitive strain was 4.3 – 4.7.[19] Hayward et al. have recently provided an estimate of ~ 4.8 measured for early trophozoites, though they did observe variation in this value in the case of mature trophozoites.[20] The degradation of haemoglobin is catalysed by a series of diverse proteolytic enzymes that include the aspartic proteases (plasmepsins I, II and IV and histoaspartic protease), the cysteine proteases (falcipains 1, 2 and 3) and a zinc metalloprotease (falcilysin).[21-23] Plasmepsin I is responsible for initially cleaving intact haemoglobin, while plasmepsin II and the other proteases act later on denatured globin.[24,25] The breakdown of the protein provides a valuable source of amino acids,[26] a small portion (about 16 %[27]) of which the trophozoite utilises for its own growth. It has been proposed that the majority of digestion takes place in order to free space for the growing trophozoite[28] while at the same time maintaining the cellular osmotic balance.[29]

As a consequence of the proteolytic breakdown of haemoglobin, haem (iron (II) protoporphyrin IX, Fe(II)PPIX) is released into an aqueous environment.[12] The metal centre is irreversibly oxidised to Fe(III), presumably by molecular oxygen, although the mechanism is not yet known. The resultant HO^-/H_2O-Fe(III)PPIX (hydroxo-/aqua-ferriprotoporphyrin IX, haematin) is toxic[30] and as such, represents a major threat to the viability of the parasite. Soluble in a lipid environment, Fe(III)PPIX has been invoked in lipid peroxidation and membrane damage.[14,30,31] In what appears to be a detoxification mechanism, malaria parasites sequester free Fe(III)PPIX into a micro-crystalline form known as haemozoin or malaria

pigment.[32] It has been shown that at least 95% of the free haem is detoxified in this manner (Figure 1.3 B).[15]

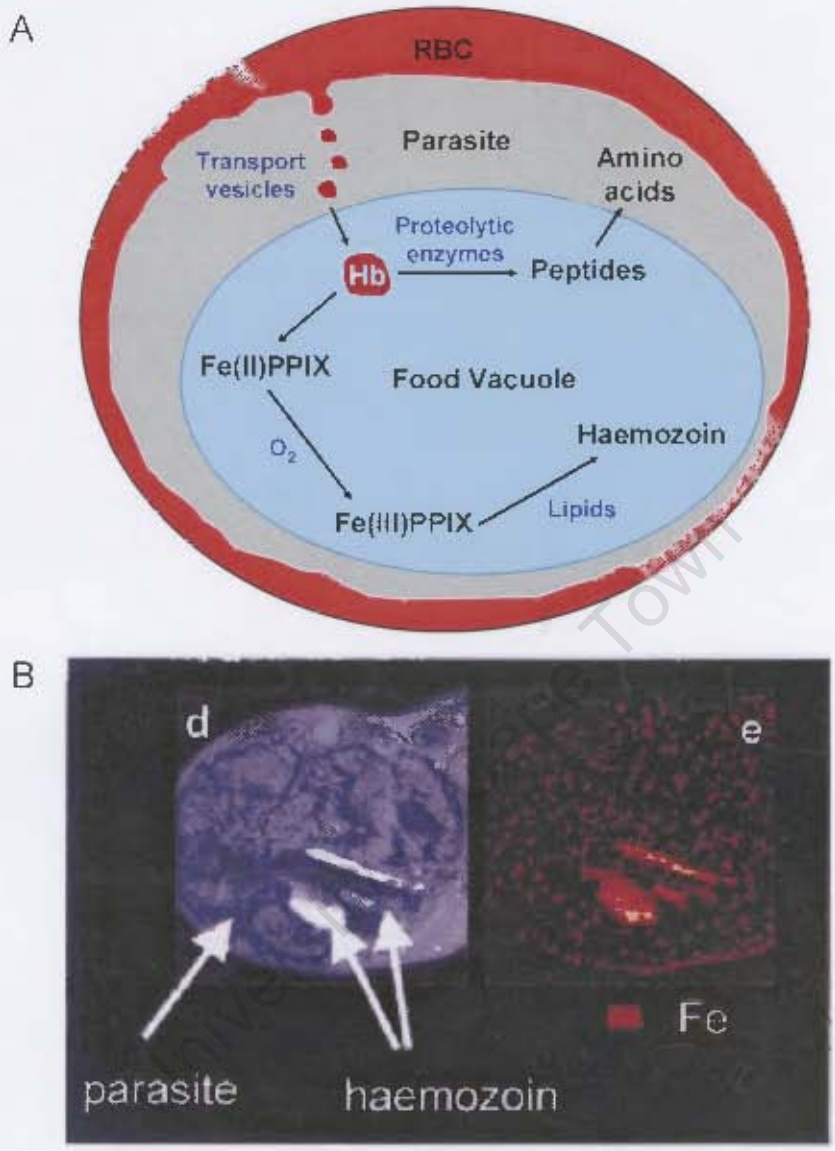

Figure 1.3 (A) A schematic representation of haemoglobin degradation and Fe(III)PPIX detoxification in the malaria parasite, *Plasmodium falciparum*. (B) The TEM (left) and ESI (right) images of a schizont-infected red blood cell showing that the distribution of Fe coincides with haemozoin crystals. Reproduced from reference 15.

We now know that this crystalline material is the same malaria pigment recognised by Lancisi in 1717. Upon rupture of a mature schizont from red blood cells, the pigment is released into the host's blood stream, ingested by macrophages and stored in the liver and spleen.[33] In cases of cerebral malaria, pigment accumulation also occurs in brain tissue.

1.5 THE NATURE OF FE(III)PPIX IN AQUEOUS SOLUTION

In the context of malaria research, a correct structural interpretation of Fe(III)PPIX in aqueous solution is imperative in order to begin to understand the mechanism of its detoxification to haemozoin. Furthermore, such a structural interpretation is likely to promote understanding of how antimalarial drugs are able to interact with Fe(III)PPIX in order to inhibit haemozoin formation.

1.5.1 The Aggregation State of Fe(III)PPIX in Aqueous Solution

1.5.1.1 The Presence of Large Aggregates

The aggregation state of aqueous Fe(III)PPIX has been the topic of much controversy in the literature. Based on diffusion measurements, early work suggested that particles with weights ranging from 50,000[34] to 145,000 and even as large as 4,000,000 with time[35] were present in solution. A subsequent diffusion study by Shack and Clark[36] concluded that in alkaline solution, Fe(III)PPIX was present in large aggregates or micelles. Furthermore, the authors concluded that within the large aggregates, Fe(III)PPIX was present as units of dimers. Given the large deviations within their data set the authors reasoned that the forces holding the units together within the aggregate were weak. Later, Blauer and Zvilichovsky[37] demonstrated by ultracentrifugation that in 1.2 M NaCl (pH 11) the distinct green complex of Fe(III)PPIX forms aggregates with average molecular weights of roughly 31,000, corresponding to 45 – 50 molecules. In their discussion of similar phenomena, Moreau et al.[38] commented that in neutral aqueous solution, dimers of Fe(III)PPIX formed aggregates of a very large size, although they were unable to provide evidence for this. Additional support for the formation of large aggregates came from kinetic studies. Based on changes observed in the absorbance of the Soret band with time, Srinivas and Rao[39] suggested that their data were consistent with three different processes resulting in the formation of complex aggregates. Kuzelová et al.[40] conducted a kinetics investigation of the interaction of monomeric Fe(III)PPIX with hemopexin and albumin. The kinetics profiles of aged solutions did not exhibit the same behaviour as fresh solutions, which the authors attributed to the formation of higher aggregates with time.

1.5.1.2 The Presence of Dimers

While the contention that Fe(III)PPIX in aqueous solution exists in the form of large aggregates retained some support over the decades, a thorough study by Brown et al.[41] published in 1970 concluded that aggregation of Fe(III)PPIX beyond dimers did not occur, at least in the concentration range that they were able to study (0.2 – 200 μM). In their investigation, the authors performed spectrophotometric measurements of the Soret band (~ 400 nm) for solutions of Fe(III)DPIX (iron(III) deuteroporphyrin IX) and Fe(III)PPIX prepared in sodium and potassium phosphate buffers (Na_2HPO_4 and KH_2PO_4) at four pH values in the range 6.64 – 8.06. They noticed marked changes in the spectra of both Fe(III)DPIX and Fe(III)PPIX as a function of increasing concentration, including a decrease in extinction and broadening of the Soret band. Such changes, being inconsistent with Beer's Law, were deemed to be consistent with the dimerisation of Fe(III)PPIX at high concentration as reported by others in the field.[42,43] Brown et al.[41] used the following relationship to explain the dimerisation process (Equation 1.1):

$$2M \overset{K}{\rightleftharpoons} D + nH^+ \qquad (1.1)$$

where *M* and *D* represent monomeric and dimeric Fe(III)PPIX respectively, *K* is the overall dimerisation constant and *n* is the number of protons released during the process. The observed dimerisation constant at a particular pH was designated K_{obs}, while the observed extinction coefficient at a particular wavelength and pH ($\varepsilon_{obs}[T]$, where T is the total Fe(III)PPIX concentration) was expected to consist of contributions from the monomeric ($\varepsilon_M[M]$) and dimeric ($\varepsilon_D[D]$) species. In the absence of non-linear least squares fitting algorithms at the time, the authors resorted to a linearisation process in order to determine values of *K* and *n*. Thus 10 data points per titration were fitted to a linear equation, for which ε_M and ε_D were treated as fixed parameters. In the case of Fe(III)PPIX, a large proportion of dimers were present even at the lowest concentrations reached. Thus ε_M data were assumed to be the same as had been determined for Fe(III)DPIX. Experimental values for ε_M, ε_D and K_{obs} are reported in Table 1.1.

Table 1.1 The pH-dependence of ε_M, ε_D and K_{obs} for Fe(III)PPIX[41]

pH	ε_M	ε_D	$10^7 K_{obs}$ / M^{-1}	log K_{obs}*
6.64	132500	-	-	-
6.98	121500	78.6	4.70	7.67
7.38	110000	81.6	10.50	8.02
8.04	95000	89.2	38.90	8.59

* These values were not reported in the original work.[41]

From linear plots, Brown et al.[41] concluded that a single proton (n = 1) was lost during the dimerisation process. Assuming the loss of one proton for each of the monomer and dimer separately (i.e. $M \rightleftharpoons M' + H^+$ and $D \rightleftharpoons D' + H^+$), fitting of the experimental data (ε_D only in the case of Fe(III)PPIX) to a linearised equation yielded an acid dissociation constant $pK_{a(D)}$ = 7.5.

1.5.2 The Nature of the Fe(III)PPIX Dimer

1.5.2.1 The Structural Interpretation of Brown et al.

In an earlier study, Brown and co-workers[44] had characterised the solid green precipitate obtained upon addition of 1 M NaOH to a solution of haemin in dimethylsulfoxide (DMSO). A band in the IR spectrum near 900 cm^{-1} provided evidence of an oxo-bridged species (Fe–O–Fe).[45] Brown et al.[44] constructed a model for the μ-oxo dimer of Fe(III)PPIX (Figure 1.4 A) in which they assumed that both five-coordinate Fe(III) centres reside 0.5 Å out of the mean porphyrin plane towards the axial oxygen atom. Furthermore, the Fe–O bond length and van der Waals distance were estimated to be 1.8 Å. Based on this geometry, the tolerance limits for the Fe–O–Fe bond angle before the planar porphyrin ring systems become distorted were found to be 165 - 180°. In conclusion to their findings regarding Fe(III)PPIX dimerisation, Brown et al.[41] proposed possible structural relationships between the monomeric and dimeric species of Fe(III)PPIX (Figure 1.4 B). These structures were based on the interpretations of the earlier study, although they assume that the Fe(III) centres are six-coordinate.

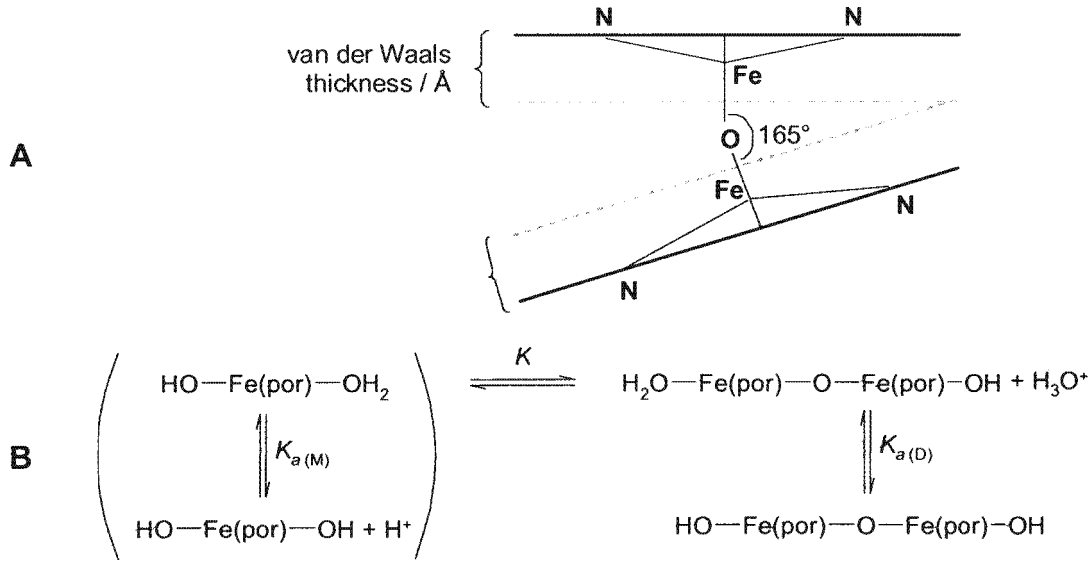

Figure 1.4 (A) The side view of the molecular model of the Fe(III)PPIX μ-oxo-dimer proposed by Brown and co-workers. Redrawn based on reference 44. The solid black lines represent the porphyrin plane. (B) A schematic representation of the structural relationship between monomeric and dimeric Fe(III)PPIX. Fe(por) represents the Fe(III) centre and the four-coordinate porphyrin ring system. Redrawn from reference 41.

1.5.2.2 Crystal Structures of μ-Oxo Dimers

While the original model of the μ-oxo dimer proposed by Brown et al.[44] is consistent with the X-ray crystal structure of synthetic μ-oxo dimers, the structural interpretations proposed for the relationship between the monomer and dimer of Fe(III)PPIIX differ from this model in terms of coordination number. In 2004 the crystal structure of μ-oxo-bis[(protoporphyrin IX dimethyl ester)-iron (III)] was determined.[46] In the absence of the crystal structure of the μ-oxo dimer of Fe(III)PPIX itself, this structure is the most closely related porphyrin yet determined. Crystallographic analysis yields an Fe–O–Fe bond angle of 170.5(2)° and an Fe–O bond length of 1.748(3) Å (Figure 1.5). In the crystal structure of μ-oxo-bis(tetraphenylporphineiron(III)), O-(Fe-TPP)$_2$,[47] each Fe(III) atom resides 0.46 Å out of the mean porphyrin plane towards the oxide ion, while the Fe–O–Fe bond angle and the Fe(III)–O bond length are 168° and 1.76 Å respectively. Both structures confirm that the Fe(III) centres have the square-pyramidal five-coordinate geometry expected for Fe(III)PPIX, thus apparently invalidating the structural interpretations reached by Brown and co-workers.[41]

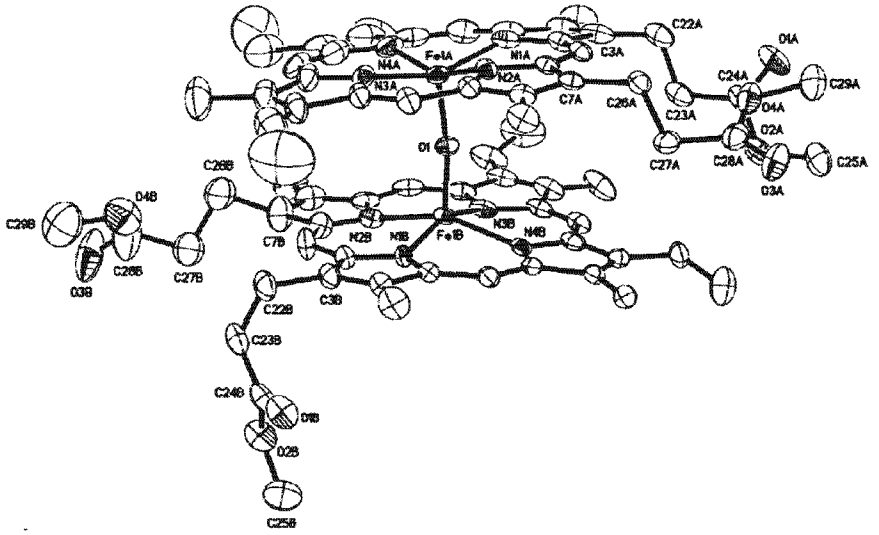

Figure 1.5 The crystal structure of μ-oxo-bis[(protoporphyrin IX dimethyl ester)-iron (III)]. Reproduced from reference 46. Thermal ellipsoids are drawn at 35% probability, while H and disordered atoms of lower occupancy have been omitted for clarity.

1.5.2.3 Spectroscopic and Magnetic Properties of μ-Oxo Dimers

It is well established that μ-oxo dimers of Fe(III) porphyrins exhibit antiferromagnetic coupling.[48] Magnetic susceptibility measurements per Fe(III) centre were performed on the μ-oxo dimer O-(Fe-TPP)$_2$ and monomeric tetraphenylporphine iron(III) chloride (Fe-TPP-Cl) and the effective magnetic moments were determined as 1.15 and 5.87 respectively (293 °K).[47] The latter measurement is consistent with a high-spin (S = 5/2) Fe(III) centre, while a value of 1.15 is consistent with an antiferromagnetic interaction.

O'Keeffe et al.[48] performed extensive investigations on a series of synthetic μ-oxo derivatives of 2,4-disubstituted Fe(III) porphyrins, including the Fe(III)PPIX dimethyl ester. Infrared spectra yielded bands between 880 and 886 cm^{-1}, consistent with the observations of Brown et al.[44] and were again assigned to the Fe–O–Fe stretching vibration. The temperature dependence of the magnetic susceptibilities for the series of compounds is consistent with a pair of antiferromagnetically coupled high-spin Fe(III) centres.[48] O'Keeffe et al.[48] further reported UV-visible spectra for the μ-oxo species dissolved in benzene, all of which show the charge-transfer (CT) bands appearing at distinctive positions around 567nm and 590 nm (Figure 1.6). In addition, the authors demonstrated that

the same species does not form spontaneously in aqueous solution but can be induced in aqueous alkaline solution upon addition of a small amount of an organic base (e.g. 10% (v/v) pyridine). Given that sterically hindered pyridines (e.g. 2,6-lutidine) are able to induce μ-oxo dimer formation, the coordination of the organic base to the Fe(III) centre was ruled out in favour of its acting as a solvating agent.

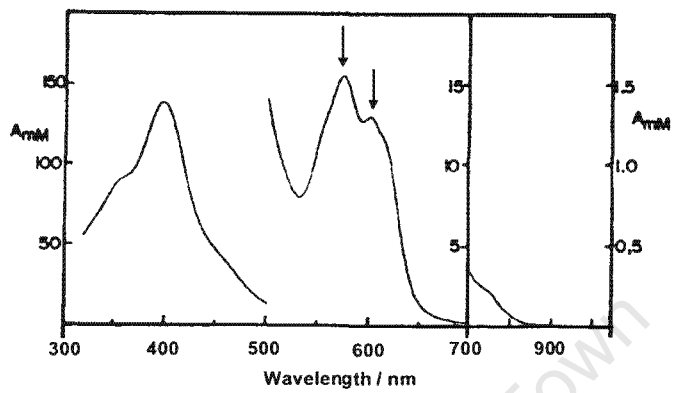

Figure 1.6 The UV-vis spectrum of μ-oxo-bis[protohemin dimethyl ester] in benzene. The characteristic charge-transfer bands are indicated with arrows. Reproduced from reference 48.

The conditions under which Brown et al.[44] obtained the green precipitate included the addition of 1 M NaOH to a solution of DMSO. Based on the evidence provided by O'Keeffe and co-workers,[48] such conditions were almost certainly conducive to induced μ-oxo dimer formation, while low ionic strength solutions at lower pH are not. However, the structural interpretations of Brown et al.[41,44] have been widely accepted, while the work of O'Keeffe et al.[48] has been largely overlooked. With the improved sensitivity of modern instrumentation allowing the investigation of Fe(III)PPIX aqueous solution with concentrations as low as 0.025 μM, a reinvestigation of the data presented by Brown et al.[41] would be an important starting point in determining the true nature of the Fe(III)PPIX aqueous dimer.

1.6 HAEMOZOIN

1.6.1 Chemical Structure Determination

Although haem had been recognised as the chromophore in malaria pigment as early as 1911,[32] early structural determinations of haemozoin suggested that it was

an Fe(III)PPIX–protein complex.[49,50] Pioneering work by Fitch and Kanjananggulpan[51] demonstrated for the first time that purified haemozoin consists entirely of Fe(III)PPIX. The crude material extracted from *P. berghei*-infected erythrocytes was subjected to extensive washing with detergents followed by exposure to a non-specific protease (to remove protein contaminants) and finally freed of lipid contaminants by chloroform/methanol extraction. This result was later confirmed by resonance Raman microspectroscopy, which demonstrated that the Fe(III)PPIX chromophore is detectable in samples of crude malaria pigment. Spectra recorded between 1000 – 1700 cm^{-1} of crude malaria pigment and solid-state haematin were almost indistinguishable apart from differing band intensities.[52] The outcome of an elemental analysis study by Slater et al.[53] corroborated that haemozoin has virtually the same composition as haematin. Furthermore, when solubilised in base, the spectrum of haemozoin was shown to be identical to that of haematin. This work went further to provide the first structural interpretation of haemozoin. The sharply resolved infrared spectrum of haemozoin (Figure 1.7 A) includes two prominent bands at 1664 and 1211 cm^{-1} that are absent from the spectrum of haematin. These peaks, which have now become marker bands for haemozoin, were assigned as C=O and C–O stretching frequencies respectively for unidentate coordination of a propionate group to the Fe(III) centre (Figure 1.7 B). The authors' conclusion that Fe(III) undergoes a change of spin state (from high to low) upon conversion of haematin to haemozoin has since been disproved by Bohle et al.[54] who used EPR and Mössbauer measurements to demonstrate that a high-spin Fe(III) species constitutes haemozoin. Finally, EXAFS data were consistent with an oxygen atom in the first coordination shell of the Fe(III) centre. The authors[53] concluded that haemozoin is a polymer of Fe(III)PPIX units linked together via propionate-Fe(III) coordination (Figure 1.8 A).

A

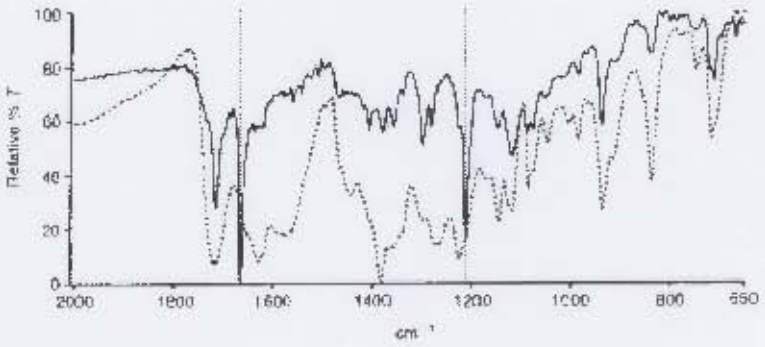

B

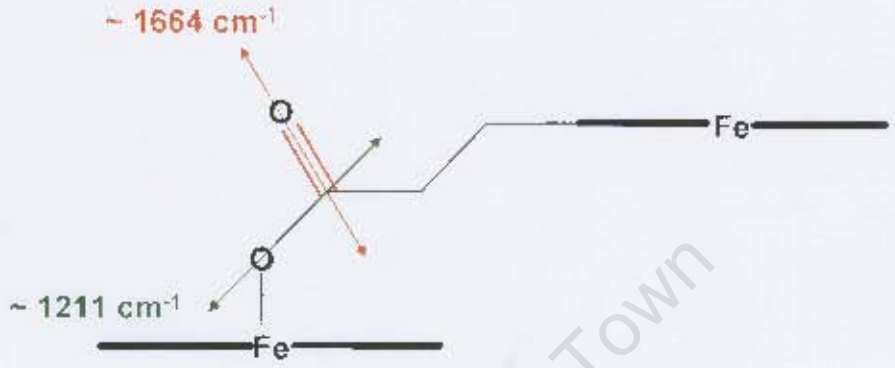

Figure 1.7 (A) The FT-IR spectra of haemozoin (solid line) and haematin (dotted line). Reproduced from reference 53. (B) A schematic representation of the proposed unidentate coordination of a propionate group to the Fe(III) centre showing the C=O and C–O stretches responsible for the sharp bands at 1664 and 1211 cm^{-1} in (A). The solid black lines represent the porphyrin plane.

Over seventy years ago, Hamsik[55] described a synthetic material (β-haematin) that displayed the same solubility properties as haemozoin.[51] Slater et al.[53] showed that the two materials give rise to identical FT-IR spectra and powder X-ray diffraction (PXRD) patterns. Bohle and co-workers[56] were later able to confirm that the synchrotron PXRD patterns of haemozoin and β-haematin are indistinguishable. They determined that the microcrystalline material belongs to a centrosymmetric space group and hence concluded that haemozoin/β-haematin consisted of antiparallel polymer chains (Figure 1.8 B). In 2000, using Rietveldt refinement to solve synchrotron PXRD data, Pagola et al.[57] determined the crystal structure of β-haematin. Unexpectedly, it was found that it is not a polymer, but rather consists of discrete dimers of Fe(III)PPIX. The propionate group of one molecule coordinates to the Fe(III) centre of the second and *vice versa* to form a centrosymmetric cyclic dimer. Hydrogen bonding between dimers, via the propionic acid groups, links these dimers together within a crystal (Figure 1.8 C).

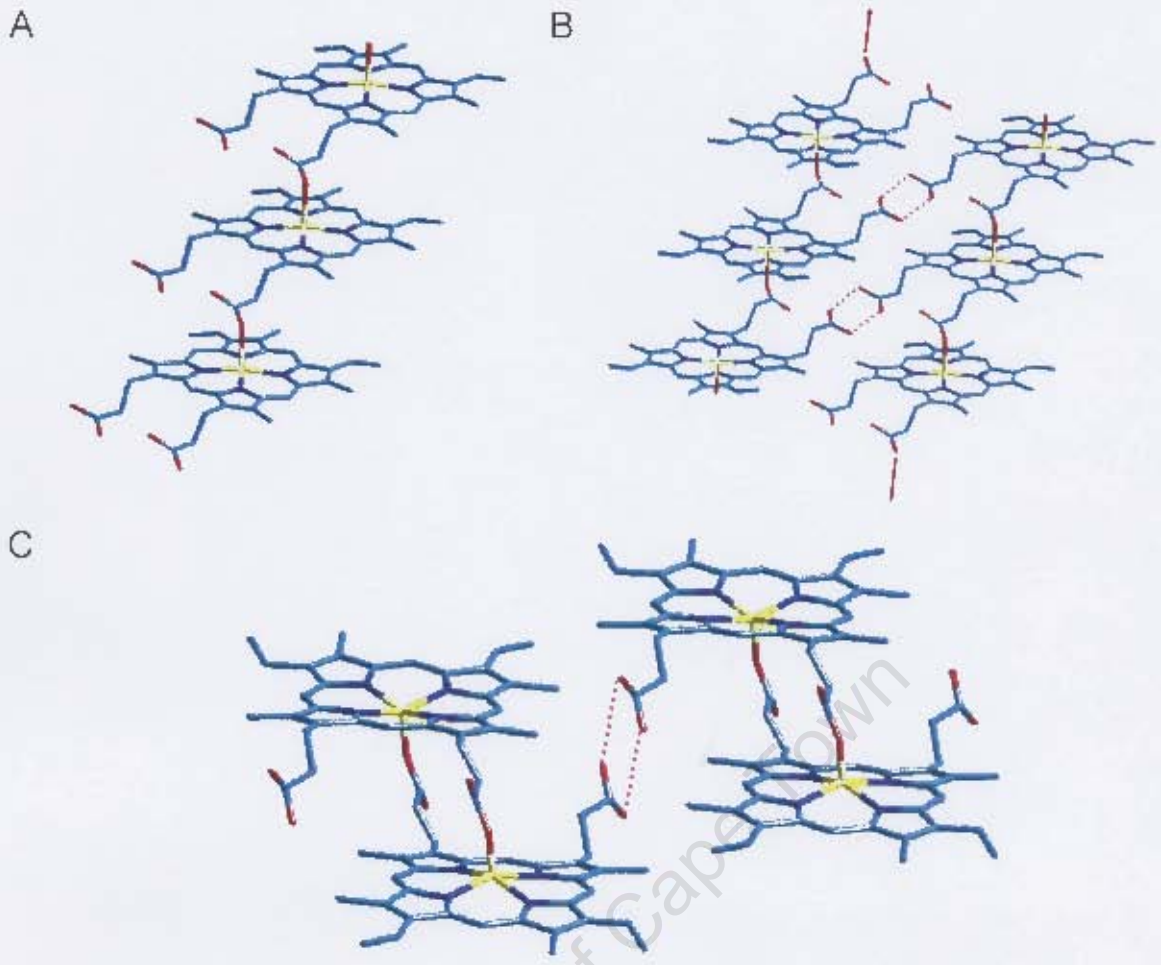

Figure 1.8 The progression in opinion and understanding of the structure of haemozoin. The linear polymer (A) suggested by Slater et al.[53] consists of Fe(III)PPIX molecules linked via coordination of propionate groups to the Fe(III) centre. Bohle and co-workers[56] put forward the idea of antiparallel polymeric chains that interact via hydrogen bonds (B). The true structure (C) consists of centrosymmetric cyclic dimers of Fe(III)PPIX linked by hydrogen bonds.[57] Hydrogen bonds are represented as pink dashed lines.

1.6.2 Methods of β-Haematin Synthesis *In Vitro* and the Mechanism of Formation

Many of the structural interpretations described above were based on experimental observations of β-haematin, the synthetic equivalent of haemozoin.[53] Under non-biological conditions, numerous methods for the synthesis of β-haematin have been developed. The majority involve the use of either organic solvents or organic acids.

In 1993, Bohle and Helms[58] described a room-temperature method of β-haematin synthesis in dry methanol using haemin (Cl–Fe(III)PPIX) and the organic base 2,6-lutidine. The mechanism most likely involves the abstraction of a hydrogen ion from the propionic acid and the chloride ligand from Cl–Fe(III)PPIX by the base (as lutidinium hydrochloride), which allows coordination to take place. An alternative synthetic route involving the initial precipitation of monomeric Fe(III)PPIX from ethanol-water mixtures using concentrated sulphuric acid (H_2SO_4) followed by a 2 hour period of standing at room temperature has been shown to produce β-haematin in good yield.[59] More recently, Huy and co-workers[60] have reported the results of an extensive study in which they investigated the ability of short-chain alcohols (*n*-butanol, *n*-propanol, ethanol and methanol) to induce β-haematin formation. The authors determined that the yield of β-haematin was proportional to the length of the alcohol chains and thus their degree of hydrophobicity. They reasoned that the solubility of haem increased the more hydrophobic the environment. Furthermore, they suggested that the alcohols could reduce the surface tension of the solution, thereby reducing the energy barrier for forming crystal nucleation sites.

In order to compare the synthetic product to haemozoin, Slater et al.[53] prepared β-haematin from haematin dissolved in 0.1 M NaOH to which they added acetic acid. The method required overnight reaction at 70°C after which extensive washing with sodium carbonate buffer (to dissolve unreacted starting material) and distilled water was necessary before the product was obtained (in 40 – 50% yield). In 1994, Egan et al.[61] described a simple method of β-haematin synthesis from 4.5 M aqueous acetic acid, which reaches completion within 1 hour at 60 °C. In order to gain deeper insight into the mechanism, the authors undertook a comprehensive kinetic investigation. They demonstrated that the formation of β-haematin from acetate medium is consistent with Avrami kinetics. Best fits of the sigmoidal kinetics to the Avrami equation yielded a value of $n = 4$. The value of n is a function of the dimensionality of crystal growth and the type of nucleation. A value of 4 indicates spherical growth (in all directions) from sporadic nucleation sites formed throughout the process. More recently, Egan and Tshivase[62] have demonstrated that β-haematin formation from a solution containing 0.050 M benzoic acid reaches completion within 2 hours (60 °C). While the efficiency of

benzoic acid, present at a concentration 90 × less than that of acetic acid, to promote β-haematin formation is far greater, the kinetics fit consistently to the Avrami equation, $n = 4$.

In their original study, Egan et al.[63] proposed that the role of acetate may be to act as a phase transfer catalyst. It was suggested that the formation of β-haematin is congruous to a mineralisation process in which the more soluble solid is precipitated first after which it converts slowly to a less soluble, more thermodynamically stable form. Through substitution at the axial ligand position, the authors proposed that the resultant negatively-charged acetate–Fe(III)PPIX complex may be more soluble than H_2O–Fe(III)PPIX alone, thereby increasing the rate at which β-haematin was able to form. However, for a series of *para*-substituted benzoates, chosen for their increasing electron-donating abilities as indicated by their Hammett* constants, the rate constant was not observed to increase as would be expected if this proposal were correct.[62] Rather, the opposite trend is observed. Thus an alternative role for the organic acids was hypothesised. Egan and Tshivase[62] suggested that the carboxylic acid functional group of both acetic and benzoic acids may disrupt the hydrogen bonding network between porphyrin propionates and axial water ligands to water molecules in the bulk environment, allowing the porphyrins to adopt an arrangement suitable for β-haematin formation. Furthermore, they reasoned that benzoic acid, given its aromatic nature, could interrupt π – stacking between adjacent porphyrins, thus explaining its greater activity (Figure 1.9).

* The Hammett constant is a measure of how electron withdrawing or releasing a substituent is.

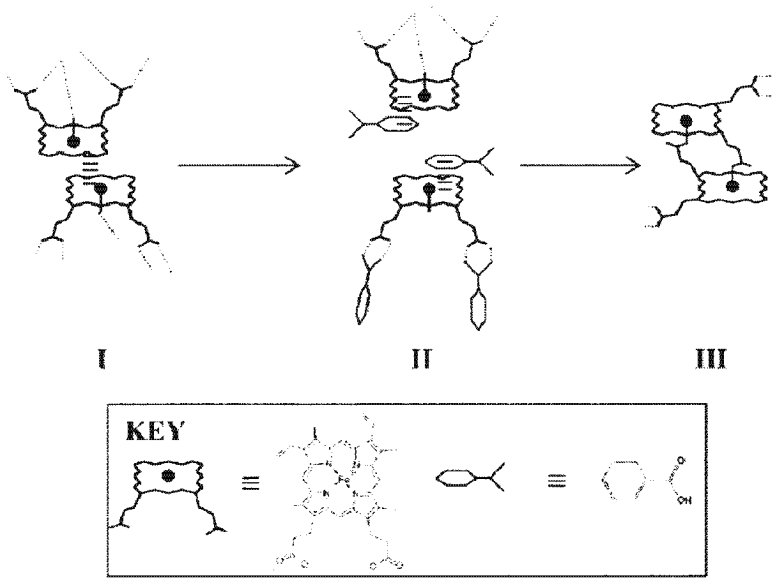

Figure 1.9 The proposed role of organic acids such as benzoic acid in the synthesis of β-haematin *in vitro*. Amorphous haematin (**I**) is able to hydrogen bond (---) to water molecules in the bulk environment as well as to neighbouring porphyrins. It is also able to π – stack (Ξ) as shown. In the presence of benzoic acid (**II**) both hydrogen bonding and π – stacking are disrupted allowing rearrangement of the porphyrins followed by the formation of β-haematin (**III**). Reproduced from reference 62.

Establishing the mechanism of formation of synthetic β-haematin is a significant feat in itself, although its direct relevance to the formation of haemozoin *in vivo* may be limited. Studies performed in both alcohols and organic acids require that Fe(III)PPIX is first solubilised from the solid state before it is able to convert to β-haematin. It is not likely that this energy-intensive sequence of events takes place in the malarial parasite. Rather the evidence suggests that crystallisation of haemozoin is initiated directly from solution.[62]

1.6.3 Mechanism of Haemozoin Formation *In Vivo*

Although the conversion of Fe(III)PPIX to haemozoin is not disputed, the mechanism of this process, proposed to be a form of biomineralisation,[63-65] remains the topic of much debate in the literature.

Observations by Slater and Cerami[66] that heat- and protease-sensitive extracts of *P. falciparum* trophozoites promote haemozoin formation while extracts of uninfected erythrocytes do not, led them to the conclusion that a "haem polymerase" enzyme was responsible. This notion of protein catalysis was supported by Chou and Fitch.[67] Contradictory results were put forward by Dorn et al.[68] who demonstrated that the previously observed "haem polymerase" activity did not in fact diminish when parasite extracts were boiled. Furthermore, exposure to a proteolytic milieu did not have any effect on activity. The authors proposed that haemozoin formation is in fact an autocatalytic process in light of increased "haem polymerase" activity in the presence of either haemozoin or β-haematin. This hypothesis relies on the presence of preformed haemozoin and thus leaves the question of initiation or nucleation unexplained. Furthermore, the *in vitro* formation of β-haematin at high temperatures in the presence of organic acids[61,63] indicates that under biological conditions, the initiation process is likely to be non-spontaneous, requiring an activator.[69]

1.6.3.1 The Involvement of Specific Proteins in Haemozoin Formation

The dependence of haemozoin nucleation on proteins,[70,71] lipids,[28,72-74] or both,[75] has received the greatest support in the literature. In 1996 Sullivan et al.[70] proposed that histidine-rich proteins (HRP), specifically HRP-2 and HRP-3, are responsible for catalysing haemozoin formation. These proteins are rich in histidine (His) and alanine (Ala) and the repetitive hexapeptide sequences Ala-His-His-Ala-Ala-Asp and Ala-His-His-Ala-Ala-Asn (where Asn is asparagine)[76] are believed to contain the binding sites of Fe(III)PPIX.[77] Pandey et al.[75] have suggested that HRP-2, as well as an additional lipid factor are necessary for haemozoin formation. Their conclusions were based on the slow rates of formation in the presence of either HRP-2 or lipid alone. The authors proposed that histidine-rich proteins are responsible for binding and converting Fe(III)PPIX to haemozoin dimers, while lipids are responsible for crystal growth by facilitating the linking of dimers via hydrogen bonding. However, it has been shown that histidine-rich proteins are present at too low a concentration in the food vacuole of *P. falciparum* to provide the required catalytic activity.[78] The hypothesis that histidine-rich proteins participate in haemozoin formation has further been thwarted by recent

evidence demonstrating that haemozoin formation in a *P. falciparum* clone that lacks the necessary genes for HRP-2 and HRP-3 proceeds as normal.[79]

Recently, a novel haem detoxification protein (HDP) has been described.[71] The authors determined that this protein is transported to the parasite food vacuole in the same way as haemoglobin, via cytostome-derived endocytotic vesicles. Recombinant isolates of this protein were investigated for their ability to bind and convert Fe(III)PPIX to β-haematin. The ability of HDP to bind Fe(III)PPIX was found to be four times greater than that of HRP-2, while β-haematin formation was found to be between 1500 and 2000 times more efficient in the presence of HDP compared to either mono-palmitic or mono-oleoly glycerols. It should be noted that these numbers are direct comparisons on a per molecule basis. As discussed below, it is likely that the role of lipids in haemozoin formation is not one of molecular catalysis and therefore this numerical factor does not appear valid. Furthermore, in the protocol followed to bring about β-haematin formation, 0.5 M sodium acetate solution was used to buffer the solutions. As described above, β-haematin formation has been shown to proceed readily in the presence of organic acids, which may have influenced the reaction in the HDP study. The authors report that HDP homologs have been identified in the genomes of *Babesia*, *Theileria* and *Toxoplasma*. These blood-feeding parasites are known not to produce haemozoin,[80] which casts doubt on the relevance of HDP in haemozoin formation in *Plasmodium*. Finally, the authors suggest that HDP catalyses the formation of haemozoin dimers *in vivo* before delivering them to lipid nanospheres for crystal assembly and growth. They dismiss the possibility of HDP acting as a nucleation site even though the formation of haemozoin, a biocrystal, necessarily implies the need for nucleation. Finally, excluding their roles in oxygen transport and electron transfer, haem prosthetic groups themselves are widely recognised as catalytic centres, in which the Fe centre is extremely labile towards axial ligand exchange. It would therefore seem somewhat unlikely that the formation of the propionate–Fe coordination link, the critical step in the formation of haemozoin dimers, would itself require a catalyst.[81]

1.6.3.2 The Involvement of Lipids in Haemozoin Formation

In 1995, Bendrat and co-workers[82] reported the "haem polymerisation" activity of a heat-resistant acetonitrile extract of natural haemozoin. Upon further investigation, active fractions were found to include the methyl esters of oleic, palmitic and stearic acids. Thus, they proposed that the activity of these lipids could account for the previously described autocatalytic activity.[68] Given that such lipid activity could be extracted from both parasitised and uninfected erythrocyes, Ridley et al.[83] proposed that an appropriate pH environment, as in the parasite's food vacuole, was key to the specificity of haemozoin formation. In a comprehensive study carried out by Fitch and co-workers,[84,85] chloroform extracts of erythrocytes infected with *P. berghei* were shown to contain 70% of the "haem polymerising" activity (HPA). Analysis of the extracts by thin layer chromatography revealed that only lipids (cholesterol, phospholipids and acylglycerols) were present. Following hydrolysis, the free fatty acids arachidonic, linoleic, oleic, palmitic and stearic acids were detected. Subsequent investigation of purified lipids indicated that arachidonic, linoleic, oleic and palmitoleic acids as well as mono- and di-acylglycerols, all of them unsaturated, were able to promote the formation of β-haematin. Saturated fatty acids (stearic and palmitic), tri-oleoylglycerol, cholesterol and di-oleoylphosphatidylethanolamine were reported to be inactive. In surmising the specific role of active lipids, Fitch et al.[84] suggested that the lipids co-precipitate with Fe(III)PPIX and provide an environment where enough of the Fe(III)PPIX is able to be solubilised and converted to haemozoin.

More recently, specific evidence that haemozoin is a lipid-mediated process, has been increasing. Using Nile Red dye (a hydrophobic fluorescent probe) in conjunction with fluorescence imaging, Jackson and co-workers[28] have performed an investigation of the membrane and neutral lipid particle content of parasitised erythrocytes. Figure 1.10 shows a series of bright field and fluorescence images of *P. falciparum*-infected red blood cells. A ring of fluorescence detected around the nuclei of early-stage parasites (Figure 1.10 A) was attributed to the endoplasmic reticulum (ER). In contrast to the diffuse fluorescence from the ER, a more concentrated signal was detected around the food vacuole of early trophozoites (Figure 1.10 B). At the time of schizogony in mature parasites, Jackson et al.

observed compartmentalised signal owing to the presence of individual merozoites. In addition, intense signal was localised at sites that were closely associated with the food vacuole (Figure 1.10 C and D). The corresponding structures were identified as neutral lipid bodies, and were found to consist predominantly of di- and triacylglycerols. The authors went on to demonstrate that suspensions of such lipids promote β-haematin formation as has been shown before.[75,84]

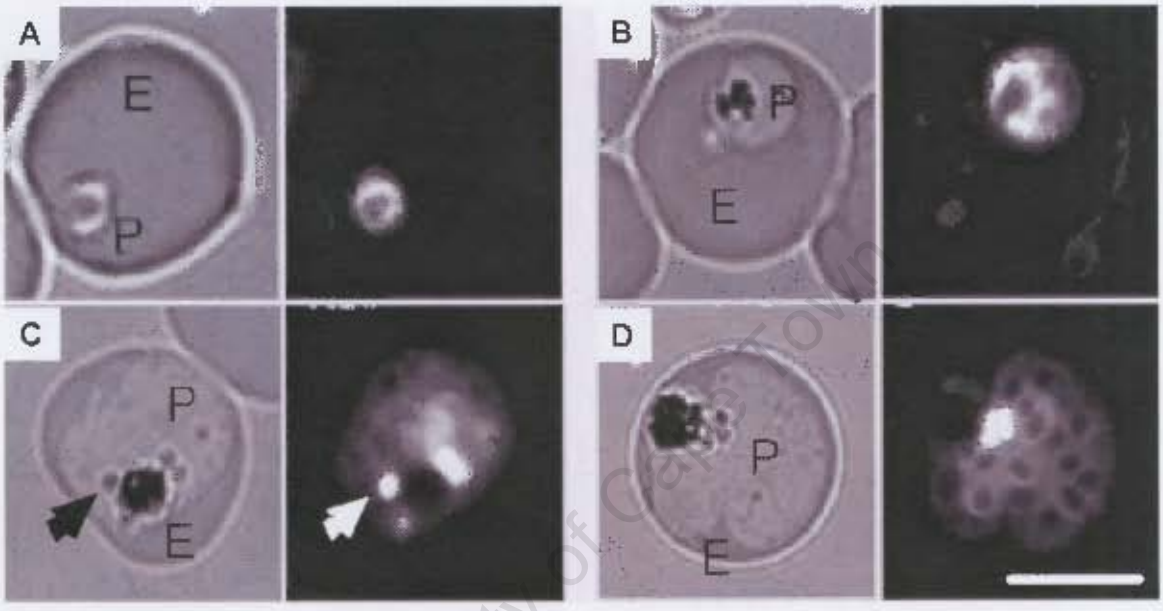

Figure 1.10 Bright field (left) and fluorescence (right) images of *P. falciparum*-infected erythrocytes that have been labelled with Nile Red dye. The various stages of parasitic growth are (A) ring, (B) early trophozoite and (C – D) mature parasites at the time of schizogony. In each case, P indicates the parasite compartment while E indicates the erythrocyte compartment. In C, the white arrow indicates sites of intense fluorescence signal associated with the food vacuole. These correspond to neutral lipid bodies and are indicated by a black arrow in the bright field image. The scale bar = 5 μm. Reproduced from reference 28.

In 2005, Oliveira et al.[86] reported transmission electron micrographs of haemozoin crystals from the luminal gut content of *Schistosoma mansoni* and *Rhodnius prolixus*, two organisms unrelated to the malaria parasite which also detoxify Fe(III)PPIX by the formation of haemozoin. These clearly demonstrate that the haemozoin crystals are present inside lipid-like droplets or in association with membrane-bound vesicles, respectively (Figure 1.11).

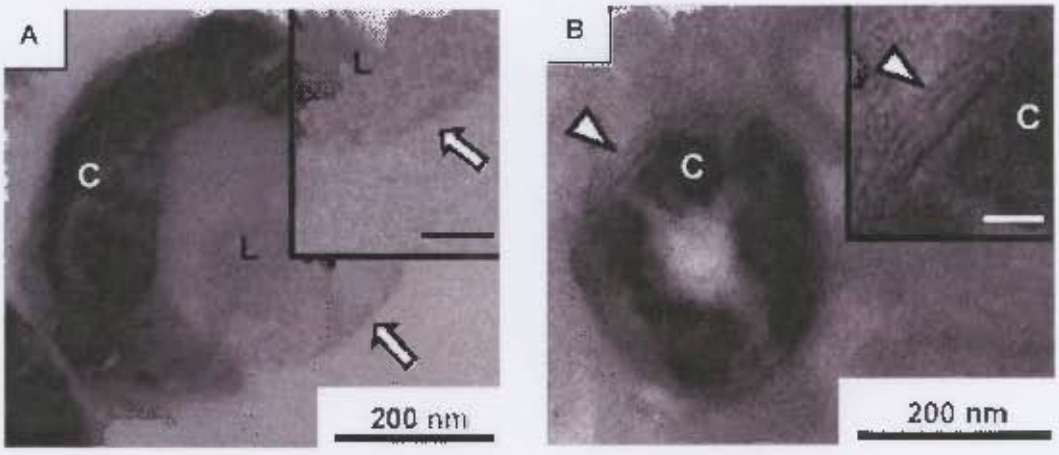

Figure 1.11 Transmission electron micrographs showing haemozoin crystals, C, inside lipid droplets, L, in the luminal gut content of *S. mansoni* (A) and in membrane-bound vesicles in *R. prolixus* (B). Reproduced from reference 86.

In a review on neutral lipids in apicomplexan parasites, Coppens and Vielemayer[72] published a striking electron micrograph in which haemozoin crystals in the digestive vacuole of *P. falciparum* were shown, for the first time, to be enveloped by neutral lipid deposits. Their work laid the foundation to a landmark investigation by Pisciotta et al. in 2007,[74] which revealed nanospheres predominantly formed of neutral lipids inside the food vacuole of *P. falciparum*. Utilising Malachite Green as a fixative agent to preserve neutral lipids during ethanol washing, haemozoin crystals were found to be completely enveloped inside these bodies (Figure 1.12). Scanning electron micrograph (SEM) images of sucrose-purified haemozoin (SPHz) show that the crystals are covered by a lipid film. By contrast, the authors demonstrated that typical ethanol and SDS washing procedures performed in the absence of Malachite Green are responsible for removing all trace of neutral lipid in association with haemozoin. This important observation is able to explain why such structures have rarely been identified before.

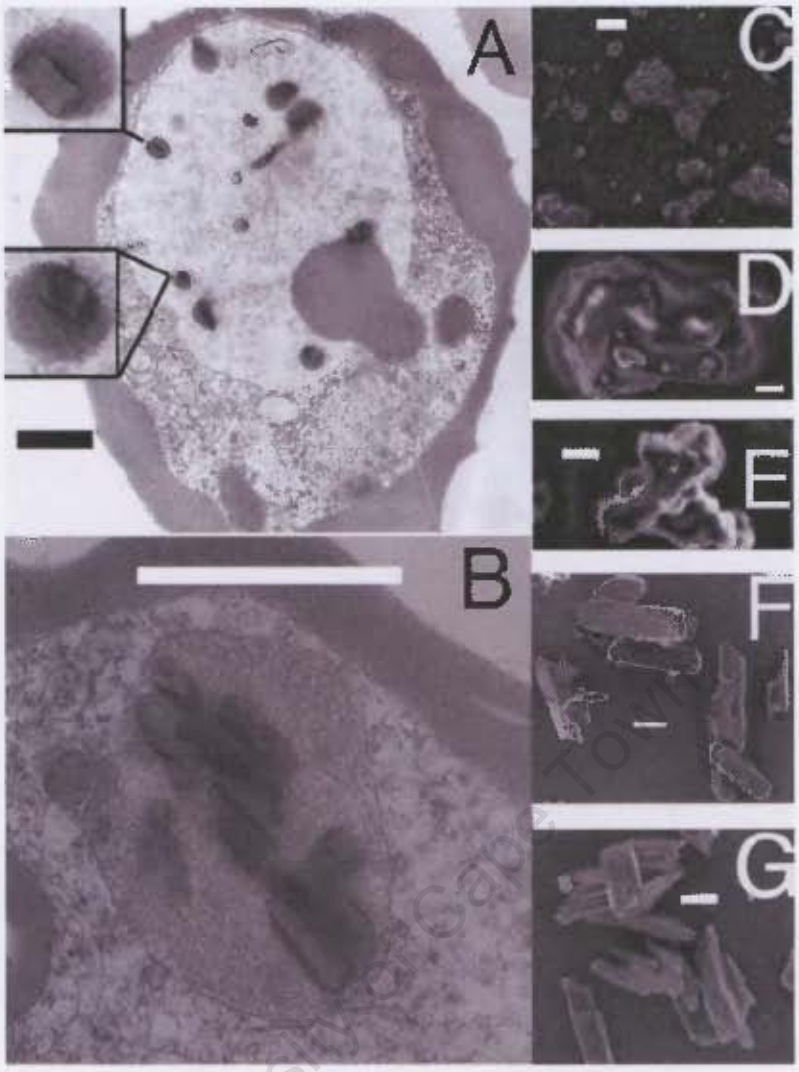

Figure 1.12 Transmission electron micrograph (TEM) images of (A) an early stage and (B) a mature *P. falciparum* trophozoite, both fixed in the presence of Malachite Green and showing haemozoin crystals enveloped by neutral lipid bodies. There is no evidence of a bilayer membrane encircling the lipid bodies (insets, A). Scanning electron micrograph (SEM) images of sucrose-purified haemozoin that has been (C – E) fixed in the presence of Malachite Green, (F) delipidated and (G) delipidated and fixed with Malachite Green. The use of a fixative agent prior to washing preserves a lipid film around haemozoin crystals (C – E) in contrast to washed (F) and subsequently fixed material (G). Scale bar: A, B = 1 µm; C – G = 0.1 µm. Reproduced from reference 74.

Samples of saponin-purified trophozoites and SPHz were analysed by SDS/PAGE and assayed using Coomassie Brilliant Blue. The SPHz fraction was free of protein (Figure 1.13 A). Western-blot analysis (Figure 1.13 B) confirmed that SPHz is not associated with significant levels of proteins specific to *P. falciparum* (Pf), namely Pf-histidine-rich protein (HRP, located in the digestive vacuole), Pf-aldolase (ALD,

located in the cytosol) or Pf-chloroquine resistance transporter (CRT, located in the digestive vacuole membrane). The lipid content of the film accompanying SPHz was analysed by thin layer chromatography (TLC) and mass spectrometry (MS). An abundance of monoacylglycerols (MAG) was detected by TLC in samples of trophozoites, enriched digestive vacuoles and SPHz, while sparing amounts of di- and tri-acylglycerols (DAG and TAG respectively) were detected in the SPHz sample compared to samples of trophozoites and enriched digestive vacuoles (Figure 1.13 C). Fatty acid methyl ester analysis indicated that palmitic and stearic fatty acids were predominant in the sample of SPHz. Electrospray ionisation tandem mass spectrometry (ESI-MS/MS) was used to determine the precise lipids associated with SPHz. The saturated monoacylglycerols MSG (monostearic glycerol) and MPG (monopalmitic glycerol) were present in significant quantities in a ratio of 2:1. Di- and tri-acylglycerols, as well as the polar lipids phosphatidylcholine and phosphatidylethanolamine, were found to be present in comparatively minimal quantities.

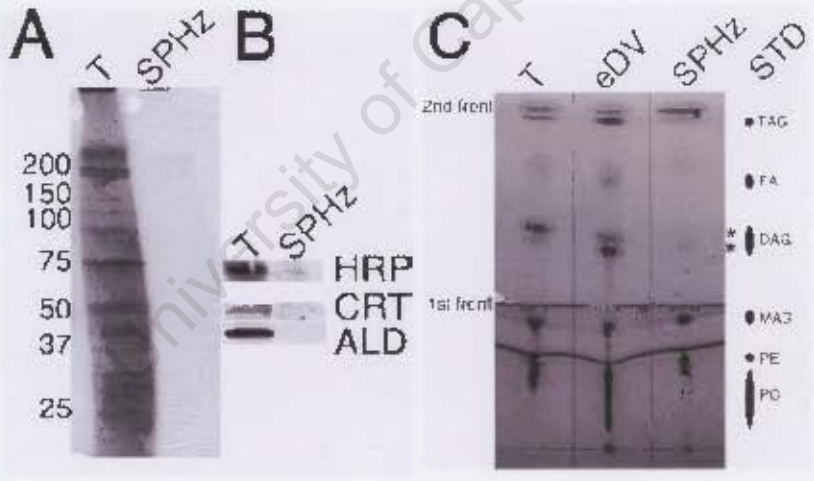

Figure 1.13 (A) SDS/PAGE separation of saponin-purified trophozoites (T) and sucrose-purified haemozoin (SPHz) followed by staining with Coomassie Brilliant Blue. Numbers provide an indication of protein molecular mass (kDa). (B) Western-blot analysis of *P. falciparum* proteins Pf-HRP (a dimer at 2 × 30 kDa), Pf-ALD (40 kDa) and Pf-CRT (48 kDa). (C) TLC analysis of trophozoites (T), enriched digestive vacuoles (eDV) and SPHz. Lipid standards (STD) indicate phosphatidylcholine (PC), phosphatidylethanolamine (PE), monoacylglycerol (MAG), diacylglycerol (DAG), non-esterified fatty acid (FA) and triacylglycerol (TAG). Conditions for separation are: 1st front: chloroform/methanol/water to separate polar lipids; 2nd front: hexane/di-isoproyl ether/acetic acid to separate neutral lipids. Reproduced from reference 74.

The ability of the lipid extracts from SPHz to promote β-haematin formation was investigated and MPG was determined to be the most active in this regard. A neutral lipid blend containing MPG/MSG/DPG (dipalmitic glycerol)/DOG (dioleic glycerol)/DLG (dilinoleic glycerol) in the ratio 2:4:1:1:1 (by volume) was found to produce β-haematin crystals rapidly within 10 minutes and the process was not inhibited by globin. Since the digestion of haemoglobin in the food vacuole will result in high concentrations of globin, it is reasonable to assume that the process of haemozoin formation should be unaffected by this protein. In explaining the role of these lipid nanospheres, the authors[74] suggested that the lipid/aqueous interface that these bodies present is key to the formation of haemozoin crystals. They postulated that free Fe(III)PPIX accumulates in the lipid and is converted to haemozoin when it makes contact with the interface and achieves the necessary protonation state according to the acidic environment. Specifically, the hydrophobic environment favours the loss of the axial water molecules upon coordination of the propionate group to the Fe(III) centre.

In order to investigate the possible role of the lipid/water interface in haemozoin formation, Egan and co-workers[73] developed a simple two-phase model system. In the original biomimetic system, organic solvent (pentanol or octanol) was used as a lipid substitute and Fe(III)PPIX was introduced close to the resultant alcohol/water (50.0 mM citrate buffer, pH 4.8) interface. Infrared spectra and powder XRD patterns as well as SEM images of the product collected from the interface after 30 minutes incubation (37°C) clearly demonstrate that the product is β-haematin. The Resonance Raman spectrum of the product formed near the pentanol/water interface was recorded *in situ* using a × 60 water immersion objective. The spectrum is consistent with haemozoin. Investigations on the effect of conditions on the model system indicated that β-haematin formation was optimal in the pH range 4.8 – 5.5 with little yield at pH conditions greater than 6. This is consistent with the pH of the food vacuole.[20] While changes to the identity of the aqueous buffer did not influence the formation of β-haematin, control experiments carried out in aqueous or organic medium alone yielded no product. In order to investigate the formation of β-haematin under conditions that more closely modeled the biological environment of the food vacuole, a multilayer of the lipid *rac*-glycerol 1-myristate (MMG) was used as a substitute for the organic solvent

layer. MMG is an example of a saturated neutral monoacylglycerol and is structurally similar to MPG and MSG determined in the study by Pisciotta and co-workers,[74] differing only by having two and four fewer $-CH_2$ units it its alkyl chain than MPG and MSG respectively. Kinetic data of β-haematin formation at the lipid/water interface were fitted to a first-order equation and yielded a half-life (5.3 minutes) that is sufficient to account for haemozoin formation *in vivo*. In total, eleven lipids were investigated. In agreement with the conclusions reached by Pisciotta and co-workers,[74] mono- and di-acyl glycerols showed good activity while the triacylglycerol TOG (trioleoylglycerol) was shown to be least active.

Molecular Dynamics (MD) simulations, performed in vacuum which is somewhat similar to a low dielectric lipid environment, have provided valuable insight into the mechanism of haemozoin formation at the lipid/water interface.[73] Results showed that two H_2O-Fe(III)PPIX molecules, when placed in a back-to-back conformation, convert rapidly (7.5 ps simulation time) to a "haemozoin precursor dimer" (Figure 1.14). In this intermediate state, the negatively charged propionate group of one molecule is electrostatically attracted to the positively charged Fe(III) centre of its partner molecule and *vice versa*. The authors suggested that a simple ligand exchange process followed by bond formation would facilitate the formation of the haemozoin dimer. In vacuum the haemozoin dimers were also observed to interact with each other via hydrogen bonding between propionic acid groups. In a simulated aqueous environment however, the previously observed electrostatic interactions in the "haemozoin precursor dimer" were disrupted, and the propionate groups were observed to interact with solvent water molecules instead. This latter observation accounts for the absence of β-haematin product from aqueous control experiments described above.

Pisciotta et al.[74,87] concluded that a non-polar neutral lipid environment is essential for haemozoin formation. More specifically, the experiments and MD simulations performed by Egan et al.[73] have provided strong evidence that a lipid/water interface is necessary for the formation of haemozoin. However, two important questions remain unanswered. Firstly, it is evident that there is a crucial link between the structure of Fe(III)PPIX in aqueous solution and the mechanism of haemozoin formation at a lipid/water interface. As discussed above (1.5.2),

Fe(III)PPIX has widely been thought to exist in aqueous solution as a μ-oxo dimer. However, the proposed mechanism of haemozoin formation at the lipid/water interface requires that this species is present as a $\pi - \pi$ (back-to-back) dimer. To date, no evidence of such a dimer of Fe(III)PPIX exists, although it is obvious that an investigation of this question would be invaluable. The second question that remains concerns the way in which haemozoin crystals are nucleated. The recent discovery of the novel haem detoxification protein (HDP) suggests that proteins may play an active role in this regard, although the authors dismissed such a notion without evidence.[71] Given that crystal growth takes place from a nucleation site, it is expected that the molecule/s responsible for nucleation would be detectable in purified samples of haemozoin.[81] Pisciotta et al.[74] were unable to detect any protein content in samples of SPHz, suggesting that proteins may in fact not be responsible for haemozoin nucleation after all. Lipid molecules were, however, detected in samples of SPHz. Interestingly, electron micrograph images of haemozoin crystals inside the food vacuole of *P. falciparum* are often noticeably aligned.[24] In combination, these two observations suggest that haemozoin formation may take place via epitaxial nucleation at the lipid/water interface, although there is no direct evidence to support this proposal to date. Finally, proteins may act as molecular "chaperones" to transport Fe(III)PPIX to the site of lipid-mediated nucleation.[73,74]

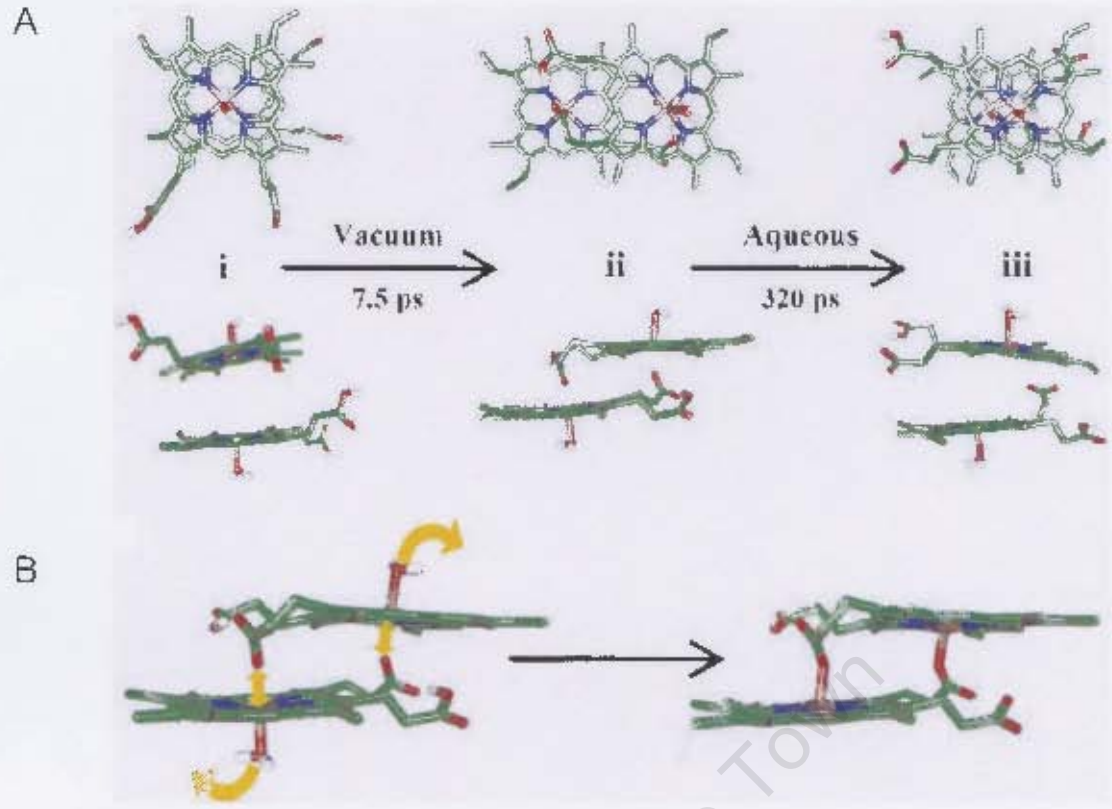

Figure 1.14 (A) The Molecular Dynamics (MD) simulation of the interaction between two monoprotonated molecules of H_2O–Fe(III)PPIX (top row shows an aerial view while the bottom line shows a side view). At the start of the simulation, the molecules were placed in a back-to-back conformation in which the extended propionate groups were far away from each other (i). In vacuum, the two molecules very quickly adopted the conformation of the "haemozoin precursor dimer" (ii). The enlarged image in (B) illustrates the coordination and loss of axial water ligands that is necessary to form the haemozoin dimer. In a water box containing 4030 explicit water molecules, the propionate groups of the "haemozoin precursor dimer" moved away from the Fe(III) centres to interact with solvent molecules (iii). Water molecules have been removed for clarity. Total simulation time = 5 ns. No further changes in conformation were observed after the times indicated. Reproduced from reference 73.

1.6.4 Oriented Crystal Nucleation at Interfaces

The proposal that haemozoin crystals form at a lipid/water interface is not unfounded. It is well established that in general, crystalline monolayers of amphiphilic molecules induce oriented nucleation of molecular and inorganic crystals as a result of structural complementarity or lattice epitaxy between the head groups of the monolayer and the exposed molecular moieties of the crystal.[88]

A Langmuir monolayer is a sheet of amphiphilic molecules oriented such that their hydrophilic heads and hydrophobic tails are arranged on opposite sides of the sheet (Figure 1.15).[89] Such an arrangement only takes place at the interface between two phases of differing hydrophilicity, of which the air/water interface is the most extreme example.

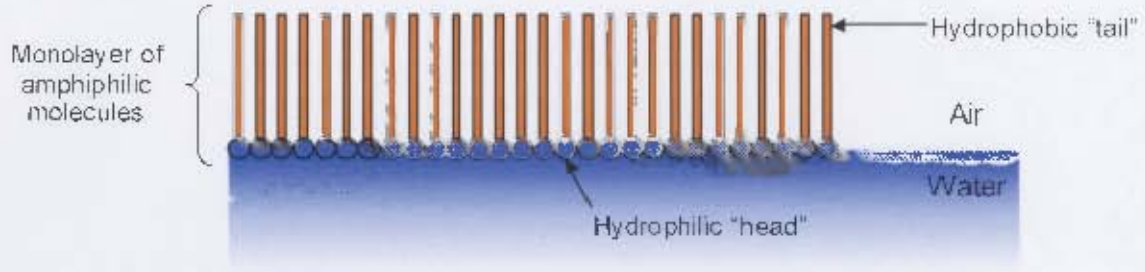

Figure 1.15 A schematic representation of a Langmuir monolayer. Amphiphilic molecules assemble as a monomolecular sheet at the air-water interface.

1.6.4.1 Case Studies of Crystal Nucleation at Interfaces

Cholesterol is an abundant sterol in animal tissues and is an important constituent of cellular membranes. When present in atypically high concentrations, cholesterol crystallisation has also been implicated in the formation of gallstones in human bile.[88,90] The organisation of cholesterol at the air/water interface has been investigated by grazing incidence X-ray diffraction (GIXD), a surface sensitive technique.[90] Measurements of the cholesterol film in an uncompressed state yielded a single broad Bragg peak in the GIXD pattern. A film thickness of 14.5 Å was calculated from the width of the integrated Bragg rod and corresponds to a monolayer. Furthermore, the authors determined that the long axis of the molecules was aligned perpendicular to the plane of the water surface. Upon compression of the film, several sharp Bragg peaks were evident in the GIXD pattern. The data corresponded to a rectangular unit cell with two molecules in the layer plane (i.e. a bilayer). Further cycles of compression and decompression yielded additional Bragg peaks with time in accordance with a crystalline trilayer. Structure analysis revealed that the molecules were in the same arrangement as the 3-D crystal lattice of cholesterol monohydrate,[88] the species present in gallstones.[91]

Fairland et al.[92] have studied the biomineralisation of calcium carbonate ($CaCO_3$). The templating effects of a monolayer of amphiphilic resorcarene-type molecules at the air/water interface were investigated with respect to the nucleation of $CaCO_3$ crystals. An amorphous phase of $CaCO_3$, induced in the presence of poly(acrylic acid-sodium salt) (PAA) and Mg^{2+} ions, was allowed to deposit and grow onto the monolayer over a period of days. By altering the ratio of PAA and Mg^{2+} ions in solution, different crystalline forms of $CaCO_3$ were obtained. Tablets and films of a similar size and morphology compared to those that constitute the nacre of mollusk shells were observed together with calcite fibres similar to the rods in sea urchin teeth.

In a final example, the oriented nucleation of crystals of inorganic salts such as sodium chloride (NaCl) has been discussed in the context of epitaxial-type growth. Jacquemain et al.[93,94] have reported that crystallites of NaCl precipitate from aqueous solution in a cubic arrangement displaying six (100) faces. However, when crystallised at a monolayer of the fluorocarbon 1H,1H,2H,2H-per-fluorododecyl aspartate (PFA), the less stable (110) face was found to be responsible for nucleation. The authors report that the (110) face contains alternating rows of Na^+ and Cl^- ions separated by a distance of 2.8 Å. At the experimental pH of ~ 7.0, the authors propose that the head-groups of the PFA monolayer are zwitterionic ($^+H_3NC(H)(R)CO_2^-$), and that the 2.6 Å distance between the NH_3^+ and CO_2^- moieties matches fairly well with the separation between point charges exhibited at the (110) face of NaCl. Thus the partial electrostatic complementarity between the PFA monolayer surface and the crystal face appears to influence the growth of the NaCl crystals, even to the point that a less stable form results.

1.6.4.2 Haemozoin Crystal Morphology

A discussion on the orientation and nucleation of haemozoin crystals cannot be appreciated without prior understanding of the habit (i.e. morphology or overall shape) and form (i.e. *hkl* type of faces) these crystals take on. The general morphology of a crystal is related to three classes of crystal faces, which are defined relative to periodic bond chain (PBC) vectors.[95] These vectors run in

directions that are parallel to the translation relating two adjacent "building units" and are periodic given the equivalence of each new "building unit" added to the crystal. Flat (*F*) faces contain two coplanar PBC vectors, stepped (*S*) faces contain one PBC vector and kinked (*K*) faces contain no PBC vectors (Figure 1.16). The attachment energy (E_{att}) is defined as the bond energy released each time an additional "building unit" is added (attaches) to the surface of a crystal face. E_{att} is expected to be relatively small for attachment to an *F*-face given that new "building units" need to attach in only one direction (Figure 1.17 A). In the same way, the relative magnitude of E_{att} is expected to increase for attachment to *S*-faces and again for attachment to *K*-faces, as new "building units" need to attach in two (Figure 1.17 B) and all three (Figure 1.17 C) directions respectively. The displacement velocity of a particular face is a measure of the rate at which it will disappear from the overall morphology (i.e. no longer be expressed) and is directly proportional to the magnitude of E_{att}. Thus, *F*-faces exhibit the slowest growth and dominate the crystal habit, while fast-growing *K*-faces are rarely observed. All other faces are *S*-faces (Figure 1.17 D).

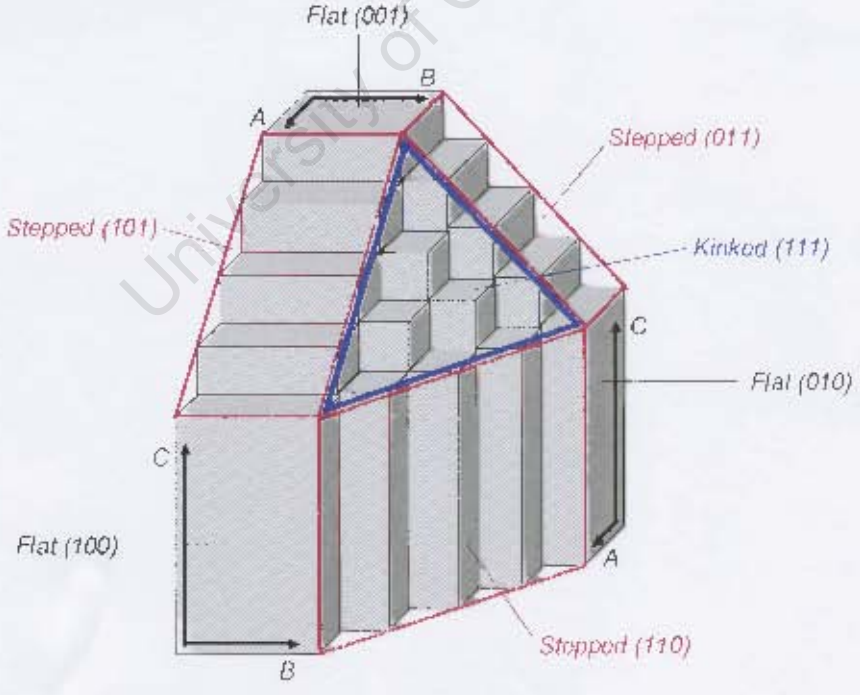

Figure 1.16 A general classification of crystal faces in accordance with the periodic bond chain vectors A, B and C. The *F*-faces (100), (010) and (001); the *S*-faces (110), (101) and (011); and the *K*-face (111) are indicated. Redrawn from reference 95.

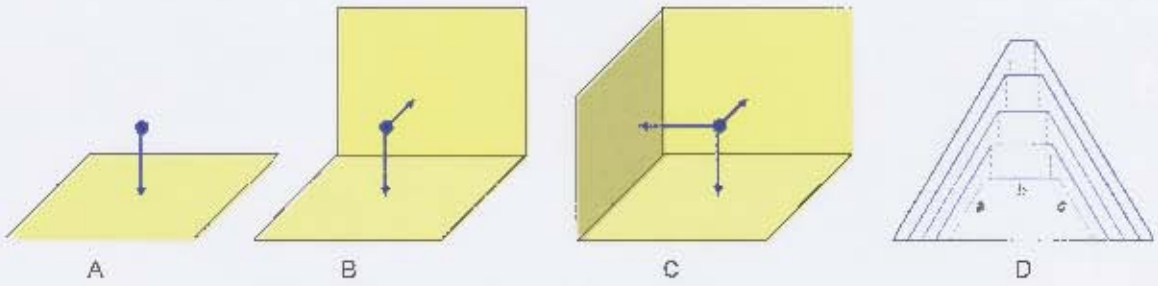

Figure 1.17 The attachment of a new "building unit" to (A) a *flat* face requires interaction in one direction; (B) a *stepped* face requires interaction in two directions and (C) a *kinked* face requires interaction in three directions as shown by the blue arrows.[95] (D) A schematic representation of crystal growth to illustrate the relationship between growth rate and the extent to which a particular face is expressed in the crystal habit. Let three faces of an arbitrary crystal be *a*, *b* and *c*. The growth rate of a particular face, as indicated by the gap between successive parallel lines, is fast in the case of *b* and relatively slower in the case of *a* and *c*. After the passage of four units of time, the slow growing *a* and *c* faces dominate the crystal habit, while the fast growing *b* face has almost disappeared completely (as indicated by the narrowing distance between dashed vertical lines).

Synthetic β-haematin and haemozoin are isostructural[55,96] and share the same unit cell (Figure 1.18 A). Based on the crystal structure of β-haematin,[57] Buller et al.[97] calculated the attachment energies for various low-index crystal faces and were able to determine the theoretical growth morphology of haemozoin crystals (Figure 1.18 B). The derived morphology is needle-like along the *c*-axis, and is dominated by the (100) and (010) *F*-faces. The (011) *S*-face is developed to a lesser extent, while the (001) *F*-face appears as a minor face in this case. The other S- and K-faces are not expressed in the morphology given very large negative attachment energies and corrugated appearances. The theoretical morphology compares favourably to samples of native haemozoin (Figure 1.19 A) and laboratory-synthesised β-haematin (Figure 1.19 B). Buller et al.[97] were further able to estimate the average crystal width-to-thickness ratio. They reasoned that the observed ratio of 1.3 ± 0.5 was consistent with the observation that many of the crystals in samples of native haemozoin were seen to lie on their wide, flat (100) faces.

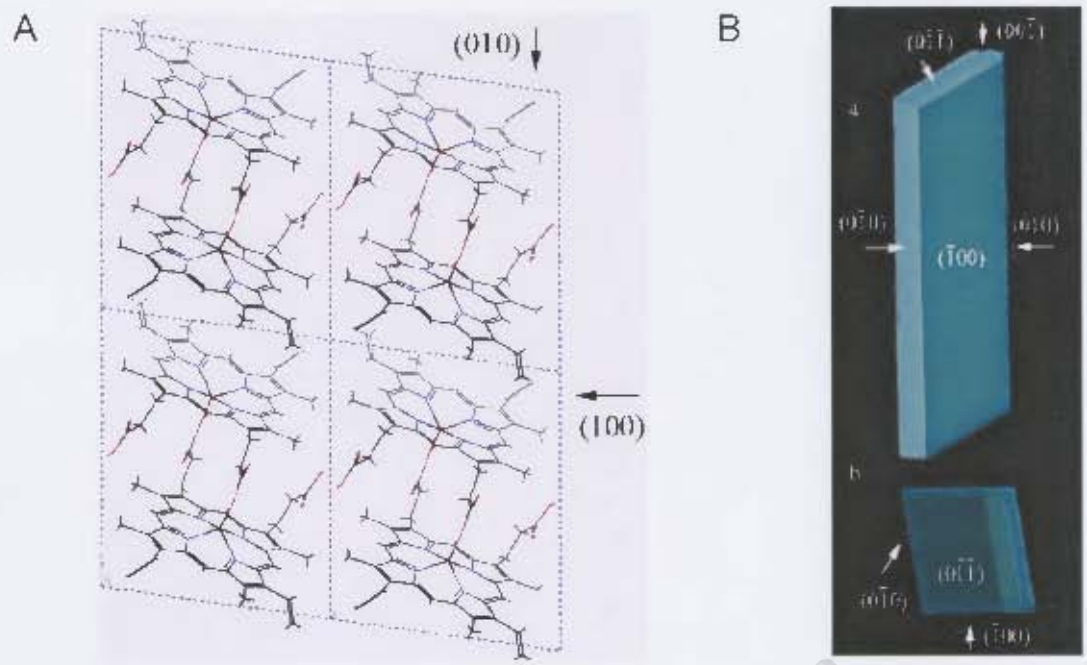

Figure 1.18 (A) The unit cell of β-haematin and packing arrangement as viewed along the *c*-axis. The (100) and (010) faces of the crystal are denoted by arrows. (B) The theoretical morphology of β-haematin crystals viewed along the *a*-axis (top) and *c*-axis (bottom). The most prominent faces are indicated. Reproduced from reference 97.

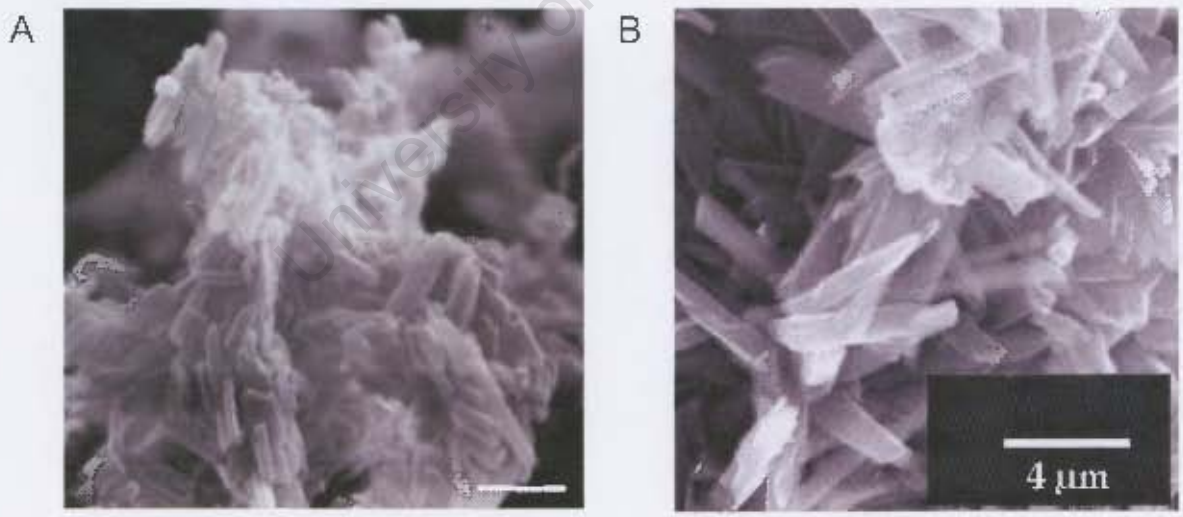

Figure 1.19 Scanning electron micrograph images of (A) haemozoin extracted from *P. falciparum* and (B) β-haematin crystals prepared under anhydrous conditions in the presence of 2,6-lutidine. The scale bars correspond to 1 and 4 µm respectively. Reproduced from references 98 and 96 respectively.

1.6.4.3 β-Haematin Crystals at the Air/Water Interface

In 2007, Solomonov et al.[99] reported monitoring the orientation of β-haematin crystals at the air/water interface by grazing incidence X-ray diffraction (GIXD) and X-ray reflectivity (XR). The "building unit" of the β-haematin dimer, Fe(III)PPIX, is considered as a bolaform amphiphile and was thus suspected to form crystalline multilayers at the air/water interface. Crystals of β-haematin were obtained within 24 hours from a bulk solution of haemin dissolved in 2,6-lutidine in chloroform. This solution was spread on the water surface of a Langmuir trough and the insoluble material subsequently transferred to a gold-covered silicon wafer for further analysis. GIXD and XR measurements of an aged bulk solution spread on the water surface revealed β-haematin crystals arranged according to a preferred orientation. The Bragg reflection corresponding to the (100) peak is almost absent from the GIXD pattern (apart from a very weak reflection near the horizon ($q_h \approx 0$)) (Figure 1.20 A). The GIXD technique is able to detect crystal planes that lie perpendicular to the interface (see Chapter 2.6 for a detailed description). Thus, the almost complete absence of the (100) reflection indicates that the crystals are floating largely on their (100) face. This was confirmed by the presence of a (100) Bragg peak according to XR (Figure 1.20 B), a technique which determines crystal planes parallel to the surface. In the direction perpendicular to the plane of the *bc* face, namely *a** (Figure 1.20 C), the domain size of the crystals was found to be 200 – 450 Å according to the Scherrer formula (see Chapter 2.6, equation 2.10).

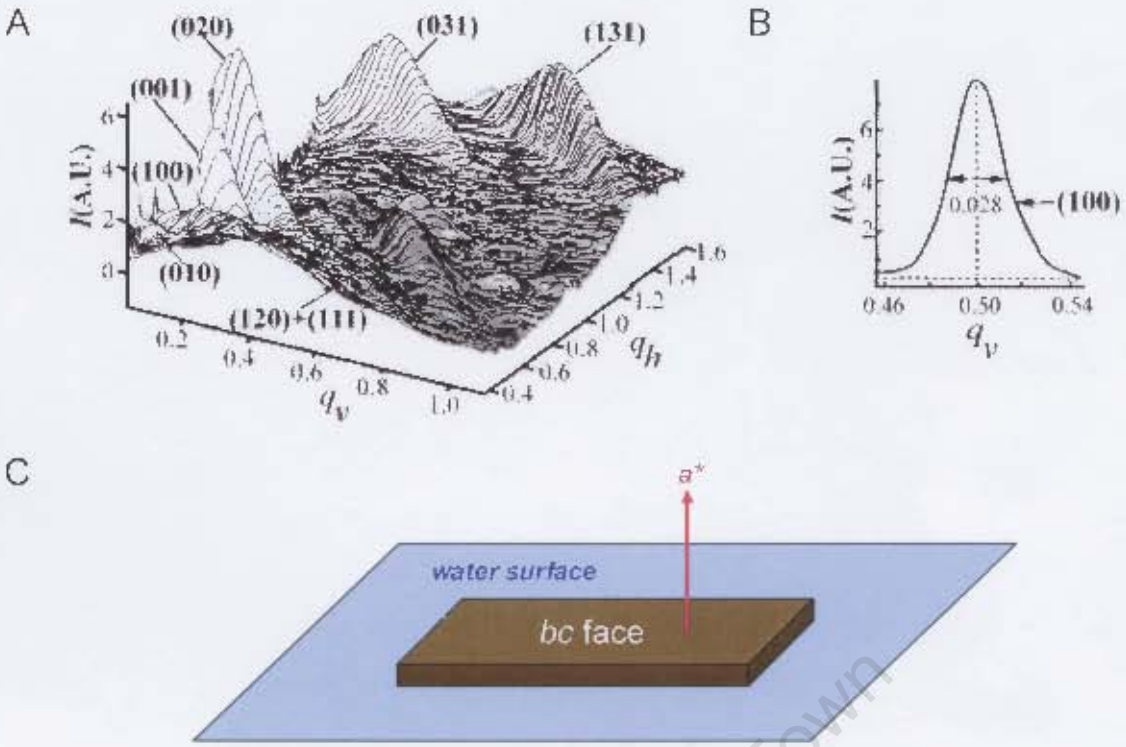

Figure 1.20 (A) The GIXD pattern $I(q_h, q_v)$ of β-haematin crystals floating on their *bc* (100) face on the water surface. The x and y axes represent the horizontal (q_h) and vertical (q_v) components of the scattering vector respectively. The positions of Bragg peaks provide information about the orientation of crystal planes. Reflections appearing at the horizon, where $q_h \approx 0$ (e.g. (100)), are of faces parallel to the surface. (B) The (100) Bragg peak determined by X-ray reflectivity. The full-width-half-maximum corresponds to a crystal coherence length L along a^* of 200 Å. (A) and (B) reproduced from reference 99. (C) A schematic diagram of a haemozoin crystal lying with its *bc* face parallel to the surface.

While the work of Solomonov et al.[99] provides interesting insight into the orientation of β-haematin crystals at the air/water interface, it does not address the more pertinent questions regarding the orientation of β-haematin crystals at the lipid/water interface and the specific role of lipid molecules. Molecular complementarity can be envisaged between the lipid head groups (hydroxyl moieties) and the propionic acid groups of the porphyrin, for example. In this case, the lipids may behave as a nucleating template for Fe(III)PPIX and thus haemozoin/β-haematin. As in the case of NaCl discussed above, it is reasonable to assume that haemozoin/β-haematin nucleated at the lipid/water interface would have a preferred orientation in order to maximise the molecular complementarity. To date however, there is no direct evidence to support these hypotheses.

1.7 QUINOLINE AND RELATED ANTIMALARIAL DRUGS

1.7.1 History of Discovery

The quinoline and related antimalarial drugs (Figure 1.21) have been the most successful class of antimalarial drug for several centuries since the discovery of quinine (QN), a quinoline methanol compound present in the bark of the *Cinchona* tree, in 1630.[100,101] The high demand for QN during World War I and a suspended supply of the drug during World War II due to Japanese occupation of Java (and therefore the *Cinchona* plantations) catalysed the research efforts of both British and German scientists to develop alternate treatments.[101] Chloroquine (CQ) became available soon after World War II and thereafter it was the drug of choice for both the prevention and treatment of malaria. This was largely due to its affordable cost, limited toxicity and excellent potency against the disease prior to the onset of resistance.

1.7.2 Site of Drug Action Within the Parasite

As described in Section 1.3, the symptoms of malaria are associated with the intraerythrocytic stage of the parasite's lifecycle. During its residency in the red blood cell, the parasite is vulnerable to drug action at several stages of its metabolism. Olliaro and Yuthavong[25] have classified the potential targets into three broad categories: (i) those related to processes taking place in the digestive food vacuole of *P. falciparum*, namely haemoglobin degradation and Fe(III)PPIX detoxification; (ii) enzymes responsible for metabolite synthesis, including glycolysis and nucleic acid synthesis; and (iii) those related to membrane processes, including transport and signalling.

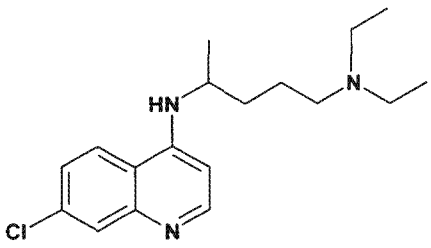

Chloroquine (CQ)

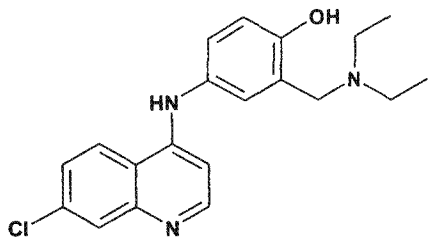

Amodiaquine (AQ)

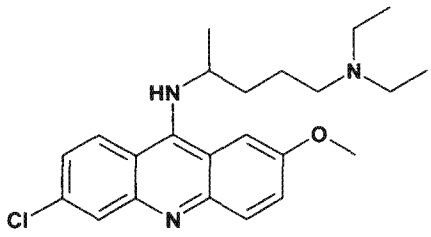

Quinacrine (QC)

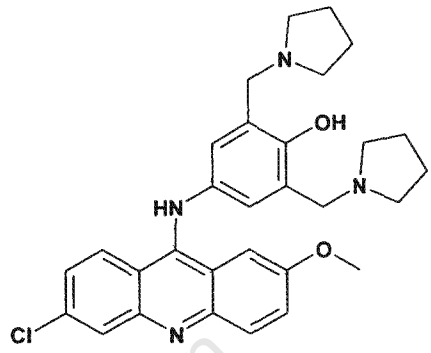

Pyronaridine (PN)

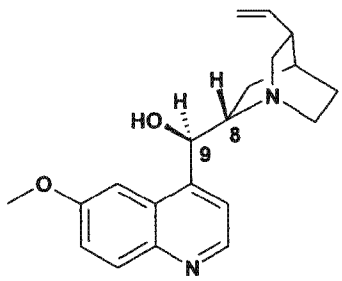

Quinine (QN): 8S, 9R

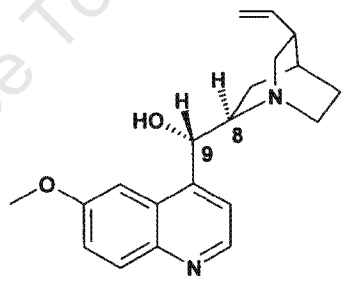

Quinidine (QD): 8R, 9S

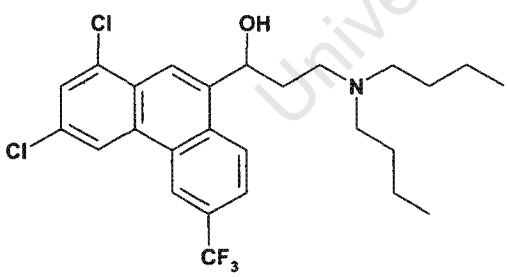

Halofantrine (Hf)

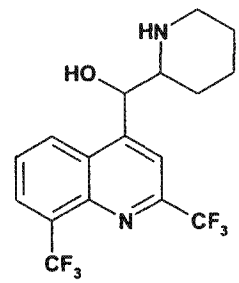

Mefloquine (MF)

Figure 1.21 The molecular structures of a selection of important quinoline and related antimalarial drugs discussed in this work.

Quinolines, specifically the 4-aminoquinolines of which CQ is an example, were originally thought to exert their antimalarial effects outside of the digestive food vacuole (extravacuolar) through interaction with DNA.[102] However, the inhibition of DNA synthesis requires elevated concentrations of drug[103] compared to the low

pharmacological levels that are necessary to kill malaria parasites.[104,105] Furthermore, it has been shown that mefloquine (MF), a quinoline methanol antimalarial, does not intercalate with DNA yet behaves as a competitive inhibitor of CQ accumulation.[106] The evidence suggests that DNA replication is an unlikely target for the quinoline antimalarial drugs. More recently it has been shown that CQ exerts a major effect inside the digestive food vacuole (intravacuolar). The drug is exclusively active against the growing stages of the parasite life cycle during which it digests haemoglobin,[107,108] suggesting that drug treatment may interfere with parasite feeding. Ultrastructural studies support the proposal that the digestive food vacuole is the site of CQ action.[17] Drug treatment has been shown to cause swelling of the parasite's digestive food vacuole as well as clumping of malaria pigment in large vesicles.[109,110] Furthermore, Saliba et al.[111] have detected radioactivity in isolated food vacuoles following treatment with [^{3}H] CQ.

1.7.3 Accumulation of Antimalarial Drugs in the Digestive Food Vacuole

Quinoline compounds are weak bases,[105] with the nitrogen atom in the quinoline ring being the site of protonation. The resonance structures for the 4-aminoquinoline nucleus can be used to demonstrate the increased basicity of the quinoline nitrogen towards protonation in this class of compound (Figure 1.22). Specifically, the lone pair of electrons belonging to the 4-amino nitrogen atom can delocalise into the quinoline ring as shown. All of the antimalarial drugs presented in Figure 1.21 contain a second protonation site in the form of their side chain terminal amine moieties. In their neutral state, the drugs are able to traverse the lipid membrane of infected erythrocytes from the blood plasma (pH 7.4) where they exist at nanomolar concentrations.[101] In an acidic environment such as the digestive food vacuole, the drugs exist as diprotic ions. In this protonated state they become impermeant to membranes and thus accumulate by a mechanism known as pH trapping.[79]

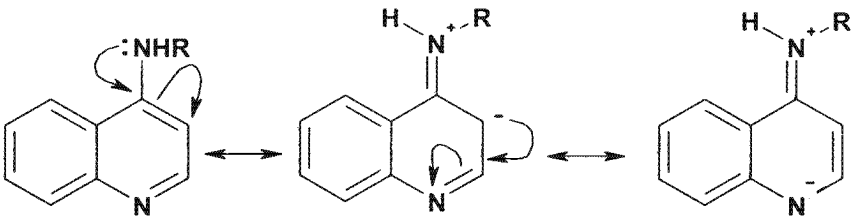

Figure 1.22 Resonance structures for the 4-aminoquinoline core of antimalarial compounds such as chloroquine showing an increased basicity of the quinoline nitrogen atom.

1.7.4 Quinolines Inhibit Haemozoin Formation in the Digestive Food Vacuole

1.7.4.1 Putative Drug Targets in the Digestive Food Vacuole

Inside the food vacuole, drugs are likely to interfere with processes associated with the digestion of haemoglobin, either directly or indirectly. Increases in vacuolar pH,[18,112] inhibition of proteolytic enzymes[113,114] or the inhibition of Fe(III)PPIX detoxification have been suggested as specific modes of action in this regard (Figure 1.23). Although drug accumulation may give rise to increased vacuolar pH, measurements show a change of only 0.25 pH units[115] in parasites exposed to CQ. Furthermore, based on this theory, all weak bases should show antimalarial activity. As this is not the case, increased vacuolar pH is more than likely not the mode of action of quinolines. Rosenthal et al. determined that micromolar concentrations of inhibitors were required to block the activity of a trophozoite proteinase.[113] Such elevated drug concentrations relative to the low pharmacological levels required to inhibit the parasite seem to nullify the second suggested mode of drug action as well.

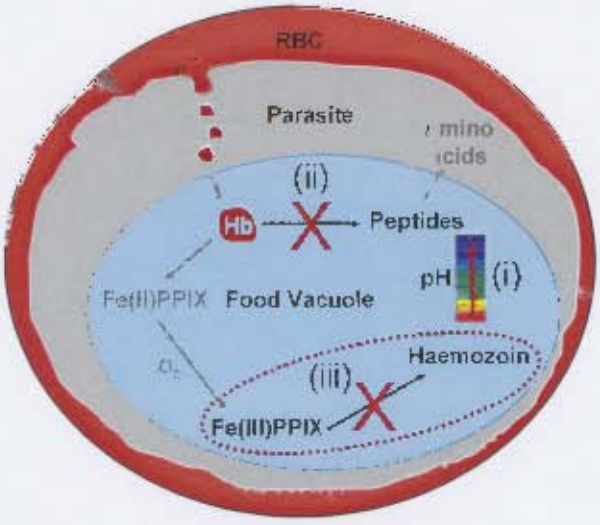

Figure 1.23 The possible modes of action of antimalarial drugs within the digestive food vacuole include (i) an increase in vacuolar pH, (ii) the inhibition of proteolytic enzymes and (iii) the inhibition of Fe(III)PPIX detoxification. The latter process is the proposed target of the important quinoline antimalarial drugs.

1.7.4.2 Identification of Fe(III)PPIX as the Drug Target

Given the ability of CQ to accumulate in the digestive food vacuole and induce pigment clumping, Macomber et al.[109] postulated that these effects were due to the drug binding to Fe(III)PPIX, although they were unable to detect the Fe(III)PPIX–CQ species within malaria parasites. In a definitive paper by Chou and co-workers,[108] dramatic increases in CQ binding following treatment of uninfected erythrocytes by protease extracts of *S. griseus* were demonstrated. On the basis that washing appeared to counteract further CQ binding, the authors reasoned that the precursor was to be found in the cell cytoplasm. Owing to its abundance in the red cell cytoplasm, haemoglobin was investigated first. As determined by equilibrium dialysis, CQ showed no affinity for the protease extract or untreated haemoglobin. Subsequent incubation of the digestion products with CQ gave rise to only two peaks in the chromatogram: one matched CQ and the second, yielding a low protein content, was ascribed to an aggregated form of Fe(III)PPIX. On reaching the conclusion that Fe(III)PPIX was indeed the receptor for CQ, Fitch and co-workers[116] summarised the important structural features believed to be necessary to fulfil its role. Firstly it has a planar ring system of 30 – 40 $Å^2$ in the form of the tetrapyrrole porphyrin core, secondly the Fe(III) centre is able to act as a nitrogen-coordinating functional group and thirdly, it has an appropriately located

propionate functional group capable of interacting with the protonated terminal amine of CQ. Evidence that proteinase inhibitors antagonise the antimalarial activity of CQ, amodiaquine (AQ), QN, MF and halofantrine (Hf) provides further support that Fe(III)PPIX, a product of haemoglobin digestion, is the drug target.[117,118] Finally, both enantiomers of CQ are active against *P. falciparum in vitro*[119] further suggesting that the drug target should be achiral. Fe(III)PPIX is achiral, while proteins, nucleic acids, carbohydrates and even haemozoin possess chiral features.[120]

The proposal that quinoline and related antimalarial compounds target Fe(III)PPIX suggests that these drugs inhibit the formation of haemozoin. Several authors have demonstrated that 4-aminoquinoline, quinoline- and phenanthrene methanol antimalarials inhibit the abiotic formation of β-haematin[61,66,121-128] and that these inhibitory activities correlate with their antimalarial activities (Table 1.2).[124,125] Interestingly, the antimalarially inactive isomers of QN, 9-epiquinine (eQN) and 9-epiquinidine (eQD), do not inhibit β-haematin formation or do so very weakly. As mentioned previously, the tick-borne *Babesia* parasite does not form haemozoin.[80] Interestingly, CQ has been shown to be ineffective against *Babesia* infection.[129] This evidence further indirectly supports the hypothesis that Fe(III)PPIX detoxification is the most likely target for this class of drugs. Specifically, quinoline antimalarials have been shown to arrest β-haematin through a decreased rate of formation.[130,131] Chong and Sullivan[130] monitored the effects of quinoline antimalarials on the kinetics of β-haematin formation using a spectrophotometric "inhibition of crystal growth (ICG)" assay. They determined for the first time that the ICG by CQ and QD is reversible since reactions proceeded to the same point of completion as uninhibited reactions, only over a longer period of time. To probe the mechanism of inhibition further, the authors performed crystallisation experiments in the presence of increased quantities of starting material (Fe(III)PPIX) or β-haematin seed crystals. An increase in the amount of Fe(III)PPIX resulted in no effect on the degree of inhibition, while an increase in the amount of β-haematin seed crystals caused a decreased delay in formation. In order to account for these observations, the authors argued that the Fe(III)PPIX–drug complex was able to reversibly associate with growth sites on the crystal surface. In a similar investigation performed by Egan and Ncokazi,[131] β-haematin

formation was brought about in 4.5 M acetate (pH 4.5, 60°C). Unreacted Fe(III)PPIX was assayed using a pyridine based (Phiβ) method[132] in which the distinct low spin pyridine complex of unconverted Fe(III)PPIX is selectively measured spectroscopically. The authors confirmed that antimalarial drugs act by decreasing the rate of β-haematin/haemozoin formation as opposed to completely blocking it. Specifically they investigated the effect of incubation time on the IC_{50} (drug concentration required to inhibit 50% β-haematin formation) value of various drugs. Contrary to the findings of Chong and Sullivan,[130] their results indicated that the behaviour of the 4-aminoquinoline compounds (CQ and AQ) differed from that of the quinoline methanol compounds (QN and QD).[131] CQ was found to be a strong inhibitor over short times while QN was the stronger inhibitor over long periods.

Table 1.2 Comparison of biological activities (IC_{50}/nM) and β-haematin inhibitory activities for the most common antimalarial compounds

COMPOUND	IN VITRO ACTIVITY	IC_{50} FOR β-HAEMATIN INHIBITION			
	IC_{50}/nM*	IC_{50}/nM#	% BHIA†	HPA/μM‡	PHIβ/EQUIV.*
Chloroquine (CQ)	14.0	–	–	24.4	1.91 ± 0.3
Amodiaquine (AQ)	7.8	–	–	15.1	1.45 ± 0.08
Quinine (QN)	34.2	29.3 ± 9.5	84 ± 1	64.8	3.5 ± 0.2
Quinidine (QD)	21.5	13.4 ± 4.6	85± 9	24.0	1.5 ± 0.1
9-epiquinine (eQN)	–	3471 ± 797	2 ± 13	–	–
9-epiquinidine (eQD)	–	2700 ± 704	12 ± 12	–	–
Mefloquine (MF)	23.4	–	–	46.9	2.9 ± 0.1
Halofantrine (Hf)	5.8	–	–	184.5	0.168 ± 0.002

* Determined for the CQ-sensitive 3D7 strain of *P. falciparum*;[125]

Determined for the CQ-sensitive D6 strain of *P. falciparum*;[121]

† Determined by Warhurst et al.;[128]

‡ Determined by Hawley et al.;[125]

* Determined by Ncokazi and Egan;[132]

– Data not determined.

Though Fe(III)PPIX detoxification has been accepted as the target process for 4-aminoquinoline compounds such as CQ and AQ, the evidence is less clear in the case of the quinoline and phenanthrene methanol compounds (e.g. QN, MF and Hf). The latter compounds are much weaker bases compared to CQ and being monoprotonated under physiological conditions are expected to accumulate less

efficiently in the digestive food vacuole of the malaria parasite.[101] In the case of MF and Hf this is compounded by the fact that these compounds are strongly lipophilic compared to the 4-aminoquinolines and may interact with serum components. A study undertaken by Famin and Ginsburg[133] has demonstrated that QN and MF interfere with haemoglobin ingestion while CQ and AQ interfere with haemoglobin digestion. Furthermore, while MF has been shown to induce morphological changes in the digestive food vacuole, these include degranulation of malaria pigment[134,135] as opposed to the clumping observed after CQ treatment.[109] These observations have led some authors to conclude that the quinoline methanol antimalarials assert their activity according to a different mechanism. However, as discussed above, proteinase inhibitors antagonise the activity of QN, MF and Hf and these compounds inhibit β-haematin formation. Thus the findings of the body of work reported here overwhelmingly support the premise that the 4-aminoquinoline *and* aryl (quinoline and phenanthrene) methanol antimalarial drugs inhibit the formation of haemozoin *in vivo*, resulting in a build up of toxic Fe(III)PPIX.[12,101,136]

The precise manner in which antimalarial drugs such as CQ inhibit the detoxification of Fe(III)PPIX to haemozoin remains unclear. Research in this field has provided three possibilities. The first is that these drug compounds form complexes with Fe(III)PPIX in solution, preventing its incorporation into haemozoin.[61,124,125] Alternatively it has been suggested that these compounds adsorb directly to the surface of growing haemozoin crystals to cap further growth.[57,97] The third possibility is really an amalgamation of the first two ideas. Sullivan et al.[122,137] have proposed that the Fe(III)PPIX–drug complex itself is responsible for capping crystal growth. These hypotheses are explored in the following sections.

1.7.5 Fe(III)PPIX–Quinoline Complexes in Solution

Early studies by Shack and Clark[36] demonstrated that nitrogen-containing compounds such as cyanide and pyridine are able to form complexes with Fe(III)PPIX. Marques and co-workers[138,139] provided further evidence of N-donor ligands being able to form complexes with Fe(III)PPIX species.

1.7.5.1 Spectroscopic Investigation of Fe(III)PPIX–Quinoline Complexes

The first qualitative evidence of an Fe(III)PPIX–CQ complex was reported by Cohen et al.[140] following a spectrophotometric study in which they noticed changes in the UV-visible spectrum of aqueous CQ whilst titrating against increasing concentrations of Fe(III)PPIX. In the absence of quantitative data, however, the evidence pointed only to the fact that such complexes do form but could in no way correlate the existence of a complex with the particular activities of any drug. Chou and Fitch[106] were the first to report association constants for complex formation between Fe(III)PPIX and several quinoline antimalarial drugs, measured by equilibrium dialysis in aqueous medium. Employing the technique of isothermal titration calorimetry, Dorn et al.[124] also measured association constants for complex formation in aqueous solution, though their results were not in agreement with the previous authors. With the benefit of hindsight it is unsurprising that the ensuing data obtained from these studies were difficult to interpret.[141] It is well known that Fe(III)PPIX has a propensity to "aggregate" in aqueous medium[36,37,41] and that aqueous solutions change with time.[39,40]

In order to circumvent the issues arising due to aggregation, studies on quinoline association have been conducted using uroporphyrin I, (uroporphyrin I)Fe(III) chloride (urohaemin I, Figure 1.24 A)[142,143] and the haem octapeptide *N*-acetylmicroperoxidase-8 (*N*-AcMP8) (Figure 1.24 B),[144] all of which show a reduced tendency to aggregate in aqueous solution. *N*-AcMP8 remains monomeric up to 30 μM in solutions of moderate ionic strength and differs from Fe(III)PPIX by having a proximal histidine residue permanently coordinated to one of the axial positions.[144] This results in a six-coordinate Fe(III) centre when a second ligand is present. Urohaemin I is a planar molecule with a chloride ion as the axial ligand at the five-coordinate Fe(III) centre. While this species is able to dimerise,[145] the conditions under which it was investigated were such that the monomeric form was present.[142,143] The data obtained in these two independent studies are not in agreement with each other, or with data collected for Fe(III)PPIX in aqueous medium. The experimental equilibrium constants for binding of CQ and QN are smaller in the case of *N*-AcMP8 compared to Fe(III)PPIX and Fe(III)uroporphyrin I. It has been suggested that the displacement of the Fe(III) centre towards the

coordinated histidine residue reduces the opportunity for ligands to coordinate to the sixth position.[144] The octapeptide chain further weakens interactions with π-donors owing to steric hindrance.[144] These experiments indicate the necessity to carry out investigations on monomeric Fe(III)PPIX itself.

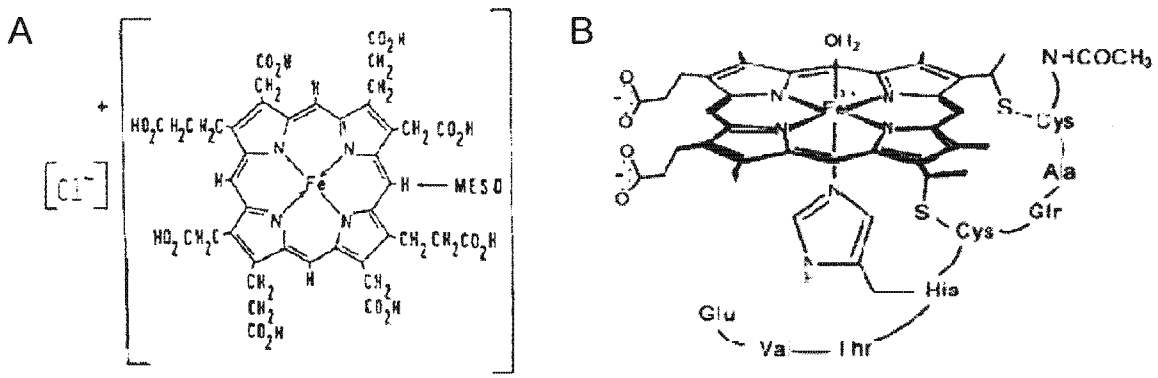

Figure 1.24 The structure of (A) (uroporphyrin I)Fe(III) chloride and (B) *N*-acetylmicroperoxidase-8 (*N*-AcMP8). These compounds have been used to investigate drug complexation owing to their reduced tendency to aggregate. (A) and (B) have been reproduced from references 142 and 144 respectively.

40% (v/v) aqueous DMSO has been used to investigate Fe(III)PPIX–drug interactions. DMSO is a moderately strong coordinating ligand[146] and under these conditions Fe(III)PPIX has been shown to be strictly monomeric.[147,148] The subsequent quenching of the Soret band (405 nm under these conditions) upon titration of Fe(III)PPIX with antimalarial drugs has provided a useful means of determining association constants, measures of stoichiometry and other thermodynamic parameters.[123,126,127,149,150] The association constants for several antimalarial compounds are reported in Table 1.3.

Table 1.3 Association constants for 1:1 complexation between Fe(III)PPIX and various antimalarial drugs in 40% (v/v) aqueous DMSO (20 mM HEPES, pH 7.5)

ANTIMALARIAL DRUG	log K
Chloroquine (CQ)	5.52 ± 0.03*
Amodiaquine (AQ)	5.39 ± 0.04*
Quinine (QN)	4.10 ± 0.02*
Quinidine (QD)	5.02 ± 0.03#
9-Epiquinine (eQN)	4.04 ± 0.03*
9-Epiquinidine (eQD)	4.37 ± 0.02†
Mefloquine (MF)	3.90 ± 0.08*
Halofantrine (Hf)	5.29 ± 0.01#, ‡

* Determined by Egan et al.;[123]

Determined by Egan et al.;[126] ‡ 30% (v/v) acetonitrile included to improve drug solubility;

† Determined by Mavuso[151] in the Egan laboratory.

Mössbauer spectroscopy provides supporting evidence of complexation in the form of distinctly different quadrupole splitting values. Upon titration with drug, the magnitude changes from 0.88 mms^{-1} for free Fe(III)PPIX[152] to 0.38 and 0.21 mms^{-1} respectively for CQ and QN complexes.[153] Resonance Raman difference spectroscopy has been used to investigate complexation between metallouroporphyrins and a series of phenanthroline derivatives.[154,155] The pattern of shifts in the π-density, core-size and oxidation-state marker lines indicate that electronic interactions contribute significantly to the association. Polarisation-resolved resonance Raman spectra[156] support the formation of Fe(III)PPIX–CQ $\pi - \pi$ complexes.

1.7.5.2 Structure of Fe(III)PPIX–Quinoline Complexes

An early spectrophotometric study on the benzene-soluble complexes of QN, QD, MF and related antimalarial drugs with Fe(III)PPIX suggested that direct coordination of the Fe(III) centre by the quinuclidine nitrogen atom of QN and QD and the piperidine nitrogen atom of MF was possible.[157] By contrast, the antimalarially inactive compound eQN showed no evidence of interaction. This was the first indication that Fe(III)PPIX–drug complexation may involve more than $\pi - \pi$ interactions. The results of a subsequent spectroscopic study by Behere and Goff[158] confirmed that coordination between QN and Fe(III)PPIX is possible.

Table 1.3 Association constants for 1:1 complexation between Fe(III)PPIX and various antimalarial drugs in 40% (v/v) aqueous DMSO (20 mM HEPES, pH 7.5)

ANTIMALARIAL DRUG	log K
Chloroquine (CQ)	5.52 ± 0.03*
Amodiaquine (AQ)	5.39 ± 0.04*
Quinine (QN)	4.10 ± 0.02*
Quinidine (QD)	5.02 ± 0.03#
9-Epiquinine (eQN)	4.04 ± 0.03*
9-Epiquinidine (eQD)	4.37 ± 0.02†
Mefloquine (MF)	3.90 ± 0.08*
Halofantrine (Hf)	5.29 ± 0.01#, ‡

* Determined by Egan et al.;[123]

Determined by Egan et al.;[126] ‡ 30% (v/v) acetonitrile included to improve drug solubility;

† Determined by Mavuso[151] in the Egan laboratory.

Mössbauer spectroscopy provides supporting evidence of complexation in the form of distinctly different quadrupole splitting values. Upon titration with drug, the magnitude changes from 0.88 mms^{-1} for free Fe(III)PPIX[152] to 0.38 and 0.21 mms^{-1} respectively for CQ and QN complexes.[153] Resonance Raman difference spectroscopy has been used to investigate complexation between metallouroporphyrins and a series of phenanthroline derivatives.[154,155] The pattern of shifts in the π-density, core-size and oxidation-state marker lines indicate that electronic interactions contribute significantly to the association. Polarisation-resolved resonance Raman spectra[156] support the formation of Fe(III)PPIX–CQ $\pi - \pi$ complexes.

1.7.5.2 Structure of Fe(III)PPIX–Quinoline Complexes

An early spectrophotometric study on the benzene-soluble complexes of QN, QD, MF and related antimalarial drugs with Fe(III)PPIX suggested that direct coordination of the Fe(III) centre by the quinuclidine nitrogen atom of QN and QD and the piperidine nitrogen atom of MF was possible.[157] By contrast, the antimalarially inactive compound eQN showed no evidence of interaction. This was the first indication that Fe(III)PPIX–drug complexation may involve more than $\pi - \pi$ interactions. The results of a subsequent spectroscopic study by Behere and Goff[158] confirmed that coordination between QN and Fe(III)PPIX is possible.

Hyperfine shifts in ^{1}H nuclear magnetic resonance (NMR) peak positions for QN were consistent with coordination of an alkoxide, which led the authors to conclude that this takes place via the deprotonated benzylic alcohol moiety rather than the quinuclidine nitrogen atom. Carried out in non-aqueous solution, the authors reasoned that the formation of the alkoxide species, and thus an overall neutral complex, was favourable in a low-dielectric medium. They suggested that the strong Lewis acid and oxophilic character of the Fe(III) centre would further promote formation of an alkoxide. The study showed that the stoichiometry of Fe(III)PPIX:QN coordination is 1:1. Coordination of QN to the μ-oxo dimer of Fe(III)PPIX was not detected.

In the absence of any crystal structure of an Fe(III)PPIX–drug complex, NMR spectroscopy and theoretical calculations have been relied upon to provide structural insight. Exploiting the paramagnetic nature of Fe(III)PPIX, Moreau et al.[38,159] were the first to use NMR spectroscopy specifically to determine the structure of Fe(III)PPIX–quinoline complexes. Shifts in the ^{1}H NMR spectra of CQ and QN were observed with increasing concentrations of Fe(III)PPIX, a result caused by rapid chemical exchange relative to the NMR timescale. Using mathematical models in analysis, the authors put forward structures of the Fe(III)PPIX–CQ and Fe(III)PPIX–QN complexes in which the quinoline ring was centred over the porphyrin ring in each case and the bulky –Cl atom and $–OCH_3$ group respectively were held away from the porphyrin core. They had assumed a co-planar arrangement of the two ring systems. While the latter point is consistent with the Hunter and Sanders model of $\pi - \pi$ interactions,[160] the relationship between the ring systems of the two molecules is not. Hunter and Sanders determined a laterally off-set relationship to be optimum. Constantinidis and Satterlee[142,143] reached similar conclusions via ^{13}C NMR studies, although they placed QN more towards the edge of the porphyrin compared to the previous authors, suggesting that it might coordinate to the Fe(III) centre through its hydroxyl group. Interestingly, both groups of authors placed one drug molecule between two porphyrins, namely Fe(III)PPIX[38,159] and Fe(III)uroporphyrin[142,143] respectively. Specifically, Moreau et al.[38] assumed a μ-oxo dimer structure for Fe(III)PPIX in their predictions.

The first theoretical attempts to model the interactions of CQ, QN and eQN with an Fe(III)porphyrin were performed *in vacuo* using Molecular Mechanics (MM) and Molecular Dynamics/Simulated Annealing (MD/SA).[144] The authors used a simplified model of *N*-AcMP8 in which an imidazole residue was coordinated to an Fe(III)porphine core to mimic the proximal histidine. Assuming coordination between the Fe(III) centre and 9-hydroxy groups of QN and eQN, quenched dynamics were used to determine all portions of the complex having rotational freedom. In addition to the orientations of the methoxy side chain of the quinoline ring and the vinyl side chain of the quinuclidine ring, the orientations of the quinoline ring relative to the quinuclidine ring as well as to the porphine core were considered to be important. The resultant structures showed that the quinoline and porphyrin ring systems were approximately co-planar, with an interplanar spacing of 3.6 Å. The benzene and pyridine rings of the quinoline nucleus were found to lie over a meso carbon and a pyrrole β-carbon respectively. In both the QN and eQN complexes, the quinuclidine ring was oriented upwards, away from the porphine ring. In the absence of a chemical bond between CQ and the Fe(III) centre, MD/SA calculations were unsuccessful. The following year, O'Neill et al.[161] published a MD/SA study of the Fe(III)PPIX complexes of chloroquine, amodiaquine and tebuquine. In contrast to the NMR-derived structures, the quinoline side chain was partially located over the porphyrin core. The authors later revised their suggestions that a salt-bridge like interaction between the quinoline side chain and propionate group was important for association.

Combining the powers of both NMR and computational methods, Leed et al.[162] put forward solution structures of Fe(III)PPIX–quinoline complexes. Distances between the paramagnetic iron centre of Fe(III)PPIX, assumed to be a μ-oxo dimer, and the protons belonging to the drug were calculated from changes in the T_1 relaxation times observed in ^{1}H NMR experiments using the Solomon-Bloembergen equation. These distance values were then used as constraints in MM/MD calculations, from which minimum energy conformations of the complexes were obtained. The reported structures for diprotic CQ, QN and QD complexed with the μ-*oxo*-dimer of Fe(III)PPIX are shown (Figure 1.25). Key features include the orientation of the quinoline nitrogen atom away from the core while the 4-amino group is located near the Fe(III) centre. In addition, there is no evidence of

coordination in the case of QN and QD and the ring systems are not entirely co-planar. Subsequently, this methodology has been applied to the investigation of complexes of monomeric Fe(III)PPIX with CQ and a series of related analogues.[98] The 100 structures determined for each complex differed by a maximum of 2 kcal mol^{-1} and were observed to have a similar range of conformations. This result was not expected based on distinctly different T_1 NMR values for marker protons (on the quinoline ring) in the different complexes. On the basis of a lack of correlation between experimental (NMR) and calculated structures, several criticisms of the approach of Leed et al.[162] and the use of the Solomon-Bloembergen equation were raised in this study. Firstly, estimate values for the correlation time (τ_c) and net spin-state per Fe(III) centre would be expected to significantly effect the determination of Fe–H distances. Secondly, the use of distance constraints, employed to compensate for the omission of solvent effects from the calculations, would not be expected to yield a true reflection of the complexes that exist in solution. Thirdly, and most importantly, a statistical error in the method was explained. In the Solomon-Bloembergen relationship, the observed T_1 relaxation time, an average for all conformations present in solution, is proportional to r^6 (where r is the Fe–H distance). In light of this, Mabotha[98] demonstrated that the average T_1 relaxation time does not represent a valid means of determining the average Fe–H distance constraints since $\langle r \rangle \neq (\langle r^6 \rangle)^{\frac{1}{6}}$.

Dascombe and co-workers[163] have used MM and Density Functional Theory (DFT) calculations to investigate the possibility that quinolines coordinate to the Fe(III) centre of Fe(III)PPIX via the aromatic nitrogen atom. The mean porphyrin plane of Fe(III)PPIX exhibits necessary distortion owing to steric interactions with the hydrogen at position 2 on the quinoline ring. The contact shifts observed in the solid-state ^{13}C and ^{15}N NMR spectra of Fe(III)PPIX–CQ do provide support for this ligand binding mode;[164] however, there is little evidence to support its existence in solution.[165]

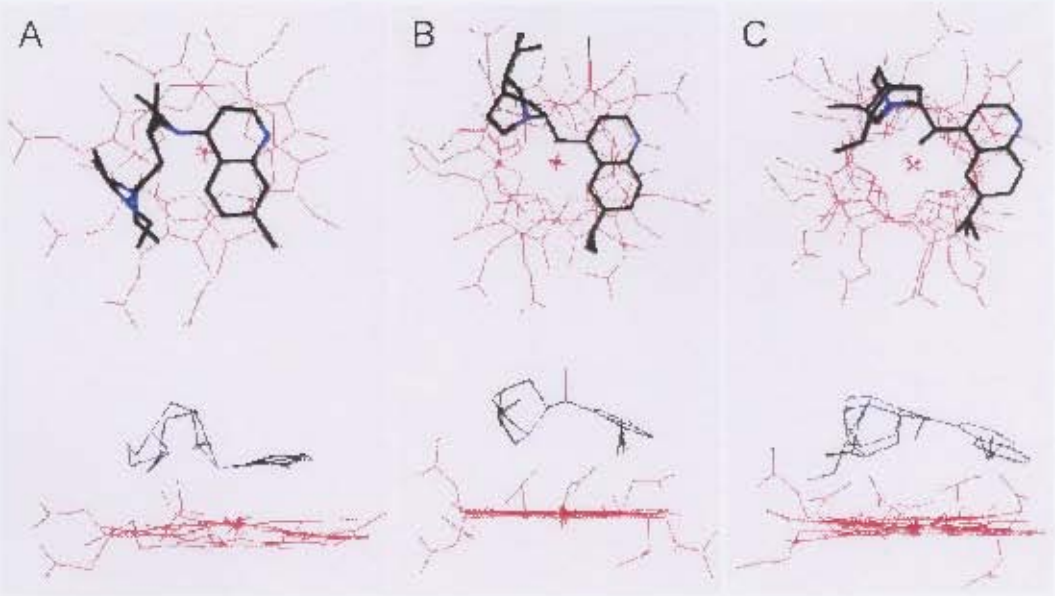

Figure 1.25 Aerial (top) and side (bottom) views of the solution structures of the complexes between diprotic chloroquine (A), quinine (B) and quinidine (C) and the μ-oxo-dimer of Fe(III)PPIX. Protons and the second Fe(III)PPIX monomer in the dimer (bottom view) have been omitted for clarity. The aerial views show that the quinoline nucleus is positioned towards the edge of the tetrapyrrole and not over the metal centre. The side chains wrap back on themselves to follow the edge of the tetrapyrrole. Reproduced from reference 162.

Quantum Mechanical (QM) modelling offers an alternative approach to conventional MM/MD calculations in that specific interactions are modelled according to the attraction between areas of high and low electron density. Vippagunta and co-workers[165] performed the first study of this kind. *Ab initio*[166] and DFT[167] calculations placed the electron-rich quinoline N side of the ring towards the edge of the porphyrin while the electron-deficient 4-amino side is directed inwards towards the core, which is suggested to be electron rich.[167] A criticism of the QM studies is the use of neutral quinolines. Given the acidic environment of the digestive food vacuole, compounds are likely to exist in a protonated state. Indeed protonation of the quinoline nitrogen atom has been shown to cause a significant redistribution of electron density, which highlights the importance of modelling the biological conditions as far as possible in order to obtain reliable structures.

1.7.5.3 Structure-Activity Relationships

Extensive studies have been carried out to investigate the structure-activity relationships for a series of 4-aminoquinoline compounds, including CQ (Figure 1.26).[127,149,166] Egan et al. [127] confirmed that the quinoline and terminal amine nitrogen atoms, being weakly basic, are necessary for drug accumulation via pH trapping, while Vippagunta et al.[166] recognised the terminal amine nitrogen atom as important in CQ drug resistance. Both research groups determined that a moderately electron withdrawing and strongly lipophilic group at the 7-position is needed to maximise the drug's biological activity. The introduction of a 7-chloro group has proven to be most effective in the inhibition of β-haematin formation. Finally, the planar electron-rich π-conjugated quinoline ring system was found to be essential for $\pi - \pi$ association.

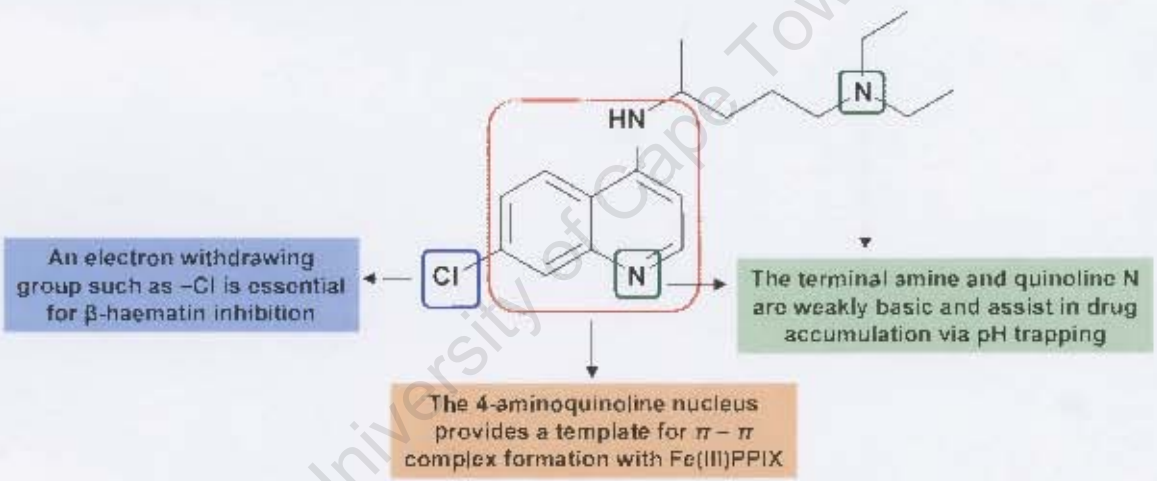

Figure 1.26 A summary of the structure-activity relationships for 4-aminoquinoline antimalarials such as chloroquine, shown here. Redrawn from reference 127.

In contrast to the 4-aminoquinoline antimalarials, determination of the structure-activity relationships for the quinoline (and phenanthrene) methanol compounds has been less clear. In 1991, a conformational analysis of the *Cinchona* alkaloids was performed using theoretical Quantum Mechanics/Molecular Mechanics (QM/MM).[168] The authors concluded that the ability of the compounds to form *inter*molecular hydrogen bonds at their receptor site was possible in the case of the *erythro* isomers (QN (8S,9R) and QD (8R,9S)) but not in the case of the *threo* isomer eQD (8R,9R). In the latter compound, given the orientation of certain groups, they suggested that *intra*molecular hydrogen bonding was more likely,

thus explaining the compound's inactivity at the receptor site. In contrast, a crystallographic study of the four *Cinchona* alkaloids (QN, QD, eQN and eQD) showed that formation of *inter*molecular hydrogen bonds with their hydroxyl and amine groups was possible in all cases.[21] However, a 90° difference in the "torsion angle" between the C9–O12 and N1–HN1 bonds in *erythro* alkaloids compared to *threo* alkaloids was observed (Figure 1.27). As a result, the authors suggested that the *threo* alkaloids would have a reduced ability to form intermolecular hydrogen bonds to cellular constituents in the same direction as the *erythro* alkaloids, and that this structural difference may be the key to explaining their differing antimalarial activities.

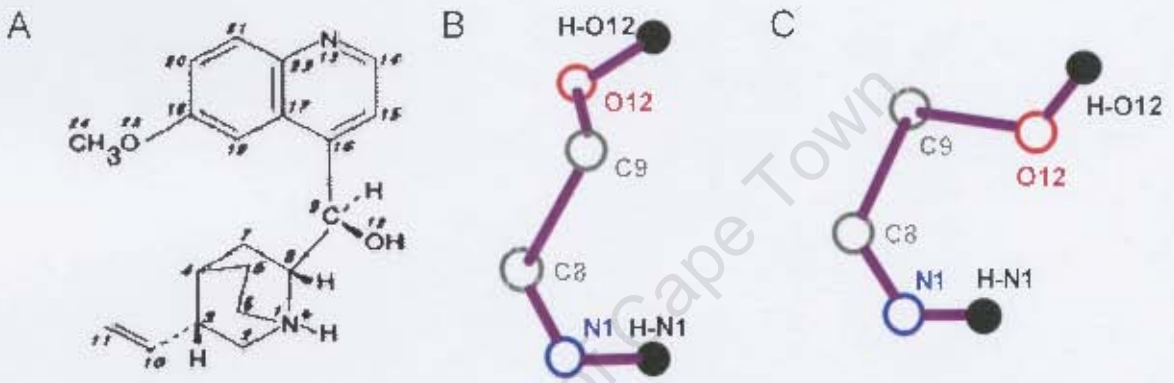

Figure 1.27 (A) The molecular structure of 9-epiquinidine showing the numbering scheme adopted by Karle et al. in italics. Reproduced from reference 121. The orientation of the HN1–N1–C8–C9–O12–HO12 segment for (B) quinidine sulfate dihydrate and (C) 9-epiquinidine hydrochloride monohydrate. Redrawn from reference 121. Karle et al. proposed that the orientation of the N1–HN1 and C9–O12 bonds would influence the direction of intermolecular hydrogen bonds formed with the hydroxyl and amine groups to cellular constituents, thus explaining the differences in activity of the *Cinchona* alkaloids.

As described in 1.7.5.2, Warhurst was the first to provide evidence for coordination between antimalarially active quinoline methanol compounds and Fe(III)PPIX.[157] In reasoning the relationship between structure and activity, Warhurst realised that active compounds (QN, QD and MF) are able to adopt both *gauche* and *trans* conformations, while inactive compounds can only access *gauche*. He suggested that only a *trans* conformer, in which the quinuclidine or piperidine nitrogen atom is in the same plane as the quinoline ring, would be able to coordinate to Fe(III)PPIX. In 2003 Warhurst et al.[128] reported that the distribution ratio of the *erythro* alkaloids from the blood plasma to the lipid membrane of erythrocytes is 55:1 compared to

4.5:1 for the *threo* alkaloids. A higher pK_a for the quinuclidine nitrogen atom in the latter compounds (~ 9.45 compared to 8.58) is expected to increase the percentage of compound that is deprotonated (and therefore ionised) at pH 7.4, thus reducing the neutral fraction that is able to cross the lipid membrane and accumulate in the acidic digestive food vacuole. Using molecular modelling, the authors further determined that the positive electric field of the quinuclidine N1–H1 proton is directed towards the quinoline ring in QN and QD, and towards the solvent in eQN and eQD (Figure 1.28). They proposed that the shorter Fe–H1 distance and the increased solvation of H1 in complexes with *threo* alkaloids might interfere with coordination, thus explaining the reduced β-haematin inhibitory activity (BHIA) of these compounds relative to the *erythro* alkaloids. More recently, da Silva et al.[159] have reported a molecular modelling study in which they determined that the *Cinchona* alkaloids are able to coordinate to Fe(III)PPIX through the quinuclidine nitrogen atom. However, as with all the previous studies discussed here, the proposed pharmacophore could not convincingly explain the differences in antimalarial activity exhibited by these compounds.

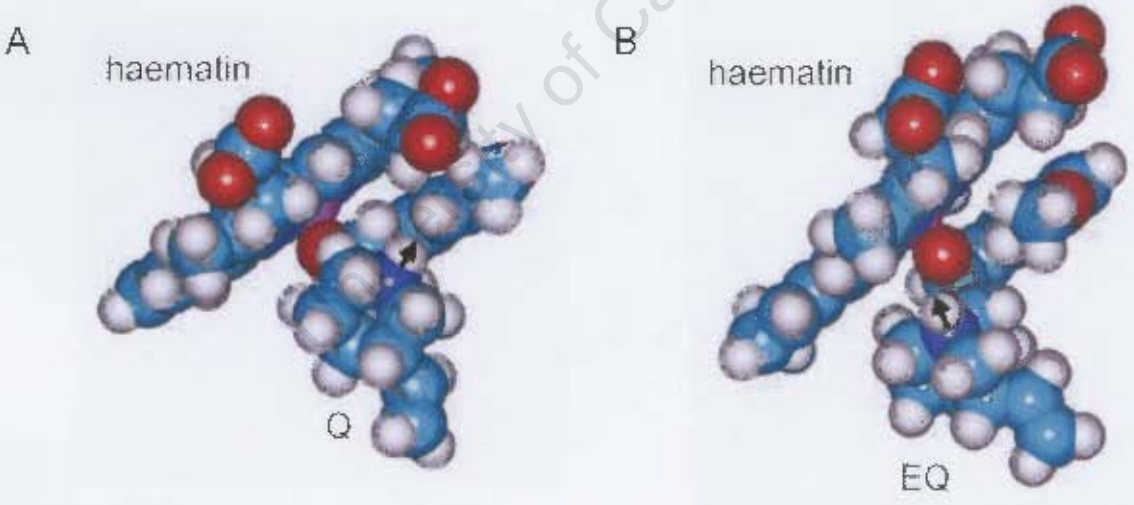

Figure 1.28 Space filling models of the complexes of Fe(III)PPIX (haematin) with (A) quinine (symbol Q) and (B) 9-epiquinine (symbol EQ). Reproduced from reference 128. The direction of the N1–H1 electric field (black arrow) is towards the quinoline ring in Q and towards solvent in EQ.

The values of log K determined spectroscopically for the *Cinchona* alkaloids[123,126,151] beg further investigation. QN, QD, eQN and eQD are diastereomerically related and yet QD associates with Fe(III)PPIX more strongly and demonstrates greater activity towards β-haematin inhibition than QN.

Surprisingly, both of the inactive isomers (eQN and eQD) associate with Fe(III)PPIX as or more strongly than QN. Such anomalies hint at the importance of determining the actual structures of the Fe(III)PPIX–alkaloid complexes in order to understand drug activity. However, despite several studies having investigated the interactions of quinoline and phenanthrene methanol compounds with Fe(III)PPIX, the structure-activity relationship for this class of compounds remains poorly understood. Displaying only stereochemical differences, the *Cinchona* alkaloids present the best chance of unravelling the mechanism of action of the aryl methanol compounds. Firstly, a correct interpretation of the speciation of Fe(III)PPIX in solution is critical. Secondly, there is an urgent need to determine definitively whether these compounds coordinate to the Fe(III) centre and if they do, whether it is via the quinoline or quinuclidine nitrogen atoms or the hydroxyl oxygen atom. Finally, the complexes of Fe(III)PPIX with the active and inactive isomers should be critically assessed for any striking differences.

1.7.6 Interactions of Quinolines with Haemozoin

By way of alternative, several studies have suggested that antimalarial drugs inhibit haemozoin formation through direct interaction with the crystal. In 1996, using electron microscope autoradiography to probe the distribution of [^{3}H] quinoline compounds inside parasitised red blood cells, Sullivan et al.[122] were able to detect CQ in close association with haemozoin pigment crystals (Figure 1.29 A). Recognising that quinolines do form complexes with Fe(III)PPIX, the authors suggested that in fact, the resultant complexes went on to inhibit haemozoin formation through inclusion at the elongation sites of what was then believed to be a growing polymer (Figure 1.29 B).[122,137] Through capping the growing polymer, the Fe(III)PPIX–quinoline complex would inhibit further sequestration of free Fe(III)PPIX, resulting in a build up of the toxic species in the digestive food vacuole.

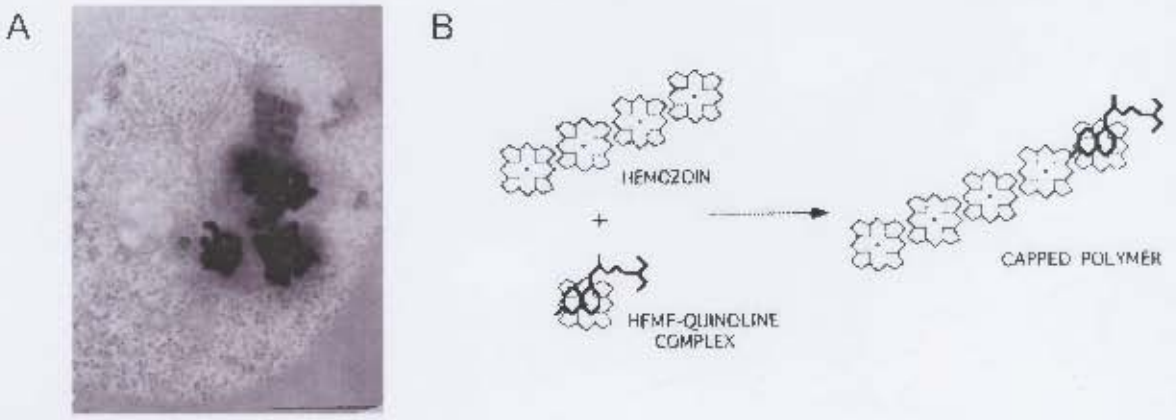

Figure 1.29 (A) An electron microscope autoradiograph of the distribution of [^{3}H] chloroquine (black patches) over haemozoin pigment crystals in the digestive food vacuole of *P. falciparum* (HB3 strain). The scale bar = 0.5 µm. (B) The proposed model of haemozoin inhibition in which the Fe(III)PPIX–quinoline complex is included into the growing haemozoin "polymer", thereby preventing further elongation. Reproduced from reference 122.

On the basis of the amount of haemoglobin per red blood cell, the dimensions and surface area of haemozoin/β-haematin crystals and the anticipated accumulation of CQ into the digestive food vacuole, Pagola et al.[57] reasoned that haemozoin inhibition takes place as a result of drug adsorption directly onto the smallest, yet fastest growing faces of the crystals. The theoretical growth morphology of haemozoin (Chapter 1.6.4.2) indicates that these are the (001) and (00$\bar{1}$) faces.[97] These faces are highly corrugated, exposing flexible propionic acid groups, vinyl and methyl groups, as well as aromatic surfaces in grooves which run parallel to the *a* axis (Figure 1.30 A). Leiserowitz and co-workers[97] have suggested that the quinoline antimalarial drugs CQ, AQ, QN and MF are able to dock into these grooves, being stabilised by close contacts with surrounding functional groups. Using mono-protonated CQ as an example, they identified the following possible interactions (Figure 1.30 B): (i) a 2.7 Å (porphyrin) $COO^-\cdots$(CQ) R_3NH^+ salt bridge, (ii) a 3.0 Å (porphyrin) $CH_3\cdots$(CQ) Cl contact, (iii) a 2.4 Å (porphyrin) C=CH$\cdots$(CQ) $N_{quinoline}$ contact and (iv) a 2.7 Å (porphyrin) C=C(π cloud)$\cdots$(CQ) $NH_{4\text{-amino}}$ contact. In addition, the planar quinoline ring is able to intercalate between planar porphyrin rings in this model. One possible criticism of the model is that quinolines were used in a monoprotonated state, making possible the (porphyrin) C=CH$\cdots$(CQ) $N_{quinoline}$ interaction. As discussed previously, antimalarial drugs are expected to accumulate in the digestive food vacuole as diprotic weak bases.

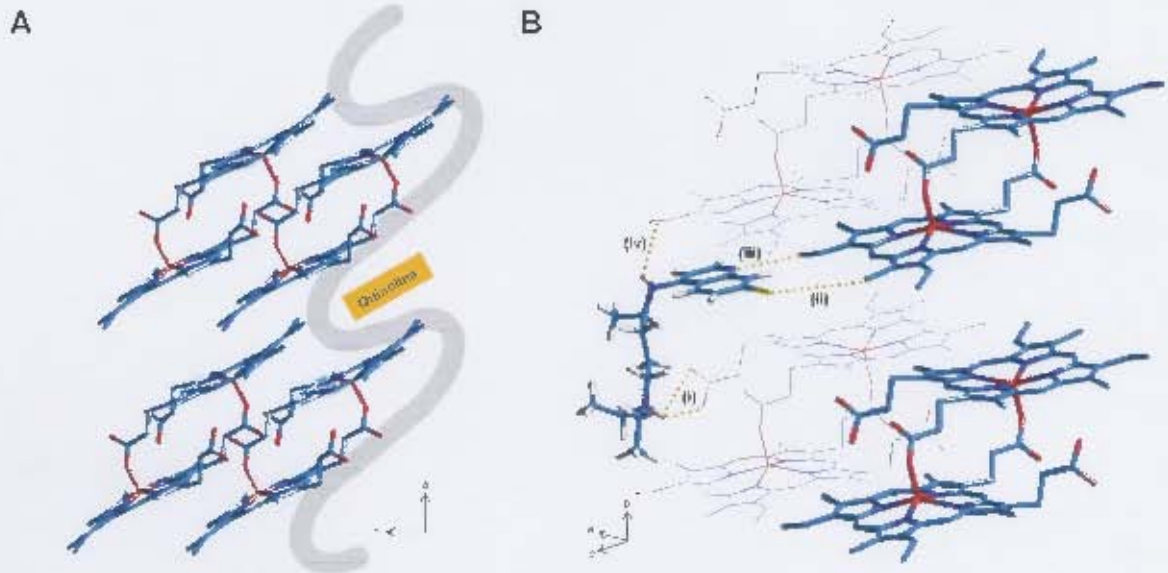

Figure 1.30 (A) A model of β-haematin viewed along the *a* axis. The corrugation of the (001) face is indicated by the grey line. Quinolines (for example chloroquine) are able to dock into the grooves and are stabilised by various close contacts discussed in the text (B). Redrawn based on reference 97.

1.7.7 Inhibition of Haemozoin Formation and Parasite Death

Having inhibited the formation of haemozoin, either by complex formation in solution or by direct capping of the crystals, the question as to how this brings about parasite death still remains: How exactly is the activity of the quinoline and related compounds "antimalarial"? Several hypotheses have been put forward, indicating that multiple mechanisms may be involved in antiplasmodial activity.

Fitch and co-workers[170] have suggested that Fe(III)PPIX and its CQ complex are able to lyse malaria parasites. In an earlier study, Chou and Fitch[30] demonstrated that normal (un-parisitised) mouse erythrocytes, when exposed to Fe(III)PPIX in solution (pH 7.4), manifested membrane damage sufficient to cause haemolysis. Furthermore, they observed increased rates of haemolysis following treatment with chloroquine. Loria et al.[14] have provided evidence that the association of Fe(III)PPIX with membranes is intensified in the presence of CQ. In support of Chou and Fitch's hypothesis, the authors suggest that the accumulation of toxic Fe(III)PPIX in the membranes may ultimately bring about parasite death. One proposal is that the concentration of free Fe(III)PPIX in membranes may promote

the peroxidation of lipids via the catalytic activity of iron. Indeed, Sugioka and co-workers[31,171] have demonstrated that Fe(III)PPIX–quinoline complexes increase the rate of lipid peroxidation compared to free Fe(III)PPIX.[31] An increase in free Fe(III)PPIX has also been invoked in the inhibition of *P. falciparum* enzymes. Using mass spectrometry, Campanale et al.[172] have shown that the activity of glyceraldehyde 3-phosphate dehydrogenase, a key enzyme in the glycolytic pathway, is decreased in the presence of Fe(III)PPIX (Ki = 0.2 μM). In the same study, glutathione reductase and protein disulfide isomerase were also investigated but were shown to be less sensitive to Fe(III)PPIX.

In a recent study, the effect of CQ treatment on the iron distribution in parasite-infected red blood cells has been investigated.[98] Images obtained using Transmission Electron Microscopy (TEM) and Electron Spectroscopic Imaging (ESI) clearly show that a redistribution of iron takes place upon treatment, with high concentrations of iron appearing in the parasite cytosol upon incubation with 30, 60 and 120 nM CQ. Though the speciation of iron was not confirmed in this study, that it is in the form of free Fe(III)PPIX is a possibility. Such a redistribution of free Fe(III)PPIX could give rise to the adverse effects described above. In addition, large numbers of transport vesicles were observed in parasites that were exposed to higher CQ concentrations.[98] Such morphological features have been previously observed,[109,110,173] and may corroborate a recent study by Fitch and Russell[174] in which they report that CQ accelerates the denaturation of haemoglobin. Furthermore, the authors propose that the antiplasmodial action of CQ is to bind Fe(III)PPIX and that the resultant complexes impair the maturation of haemoglobin-filled endosomes, thus disrupting parasite feeding.

1.8 DRUG RESISTANCE MECHANISMS

The emergence of drug-resistant malaria is the driving force behind the research effort to develop new and effective antimalarial compounds. The molecular basis of drug resistance has not been conclusively established and while this topic is not a direct focus of the current work, it is nonetheless important.

Studies have demonstrated that CQ-resistant malaria parasites accumulate drug less efficiently compared to CQ-sensitive strains,[101,175] implicating the digestive food vacuole in the process of drug resistance.[111] Owing to the fact that CQ is a diprotic weak base and accumulates in the digestive food vacuole via pH trapping, early work on pH-dependent drug partitioning[176] indirectly supported the hypothesis that CQ-resistant parasites have an increased vacuolar pH compared to sensitive strains. This would manifest as reduced accumulation. It has been suggested that in fact the vacuolar pH in CQ-resistant parasites is lower that in CQ-sensitive parasites,[177] however this has been disputed. Bray and co-workers[178] determined that fluorescence emanating from the accumulation of the weak base acridine orange was concentrated in the parasite cytosol as opposed to the digestive food vacuole, indicating discrepancies in the previous authors' experimental method and pH evaluation. An independent study subsequently concluded that the vacuolar pH values for both resistant and sensitive parasites are similar.[20]

The ability of amiloride, a specific inhibitor of Na^+/H^+ exchange, to inhibit CQ uptake led to the suggestion that CQ import (instead of Na^+) takes place via this carrier in exchange for protons.[179] Impaired function of the exchanger would manifest as reduced CQ accumulation. Bray et al.[180] have challenged this hypothesis, demonstrating that a decrease in the concentration of competing Na^+ does not lead to increased CQ accumulation. Furthermore, amiloride was shown to competitively bind Fe(III)PPIX. Consequently the authors have proposed that CQ-resistance is due to a decrease in access to Fe(III)PPIX.

As an alternative hypothesis, Krogstad et al.[181] proposed that decreased CQ accumulation was directly related to increased drug efflux from the digestive food vacuole. The authors determined that CQ-resistant parasites release CQ 40 – 50 times more quickly than sensitive strains. Since the possible contribution of increased vacuolar pH in resistant parasites to drug efflux is insignificant, it would seem that the permeability of the digestive food vacuole membrane towards CQ in CQ-resistant parasites must be enhanced.[182] It has been suggested that CQ either leaks out of the digestive food vacuole through a channel or is actively transported across the membrane.

Genetic studies have revealed that mutations in two genes that encode transmembrane proteins may be the basis of resistance to quinoline drugs. The 424 amino acid protein *P. falciparum* CQ-resistance transporter (*Pf*CRT) is coded by the gene *pfcrt* on chromosome 7,[183] and contains several mutations which always include a critical K76T mutation in resistant strains.[184] The result is that a polar, positively charged lysine residue (K) is substituted by a neutral, hydrophillic threonine residue (T).[185] *P. falciparum multiple drug resistance gene 1* (*pfmdr1*) on chromosome 5 encodes P-glycoprotein homologue 1 (*Pf*Pgh1), a 162 kDa member of the ATP-binding cassette (ABC) transport proteins.[186,187] Residue changes (particularly N86Y[188]) and increased expression of this protein have been correlated with resistance in the case of the arylaminoalcohol antimalarials QN, QD, MF and Hf.[189]

The mechanism by which quinoline resistance arises as a result of these gene mutations is not definitively understood. However, *Pf*CRT is thought to act as either a channel (enabling passive leaking) or a transporter (facilitating active transport).[182] The passive passage of protonated CQ through *Pf*CRT down its electrochemical gradient may be expected to increase in resistant strains owing to decreased electrostatic repulsion as a result of the K76T mutation. Alternatively, the K76T mutation may cause an active carrier to transform from one that allows CQ to leave the digestive food vacuole only if external CQ is available for import to one that drives the net co-transport of protons and CQ out of the vacuole.

Strategies to reverse resistance include the use of combination therapies, drug rotation, the re-design of existing drugs and finally, the development of resistance reversers.[190] The redesign of existing drugs has proved successful in circumventing drug resistance. For example, chloroquine analogues displaying shortened side chains[191-193] as well as side chains inclusive of an organometallic ferrocene moiety[194] have demonstrated similar success with respect to overcoming resistance. Since the viability of the drug target is not threatened by drug resistance, a better understanding of the mechanism of action of quinoline antimalarials is likely to be of great value to the discovery and design of new antimalarials.

1.9 AIMS AND OBJECTIVES

1.9.1 Aims

Having reviewed the literature thoroughly, three significant issues for which satisfactory answers do not exist were identified. Hence the aims of this thesis project were to:

1. Determine the speciation of Fe(III)PPIX in aqueous solution;
2. Gain deeper insight into the role of the lipid/water interface in nucleating and orienting β-haematin crystals;
3. Probe the relationship between structure and biological activity in the case of the Fe(III)PPIX complexes of the quinoline and phenanthrene methanol compounds.

1.9.2 Objectives

In order to accomplish these aims, the specific objectives of this thesis project were to:

1. Spectroscopically measure the dimerisation of Fe(III)PPIX in aqueous solution as a function of pH at biological ionic strength;
2. Compare the UV-visible and ^{1}H NMR spectra, rates of diffusion and magnetic properties of aqueous Fe(III)PPIX to the induced μ-oxo dimer;
3. Characterise the product formed at the lipid/water interface using Raman spectroscopy;
4. Perform Grazing Incidence X-ray Diffraction (GIXD) and X-ray Reflectivity (XR) measurements to probe the role of lipids, specifically their –OH head groups, in nucleating and orienting β-haematin crystals at the lipid/water interface;
5. Attempt to crystallise Fe(III)PPIX complexes of quinoline and phenanthrene methanol compounds in order to determine a common mode of interaction;
6. Investigate the Fe(III)PPIX-quinine, -quinidine, 9-epiquinine and 9-epiquinidine complexes computationally in an attempt to correlate their structure and biological activity.

2. THEORETICAL BACKGROUND TO PHYSICAL TECHNIQUES USED

2.1 INTRODUCTION

The work reported in this thesis has been achieved using several physical chemistry methods, each of which has its own historic relation and use in the field of malaria research. It is necessary in each case to have an understanding of the theory behind the methods in order to interpret the data. Firstly, much work towards understanding Fe(III)PPIX species in solution was achieved using UV-visible spectroscopy. The electronic spectrum of porphyrin compounds is unique and its features are described below. Two complementary vibrational spectroscopic methods, namely infrared and Raman spectroscopy, were also used. Principle Components Analysis (PCA) is a multivariate data analysis method, applied in this work to Raman spectroscopic data. Finally, a two dimensional crystallographic analysis, employing grazing incidence X-ray diffraction (GIXD) and X-ray reflectivity (XR) measurements, was undertaken for part of this work.

2.2 UV-VISIBLE SPECTROSCOPY

2.2.1 The Electronic Spectrum of Aqueous Fe(III)PPIX

The absorbance of UV-visible radiation by Fe(III)PPIX molecules in solution causes excitation of π-electrons in the porphyrin core. The molecular orbital diagram for the Fe(III) centre as well as the porphyrin core (together the chromophore), determined from the Huckel LCAO-molecular orbital model, is shown in Figure 2.1.[195-197] The Fe(III) centre in Fe(III)PPIX is high-spin, so that each of the five d-orbitals is singly occupied by an electron (spin state S = 5/2). The porphyrin core in its simplest arrangement excluding peripheral groups is considered to have D_{4h} symmetry.[198] Upon excitation, an electron from each of the singly degenerate highest occupied (a_{2u}) and next three highest occupied (a_{1u}, b_{2u} and a'_{2u}) π molecular orbitals is excited to the lowest unoccupied molecular orbitals, in this case, the doubly degenerate e_g (π^*) orbitals.

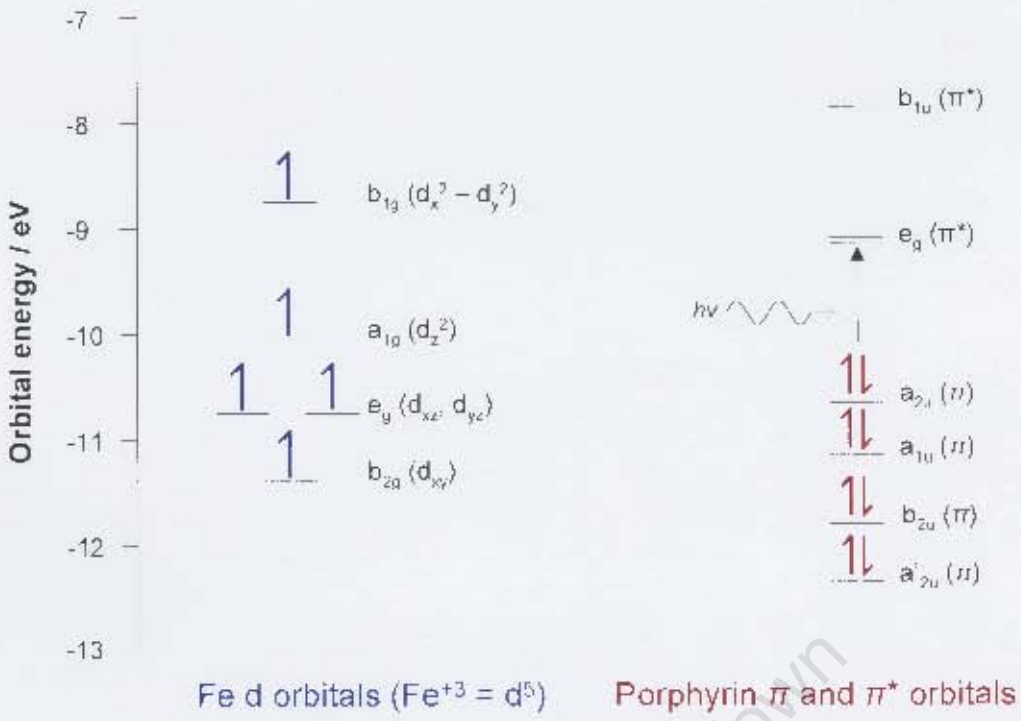

Figure 2.1 The molecular orbital (MO) diagram for the chromophore of Fe(III)PPIX. This includes the Fe(III) centre as well as the conjugated porphyrin ring system.

These transitions give rise to the main bands in the UV-visible spectrum of Fe(III)PPIX (Figure 2.2). Owing to similarities in energy and symmetry of the transition moments to the first and second excited states (e_g (π^*) ← (a_{2u}, a_{1u})), strong mixing occurs. This may be additive in which case the transition is of higher energy and gives rise to the Soret (or B) band, or alternatively subtractive in which case the transition is of lower energy and gives rise to the Q band. Transition moments to the third and fourth excited states (e_g (π^*) ← (b_{2u}, a'_{2u})) mix in a similar manner to produce the L and N bands respectively. The N band is however more intense due to intensity stealing from the extremely intense Soret band. Additional splitting of the Soret and Q bands occurs owing to differing interactions with radiation polarised in the x and y planes due to the non-symmetric arrangement of substituents on the porphyrin. Further splitting arises because electrons in the e_g (π^*) orbitals may be promoted to a vibrationally excited state. The vibrational ground state and excited state bands are designated B(0,0) and B(1,0) and Q(0,0) and Q(1,0) for the Soret and Q bands respectively. The electronic spectrum of Fe(III)PPIX includes two additional Charge-Transfer (CT) bands, which occur as a result of electronic transitions from the ligand to the Fe(III) centre. These are designated CTI: $d_\pi \leftarrow a_{2u}$ and CTII: $d_\pi \leftarrow a_{1u}$.

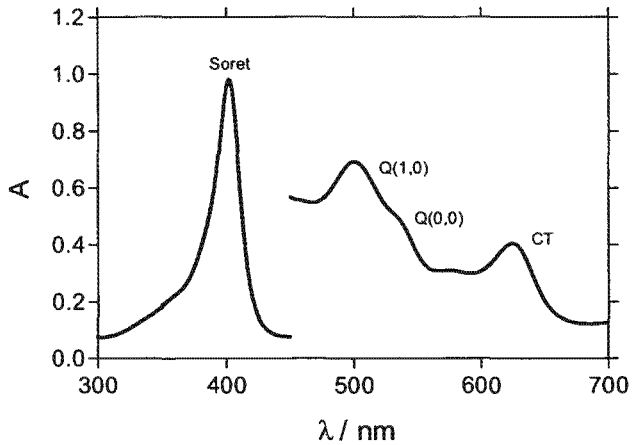

Figure 2.2 The UV-visible spectrum of monomeric Fe(III)PPIX in 40% (v/v) aqueous DMSO. The bands due to the major electronic transitions of the porphyrin core are labelled: Soret (B), Q and CT.

2.2.2 Spectral Changes Accompanying the Dimerisation of Fe(III)PPIX in Aqueous Solution

In mixed aqueous solutions such as 40% (v/v) aqueous DMSO, where Fe(III)PPIX has been shown to be monomeric,[148] the Soret band displays a decreased absorption intensity upon formation of $\pi - \pi$ complexes with quinoline antimalarials.[123] This is referred to as the hypochromic effect.[165,199] The same effect is observed for Fe(III)PPIX in aqueous solution and has been attributed to dimerisation.[41]

Such effects have been observed upon dimerisation of *N*-acetylmicroperoxidase-8 at high ionic strength and have been explained using a modified version of molecular exciton theory.[200] Essentially, the electric field of an incident photon is able to induce electrostatic coupling of the principal plane-polarised transition dipoles of interacting chromophores. Since the distance between interacting dipoles (a few Å) is much smaller than the photon wavelength (a few hundred nm), the oscillating electric field is able to interact with both molecules of the dimer simultaneously. The outcome is geometry dependent and three general cases may arise. In the first case, which is most common in $\pi - \pi$ dimers, the two dipoles may align parallel or antiparallel to one another (Figure 2.3 A). Excitation of the first arrangement leads to a higher-energy allowed exciton state, while excitation of the latter leads to a lower-energy forbidden exciton state. A higher energy corresponds

to a shorter wavelength and hence a blue, or hypsochromic shift is observed. Alternatively, two monomers may be covalently linked in a coplanar fashion. In this case the two transition dipoles may align in a head-to-tail or head-to-head arrangement (Figure 2.3 B). Excitation in the first situation gives rise to a lower-energy allowed exciton state, while the latter leads to a higher-energy forbidden exciton state. A lower energy corresponds to a longer wavelength and hence a red, or bathochromic shift is observed. In solution, neither of the first two cases is likely to dominate. Rather a third situation, in which the transition dipoles of interacting chromophores are obliquely oriented relative to one another, is more likely (Figure 2.3 C). In this case, the almost head-to-head arrangement gives rise to a higher-energy exciton state that is blue shifted, while the almost head-to-tail arrangement gives rise to a lower-energy allowed exciton state that is red shifted. While the integrated intensity of the absorption envelope is expected to remain unchanged, the result of the band splitting described above is an apparent decrease in absorbance and subsequent band broadening.[201] The formation of a π – π complex further reduces the symmetry of the individual molecular environments, which may result in additional splitting of the Soret B(0,0) and B(1,0) bands.

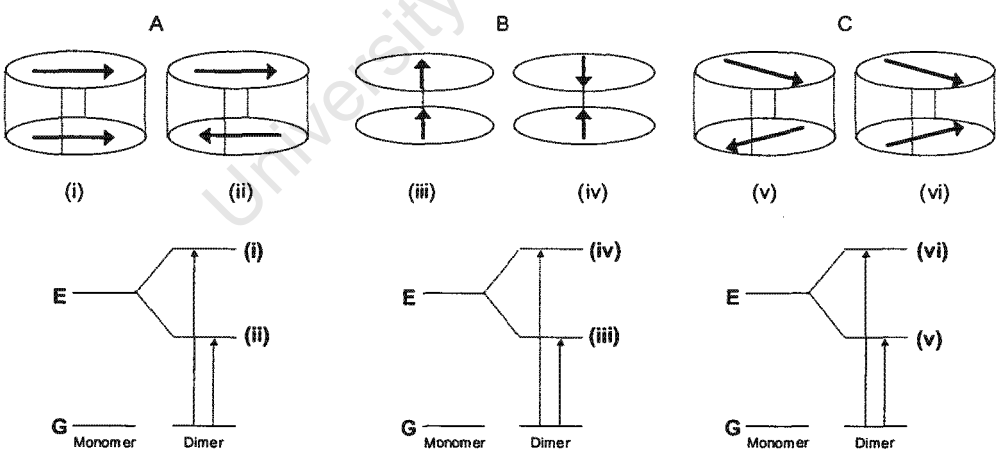

Figure 2.3 A schematic representation of the electrostatic coupling of transition dipoles of interacting chromophores, and the corresponding transitions from the ground state (symbol G) to allowed (solid vertical arrows) and forbidden (dashed vertical arrows) exciton states (symbol E). (A) The parallel (i) and antiparallel (ii); (B) the head-to-tail (iii) and head-to-head (iv) and (C) the oblique almost head-to-tail (v) and almost head-to head (vi) arrangements of transition moment dipoles. The latter two arrangements (C) represent the general case.[200]

2.3 INFRARED (IR) SPECTROSCOPY

This method detects vibrational characteristics of functional groups present within a molecule.[199] Where the frequency of IR radiation matches the energy difference between the ground and an excited state, this energy is directly absorbed by the molecules, causing chemical bonds to either stretch, contract or bend in an excited vibrational state. IR activity depends on there being changes in the dipole moment as a result of the absorption, so that asymmetric vibrations give rise to the most intense absorptions.[202] IR intensity is measured as a function of wavenumber, $\bar{\nu}$. Different functional groups vibrate at different frequencies depending on the atoms involved and therefore appear at different wavenumbers. The two methods described below differ in their methods of data collection.

2.3.1 Fourier Transform-Infrared Spectroscopy (FT-IR)

A globar light source produces all IR frequencies at once.[199] Inside the interferometer (Figure 2.4), the incoming radiation is split into two separate beams. One is then reflected off a fixed mirror and the other off a moving mirror, which introduces a path difference. The two beams interfere with each other to produce a new, recombined beam called an interferogram. This encodes all the frequencies from the original light source. During interaction with the sample, some frequencies from the interferogram signal are absorbed; the remaining signal is therefore unique to the sample being analysed. The detected interferogram is finally Fourier transformed into the typical spectrum of absorbance (or transmittance) as a function of wavenumber.

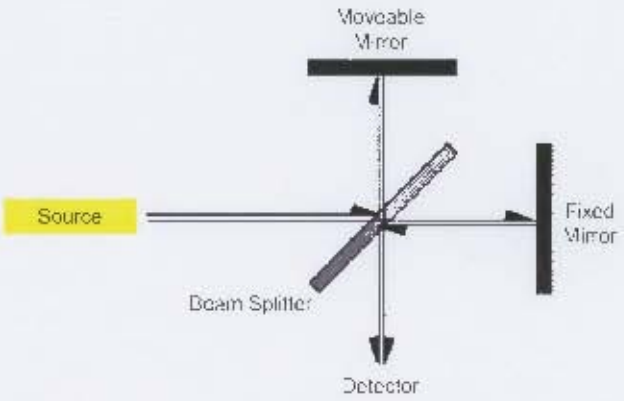

Figure 2.4 A schematic diagram of the interior of a Michelson interferometer.[203]

2.3.2 Attenuated Total Reflectance-Infrared Spectroscopy (ATR-IR)

Unlike the previous technique, this method of characterisation is most useful for solid samples and those through which light is not easily transmitted.[204] The sample is pressed into very close contact with the top surface of an IR transmitting crystal, usually zinc selenide (ZnSe) or germanium (Ge) (Figure 2.5). Exploiting the principles of total internal reflection,[205] the incident beam is reflected several times between the top and bottom of the crystal. The evanescent wave produced as a result penetrates angstroms into the sample. The detector measures the absorbance by the sample from the damped signal of the output beam.

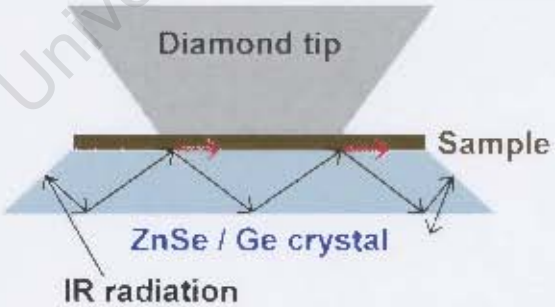

Figure 2.5 A schematic representation of the instrument and sample arrangement in an ATR-IR measurement.[204] The sample is pressed into very close contact with a ZnSe or Ge crystal by a diamond tip. As infrared radiation is reflected through the crystal, an evanescent wave (→) is produced which interacts with the sample and results in a damped signal of the output beam.

2.3.3 Infrared Spectroscopy Applied to Haemozoin Studies

As described in section 1.6, haemozoin is composed of bicyclic dimers of Fe(III)PPIX, each one hydrogen bonded to its neighbour.[57] Formation of these dimers is as a result of charge-assisted coordination of the propionate side chain ($R–CH_2–CH_2–COO^-$) to the Fe(III) centre. IR spectroscopy can be used to distinguish Fe(III)PPIX from haemozoin and its synthetic counterpart β-haematin. The most intense peaks corresponding to β-haematin occur respectively around 1662 and 1210 cm^{-1} for the C=O and C–O stretches of the coordinated propionate group.[53]

2.4 RAMAN SPECTROSCOPY

Whereas IR spectroscopy is an absorbance technique, Raman spectroscopy is a scattering technique.[202] The two methods are complementary as some vibrations that are detectable with the IR method are not by Raman and *vice versa*. Incident radiation is of a single frequency and when it interacts with the sample, it distorts, or polarises, the electron clouds around bonds.[202] Thus the requirement for Raman activity is that the molecule of interest should have large electron systems that are readily polarisable. In contrast to IR, symmetric vibrations usually give rise to the most intense signal.[202]

Elastic, or Rayleigh, scattering occurs when both incident and scattered photons have the same energy. Alternatively, if the scattered photon leaves with either a lower (Stokes) or a higher (anti-Stokes) energy compared to the incident photon, this is termed Raman scattering (Figure 2.6).[198,202] Due to the smaller population of the excited states, anti-Stokes scattering is expected to be less intense and typically Stokes scattering is measured experimentally.[202] The differences in energy between the incident and scattered photons depend on the nature of the sample and therefore can be analysed for structural information. To the advantage of the Raman spectroscopist is the fact that the process is not quantised and any number of induced virtual states can exist. This allows the use of any laser frequency to irradiate the sample.[198]

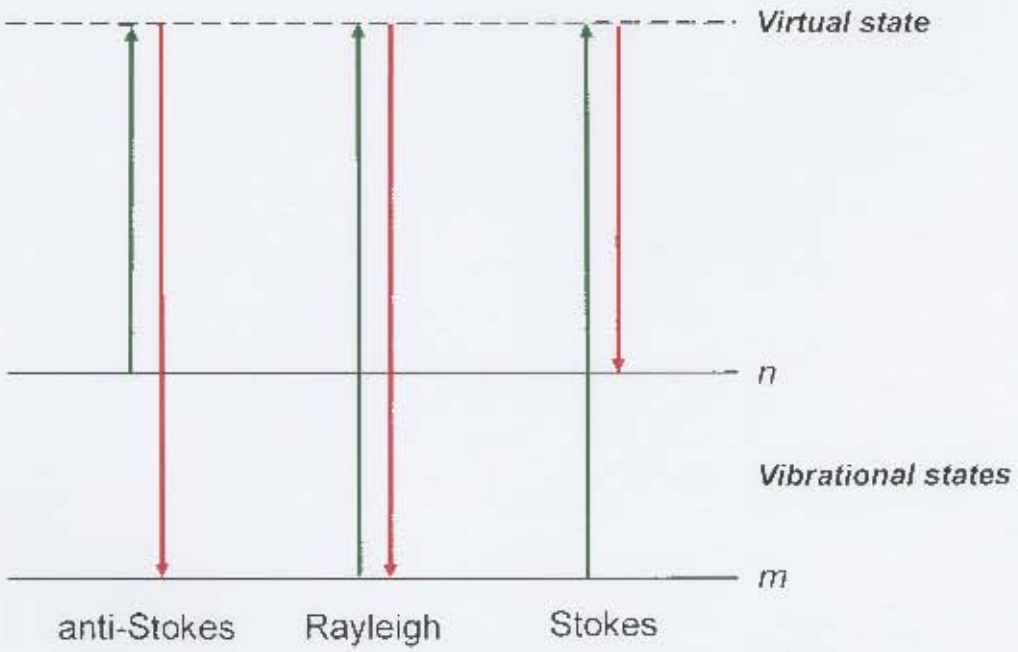

Figure 2.6 A schematic diagram of the Rayleigh and Raman scattering processes. Absorption of energy, either from the ground vibrational state, *m*, or an excited state, *n*, to an induced virtual state, is indicted by green arrows. Scattered energy is given by red arrows. Reproduced from reference 198.

2.4.1 Resonance Raman (RR) Spectroscopy

In the case that a particular chromophoric molecule gives rise to an electronic transition at a frequency which can be matched by an experimental laser, the sample may be expected to give rise to RR scattering.[198,206] In this case, vibrational modes associated with this particular transition will be enhanced relative to the normal Raman spectrum. One advantage of this is that it reduces the complexity of a spectrum as peaks affected may be easily identified and assigned. Furthermore, this feature has made it possible to selectively study molecules that behave accordingly in living cells, such as porphyrins.[207] Water is a particularly weak Raman scatterer, which makes this technique advantageous when studying live cells.[198] Improved confocality and control of the laser spot size have meant that distinctions can be made at a subcellular level. Reduced sample size and preparation time are further advantages of the Raman technique.

The correlation between the excited state structure of a molecule and its associated RR intensities has been explained in terms of type A and type B

scattering.[208,209] Type A modes are expected to be totally symmetric based on their non-zero values for the product of the Frank-Condon integrals. Type B scattering is the result of mixing between nearby electronic transitions and can result in modes of any symmetry.[210]

2.4.2 Raman Features of Fe(III)PPIX-Containing Molecules

As described above, the UV-visible spectrum of Fe(III)PPIX, an example of a metalloporphyrin, is characterised by the Soret band (~ 400 nm) and the Q and CT bands (~ 500 – 650 nm). Type A RR scattering is expected for incident radiation converging on the wavelength of the Soret band while type B scattering is expected when exciting with wavelengths coinciding with the Q and CT bands (Figure 2.7 A).[209] By direct implication, Raman spectroscopy, in particular RR, is expected to be a useful technique for the study of Fe(III)PPIX species.

The porphyrin core of Fe(III)PPIX is highly symmetrical, having a four-fold principal axis around the Fe(III) centre. In addition it has four perpendicular C_2 axes and a horizontal mirror plane, thus having idealised D_{4h} symmetry (Figure 2.7 B).[198] Disregarding peripheral groups beyond the first carbon atom and reducing the hydrogen atoms to point masses, the 37-atom molecule has 71 (2N – 3) in-plane vibrational modes (Equation 2.1), of which the *g* modes are Raman active. In addition, there are 34 out-of-plane vibrational modes (Equation 2.2). These are typically weak in biological samples and are not considered valuable for analysis and identification.

$$\Gamma_{in\text{-}plane} = 9A_{1g} + 8A_{2g} + 9B_{1g} + 9B_{2g} + 18E_u \qquad (2.1)$$

and

$$\Gamma_{out\ of\ plane} = 3A_{1u} + 6A_{2u} + 5B_{1u} + 4B_{2u} + 8E_g . \qquad (2.2)$$

where E_u and E_g modes are doubly degenerate.

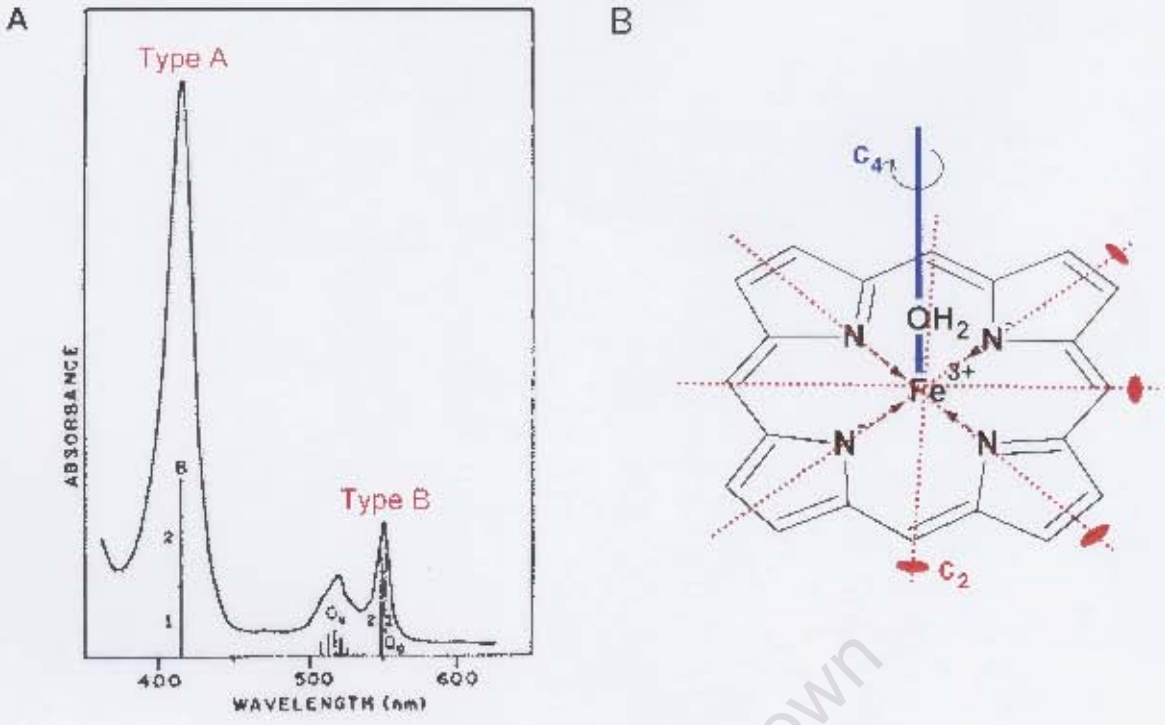

Figure 2.7 (A) The electronic spectrum of Fe(III)PPIX showing the characteristic Soret and Q bands and the type of scattering associated with the bands. Reproduced from reference 209. (B) The porphyrin core of Fe(III)PPIX showing the symmetry elements contributing to an idealised D_{4h} assignment.

Abe et al.[211] were the first group to produce a relatively complete set of band assignments, having carried out extensive studies on model compounds, namely nickel(II) porphyrin complexes. It became apparent that certain bands in the Raman spectra of haem species were marker bands for specific molecular features. From a study of several haem proteins it was concluded that the principal component of the ν_2 band appeared at 1584 and 1566 cm^{-1} for low and high spin configurations respectively.[212] Furthermore, the π-electron density or oxidation state marker band (ν_4) appears near 1375 cm^{-1} for Fe(III) and near 1355 cm^{-1} for Fe(II) species.[212]

2.4.3 Raman Spectroscopy Applied to Haemozoin Studies

Ong et al.[213] were the first to provide evidence of the usefulness of Raman spectroscopy to identify haemozoin inside red blood cells infected by *Plasmodium berghei*. Using a laser excitation wavelength of 632.8 nm, Wood et al.[214] later showed that the Raman spectra of haemozoin located within the digestive vacuole

of *Plasmodium falciparum*, and synthetic β-haematin are very similar (Figure 2.8). Indeed, the latter spectrum is very similar to one recorded by Bohle et al. of β-haematin.[215] Marker bands in the spectrum of haemozoin confirm that the iron centre is high spin Fe(III) (1569 cm^{-1} and 1376 cm^{-1} respectively). The same profile is seen for β-haematin with peaks appearing at 1569 and 1375 cm^{-1}. These and other bands have been previously assigned (Table 2.1).[52,215,216] A most recent publication by Frosch and co-workers revealed a previously unnoticed band at 1655 cm^{-1}, which is assigned to two normal modes located at the two propionate/propionic acid side chains.[217]

Table 2.1 Selected band assignments for synthetic β-haematin (632.8 nm)[198]

RAMAN SHIFT / cm^{-1}	ASSIGNMENT	SYMMETRY TERM	LOCAL COORDINATE
1628	ν_{10}	B_{1g}	$\nu(C_\alpha C_m)_{asym}$
1570	ν_2	A_{1g}	$\nu(C_\beta C_\beta)$
1551	ν_{11}	B_{1g}	$\nu(C_\beta C_\beta)$
1376	ν_4	A_{1g}	ν(pyrrole half-ring)$_{sym}$
1240	ν_{42}	E_u	$\delta(C_mH)$, methine
1219	ν_{13}	B_{1g}	$\delta(C_mH)$, methine
1120	ν_{22}	A_{2g}	$\nu(C_\alpha N)$
797	ν_6	A_{1g}	ν(pyrrole breathing)
754	ν_{15}	B_{1g}	ν(pyrrole breathing)
679	ν_7	A_{1g}	δ(pyrrole deformation)$_{sym}$
514	-	-	ν(Fe-O)
345	ν_8	A_{1g}	ν(Fe-N)

ν indicates an in-plane mode; δ indicates a deformation mode.

To confirm the location of haemozoin in malaria-infected red blood cells, Wood et al.[214] went on to image the 1374/6 cm^{-1} band using 760 nm excitation radiation. This band is absent from oxyhaemoglobin, a low-spin Fe(II) species. This method demonstrates, as expected, that haemozoin is concentrated in the digestive food vacuole (Figure 2.9).

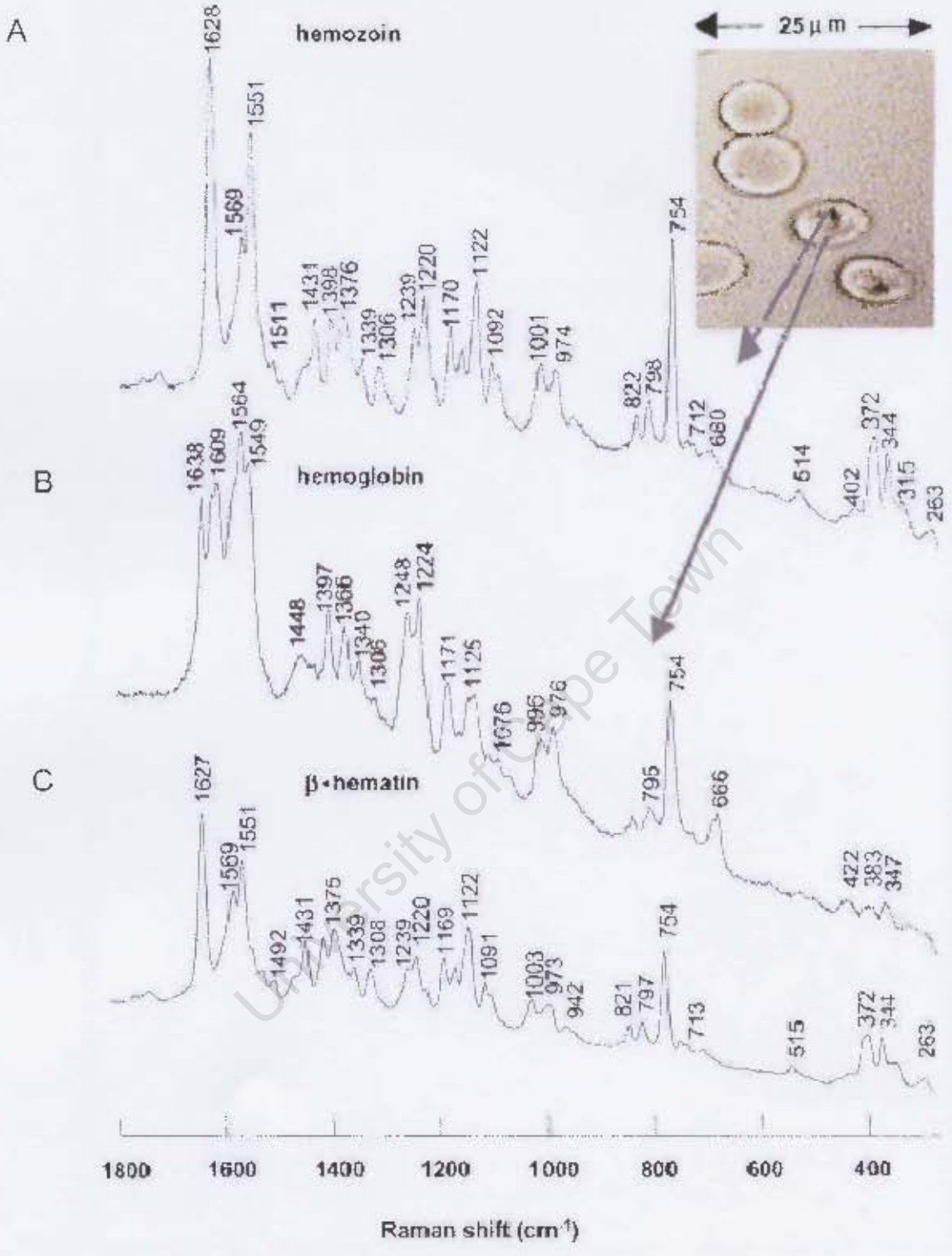

Figure 2.8 Raman spectra (632.8 nm excitation) of haemozoin (A) and haemoglobin (B) inside a *P. falciparum*-infected red blood cell. The inset shows a photomicrograph of the red blood cells while the arrows indicate the cellular areas from which the spectra were recorded. The spectrum of synthetic β-haematin (C) is provided for comparison. Reproduced from reference 214.

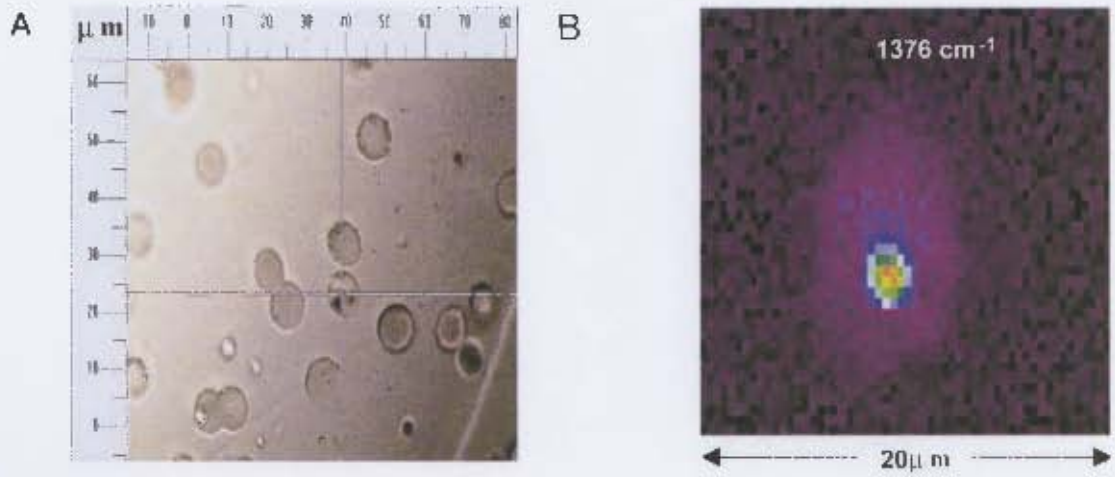

Figure 2.9 (A) Photomicrograph of normal and parasitised (crosshairs) red blood cells. The dark brown spot in the bottom left quadrant of the marked cell is haemozoin. (B) Raman-generated image of the 1376 cm^{-1} band corresponding to haemozoin, showing that this high-spin Fe(III) species is localised in the malaria parasite's digestive food vacuole. Reproduced from reference 214.

Resonance Raman spectroscopy is suited to the study of porphyrins such as Fe(III)PPIX and β-haematin given the extensive electronic system of the porphyrin chromophore. In addition to the Soret, Q and charge transfer bands, a small, broad electronic transition around 867 nm has recently been identified in the UV-visible spectrum of haemin during its acidification to form β-haematin.[218] The authors assigned this as a z-polarised charge transfer transition and explained its existence due to π-stacking of β-haematin units resulting in excitonic interactions. The use of near-infrared laser excitation wavelengths would be expected to produce band enhancement due to the resonance Raman effect. Indeed, a number of bands in the Raman spectrum of β-haematin show enhancement when recorded using an 830 nm laser excitation wavelength (Figure 2.10).[218] Notably, the increased intensity of the ν_4 band (1375 cm^{-1}) is a dominant feature.

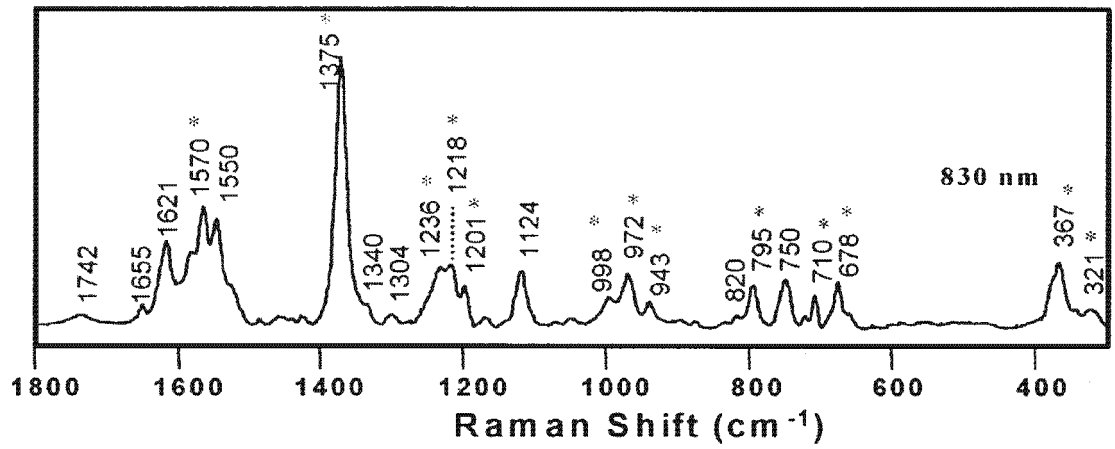

Figure 2.10 The 830 nm Resonance Raman spectrum of β-haematin. Asterisks mark bands that are enhanced; most notable is ν_4 at 1375 cm^{-1}. Reproduced from reference 218.

2.5 PRINCIPLE COMPONENTS ANALYSIS

In spectroscopy, a set of spectra of either a solid or biological sample, recorded from different locations within the sample, would be expected to display variations due to sample thickness, heterogenous composition, instrumental variations and detector noise at any given instant. Principle Components Analysis (PCA) is a multivariate data analysis tool that is used to uncover contributory descriptors[219] by which to re-express an original data set.[220] In this way, meaningful data may be discerned from that which is either redundant or simply noise.[220]

In an n-dimensional data set, where n is usually greater than 3, the function of PCA is to generate a new coordinate system that illustrates the maximum variability, thus reducing the dimensionality of the original data set.[221] The first step in the process is to standardise all data by subtracting the mean and dividing by the standard deviation. The data retain their original positions relative to one another, while the centroid of the data set shifts to zero on the new coordinate system. The axes of the new coordinate system are defined as Principle Components (PCs). The first PC is chosen such that it passes through the maximum variation in the data set as well as the centroid and minimises the square of the distance between each individual datum and itself. Subsequent PCs are established in the same way except that they should not correlate with existent PCs and are thus orthogonal. In order to determine how many PCs are required to

perform an analysis, the associated eigenvalues of each PC, which explain the amount of variance accounted for by each axis, are expressed as a percentage of the sum of all eigenvalues. PC1 and PC2 usually explain the majority of the variance while remaining PCs describe insignificant amounts. A maximum of 6 PCs were used in this current work.

PCA generates two useful representations of the newly ordinated data set. The *scores plot* is a projection of the data set onto any two orthogonal PCs and is used to identify the position that each individual datum holds relative to a principle component.[219] The *loadings plot* indicates the weight or influence that each of the original descriptors has in defining a particular PC. In the context of this work, each spectrum recorded of a sample constitutes an individual datum. The original descriptors refer to the wavenumbers of peaks in a spectrum. Figure 2.11 is a generalised illustration of the basic principles of PCA.

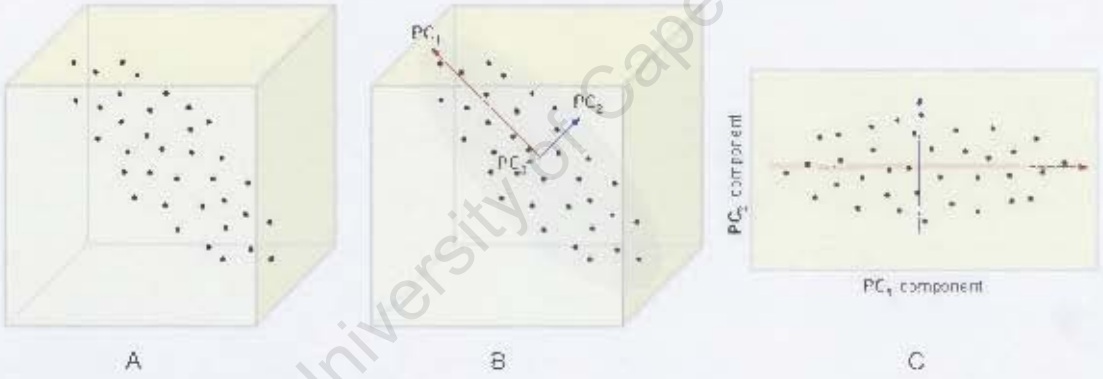

Figure 2.11 An illustration of Principle Components Analysis (PCA). (A) A generalised 3-dimensional data set is shown. (B) The data set is ordinated relative to a new coordinate system in which three orthogonal Principle Components (PCs) describe the directions of maximum variance. The length of the arrows indicates the relative variance described by each PC. (C) A scores plot of the data projected onto PC_1 and PC_2. Reproduced from reference 222.

2.6 TWO-DIMENSIONAL CRYSTALLOGRAPHY

2.6.1 Introduction

An interpretation of the data obtained after performing grazing incidence X-ray diffraction (GIXD) and X-ray reflectivity measurements (XR) first requires an

understanding of how crystallography from a two-dimensional surface differs from diffraction in a three-dimensional crystal. Such concepts are discussed first before proceeding to the details of the two methods of data collection.

2.6.2 Criteria for Diffraction: The Scattering Vector, Q

Three-dimensional crystals can be thought of in terms of sets of crystal "planes"; however it is the electron clouds of the atoms themselves that are responsible for the scattering of X-rays. A set of these planes, with an interplanar spacing *d*, will give rise to diffraction when Bragg's law is satisfied.[223]

The illustration in Figure 2.12 explains the origin of the scattering vector, Q, as the basis for diffraction. Let O and A be two arbitrary lattice points on consecutive "planes" of atoms. The incident and diffracted beams, represented as grey dashed lines in the direction of the arrowheads, make angles with the "planes" θ. S_0 and S are unit vectors parallel to the incident and diffracted beams respectively.

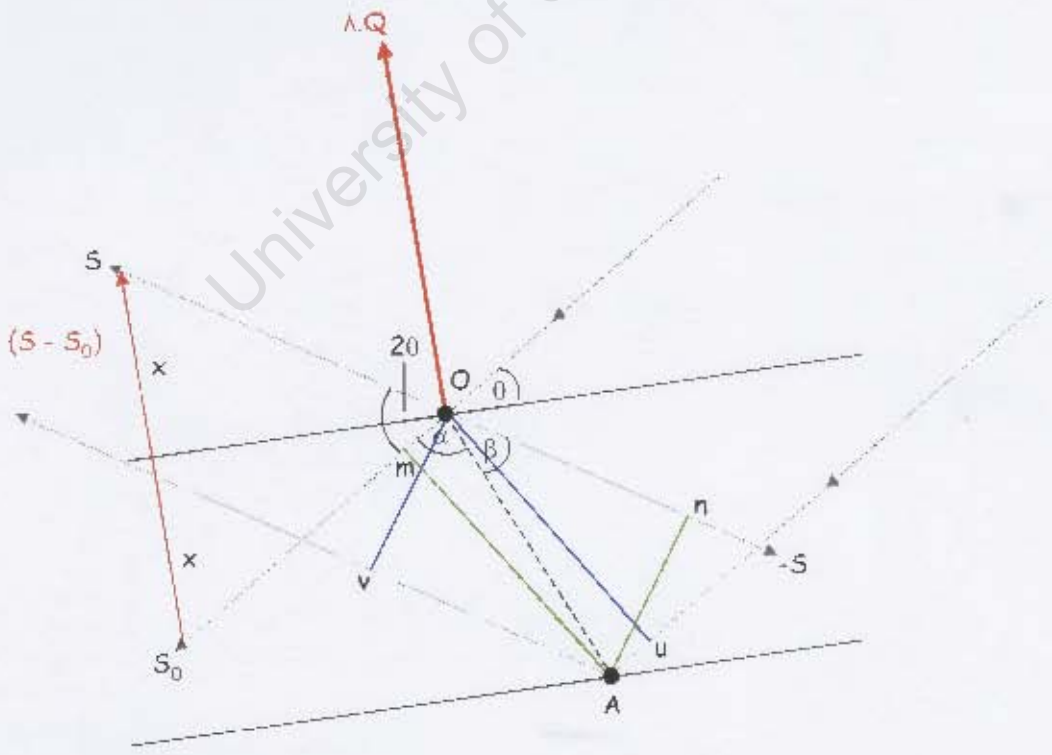

Figure 2.12 The origin of the scattering vector, Q.

The path difference, δ, between the beams reaching and leaving O and A can be expressed in the following equation set, where S_0 and S are unit vectors in the direction of the incident and diffracted beams respectively (2.3):

$$\delta = (uA + Av) = (mO + On)$$

$$mO = OA\cos\alpha \; and \; On = OA\cos\beta.$$

$$\vec{S_0}.\vec{OA} = |S_0||OA|\cos\alpha \qquad (2.3)$$

$$-\vec{S}.\vec{OA} = |-S||OA|\cos\beta$$

$$\therefore \delta = \vec{S_0}.\vec{OA} - \vec{S}.\vec{OA} = -\vec{OA}\left(\vec{S} - \vec{S_0}\right)$$

The phase difference, φ, for the two waves reaching and leaving O and A is given by the equations 2.4a and 2.4b:

$$\varphi = \frac{2\pi\delta}{\lambda} = -\frac{2\pi\left(\vec{OA}(\vec{S} - \vec{S_0})\right)}{\lambda} \qquad (2.4a)$$

By definition the scattering vector Q has a magnitude equal to $\frac{(\vec{S} - \vec{S_0})}{\lambda}$ and therefore the phase difference is summarised as: $\varphi = -2\pi\vec{Q}.\vec{OA}$ (2.4b)

Consulting Figure 2.12, it can be seen that $\sin\theta = x/\vec{S} = x/\vec{S_0}$. Since the magnitude of unit vectors is 1, sin θ = x. It is easily seen that $2x = (\vec{S} - \vec{S_0}) \therefore (\vec{S} - \vec{S_0}) = 2\sin\theta$. Therefore, the scattering vector, Q, has a magnitude equal to $\frac{2\sin\theta}{\lambda}$.

Diffraction is observed only when the path difference, δ, is a multiple of the wavelength, λ, which results in constructive interference. Thus only certain θ values will satisfy this requirement, of which Bragg's law is a summary.

2.6.3 Criteria for Diffraction: The Ewald's Sphere

By comparison to the discussion above, the Ewald's sphere[223] (Figure 2.13) is a useful representation to demonstrate the criteria for diffraction more simply. The diameter of the imaginary sphere is set at 2/λ. A crystal is placed at the centre of the sphere such that the incident X-rays make an angle θ with a set of crystal planes. The Ewald's sphere is constructed such that the incident beam terminates at the origin of the reciprocal lattice (hkl = 000). This is an array of points, each one describing a set of planes in the crystal. Each point represents the end of a vector drawn perpendicular to the respective set of planes and equal in magnitude to the reciprocal of the interplanar spacing, *d*. Diffraction occurs when the Ewald's sphere coincides with a point (hkl) in the reciprocal lattice. The vector S_0 is coincident with the incident X-rays while the vector S is coincident with the diffracted beam. The vector spanning the distance between (000) and (hkl) is called the scattering vector, Q. The relationship between the Ewald's sphere geometry and Bragg's law is expressed in the following equations (2.5 – 2.8):

$$\sin\theta = \frac{Q}{2/\lambda} = \frac{Q\lambda}{2} \qquad (2.5)$$

$$\therefore 2\sin\theta = Q\lambda \qquad (2.6)$$

$$and\ Q = \frac{2\sin\theta}{\lambda} \qquad (2.7)$$

This is the same relationship that was arrived at in the previous section, however its derivation is now much more simple. Bragg's law is expressed by equation 2.8:

$$(n)\lambda = 2d\sin\theta \therefore \frac{2\sin\theta}{\lambda} = \frac{1}{d} \text{ for the case where n = 1.} \qquad (2.8)$$

It can be seen that the scattering vector Q is equal in magnitude to the reciprocal of the interplanar spacing, *d*. As seen from the Ewald's sphere, diffraction occurs when Q coincides with a reciprocal lattice point.[94]

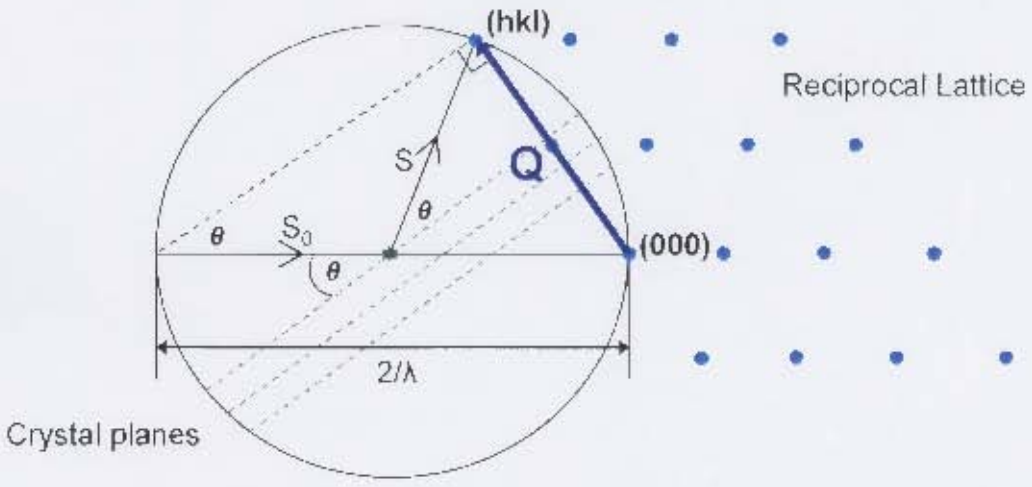

Figure 2.13 The Ewald's sphere, used to demonstrate the criteria for diffraction. The details are provided in the text, however this model importantly demonstrates that the scattering vector, Q, must coincide with a reciprocal lattice point in order for diffraction to occur.

2.6.4 Surface-Specific X-Ray Methods

In conventional three-dimensional crystallography, the measured intensity is directly proportional to the number of "scatterers" present within the crystal volume.[224] Using incident radiation with wavelengths of the order of 1 Å, X-rays are able to detect sample to depths of micrometres to millimetres. By stark contrast, the third dimension is almost completely lost for crystals formed at an interface.[94] In this case, the crystalline material extends in a two-dimensional manner across the surface, penetrating up to 100 Å only. In order to study two-dimensional crystals at interfaces, controlling scattering such that it occurs only from the surface region is a pre-requisite. This is achieved by tailoring the angles that incident X-rays make with the surface.[274]

2.6.4.1 Total External Reflection

The phenomenon of total external reflection[94,224] underlies the techniques that have been designed to investigate two-dimensional crystals at air/liquid interfaces. In the case that incident radiation is either UV, visible or IR light (Figure 2.14 A), the light is bent towards the normal upon entering a medium that is more dense compared to where it was propagated (refractive index n_2 (medium) > n_1 (air)).[205]

In contrast, when X-rays are used to irradiate a sample, n_2 is typically smaller than n_1 and light is bent away from the normal (Figure 2.14 B). In cases where incident X-rays meet the surface at an angle greater than the critical value, the incident wave is totally reflected while an evanescent wave is refracted along the surface.[205] This wave varies exponentially with distance perpendicular to the direction of propagation and is able to penetrate the sample only tens of angstroms (Figure 2.14 C).

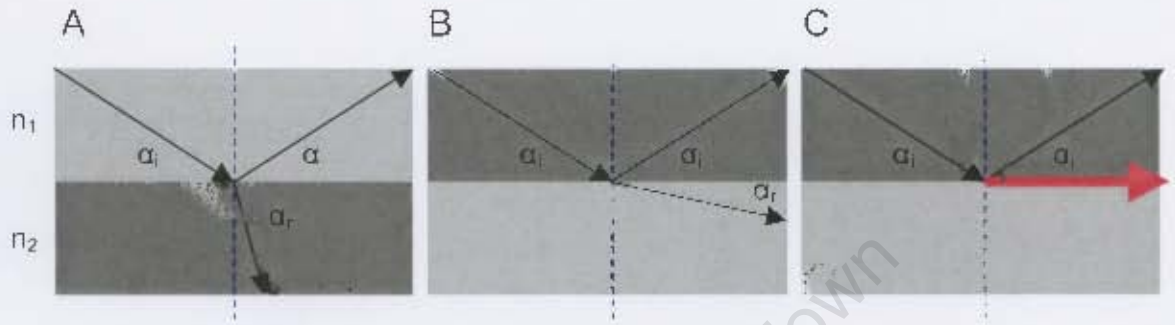

Figure 2.14 A schematic representation of the principles behind the phenomenon of total external reflection. (A) When incident radiation is UV, visible or IR light, it is bent towards the normal when entering an optically denser medium. (B and C) When incident radiation is in the form of X-rays, air is optically denser than matter. Light is bent away from the normal if the angle of incidence (α_i) is less than the critical angle (B). If the angle of incidence (α) exceeds the critical angle, refracted light travels parallel to the surface in the form of an evanescent wave, → (C). In all figures, n_1 and n_2 are the refractive indices of the incident medium (air) and the destination medium. Light grey represents less dense while dark grey indicates more dense as determined by the type of radiation.

2.6.4.2 The Reciprocal Lattice in Two Dimensions

The reciprocal lattice arising from a two-dimensional crystal array extends as a set of continuous rods, called Bragg rods, in a perpendicular direction relative to the plane of the array.[94] Remembering that the third dimension (*c*) is almost completely lost in two-dimensional systems, Figure 2.15 allows visual conceptualisation of this phenomenon. Figure 2.15 A shows the real space two-dimensional array, with periodicity extending in the *a* and *b* directions only. The reciprocal lattice is shown in Figure 2.15 B. Given that distance in reciprocal space is inversely proportional to distance in real space, a zero dimension in *c* in real

space in turn means that in reciprocal space, "points" are infinitely close together and form continuous rods. These Bragg rods are indexed in the form (hk).

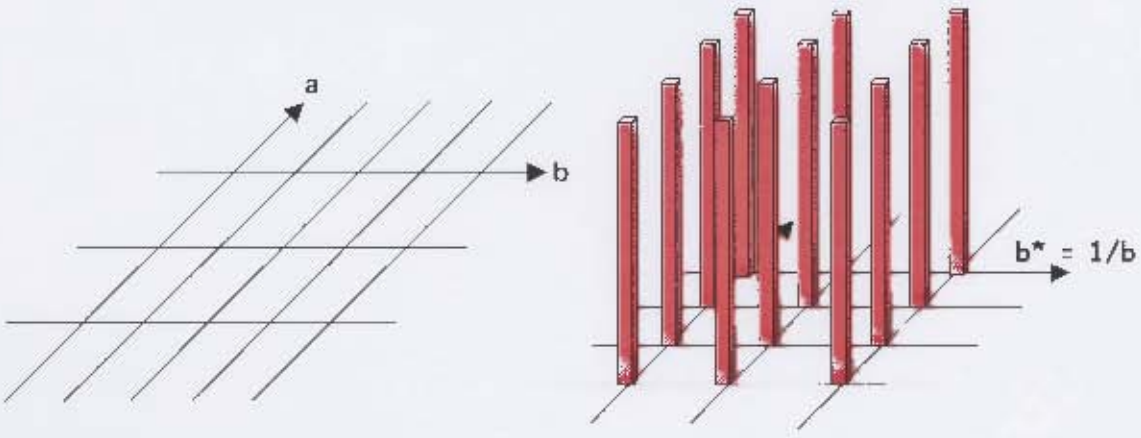

Figure 2.15 A two dimensional crystal array (A) gives rise to a reciprocal lattice (B) that extends as continuous Bragg rods.

2.6.4.3 Grazing Incidence X-Ray Diffraction

When the incident angle is less than or equal to $0.85\alpha_{crit}$ the penetration depth of the evanescent wave is limited.[94] In the case that crystalline material forms within this depth, the evanescent x-rays may be diffracted and so provide structural information in a similar fashion to three-dimensional x-ray crystallography. Diffraction of the evanescent wave is called grazing incidence x-ray diffraction (GIXD).[225]

GIXD measures diffraction from "planes" in the two-dimensional crystal lattice that are perpendicular to the surface at which the crystals form. The scattering vector Q = $k_f - k_i$, where k_i and k_f are the vectors of the incident and diffracted waves respectively, has components which are horizontal (q_{xy} or q_{hor}) and vertical (q_z or q_{vert}) to the plane of the two-dimensional array (Figure 2.16). The q_z components are coincident with Bragg rods. For diffraction to occur, q_{xy} must end on one such (hk) Bragg rod.[94,224]

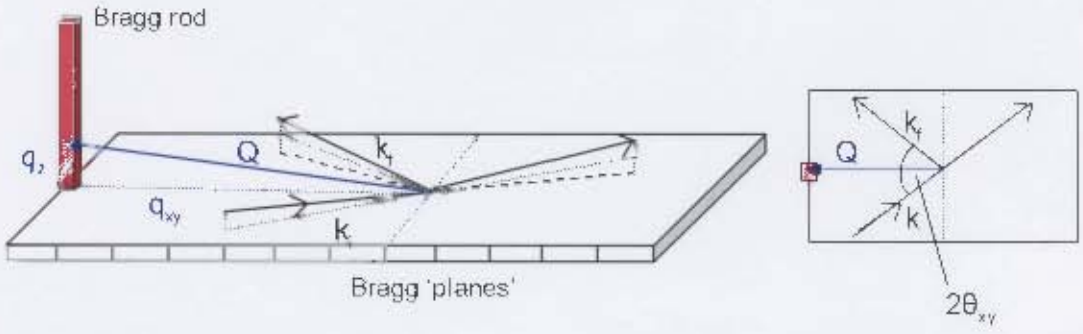

Figure 2.16 A side (left) and aerial (right) view of the scattering geometry in GIXD measurements.

Scanning over a particular $2\theta_{xy}$ range, where $2\theta_{xy}$ is the angle between the projections of the incident and diffracted beams in the horizontal plan, yields data from which the following structural information can be extracted:[224,226]

1. *The interplanar spacing, d*: This is related to the position of the Bragg peaks in q_{xy} units:

$$d = \frac{2\pi}{q_{xy}} = \frac{\lambda}{2\sin\theta_{xy}} \qquad (2.9)$$

2. *The crystalline coherence length, L*: This is related to the inverse of the full-width at half-maximum (FWHM) of a peak and is determined according to the Scherrer formula:

$$L = \frac{0.9 \times 2\pi}{FWHM} \qquad (2.10)$$

3. *The structure factor, F*: This can be calculated from the intensity at a particular value of q_z in a Bragg rod:

$$I_{hk}(q_z) = r\left|F_{hk}(q_z)\right|^2 \qquad (2.11)$$

where *r* is a factor included to compensate for X-rays reflected at the surface.[227]

2.6.4.4 Specular X-Ray Reflectivity

X-ray reflectivity (XR) measures reflections from "planes" which are parallel to the plane of the surface and provides information about the variation in the electron density in the direction perpendicular to the surface. This gives rise to a vertical scattering vector according to the geometry shown in Figure 2.17. The angles of incidence and reflectance, α_i and α_f respectively, are assumed to be the same and Q is in the same plane as the incident and reflected waves.

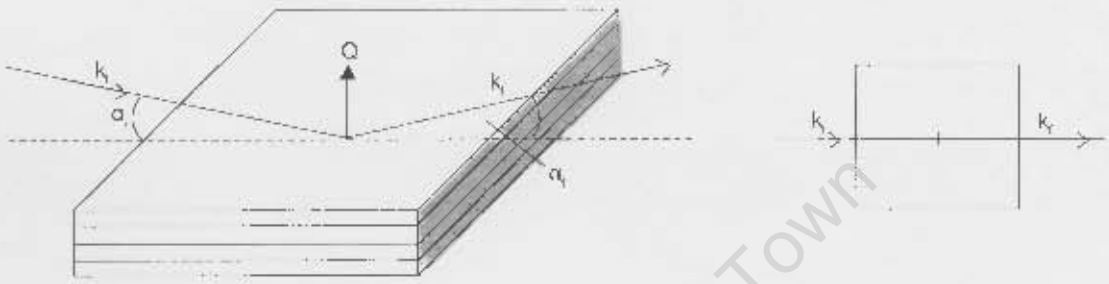

Figure 2.17 A side (left) and aerial (right) view of the scattering geometry in XR measurements.

The Fresnel law of optics describes the specular reflectivity for a perfectly-reflecting (ideal) surface[205] as a function of the perpendicular component of the scattering vector ($R_F(q_z)$).[94] Limited by the small angle of incidence in surface-specific X-ray experiments, the reflectivity expression is simplified. The measured reflectivity $R(q_z)$ is related to the vertical electron density $\rho(z)$ by equation 2.12.[94,226] This equation is applicable in cases where $\rho(z)$ does not vary in a step-like manner between two values but rather varies continuously in the surface region.

$$\frac{R(q_z)}{R_F(q_z)} = \left| \frac{1}{\rho_w} \int \frac{d\rho}{dz} e^{(iq_z z)} dz \right|^2 \qquad (2.12)$$

where ρ_w is the electron density of water (0.334 e Å^{-3}) and $q_z = (4\pi/\lambda) \sin \alpha$.

Much work has been done to characterise monolayers of phospholipids and fatty acids[228] which, being amphiphilic, have hydrophilic heads and hydrophobic tails. A two-slab model has been developed in order to approximate $\rho(z)$ and aid

interpretation of reflectivity data.[228] In this model one slab represents the row of "heads" and the other the row of "tails". The derivation however is not relevant to this thesis.

Varying the angle of incidence in a typical range of $0.5\alpha_c \leq \alpha_i \leq 30\alpha_c$, where α_c is the critical angle for total internal reflection, yields data from which information about the film "thickness" can be obtained. The value of q_z at the first minimum in the normalised reflectivity curve can be used to calculate l_T and l_H, the lengths of the "tail" and "head" regions respectively, according to this simple approximation:[226]

$$q_{min} = (l_T + \tfrac{1}{2} l_H) \approx \tfrac{3}{2}\pi \qquad (2.13)$$

3. MATERIALS, INSTRUMENTATION AND GENERAL METHODS

3.1 MATERIALS

The materials used in this work are listed in Table 3.1, together with their commercial source. All compounds were of AR or higher grade and were used without further purification.

Table 3.1 Materials and their commercial source

COMPOUND	COMMERCIAL SOURCE
Solids	
Bovine haematin (H_2O/HO^--Fe(III)PPIX)	Sigma
Bovine haemin (Cl-Fe(III)PPIX)	Sigma
Sodium hydroxide pellets (NaOH)	Kimix / Sigma
N-2-hydroxyethylpiperizine-N'-2-ethanesulfonic acid (HEPES)	Sigma
Sodium perchlorate monohydrate ($NaClO_4.H_2O$)	Merck
Sodium acetate trihydrate	Sigma
Sodium cyanide (NaCN)	Sigma
Citric acid monohydrate (Citrate)	Merck
Rac-glycerol 1-myristate (MMG)	Sigma
Liquids and Solutions	
Nitric acid 55% (HNO_3)	Merck
Hydrochloric acid 32% (HCl)	Orion Chemicals
Glacial acetic acid	Continental Laboratory Suppliers
Pyridine	BDH
Methanol	Kimix
Acetone	Kimix
^{1}H NMR Solvents	
Deuterium Oxide (D_2O) (99.9 Atom % D)	Sigma
Sodium Deuteroxide (NaOD) (30 Wt. % Solution)	Sigma
Pyridine-D5 (C_5D_5N) (Min. 99.96 Atom % D)	Sigma
Dimethyl sulfoxide-D6 ($(CD_3)_2SO$)	Sigma
Methyl-D3 Alcohol-D (CD_3OD) (99.8+ Atom % D)	Sigma

Table 3.1 continued. Materials and their commercial source

Antimalarial Drugs	
Chloroquine diphosphate (CQ)	Sigma
Quinine sulphate dihydrate (QN)	BDH
Quinidine sulphate dihydrate (QD)	Sigma
Mefloquine hydrochloride (MF)	Roche
Amodiaquine dihydrochloride dihydrate (AQ)	Sigma
Quinacrine dihydrochloride (QC)	Sigma
Pyronaridine phosphate (PN)*	World Health Organisation
Halofantrine hydrochloride (Hf)*	Glaxo SmithKline

* These compounds were provided by kind donation.

3.2 INSTRUMENTATION

3.2.1 pH Measurements

All pH measurements were performed using a glass pH electrode on a Crison MicropH 2000 pH meter. Standard phosphate buffer solutions (BDH Laboratory Supplies), at pH 4.00 ± 0.02 and 7.00 ± 0.02 (20 °C) were used to calibrate the electrode before use.

3.2.2 UV-Visible Spectroscopy

UV-visible spectra and single wavelength readings were recorded using a Varian CARY 100 UV-Visible Spectrophotometer. Quartz cuvettes of 10 cm (SUPRASIL®, Hellma) and 1 cm path lengths were used in the spectrophotometer. Following washing (in between or after measurements), cuvettes were blow dried with air.

3.2.3 Water Bath

Measurements which necessitated temperature control were thermostatted as required using a YIH DER BL-710 water bath circulator.

3.2.4 Nuclear Magnetic Resonance (NMR) Spectroscopy

^{1}H NMR spectra were recorded on a Varian Unity 400 MHz spectrometer at the University of Cape Town. Samples were prepared in deuterated solvent. Standard 5 mm glass NMR tubes were used.

3.2.5 Infrared (IR) Spectroscopy

FT-IR spectra were recorded at UCT using a Perkin-Elmer spectrophotometer. ATR-IR spectra were recorded at the Centre for Biospectroscopy, Monash University using a Bruker IFS Equinox FTIR system fitted with a Golden Gate TM single bounce diamond Micro-ATR (Attenuated Total Reflectance).

3.2.6 Electron Microscopy

Scanning electron microscopy (SEM) was carried out using a Leica S440 scanning electron microscope.

3.2.7 Resonance Raman (RR) Spectroscopy

RR spectra were recorded on a Renishaw system 2000 spectrometer with a 785 nm diode laser. The system is equipped with a BH2-UMA Olympus optical microscope. Spectra were recorded using a Zeiss × 50 objective. Data sets of between 20 and 30 spectra were recorded of each sample and the laser exposure for each scan was 15 – 20 s. The laser was used at 5 – 50% power depending on the quality of the spectra and the cut off for sample degradation.

3.2.8 Centrifugation

Large volumes (50 – 80 ml) were centrifuged in transparent polycarbonate Nalgene® centrifuge tubes using an Eppendorf 5810R centrifuge. The pellet was collected at 10,000 rpm after 10 – 15 minutes. Small volumes (0.5 – 2 ml) were centrifuged in plastic Eppendorf tubes using an Eppendorf 5410 centrifuge with a maximum speed of 14,000 rpm.

3.3 COMPUTER SOFTWARE

The computer software used during this thesis project is listed in Table 3.2.

Table 3.2 The computer software used in this thesis project

PROGRAMME	VERSION	USE	REFERENCE
FIT	1.08	Non-linear least squares fitting	229
GraphPad Prism	3.0	Analysis and graphing of scientific data	230
HYPERCHEM	7.5	Molecular modeling	231
OPUS	6.0	Spectral processing	232
The Unscrambler	9.2	Principal Components Analysis (PCA)	233
Endnote	4.0	Bibliography	234

3.4 GENERAL PREPARATIONS

Where water is specified for sample preparation, in all cases excluding NMR, this refers to glass distilled water. During preparation, small volumes (100 – 5000 µl) were delivered using Eppendorf micro pipettes. Solutions that required extensive stirring were mixed on a press-to-mix Snijders Analyser 34524.

0.20 M HEPES Buffer, pH 7.5

11.9155 g HEPES acid was dissolved in 200 ml distilled water. The pH was adjusted to 7.5 using a concentrated solution of sodium hydroxide (NaOH). The solution was transferred quantitatively and made to volume in a 250.0 ml volumetric flask.

0.1 M NaOH Solution

Solid pellets (3.9996 g, 100 mmol) of NaOH were dissolved in distilled water to a total volume of 1000 ml.

4. THE SPECIATION OF FE(III)PPIX IN AQUEOUS SOLUTION

4.1 INTRODUCTION

Interest in understanding the solution chemistry of Fe(III)PPIX began owing to its role as a prosthetic group in catalytic bio-molecules such as haemoproteins,[36,44] but decreased as more sophisticated methodologies and instruments allowed direct investigation of the proteins. Today, interest in this molecule is increasing again as a result of it being recognised as a contributor to many pathological conditions. These include atherogenesis (the process by which plaques form in the inner lining of arteries),[235] intestinal carcinogenesis,[236,237] hemolysis,[238] and vascular inflammation.[239]

Within the scope of this thesis, interest towards understanding the chemistry of Fe(III)PPIX in solution is a result of it being a by-product of digestion of blood feeding organisms, of which the malaria parasite, *P. falciparum*, is one example. As described in Chapter 1.4, the malaria parasite digests large quantities of host cell haemoglobin, sequestering at least 95%[15] of the released Fe(III)PPIX into crystalline haemozoin as a means of detoxification. A sound understanding of the solution chemistry of Fe(III)PPIX is essential if we are to determine the mechanism of haemozoin biocrystallisation.[63,64] As discussed in Chapter 1.7, complex formation between antimalarial drugs and aqueous Fe(III)PPIX is believed to inhibit haemozoin formation, resulting in a build-up of toxic Fe(III)PPIX. Understanding the structure of these solution-state complexes is central to the research effort to design new antimalarial compounds and rests, to a large extent, on understanding the solution chemistry of Fe(III)PPIX.

4.2 METHODS

This section describes the details of methods used specifically in the investigation of Fe(III)PPIX in aqueous solution. The materials used have been previously listed in Table 3.1.

4.2.1 Washing of Glassware and Cuvettes

Cuvettes, as well as glassware used to store Fe(III)PPIX solutions, were washed with a concentrated NaOH solution (prepared by dissolving pellets in water to form a thick slurry), followed by water and then a 1M HNO_3 solution. A final thorough rinsing with glass-distilled water was carried out before the glassware was dried. Cuvettes were blow dried with air and remaining glassware was oven dried at 393 K. A 25 µl Hamilton syringe was used to deliver the small volumes of Fe(III)PPIX solution to the cuvette during spectrophotometric titrations. The Hamilton syringe used for dispensing Fe(III)PPIX solutions was rinsed periodically with NaOH followed by extensive water washing to remove Fe(III)PPIX residues from the sides of the glass.

4.2.2 Spectra of Fe(III)PPIX

4.2.2.1 Sample Preparation

0.1 M NaOH was flushed with argon (for approximately 20 minutes) prior to it being used to prepare Fe(III)PPIX solutions. Fresh Fe(III)PPIX solutions were prepared for each experiment and these were protected from direct exposure to light.

*Fe(III)PPIX Stock Solution (**1**):*

A 0.995 mM solution of Fe(III)PPIX was prepared by dissolving haematin (6.3 mg, 9.945 µmol) in 0.1 M NaOH. The initial solution was mixed thoroughly and allowed to stand in the dark to ensure complete dissolution of the solid before being made to volume in a 10.0 ml volumetric flask with 0.1 M NaOH.

4.2.2.2 Experimental Procedures

The effects of concentration on the spectrum of aggregated Fe(III)PPIX were monitored by titrating stock solution **1** into a solution of 50.0 mM HEPES (various pH conditions, adjusted to physiological ionic strength (μ = 154 mM) with $NaClO_4$). Spectra were recorded in the range 300 – 800 nm, corrected for dilution and plotted in terms of their extinction coefficients (ε = A / c, l = 1 cm).

Induced μ-oxo Dimer of Fe(III)PPIX:

As has been previously shown, the μ-oxo dimer of Fe(III)PPIX can be induced by the inclusion of 10 % (v/v) pyridine in an aqueous alkaline solution.[48] 10% (v/v) pyridine was added to a 7.0 μM solution of Fe(III)PPIX in 0.1 M NaOH (prepared from stock solution **1**). The spectrum of the solution was recorded in the range 300 – 800 nm.

4.2.3 Beer's Law Measurements and Spectrophotometric Titrations

4.2.3.1 Sample Preparation

*Fe(III)PPIX Stock Solution (**2**):*

A tenfold dilution of stock solution **1** was prepared in 0.1 M NaOH in a 10.0 ml volumetric flask. The final concentration of stock solution **2** was 0.0995 mM.

All Fe(III)PPIX solutions were transferred to 25 ml glass storage vials, which had been wrapped with aluminium foil. They were stoppered and used within four hours.

HEPES Buffers:

50.0 mM HEPES buffer solutions were prepared in the pH range 6.0 – 9.0. Though the useful pH range of this buffer (6.8 – 8.2) was recognised, HEPES was used throughout for consistency and the pH measured before and after each titration to confirm that the pH had remained constant. Fresh solutions were prepared weekly. HEPES acid (1.192 g, 5.0 mmol) was dissolved in a small volume of water together with an appropriate mass $NaClO_4$ to give a final ionic strength of 154 mM

(Table 4.1). The pH of the solution was adjusted using a concentrated NaOH solution before being transferred quantitatively and made to volume in a 100.0 ml volumetric flask with water.

The contribution from HEPES base, B^-, to the ionic strength can be calculated from its equilibrium with HEPES acid, BH (equation 4.1 and 4.2):

$$BH \overset{K}{\rightleftharpoons} B^- + H^+ \qquad (4.1)$$

$$K_a = \frac{[B^-][H^+]}{[BH]}$$

$$[BH] = \frac{[B^-][H^+]}{K_a}$$

$$[B_T] = [BH] + [B^-] = \frac{[B^-][H^+]}{K_a} + [B^-]$$

$$[B_T] = [B^-]\left(\frac{[H^+]}{K_a} + 1\right)$$

$$\therefore [B^-] = \frac{[B_T]}{\left(\frac{[H^+]}{K_a} + 1\right)} \qquad (4.2)$$

where $[B_T]$ = 50.0 mM, the pK_a for acid dissociation of HEPES = 7.5 and the acid concentration, $[H^+]$, is determined by the final pH of the solution.

The required concentration of sodium perchlorate to obtain the desired ionic strength is given by equation 4.3:

$$[NaClO_4.H_2O] / mM = (154 - [B^-]) / mM \qquad (4.3)$$

The calculated contributions for each component are reported in Table 4.1.

Table 4.1 The concentration of [B^-] and the corresponding concentration and mass of $NaClO_4.H_2O$ added for each pH value so that the final ionic strength of the 50.0 mM HEPES solutions (V = 100 ml) is 154 mM

pH	$[H^+]$ / M	$[B^-]$ / mM	Required $[NaClO_4.H_2O]$ / mM	Actual Mass $NaClO_4.H_2O$ / g	Final μ / mM
6.00	1.000×10^{-6}	1.53	152.47	2.1415	154.0
6.26	5.495×10^{-7}	2.72	151.28	2.1248	154.0
6.89	1.288×10^{-7}	9.85	144.15	2.0220	153.8
7.20	6.310×10^{-8}	16.69	137.31	1.9286	154.0
7.41	3.890×10^{-8}	22.42	131.58	1.8521	154.3
7.69	2.042×10^{-8}	30.38	123.62	1.7324	153.7
8.06	8.710×10^{-9}	39.20	114.80	1.6116	153.9
8.48	3.311×10^{-9}	45.26	108.74	1.5273	154.0
8.98	1.047×10^{-9}	48.40	105.60	1.4832	154.0

4.2.3.2 Experimental Procedures

For both the Beer's law plots and the spectrophotometric titrations, a blanket of argon was maintained inside the measuring compartment of the spectrophotometer, which was operated at a temperature of 299 K (26°C). A 10 cm path length cuvette was used for lower concentrations while a standard 1 cm cuvette was used for higher concentrations. Buffer solution (20.0 ml for 10 cm cuvette, 2.0 ml for 1 cm cuvette) was dispensed into the cuvettes using either a 5.0 or 2.0 ml Eppendorf micropipette. The cuvette was then covered with parafilm and flushed with Argon (approximately 10 minutes) before being allowed to equilibrate in the spectrophotometer prior to beginning the experiments.

Beer's Law Measurements:

Beer's law states that there is a direct correlation between the transmission of light through a solution and the concentration of the solution in question.[199] The law is summarised in equation 4.4:

$$A = \varepsilon c l \qquad (4.4)$$

where A is the absorbance through the solution in question, ε is the molar absorptivity (extinction coefficient), c is the concentration of the solution in question and l is the path length of light through the cuvette.

This experiment was performed in order to show that A_{347} conforms to Beer's law. Measurements were conducted at pH 7.69 where adsorption of Fe(III)PPIX to the sides of the glass cuvette was deemed less problematic compared to lower pH values.

5.0 and 10.0 µl aliquots of stock solutions **1** and **2** were titrated into 50.0 mM HEPES buffer, pH 7.69 which had been flushed with argon prior to beginning the experiment. The solution was stirred with a glass rod after each addition and the absorbance measured at 347 nm. All data were corrected for dilution. A plot of A_{347} data with respect to Fe(III)PPIX concentration gave rise to a straight line from which the extinction coefficient (ε_{347}) was obtained by linear regression.

Spectrophotometric Titrations:
Triplicate titrations were performed in 50.0 mM HEPES buffer, μ = 154 mM, at pH values of 6.00, 6.26, 6.89, 7.20, 7.41, 7.69, 8.06, 8.48 and 8.98 in the Fe(III)PPIX concentration range 0.025 – 69 µM.

To the 10 cm cuvette: 200 µl of stock solution **2** in 5.0 and 10.0 µl aliquots, followed by 100 µl of stock solution **1** in 5.0 and 10.0 µl aliquots, was added to give a final Fe(III)PPIX concentration of 5.5 µM.

To the 1 cm cuvette: up to 150 µl of stock solution **1** in 10.0 µl aliquots was added to give a final haematin concentration of 69 µM.

After each addition, the solutions were stirred thoroughly with a glass rod and the absorbance measured at 347 and 393 nm. The data were corrected for dilution as before. Upon addition of the small cumulative volumes of Fe(III)PPIX stock solutions, deviations from the prepared pH of all solutions were found to be minimal.

ε_{347}, determined for each pH value from the average of three Beer's law measurements (A_{347} data), was found to be independent of the aggregation state of the porphyrin. It was used to correct for errors in concentration as a result of adsorption of Fe(III)PPIX onto glass surfaces during the experiment.

Accurate concentrations at each data point were determined by dividing A_{347} by ε_{347} (i.e. c = $A_{347}/\varepsilon_{347}$). ε_{393} (A_{393}/c) values were then determined according to equation 4.5:

$$\varepsilon_{393} = \frac{A_{393}}{A_{347}} \times \varepsilon_{347} \qquad (4.5)$$

The observed extinction coefficient (ε_{393}) at any point comprises the extinction coefficient of monomeric Fe(III)PPIX (designated $\varepsilon_{393,M}$) and that of the dimer (designated $\varepsilon_{393,D}$) and is expressed mathematically in equation 4.6:

$$\varepsilon_{393} = \varepsilon_{393,M} + (2\varepsilon_{393,D} - 2\varepsilon_{393,M})\left(\frac{[D]}{[M_T]}\right) \qquad (4.6)$$

The total Fe(III)PPIX concentration, $[M_T]$, is known experimentally and [D] is given by equation 4.7.

Recalling the model of Fe(III)PPIX dimerisation proposed by Brown and co-workers (Equation 1.1, p 7),[41] the following relationships between the Fe(III)PPIX monomer, M, and the dimer, D, can be determined:

$$K_a = \frac{[D][H^+]^n}{[M]^2}; K_{obs} = \frac{K_a}{[H^+]^n} = \frac{[D]}{[M]^2}$$

$$[M_T] = [M] + 2[D]$$

where K_{obs} is the observed dimerisation constant at any fixed pH. Substitution for $[M]$ and subsequent solving for $[D]$ in terms of $[M_T]$ gives rise to equation 4.7:

$$[D] = \frac{(4K_{obs}[M_T]+1) \pm \sqrt{(4K_{obs}[M_T]+1)^2 - 16K_{obs}^2[M_T]^2}}{8K_{obs}} \qquad (4.7)$$

Experimental data (ε_{393} and $[M_T]$) were fitted to equations 4.6 and 4.7 using non-linear least squares fitting.

4.2.4 The Effect of pH on the Visible Spectra of Fe(III)PPIX

4.2.4.1 Sample Preparation

Fe(III)PPIX Monomer in 80% (v/v) Aqueous Methanol

*Fe(III)PPIX Stock Solution (**3**):*

A 10.0 mM stock solution of Fe(III)PPIX was prepared by dissolving haematin (12.7 mg, 20 µmol) in 1.0 ml of 0.1 M NaOH to which 1.0 ml methanol was added.

HEPES Buffer:

An 80% (v/v) aqueous methanol solution containing 50.0 mM HEPES (µ = 154 mM) was prepared in a 100.0 ml volumetric flask by dissolving HEPES (1.192 g, 5.0 mmol) and $NaClO_4.H_2O$ (1.461 g, 10.4 mmol) in 15 ml water. The pH was adjusted using known volumes of a concentrated NaOH solution to ~ 12. The aqueous volume was made up to 20 ml with water. The solution was made to volume with methanol (~ 80 ml).

4.2.4.2 Experimental Procedures

20.0 µl of stock solution **3** was added to 2.0 ml of 80% (v/v) aqueous methanol HEPES buffer in a quartz cuvette, to give a working concentration of 0.1 mM. A concentrated mixture of 50 % (v/v) methanol-$HClO_4$ was prepared to ensure that only small additions would be needed to bring about pH changes. A maximum volume of 25.0 µl was added in aliquots of 1 and 2 µl. After each addition, the solution was stirred and both the pH and the absorbance of the charge transfer (CT) band (610 nm) were recorded. The final solution contained 79.3 % (v/v) methanol. Data were corrected for dilution and fitted to a one pK_a model.

Fe(III)PPIX Dimer in Aqueous Solution:

A series of 0.1 mM Fe(III)PPIX aqueous solutions containing 50.0 mM HEPES buffer and with an adjusted ionic strength (µ = 154 mM) were prepared to different pH values. The absorbance of the charge transfer (CT) band at 610 nm was

recorded for each solution. The absorbance data were fitted to both a one and two pK_a model.

4.2.5 Diffusion Measurements

4.2.5.1 Sample Preparation

Solution **4**: Two 1.03 mM solutions of Fe(III)PPIX containing 50.0 mM HEPES buffer (μ = 154 mM) were prepared by dissolving haematin (16.3 mg, 25.7 μmol) in a small amount of 0.1 M NaOH. The pH of each solution was adjusted (to 6.90 (*solution* **4a**) and 12.00 (*solution* **4b**) respectively) before being made to volume with water in a 25.0 ml volumetric flask.

Solution **5**: A 1.02 mM solution of the biscyano complex of Fe(III)PPIX (containing 50.0 mM HEPES buffer (μ = 154 mM)) was prepared by first dissolving haematin (16.2 mg, 25.6 μmol) in 0.1 M NaOH followed by the addition of 16 mM NaCN as previously described.[138] The solution was made to volume in a 25.0 ml volumetric flask with 0.1 M NaOH. The final pH of the solution was 12.00.

Solution **6**: A 1.02 mM solution of the μ-oxo dimer of Fe(III)PPIX was prepared by first dissolving haematin (16.2 mg, 25.6 μmol) in 0.1 M NaOH followed by the addition of 10% (v/v) pyridine.[48] The solution was made to volume in a 25.0 ml volumetric flask with 0.1 M NaOH. The final pH of the solution was 12.00.

4.2.5.2 Experimental Procedures

A simple diffusion cell previously described by Linder et al. was used to perform the diffusion measurements.[240] In each perspex unit there are four columns, each of which spans the top and bottom sections. However, for ease of description and illustration (Figure 4.1), it has been assumed that only two columns are present. The lower chamber of one column was completely filled as shown with the relevant Fe(III)PPIX solution (**4a**, **4b**, **5** or **6**), while the second column was completely filled with aqueous buffer. With the bottom section fixed in place, rotation of the top section through 180° brought aqueous buffer into contact with the Fe(III)PPIX

solution. Diffusion of Fe(III)PPIX into the aqueous buffer was allowed to proceed for 60 minutes at ambient temperature (which was recorded) before the top section was rotated 90° in order to isolate the top chamber. The solution from the top chamber of the experimental cell was thoroughly mixed in each case and analysed at 347, 396 and 421 nm for the aqueous, μ-oxo and biscyano species respectively.

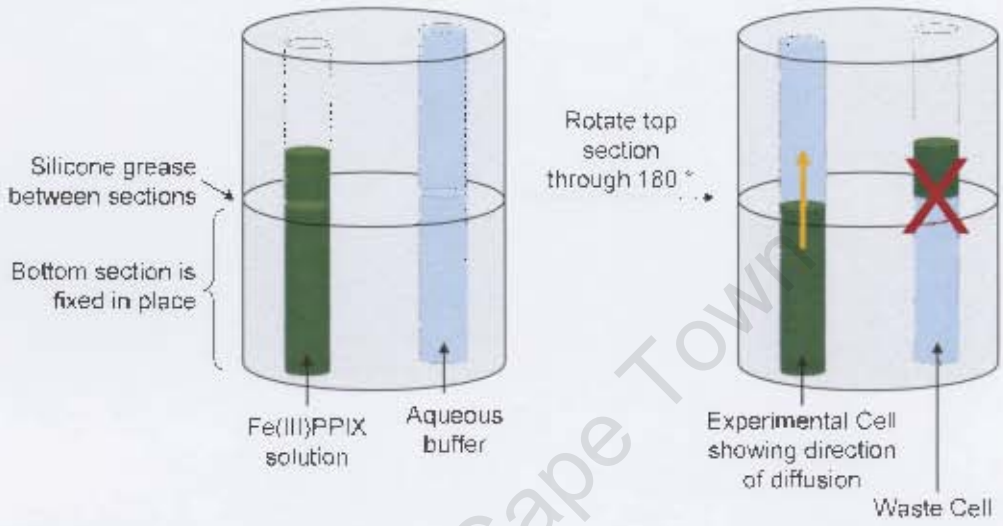

Figure 4.1 Schematic of the diffusion apparatus used for diffusion measurements.

This method relies on the fact that the concentration of Fe(III)PPIX in the lower chamber is sufficiently high that it remains essentially constant throughout the experiment. The diffusion coefficient, D, for each solution was calculated from equation 4.8:[240]

$$D = \left(\frac{Ch}{C_0}\right)^2 \frac{\pi}{t} \qquad (4.8)$$

where C_0 is the initial concentration of Fe(III)PPIX in the lower chamber, C is the final concentration of Fe(III)PPIX in the isolated upper chamber, h is the height of the upper chamber and t is the time allowed for diffusion.

4.2.6 ^{1}H Nuclear Magnetic Resonance Spectroscopy

4.2.6.1 Sample Preparation

*Fe(III)PPIX Stock Solution (**7**):*
A 20.0 mM solution of Fe(III)PPIX was prepared by dissolving haematin in 0.1 M NaOD in D_2O.

^{1}H NMR spectra were recorded in the chemical shift range -20 to 80 ppm for the following Fe(III)PPIX solutions:

Solution **8**: Two 10.0 mM solutions of Fe(III)PPIX were prepared from stock solution **7**. In each case, 0.5 ml of **7** was adjusted to a pH value of either 10.20 (*solution* **8a**) or 8.70 (*solution* **8b**) using 0.1 M $HClO_4$ and then made up to a final volume of 1.0 ml with D_2O.

Solution **9**: A 20.0 mM solution of Fe(III)PPIX in DMSO was prepared by dissolving haemin (owing to the poor solubility of haematin in this solvent) in d_6-DMSO.

Solution **10**: A 1.0 ml solution of the induced μ-oxo dimer of Fe(III)PPIX was prepared from 0.25 ml of **7** by the inclusion of 10% (v/v) d_5-pyridine (0.10 ml). The solution was made to a final volume of 1.0 ml with D_2O.

4.2.7 Magnetic Susceptibility Measurements

Magnetic susceptibility measurements were made using the solutions described below according to the Evans method.[241-243]

4.2.7.1 Sample Preparation

*Fe(III)PPIX Stock Solution (**11**):*
A 2.0 ml stock solution of Fe(III)PPIX was prepared by dissolving an accurately weighed mass of haematin (approximately 10 mg) in 0.1 M NaOD in D_2O.

Solution **12**: The pH of 0.10 ml of **11** was adjusted to 8.00 using 0.1 M $HClO_4$ and made to a final volume of 1.0 ml with D_2O.

Solution **13**: 0.10 ml of **11** was mixed with 10% (v/v) d_5-pyridine (0.10 ml) and the volume of the solution of made up to 1.0 ml with D_2O.

4.2.7.2 Experimental Procedures

A co-axial NMR tube was used for these experiments. This consists of a narrow glass tube inserted into a regular 5 mm NMR tube. The sample solution was placed in the inner tube while the reference solution (in each case, the solvent system with Fe(III)PPIX omitted) was placed in the outer tube.

The ^1H NMR spectrum of the solvent (H_2O) peak was measured for both the sample and the reference solutions and the difference in chemical shift between them (Δf/Hz) was determined. In the presence of the paramagnetic Fe(III)PPIX species, the H_2O peak shifted downfield relative to the reference H_2O peak. Therefore, $\Delta f = f_{reference} - f_{sample}$ has a negative value.[244]

The mass susceptibility (χ_g) of the dissolved Fe(III)PPIX was determined from equation 4.9:[243]

$$\chi_g = \frac{-3\Delta f}{4\pi f m} + \chi_0 \qquad (4.9)$$

where f is the operating frequency of the spectrometer (399.952 MHz), m is the mass concentration (g/ml) of Fe(III)PPIX and χ_0 is the mass susceptibility of the solvent (-7.22×10^{-7} g^{-1} for H_2O[245]).

Multiplying together χ_g and the molecular weight of the paramagnetic species gives the molar susceptibility (χ_M), which is then used to calculate the magnetic moment, μ, according to equation 4.10:

$$\mu = 2.84\sqrt{\chi_M T} \qquad (4.10)$$

where T is the temperature of the sample in the spectrometer.

The total molecular spin quantum number (S) was calculated from equation 4.11:

$$\mu = 2\sqrt{S(S+1)} \qquad (4.11)$$

4.2.8 Molecular Modelling

Molecular Dynamics/Simulated Annealing (MD/SA) calculations were performed using the MM+ forcefield in HYPERCHEM,[231] together with modified parameters for the purpose of modelling porphyrins.[246-248] A back-to-back Fe(III)PPIX $\pi - \pi$ dimer was constructed from the energy-minimised (Polak-Ribiere algorithm) 5-coordinate Fe(III) porphyrin. 25 MD/SA simulations were performed with heating from 0 – 150 K over 5 ps, run times of 5 – 12 ps and slow cooling over 20 ps in steps of 0.010 ps. Final structures were processed through a second geometry optimisation.

4.3 RESULTS

4.3.1 Adsorption of Fe(III)PPIX onto Glass and Plastic Surfaces

It has been recognised that organic molecules adsorb onto glass and plastic surfaces, a process that can result in significantly altered concentrations, especially of dilute solutions.[249] Such adsorption is likely from solutions of Fe(III)PPIX given the hydrophobic nature of the porphyrin core, and would therefore be expected to contribute to the apparent time-dependent instability observed in such solutions.[36,141] Indeed, this behaviour has been noted even in solutions of Fe(III)PPIX in 40% (v/v) aqueous DMSO,[123,126] where the measured absorbance has been observed to decrease with time. Though not reported, it was verified that this behaviour was not a result of oxidation or photodegradation by keeping solutions under an inert atmosphere and in the dark. Furthermore, the use of new glassware or thorough washing of previously used glassware according to methods described in Section 4.2.1, has been recognised to improve the stability of Fe(III)PPIX solutions.

The propensity for Fe(III)PPIX to adsorb onto glass and plastic surfaces from purely aqueous solutions is expected to be even more significant compared to

mixed aqueous-organic systems. This process was investigated in some detail in order to understand in advance its underlying contribution to all further experiments conducted in aqueous medium.

The UV-vis spectrum of a 4.9 μM solution of Fe(III)PPIX in 50.0 mM HEPES buffer, pH 6.9, μ = 154 mM, was recorded in the range 300 – 800 nm (Figure 4.2, i). The quartz cuvette was then thoroughly washed with distilled water and air-dried. Subsequently, the spectrum of HEPES buffer, used to blank the spectrophotometer prior to the first spectrum, was recorded in the same wavelength range. However, residual Fe(III)PPIX is clearly discernable in the baseline (Figure 4.2, ii and iii). The Fe(III)PPIX solution was introduced into the cuvette for three additional cycles and after each, the absorbance of the residual Fe(III)PPIX was seen to increase. Only when the cuvette was washed according to methods described in Section 4.2.1 did the baseline reflect no traces of residual Fe(III)PPIX.

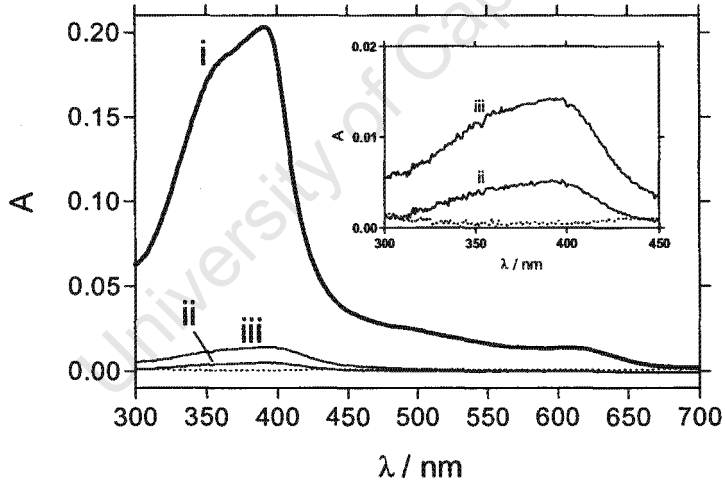

Figure 4.2 The adsorption of Fe(III)PPIX on the surfaces of a quartz cuvette. The UV-vis spectrum (i) of a 4.9 μM solution of Fe(III)PPIX in 50.0 mM HEPES buffer, pH 6.9, μ = 154 mM. The inset shows an expansion of the Soret region of spectra of residual Fe(III)PPIX recorded from blank buffer solution after the first (ii) and final (iii) introductions of Fe(III)PPIX into the cuvette. The dotted line confirms that the baseline returns to its original absorbance after thorough washing of the cuvette with concentrated NaOH and 1 M HNO_3 followed by distilled water.

The use of plastic apparatus, such as stirring rods and air-displacement pipette (Gilson or Eppendorf) tips, further contributes to the problem of adsorption. The

absorbance spectra of two solutions, prepared by delivering the same volume of stock solution with either a plastic pipette tip or a glass Hamilton microsyringe, are shown in Figure 4.3. The use of a plastic pipette tip results in an approximate 6% decreased absorbance relative to a glass microsyringe. Furthermore, plastic pipette tips are noticeably discoloured after use. For this reason, plasticware was avoided as far as possible in all subsequent experiments.

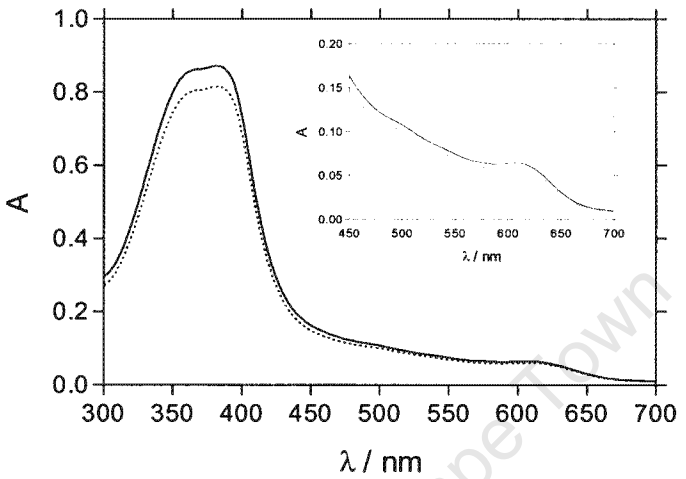

Figure 4.3 The adsorption of Fe(III)PPIX onto the plastic surfaces of apparatus. The UV-vis spectra of 19 μM solutions of Fe(III)PPIX in 50.0 mM HEPES buffer, pH 6.9, μ = 154 mM, prepared by delivering equal volumes of a stock solution using either a glass Hamilton microsyringe (solid line) or a plastic pipette tip (dotted line).

It should be noted that owing to the specific surface characteristics of the glassware used together with the details of its previous treatment, as well as the concentration of and time over which Fe(III)PPIX solutions are left in contact with the glass surfaces, the observations described above are not quantitatively reproducible.

4.3.2 Accurate Determination of Fe(III)PPIX Concentrations

The effects of adsorption described above are in fact concentration-dependent, and are expected to be more significant in dilute solutions. In this Chapter, the aggregation of Fe(III)PPIX in aqueous solution is the main focus. This too is a concentration-dependent process, with Fe(III)PPIX expected to be monomeric at very low concentrations and dimerised or aggregated at elevated concentrations.

Given the overlap, it was essential to find a way to correct for adsorption effects before proceeding to further analysis.

The effects of increasing concentration on the spectrum of aggregated Fe(III)PPIX in aqueous solution are shown in Figure 4.4 below. Displayed in the form of extinction coefficient as a function of wavelength, the series of spectra show that the Soret band (393 nm) decreases with increasing concentration as is expected (refer to section 2.2.2), while an apparent isosbestic point occurs at about 347 nm. At this wavelength the extinction coefficient is independent of Fe(III)PPIX concentration. It must be emphasised that these spectra were collected in a new cuvette and that exceptional care was taken to avoid adsorption.

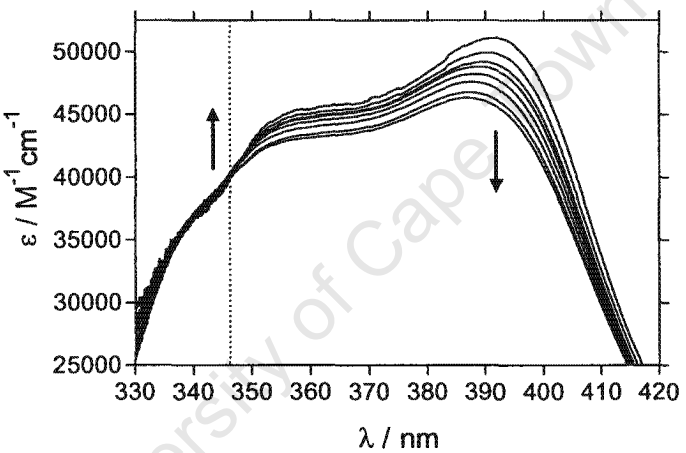

Figure 4.4 The effect of increasing concentration on the UV-vis spectra (displayed in terms of extinction coefficients) of aqueous solutions of Fe(III)PPIX, 50.0 mM HEPES buffer, pH 8.06, μ = 154 mM. The Fe(III)PPIX concentration ranged between 0.4 – 2 μM. Arrows show the direction of change with increasing concentration, while the dotted vertical line indicates the presence of an isosbestic point at about 347 nm.

To confirm the presence of the isosbestic point at 347 nm, a Beer's law titration was carried out to determine the relationship between absorbance and concentration. The Beer's law plot at 347 nm (Figure 4.5 A) is linear over the entire concentration range (0.025 – 30 μM) while that of the Soret band maximum (Figure 4.5 B) deviates markedly from Beer's law. Linear regression of the Beer's law data at 347 nm yields the extinction coefficient at this wavelength, ε_{347}. As described in section 4.2.1.3, accurate determinations of Fe(III)PPIX concentrations could then be made. The standard operating procedure for spectrophotometric titrations was therefore to measure the absorbance at both 347 and 393 nm, to

calculate accurate concentrations using ε_{347} and to determine accurate values of ε_{393} according to equation 4.5.

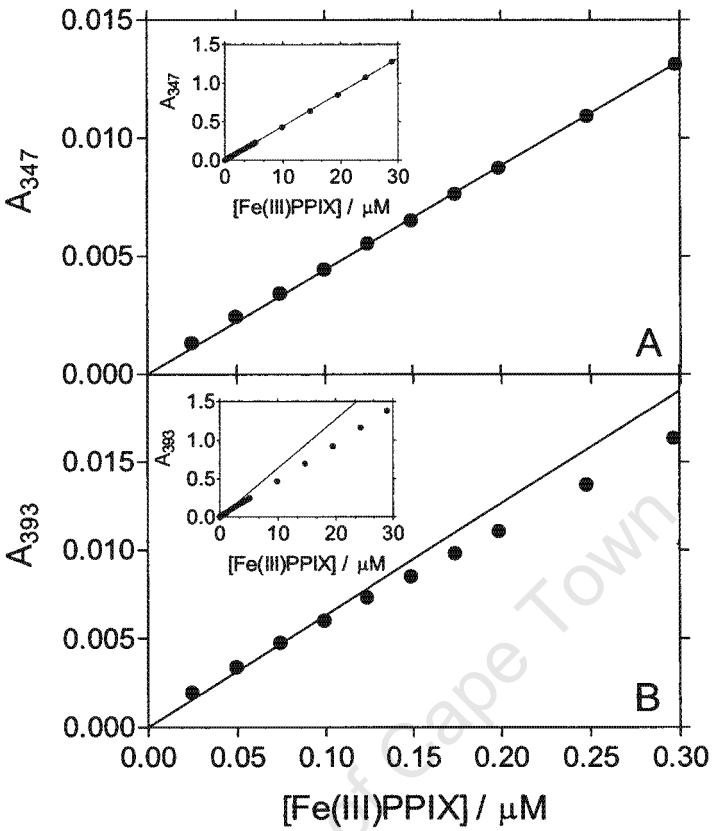

Figure 4.5 Beer's law plots of (A) A_{347} and (B) A_{393} as a function of Fe(III)PPIX concentration between 0.025 and 30 μM (50.0 mM HEPES, pH 7.69, μ = 154 mM). In A, a straight line was fitted to the first ten data points (0.025 – 0.3 μM). It passes through the origin and all remaining points without adjustment to the slope, even when extrapolated 100-fold (inset). This is not the case in B, where the straight line can only be manually fitted to the first four data points and had to be forced through the origin. Deviations below the line, owing to the aggregation of Fe(III)PPIX, are already evident from 0.1 μM and are very marked at higher concentrations (inset) where the data fall on a straight line of lower slope.

4.3.3 The Aggregation State of Fe(III)PPIX

Spectrophotometric titrations were carried out over the pH range 6.0 – 9.0 to obtain measurements of ε_{393} from A_{393}, A_{347} and ε_{393} according to equation 4.5. Figure 4.6 displays representative plots of the dependence of ε_{393} on Fe(III)PPIX concentration. In all cases, the data conform to a dimerisation model (equations 4.6 and 4.7), with no evidence of formation of higher aggregates over the entire

concentration range in which absorbance measurements are reliable (using 10- and 1-cm cuvettes, a 0.025 – 30 μM concentration range, corresponding to A = 0.015 – 2.00, was feasible). Countering the effects of adsorption by using equation 4.5, the titrations were reproducible up to four hours after preparation of the Fe(III)PPIX stock solutions. The stability of the solutions beyond this time was not investigated.

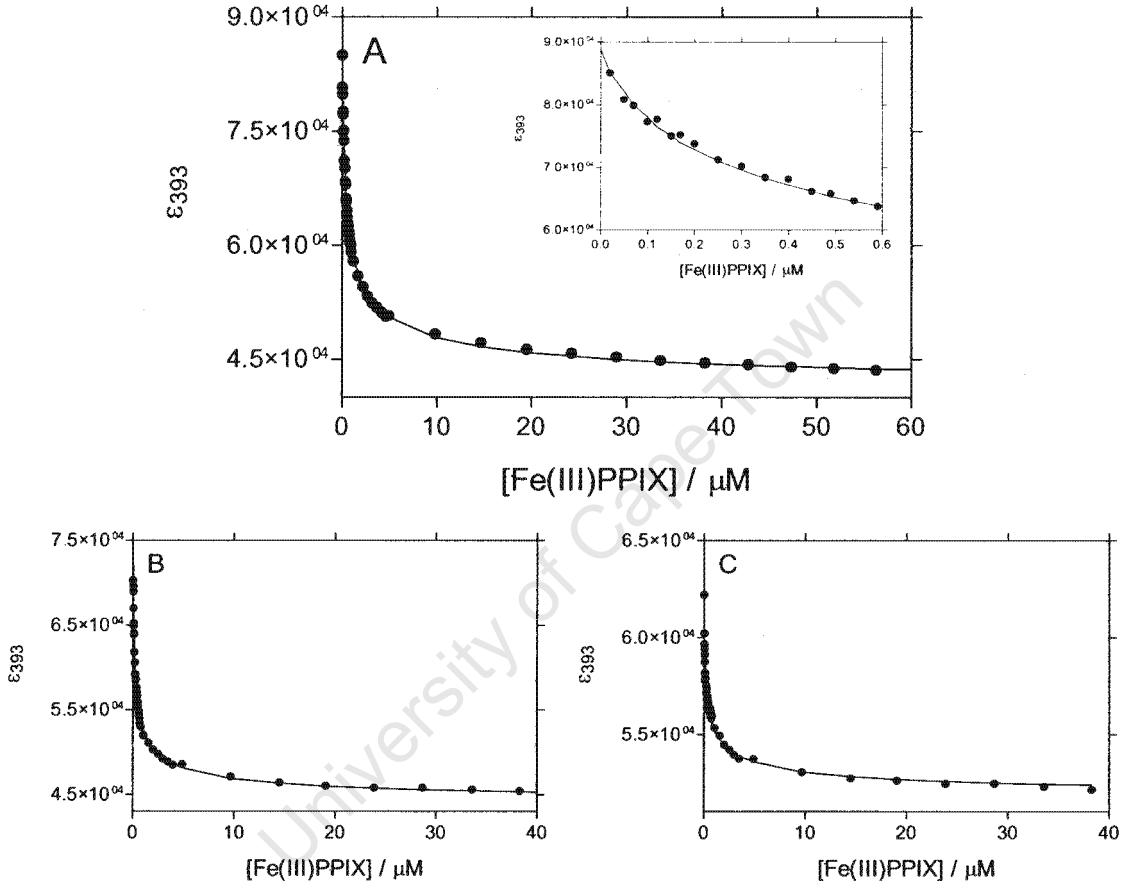

Figure 4.6 The dependence of the Soret band extinction coefficient (ε_{393}) of aqueous Fe(III)PPIX (50.0 mM HEPES, μ = 154 mM) on concentration at (A) pH 6.89, (B) pH 7.43 and (C) pH 8.98. In all cases, the solid lines are best fits of the data to a dimerisation model (equations 4.6 and 4.7). The inset in A shows that the data conform to this model even at very low concentrations.

4.3.4 The Effect of pH on Fe(III)PPIX Dimerisation

Fitting of experimental data to the dimerisation model described by equations 4.6 and 4.7 allows extraction of three parameters, namely the extinction coefficients at 393 nm for the monomer ($\varepsilon_{393,M}$) and dimer ($\varepsilon_{393,D}$) as well as the observed

dimerisation constant ($K_{D,obs}$). These parameters are dependent on pH as can be seen from the values reported in Table 4.2.

Table 4.2 Observed log dimerisation constants (log $K_{D,obs}$) and extinction coefficients at 393 nm for the monomer ($\varepsilon_{393,M}$) and dimer ($\varepsilon_{393,D}$)

pH	log $K_{D,obs}$*	$\varepsilon_{393,M}$ / 10^4 M^{-1} cm^{-1} *,#	$\varepsilon_{393,D}$ / 10^4 M^{-1} cm^{-1} *,#
6.00	6.3 ± 0.3	9.9 ± 1.1	3.6 ± 0.1
6.26	6.44 ± 0.04	9.7 ± 0.4	4.07 ± 0.07
6.89	6.6 ± 0.1	8.3 ± 0.4	4.08 ± 0.06
7.20	6.72 ± 0.03	7.9 ± 0.6	4.5 ± 0.2
7.43	6.82 ± 0.06	8.0 ± 0.4	4.5 ± 0.2
8.06	6.49 ± 0.06	6.5 ± 0.4	4.9 ± 0.2
8.48	6.30 ± 0.03	6.5 ± 0.2	5.2 ± 0.1
8.98	6.3 ± 0.1	5.9 ± 0.1	5.07 ± 0.08

* Mean ± standard error of the mean for at least three determinations.

Expressed per mole of Fe(III)PPIX.

The pH dependence of $\varepsilon_{393,M}$ appears to be consistent with a single deprotonation process (Figure 4.7 A), although the relatively large data scatter attributed to a rather low fraction of monomeric Fe(III)PPIX even at the lowest measurable concentrations, prevents a conclusive fit ($pK_{a,M}$ = 7.1 ± 0.2). The pH dependence of monomeric Fe(III)PPIX was thus investigated in 80% (v/v) aqueous methanol. UV-vis spectra reveal marked changes over the entire spectrum (300 – 800 nm) as a function of pH (Figure 4.7 B), which are most likely owing to the deprotonation of the axial water ligand as the pH increases. In order to confirm this, changes in the absorbance of the charge transfer (CT) band at 610 nm of Fe(III)PPIX in 80% (v/v) aqueous methanol were monitored as a function of pH. The data conform to a single deprotonation process (Figure 4.7 C) and the fit yields a single $pK_{a,M}$ value (7.11 ± 0.05) that is essentially the same as that obtained in aqueous solution.

The pH dependence of $\varepsilon_{393,D}$ is difficult to fit directly to deprotonation models owing to only very small changes in magnitude. However, given that the dimer is overwhelmingly the dominant species in aqueous solution at relatively high concentrations, it can be readily investigated independently. Once more, UV-vis spectra show marked changes over the entire spectrum (300 – 800 nm) as a

function of pH (Figure 4.7 D). In keeping with the monomeric species, these variations may be due to changes at the axial ligands of the two Fe(III)PPIX molecules involved in dimer formation. Changes in the absorbance of the charge transfer (CT) band at 610 nm of aqueous Fe(III)PPIX as a function of pH are consistent with two consecutive deprotonation processes (Figure 4.7 E), yielding pK_a values of 7.16 ± 0.06 ($pK_{a,D1}$) and 8.56 ± 0.08 ($pK_{a,D2}$) respectively. The data are not consistent with a single deprotonation process (Figure 4.7 F).

Given the above observations of both the monomer and dimer of Fe(III)PPIX, Scheme 4.1 is presented as a plausible explanation of the overall dimerisation process in aqueous solution.

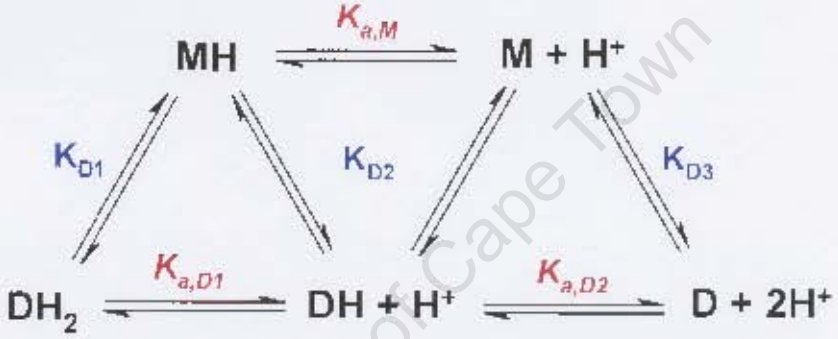

Scheme 4.1 The proposed model for the dimerisation of Fe(III)PPIX. M and D represent the monomer and dimer respectively. As indicated, a single equilibrium dissociation constant is expected for the deprotonation of the monomeric species MH ($K_{a,M}$), while two such constants are expected for the dimer: $K_{a,D1}$ and $K_{a,D2}$. As shown, the observed dimerisation constant ($K_{D,obs}$) is a pH-dependent mixture of three different dimerisation constants: K_{D1}, K_{D2} and K_{D3}.

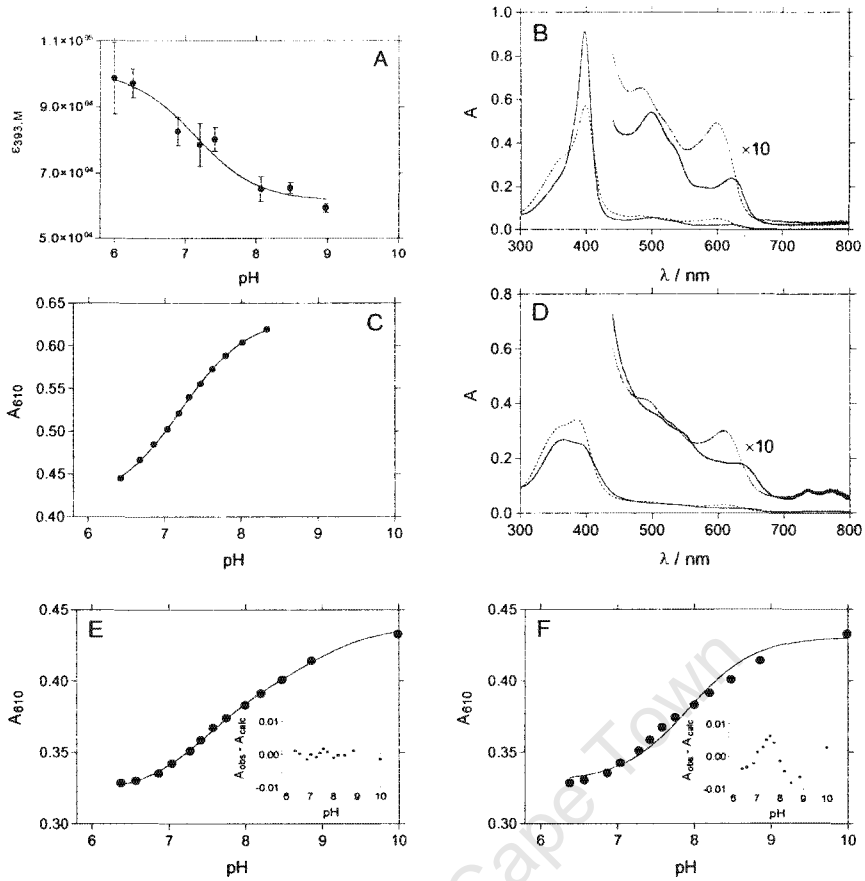

Figure 4.7 The effect of pH on Fe(III)PPIX dimerisation. (A) The dependence of the extinction coefficient of monomeric Fe(III)PPIX in aqueous solution ($\varepsilon_{393,M}$) on pH. The solid line is the best fit of the data to a single deprotonation process yielding a p$K_{a,M}$ of 7.1 ± 0.2. (B) The changes with pH in the UV-vis spectrum of 7 μM Fe(III)PPIX (μ = 154 mM) in 80% (v/v) aqueous methanol. The solid line is of the spectrum recorded at pH 5.536 (50.0 mM MES buffer) while the dotted line is of the spectrum recorded at pH 8.862 (50.0 mM CHES buffer). (C) The changes in A_{610} of Fe(III)PPIX in 80% (v/v) aqueous methanol. The solid line is the best fit of the data to a single deprotonation process yielding a p$K_{a,M}$ of 7.11 ± 0.05. In (B) and (C), pH measurements were made in the aqueous methanol solutions. (D) The changes with pH in the UV-vis spectrum of 7 μM aqueous Fe(III)PPIX (μ = 154 mM). The solid line is of the spectrum recorded at pH 6.029 (50.0 mM MES buffer) while the dotted line is of the spectrum recorded at pH 9.669 (50.0 mM CHES buffer). (E) The changes in A_{610} of aqueous Fe(III)PPIX. The solid line is the best fit of the data to two consecutive deprotonation processes yielding two pK_a values: 7.16 ± 0.06 (p$K_{a,D1}$) and 8.56 ± 0.08 (p$K_{a,D2}$). Residuals are shown in the inset. (F) The changes in A_{610} of aqueous Fe(III)PPIX. The solid line is the best fit of the data to a single deprotonation process. Residuals, shown in the inset, demonstrate systematic deviations.

The pH dependence of the observed dimerisation constant, $K_{D,obs}$, can be described as follows (equations 4.12 – 4.15):

$$K_{D,obs} = K_{D3} \frac{\left(1 + \frac{[H^+]}{K_{a,D2}} + \frac{[H^+]^2}{K_{a,D2}K_{a,D1}}\right)}{\left(1 + \frac{[H^+]}{K_{a,M}}\right)^2} \quad (4.12)$$

$$K_{D2} = K_{D3} \frac{K_{a,M}}{K_{a,D2}} \quad (4.13)$$

$$K_{D1} = K_{D3} \frac{K_{a,M}^2}{K_{a,D1}K_{a,D2}} \quad (4.14)$$

and

$$K_{D,obs} = \frac{[D]_T}{[M]_T^2} \quad (4.15)$$

where $[D]_T$ and $[M]_T$ are the total concentrations of Fe(III)PPIX dimer and monomer, regardless of protonation state.

That the observed dimerisation constants (log $K_{D,obs}$) are consistent with the model presented in Scheme 4.1 is shown in Figure 4.8. A best fit of the experimental data to equation 4.12 allows extraction of K_{D3}. Values of K_{D2} and K_{D1} are obtained through calculation according to equation 4.13 and 4.14 respectively. The fitted and calculated parameters, together with the experimentally determined values are reported in Table 4.3.

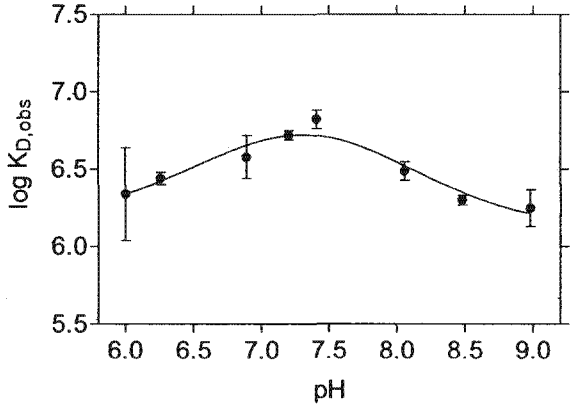

Figure 4.8 The dependence of the log observed dimerisation constants on pH. The solid line is the best fit of the data to equation 4.12, which is derived based on Scheme 4.1.

Table 4.3 Fitted, calculated and experimentally determined constants according to Scheme 4.1 to describe the dependence of Fe(III)PPIX dimerisation on pH

PARAMETER	EXPERIMENTAL VALUE	FITTED OR CALCULATED VALUE
$pK_{a,M}$	7.11 ± 0.05*	7.3 ± 0.2
$pK_{a,D1}$	7.16 ± 0.06	6.2 ± 0.3
$pK_{a,D2}$	8.56 ± 0.08	8.5 ± 0.3
$\log K_{D1}$	-	6.2#
$\log K_{D2}$	-	7.3†
$\log K_{D3}$	-	6.1 ± 0.1

* Determined in 80% (v/v) aqueous methanol.

Calculated from equation 4.14. † Calculated from equation 4.13.

4.3.5 Diffusion Measurements

The evidence arising from the spectrophotometric studies described above strongly suggests that aqueous Fe(III)PPIX forms dimers and not higher aggregates. The formation of higher aggregates via hydrogen bonding between the propionate groups as opposed to $\pi - \pi$ interactions of the porphyrin chromophores however cannot be ruled out, although in an aqueous environment, strong hydrogen bonding competition would be expected from water molecules.

Diffusion measurements were therefore undertaken in order to independently substantiate the conclusion that Fe(III)PPIX dimerises but does not form higher aggregates in aqueous solution. Theoretically, the diffusion coefficient, D, of the diffusing species can be determined from the Stokes-Einstein relationship:[250]

$$D = \frac{k_B T}{6\pi\eta a} \qquad (4.16)$$

where k_B is the Boltzmann constant, η is the viscosity of the solution and a is the hydrodynamic radius of the diffusing particle. The latter point causes some difficulty for measurements carried out in an aqueous medium, as it is extremely difficult to predict the extent of the hydration shell. However, it was reasoned that this approach would still be able to distinguish between proposed massive aggregates on the one hand and dimers (or at least small oligomers) on the other as predicted above, especially as the comparison would be made between related

species. Further it was recognised that an empirical relationship between the diffusion coefficients of planar, delocalised organic molecules (polyaromatic hydrocarbons, PAHs) and their molar volumes could provide a valid means of size comparison.[251]

In order to have some value to benchmark experimentally-determined diffusion coefficients against, that of the unhydrated Fe(III)PPIX monomer, approximated by a sphere of radius 4.8 Å, was calculated (using equation 4.16). Assuming the solution to have the same viscosity as water and an operating temperature of 293 K, the predicted diffusion coefficient was calculated to be 4.5×10^{-10} m^2 s^{-1}. The hydrated species was expected to diffuse at a slower rate, migration being retarded by the hydration shell. The extent of the retardation cannot, however, be predicted. Furthermore, the diffusion coefficient of the Fe(III)PPIX dimer was expected to be yet smaller than that of the monomer while still within about the same order of magnitude. Massive aggregates would be expected to diffuse so slowly that their diffusion coefficients would be reduced by orders of magnitude.

The species investigated were aqueous Fe(III)PPIX (pH 6.90 and 11.90), the induced μ-oxo dimer of Fe(III)PPIX (10% (v/v) aqueous pyridine in 0.1 M NaOH, pH 12.00) and the monomeric, low-spin biscyano complex of Fe(III)PPIX (16 mM NaCN, pH 12.00). The UV-vis spectrum of the induced μ-oxo dimer of Fe(III)PPIX (Figure 4.9 A) shows the characteristic features for such a species,[48] while a Beer's law plot of the biscyano complex of Fe(III)PPIX at 421 nm (Figure 4.9 B) confirmed that it is indeed monomeric. The concentration range of the Beer's plot is limited by the absorbance of the species, which exceeds a value of 1.5 for concentrations greater than 20 μM. However, within the measurable range, the entire spectrum remained unchanged after each addition, indicating that the species is independent of concentration at all wavelengths. Presumably the biscyano complex of Fe(III)PPIX remains monomeric even at the concentration of the diffusing solution (1.02 mM). The experimentally-determined diffusion coefficients for all species are reported in Table 4.4.

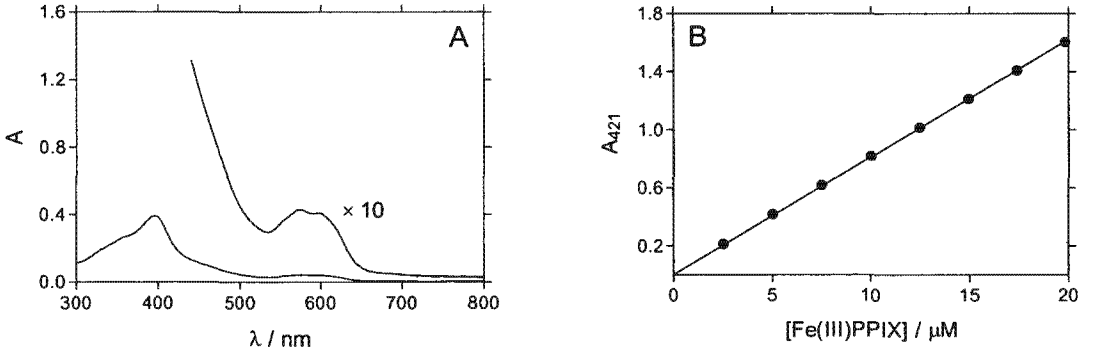

Figure 4.9 (A) The UV-visible spectrum of Fe(III)PPIX dissolved in 0.1 M NaOH containing 10% (v/v) pyridine. (B) The Beer's law plot (A_{421}) of the biscyano complex of Fe(III)PPIX in the concentration range 2.5 – 20 μM. Linearity over the entire concentration range confirms that this species is monomeric.

Table 4.4 Diffusion coefficients, D, calculated according to equation 4.16 and measured using the apparatus described in section 4.2.5

CONDITIONS	SPECIES PRESENT	10^{10} D / m^2 s^{-1}
Estimated, unhydrated	Monomer	4.5
Aqueous, pH 6.90	Aqueous aggregate	1.0 ± 0.2
Aqueous, pH 11.90	Aqueous aggregate	1.2 ± 0.1
10% (v/v) aqueous pyridine in 0.1 M NaOH, pH 12.00	μ-oxo dimer	1.1 ± 0.1
16 mM NaCN, pH 12.00	Monomeric biscyano complex	1.9 ± 0.2

The diffusion coefficient of the monomeric biscyano complex is nearly twice that of the aqueous aggregate and μ-oxo dimer, indicating that the aqueous species is more than likely a dimer. However, as discussed above, uncertainties in the size of accompanying hydration shells means that small oligomers (trimers and tetramers) cannot be totally excluded. These experiments do indicate that massive aggregates of Fe(III)PPIX are not present in aqueous solution.

The relationship between the log diffusion coefficients (log D) of PAHs in aqueous solution and their log molar volumes (log V_b) is linear.[251] A plot of this relationship for data extracted from Gustafson and Dickhut is shown in Figure 4.10. Extrapolation of the regression line shows that data for the aqueous Fe(III)PPIX species and the biscyano Fe(III)PPIX complex are consistent with this trend, if molar volumes are approximated to that of a dimer and monomer respectively.

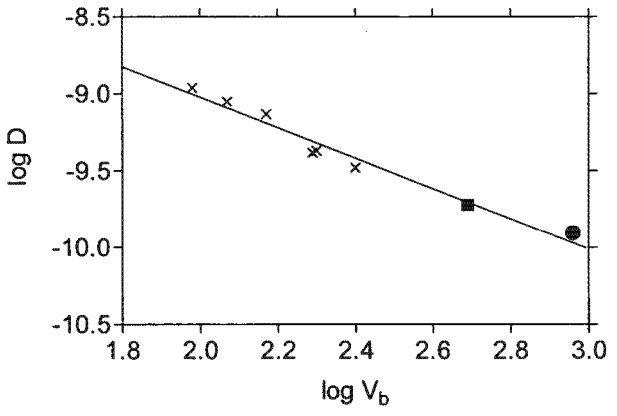

Figure 4.10 The dependence of log D (diffusion coefficient) on log V_b (molar volume) for a series of planar, delocalised organic molecules. Data extracted for polyaromatic hydrocarbons[251] are represented as crosses (×), while data for the aqueous Fe(III)PPIX dimer (●) and the monomeric biscyano Fe(III)PPIX complex (■), determined from this present study, are included. The molar volumes were estimated as follows: $V_b = M_m/\rho$. M_m for the aqueous Fe(III)PPIX dimer was assumed to be 1266 $gmol^{-1}$ (2 × 633 $gmol^{-1}$ for H_2O-Fe(III)PPIX) and calculated as 667 $gmol^{-1}$ for the biscyano Fe(III)PPIX complex. The density for both species was approximated to that of haematin, measured by flotation in chloroform/acetone to be 1.3753 gml^{-1}. Experimental diffusion data were corrected to 298 K for purposes of comparison.

4.3.6 ^{1}H Nuclear Magnetic Resonance Spectroscopy

In order to investigate the nature of the aqueous dimer of Fe(III)PPIX further, high-field ^{1}H NMR spectra of this and the induced μ-oxo dimer (in 10% (v/v) aqueous alkaline pyridine) were recorded. The spectrum of the aqueous species (Figure 4.11 A) is strikingly different to that of the induced μ-oxo dimer (Figure 4.11 B). Most noticeably, the spectrum of the induced μ-oxo dimer lies within the normal ^{1}H NMR spectral range (0 – 10 ppm), while that of the aqueous dimer of Fe(III)PPIX lies within the spectral range -10 – 60 ppm. The former observation, consistent with ^{1}H NMR spectra of some μ-oxo-bis[2,4-disubstituted iron(III) deuteroporphyrin dimethyl esters],[48] is attributed to antiferromagnetic coupling between electrons at the two Fe(III) centres across the oxo-bridge. The influence of the paramagnetic Fe(III) centre in the spontaneously formed aqueous dimer of Fe(III)PPIX is responsible for chemical shifts as far downfield as 60 ppm. The spectrum of the spontaneously formed aqueous dimer shows close resemblance to that of the haemin dimethyl ester in chloroform.[252] Noting the obvious absence of the peaks

for the methyl groups of the methyl ester side chains, the spectrum of the spontaneously formed aqueous dimer (Figure 4.11 A) includes diagnostic features for high-spin, five-coordinate Fe(III) porphyrins, as identified by Budd and co-workers.[252] For comparison, the spectrum of a high-spin six-coordinate species formed spontaneously in DMSO (Figure 4.11 C) was recorded. It is in agreement with that reported by Budd and co-workers,[252] with sharp, distinct peaks contrasting the broad signals of the high-spin, five-coordinate species. Tentative assignments for all species are made on the spectra and discussed in the figure caption.

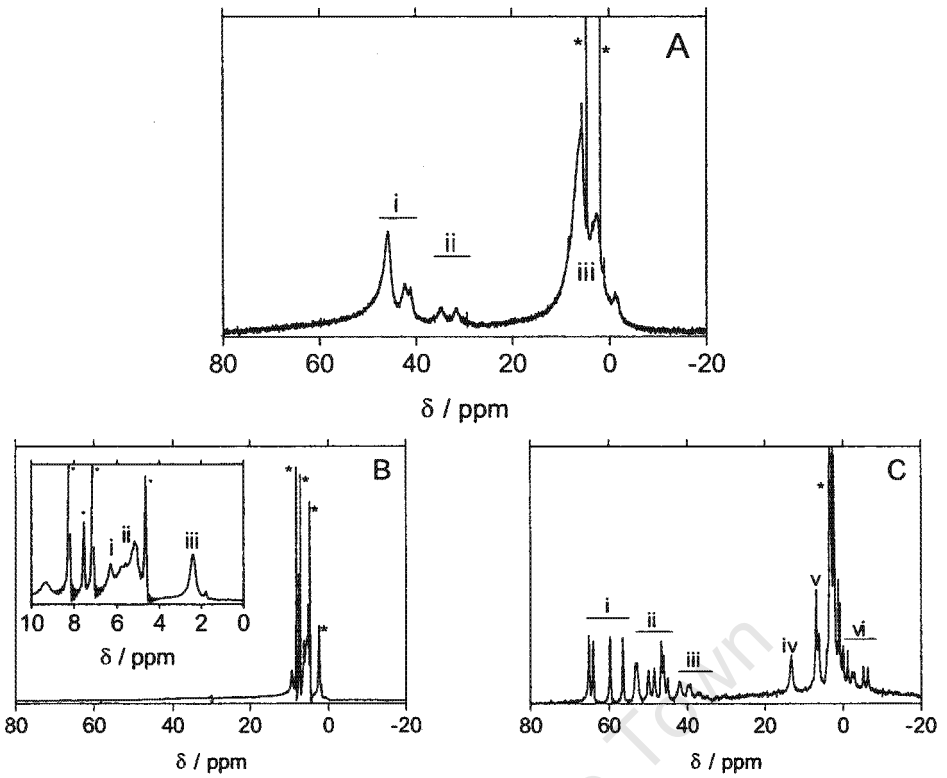

Figure 4.11 (A) The high-field ^{1}H NMR spectrum of the spontaneously formed dimer of Fe(III)PPIX in D_2O. Tentative assignments of peaks, based on the spectrum reported by Budd an co-workers,[252] are as follows: (i) methyl groups, (ii) vinyl α-CH and propionyl α-CH_2, (iii) *cis* and *trans* vinyl β-CH_2 and propionyl β-CH_2. Signals for the porphyrin *meso* protons are thought to be broad and probably underlie the prominent peaks in the 25 – 55 ppm range. (B) The high-field ^{1}H NMR spectrum of the μ-oxo dimer of Fe(III)PPIX induced in 10% (v/v) aqueous d_5-pyridine in 0.1 M NaOD/D_2O. Tentative assignments of peaks (indicated in the inset), based on spectra reported by O'Keeffe an co-workers,[48] are as follows: (i) propionyl α-CH_2, (ii) methyl groups and (iii) propionyl β-CH_2. Signals for the porphyrin *meso* protons are thought to be broad and probably underlie the prominent propionyl α-CH_2 and methyl signals. The signal at about 9.5 ppm may arise from the vinyl α-CH groups which are not present in the derivatives described by O'Keeffe et al. (C) The high-field ^{1}H NMR spectrum of Fe(III)PPIX in d_6-DMSO. Tentative assignments of peaks, based on the spectrum reported by Budd et al.,[252] are as follows: (i) methyl groups, (ii) vinyl α-CH and propionyl α-CH_2, (iii) porphyrin *meso* H, (iv) propionic acid COOH group, (v) propionyl β-CH_2 and (vi) *cis* and *trans* vinyl β-CH_2. In all spectra, solvent peaks are marked with an asterisk (*).

Thus, the results of the ^{1}H NMR investigation strongly support the conclusion that the Fe(III)PPIX dimer formed spontaneously in aqueous solution is not a μ-oxo dimer.

4.3.7 Magnetic Susceptibility Measurements

Magnetic susceptibility measurements were performed at 303 K according to the Evans NMR method,[241-243] which is described in detail in section 4.2.7. The observed paramagnetic shifts in the signal for solvent water, owing to the presence of Fe(III)PPIX species, are shown for the spontaneously formed aqueous Fe(III)PPIX dimer (Figure 4.12 A) and the induced μ-oxo dimer in 10% (v/v) aqueous alkaline pyridine (Figure 4.12 B). The observed paramagnetic shifts correspond to an average magnetic moment, μ, per Fe(III) centre of 4.21 in the case of the spontaneously formed aqueous dimer of Fe(III)PPIX and 1.04 in the case of the induced μ-oxo dimer. The former observation is consistent with an admixed-intermediate spin state (S = 3/2, 5/2),[253] while the latter is close to the expected value of 1.1 for a μ-oxo dimer species.[48] It should be noted that due to the use of the incorrect formula, for a continuous wave instrument with a perpendicular field as opposed to a modern NMR instrument with a parallel field, these values were previously published as 5.99 (corresponding to S = 5/2) and 1.94 respectively.[254]

These measurements support the conclusions of the spectroscopic investigations reported above in demonstrating that the spontaneously formed aqueous dimer of Fe(III)PPIX is not a μ-oxo dimer, contrary to what has been claimed in the past.[41]

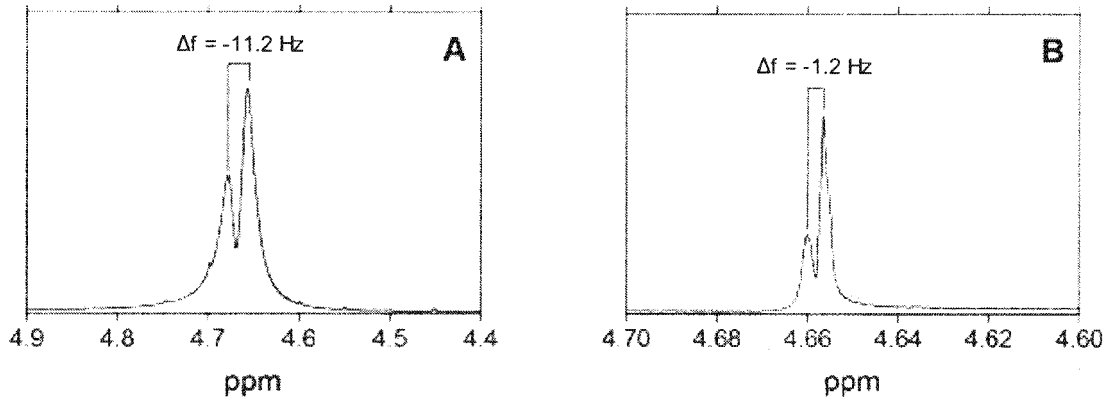

Figure 4.12 The determination of the magnetic moment of Fe(III)PPIX species according to the Evans NMR method. The paramagnetic shift in the NMR signal of water owing to (A) 5.48 × 10^{-4} gml^{-1} aqueous Fe(III)PPIX (pH 8.00) and (B) 5.00 × 10^{-4} gml^{-1} of the μ-oxo dimer of Fe(III)PPIX induced in 10% (v/v) aqueous alkaline pyridine. The downfield shifts are shown relative to the solvent water signal (larger peak) in both blank solutions (i.e. aqueous (pH 8.00) and 10% (v/v) aqueous alkaline pyridine respectively without Fe(III)PPIX) and were determined at 303 K using a co-axial tube. The molecular weights of the paramagnetic species, determined per Fe centre, were taken as 632.5 for aqueous Fe(III)PPIX and 623.5 for the μ-oxo dimer due to sharing of the bridging oxygen atom.

4.3.8 A Model for the Aqueous Dimer of Fe(III)PPIX

In light of the evidence presented above, a new model for the aqueous dimer of Fe(III)PPIX was needed. The proposed structure is of two five-coordinate Fe(III)PPIX molecules that interact primarily through $\pi - \pi$ or stacking interactions of their unligated faces, and as a result, have their axial $H_2O/^-OH$ ligands directed outwards. Such a model is able to account for the pH dependence of dimerisation as shown in Scheme 4.2. Given that the experiments reported in this chapter were conducted at a pH range (6 – 10) above the pK_a of the carboxylic acid side chains of Fe(III)PPIX, these side chains were explicitly assumed to exist in their carboxylate state and thus not be involved in the deprotonation equilibria. This model is supported by the X-ray crystal structures of the related porphyrins haemin (Cl-Fe(III)PPIX, Figure 4.13 A)[255] and aqua-iron(III)octaethylporphyrin perchlorate ($Fe(OEP)(H_2O)]ClO_4$, Figure 4.13 B).[253] A lateral displacement of the two porphyrin molecules relative to each other, determined to be the optimum geometry for interactions of this kind,[160] is evident in the X-ray crystal structures. A model of the aqueous dimer of Fe(III)PPIX would be expected to agree with these observations.

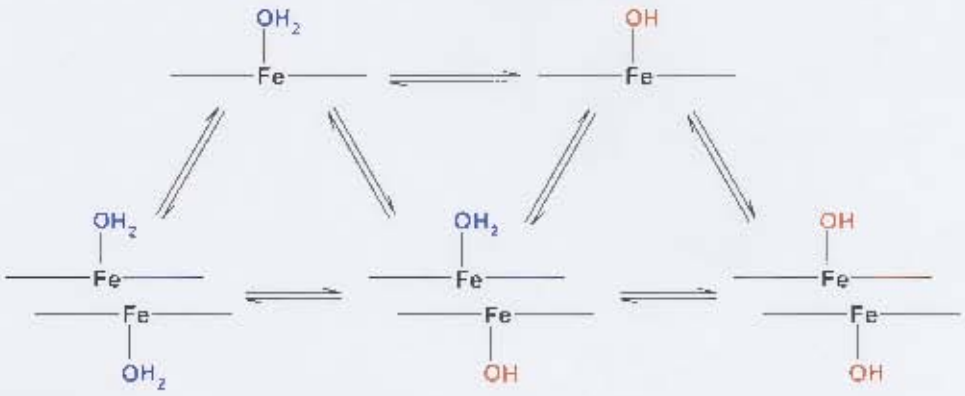

Scheme 4.2 The proposed relationship between the structure of the Fe(III)PPIX monomer and dimer and the pH-dependent behavior of aqueous Fe(III)PPIX. The axial water (H_2O) and hydroxyl (OH) ligands are coloured blue and orange respectively to emphasise the protonation state of each species.

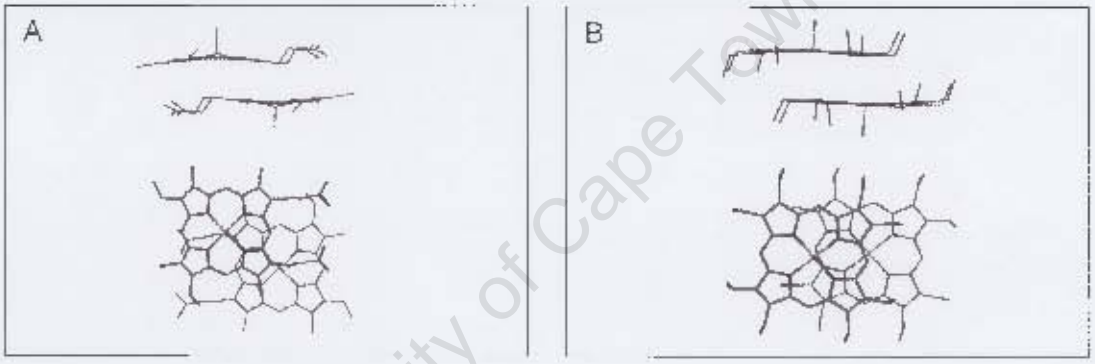

Figure 4.13 The X-ray crystallographic structures of (A) haemin[255] and (B) aqua-iron(III)octaethylporphyrin perchlorate, reproduced from references 255 and 253 respectively. The structures were extracted from the Cambridge Structural Database[256] (reference codes CHEMIN and HECZUK respectively) and displayed using XSEED[257] (included solvent molecules and counter ions have been removed for clarity). In both cases, the top (side-on) and bottom (aerial) views highlight the lateral displacement of the two molecules relative to one another.

The details of an extensive computational study by H. M. Marques, carried out to explore the possible structure/s of the aqueous Fe(III)PPIX dimer, were reported in a publication on the current work.[254] Molecular Dynamics (MD)/ Simulated Annealing (SA) calculations were carried out using restraints, whereby the two Fe(III) centres were connected via two dummy atoms. This allowed the use of high simulation temperatures (1000 K) in order to thoroughly explore all conformational space.

In this thesis project, MD/SA calculations were performed unrestrained at low temperature (maximum 150 K) in order to test the validity of the structures returned by the above method. An example of the lowest energy structure returned by this method is shown in Figure 4.14 A, attesting to the predictions made that the spontaneously formed aqueous dimer of Fe(III)PPIX is most probably a $\pi - \pi$ dimer as described above. A comparative model structure, returned from high-temperature molecular dynamics calculations in which dummy atoms were used to connect the two porphyrins, is shown in Figure 4.14 B.

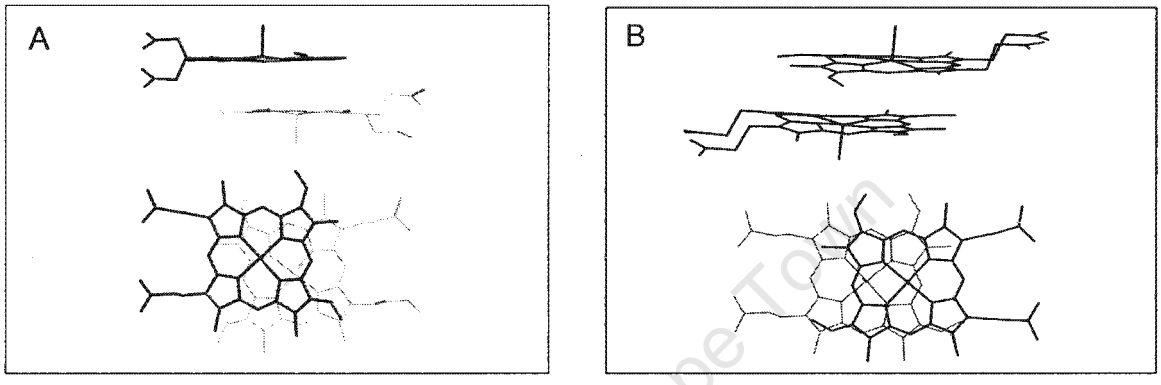

Figure 4.14 The lowest energy structure of the aqueous dimer of Fe(III)PPIX returned by (A) low-temperature, unrestrained MD/SA calculations and (B) high-temperature, restrained MD/SA calculations. Calculations were performed using HYPERCHEM.[231]

4.4 DISCUSSION

The aim of the investigations reported in this Chapter was to determine the speciation of Fe(III)PPIX in aqueous solution as a means of gaining deeper insight into the mechanism of haemozoin formation and the structure of Fe(III)PPIX-antimalarial complexes.

Several authors have previously investigated aqueous solutions of Fe(III)PPIX and concluded that they are problematic, giving rise to data that is non-reproducible and therefore difficult to interpret.[141,147,258] For the most part, these observations have been attributed to aggregation[39,40,42,259] or oxidation.[36,260] The adverse effects of adsorption on the behaviour of Fe(III)PPIX have been brought to the fore in the present work and are more than likely the cause of the previously observed instability of aqueous solutions of Fe(III)PPIX. It has been successfully demonstrated however, that through the careful treatment and washing of

glassware, and the avoidance of plasticware, reproducible data are obtainable up to four hours post preparation, providing the actual Fe(III)PPIX concentration is obtained using ε_{347} which is unaffected by dimerisation.

Concerning the speciation of Fe(III)PPIX, the first point of contention in the literature has been to establish the size of the aggregate. A study published by Brown et al.[41] in 1970 regarding the aggregation of haematin and deuterohaematin in aqueous solution concluded that decreases in the extinction and broadening of the Soret band of aqueous Fe(III)PPIX (0.2 – 200 μM, pH 6.98) result from dimerisation at higher concentration. This is in contrast to several other authors who have suggested that Fe(III)PPIX forms higher aggregates in aqueous solution.[36-40]

In the absence of non-linear fitting algorithms at the time, Brown et al.[41] resorted to linearisation of their spectrophotometric data (3 pH values, μ = 0.1 M (NaCl), 10 data points each) for purposes of analysis and assumed that the extinction coefficient of monomeric Fe(III)PPIX (ε_M) was the same as that for Fe(III)deuteroporphyrin (Chapter 1.5). The differing conclusions reached on the basis of this present work and the study presented by Brown et al.[41] can be attributed, in part, to the improved sensitivity of instrumentation allowing the detection of extremely low sample concentrations and the use of non-linear least squares fitting. The data obtained in this investigation (8 pH values in the range 6 – 9, μ = 154 mM ($NaHClO_4$), 30 – 40 data points each) were fitted to an equation describing a dimerisation process and are consistent with Fe(III)PPIX dimerisation over the entire concentration range 0.025 – 60 μM. Values of $K_{D,obs}$, ε_M and ε_D were obtained directly from the fitted data, and while values of ε_D were in agreement with Brown and co-workers,[41] values of $K_{D,obs}$ and ε_M were considerably smaller. Fe(III)PPIX dimerisation is supported by diffusion measurements conducted at ~ 1 mM, which conclusively exclude the existence of very large aggregates. Given some uncertainty in the extent of hydration of Fe(III)PPIX in aqueous solution, the presence of small oligomers cannot be ruled out. However, that the diffusion constant of the monomeric biscyano complex of Fe(III)PPIX is nearly twice that of aqueous Fe(III)PPIX, suggests that the latter is most probably

a dimer. This is further supported by the relationship between diffusion coefficient and molar volume.

The conclusion reached by Brown et al.[41] was that dimerisation is accompanied by the loss of a single proton, and that both monomeric and dimeric Fe(III)PPIX conform to single acid deprotonation equilibria. While the present study has confirmed this with respect to monomeric Fe(III)PPIX, in contrast it was found that the dimer undergoes two consecutive deprotonation equilibria. Furthermore, dimerisation is not accompanied by any proton loss and the pH-dependence of this process follows a bell-shaped curve as opposed to the linear relationship proposed by Brown and co-workers.[41]

Having established that Fe(III)PPIX exists in aqueous solution as a dimer, the precise nature of the dimer then fell under the spotlight. In this respect, the study conducted by Brown et al.[41] has again been the authority for almost four decades. Their structural interpretation was based on the earlier infrared characterisation of a green precipitate obtained in high yield by the addition of 1 M NaOH to a haemin solution in DMSO.[44] A strong band at 903 cm^{-1} in the IR spectrum was attributed to the stretching frequency of the Fe–O–Fe oxo bridge. The existence of X-ray crystal structures of the μ-oxo dimers of related porphyrins[47] provided further support for their conclusions. Thus, the contention that Fe(III)PPIX exists in aqueous solution as a μ-oxo dimer has prevailed, despite a noteworthy investigation carried out by O'Keeffe et al.[48] in which strong evidence that the spontaneous formation of the μ-oxo dimer does not occur was provided. Rather, these authors demonstrated that such a species could be *induced* in the presence of a small amount of organic base in aqueous alkaline solution.

The results of the current investigation are indeed unable to confirm the existence of the Fe(III)PPIX μ-oxo dimer in aqueous solution. Firstly, the UV-vis spectrum of aqueous Fe(III)PPIX does not reflect the characteristics of those reported for known μ-oxo dimers or that of the μ-oxo dimer induced by inclusion of 10% (v/v) pyridine in aqueous alkaline solution.[48] Secondly, the ^{1}H NMR spectrum of aqueous Fe(III)PPIX is broad (-10 – 60 ppm) and exhibits features that are consistent with a high-spin, five-coordinate paramagnetic species, very similar to

the monomeric Cl–Fe(III)PPIX dimethyl ester in chloroform.[252] By contrast, the ^{1}H NMR spectrum of the induced μ-oxo dimer was recorded in the normal 0 – 10 ppm range. The lack of strong paramagnetic broadening is attributed to strong antiferromagnetic coupling expected for such species. Furthermore, the ^{1}H NMR spectrum of aqueous Fe(III)PPIX is inconsistent with that recorded of an analogous six-coordinate species, discounting Brown and co-workers'[41] original hypothesis that the Fe(III)PPIX dimer is six-coordinate. Finally, magnetic susceptibility measurements are not in agreement with the presence of the μ-oxo dimer, though discussion of this is reserved until later. Interestingly, major differences in the Mössbauer parameters for precipitates from solutions of Fe(III)PPIX and the Fe(III)PPIX μ-oxo dimer recorded at 78 K[153] further serve to highlight the difference between the two species. The former gives an asymmetric pattern with only one prominent peak, while the latter exhibits a symmetric doublet that is characteristic of antiferromagnetic coupling.

Based on the evidence presented above, the widely held view that aqueous Fe(III)PPIX exists as a μ-oxo dimer could not be confirmed. Instead, the data convincingly point towards a new model of Fe(III)PPIX dimerisation and the conclusion of this work is that five-coordinate Fe(III)PPIX exists in aqueous solution as a $\pi - \pi$ (or stacked) dimer, with interactions between the unligated hydrophobic faces of the two porphyrin molecules while the axial hydrophilic H_2O/$^-$OH ligands are directed outwards.

The observation that Fe(III)PPIX is a five-coordinate species is consistent with the crystal structures of numerous analogous structures which have oxygen donors as axial ligands. Examples include Cheng et al.'s aquo(octaethylporphinato)iron(III) perchlorate (Fe(OEP)(H_2O)]ClO_4),[253] Oumous's acetato(5,10,15,20-tetra-p-tolylporphyrin)iron(III) (Fe(TpTP)(OAc))[261] and the methoxy complexes of iron(III) mesoporphyrin dimethyl ester,[262] iron(III)tetraphenylporphyrin (Fe(TPP))[263] and iron(III)octaethylporphyrin (Fe(OEP)).[264] Furthermore, the proposed model of dimerisation is consistent with the crystal structures of Fe(OEP)(H_2O)]ClO_4[253] and haemin,[255] the latter having an identical molecular structure to Fe(III)PPIX except for an axial chloride ligand as opposed to H_2O/$^-$OH. More recently, the aggregation behaviour of PPIX has again been investigated.[265] On the basis of UV-vis,

fluorescence emission and resonant light scattering experiments, the authors determined that PPIX exists as a monomer in the pH range 0 – 3, a dimer beyond pH 8 and a high aggregate in between (pH 3 – 8). In the context of the present study, the energy-minimised structural model of the dimer present at pH > 8 is of particular interest. Shown in Figure 4.15, the proposed model is of a $\pi - \pi$ dimer, interacting in a head-to-tail, face-to-face arrangement and laterally displaced relative to one another.

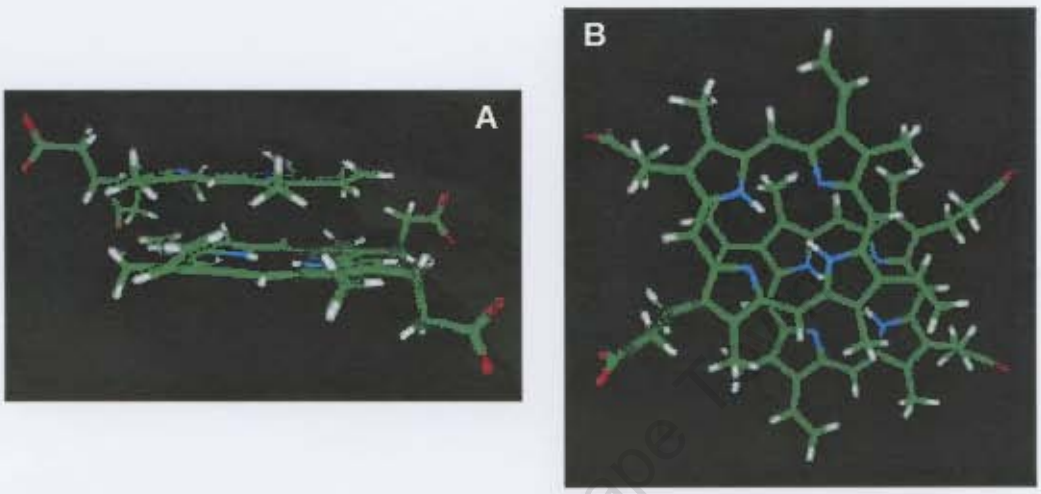

Figure 4.15 Molecular model of the proposed head-to-tail, face-to-face $\pi - \pi$ dimer of PPIX. pH 12, viewed (A) side on and (B) from the top in order to demonstrate the offset relationship between the two molecules. Reproduced from reference 265.

In favour of the proposed $\pi - \pi$ (or stacked) model of the aqueous Fe(III)PPIX dimer is its ability to account for the following behaviour observed experimentally:

i. The UV-vis spectrum of aqueous Fe(III)PPIX at an acidic pH shows the typical broad and weakened Soret band which has been attributed to dimerisation. That such a species exists at an acidic pH is in contrast to the μ-oxo dimer, which upon protonation would almost certainly be unstable as a μ-aqua dimer (Fe—$(H_2O)^{2+}$—Fe) and consequently monomerise.

ii. The observed UV-vis spectrum of aqueous Fe(III)PPIX is not consistent with the characteristic spectrum reported for μ-oxo dimer species.[48]

iii. A single deprotonation process was detected for the monomeric H_2O-Fe(III)PPIX species in 80% (v/v) aqueous methanol and at low concentration, which can be attributed to the deprotonation of the single axial H_2O ligand to form HO-Fe(III)PPIX. A single deprotonation process

was observed by Brown et al.,[41] however they did not correlate this to any one structure.

iv. Two consecutive deprotonation processes were observed for the aqueous dimer, which can be attributed to the deprotonation of the two axial H_2O ligands in turn.

v. The pH dependence of dimerisation is bell-shaped and at any particular pH the observed dimerisation constant is a combination of three different dimerisation constants, K_{D1}, K_{D2} and K_{D3}. These three constants arise from the formation of the $[H_2O\text{-}Fe(III)PPIX]_2$, $[H_2O\text{-}Fe(III)PPIX]\cdot[HO\text{-}Fe(III)PPIX]$ and $[HO\text{-}Fe(III)PPIX]_2$ dimeric species respectively. The strength of interaction between the two porphyrin molecules, and thus the magnitude of the dimerisation constants, is dependent on the nature of the porphyrin core. Under conditions in which an H_2O ligand is coordinated to the Fe(III)centre, the porphyrin core carries a +1 charge (Fe(III) + $2N^-$ = (+3 + (-2)) = net +1). However, when ^-OH is the axial ligand, the porphyrin core is neutral (Fe(III) + $2N^-$ + ^-OH = (+3 + (-2) + (-1)) = 0). Thus, when the dimer exists in its $[H_2O\text{-}Fe(III)PPIX]\cdot[HO\text{-}Fe(III)PPIX]$ form, additional stability is expected to be incurred as a result of cation-π interactions.[266] At high pH, the interaction of two neutral porphyrin cores, as in $[HO\text{-}Fe(III)PPIX]_2$, is likely to result purely from dispersion interactions. In the case of $[H_2O\text{-}Fe(III)PPIX]_2$, which exists at low pH, cation-π interactions are expected to be destabilised by Coulombic repulsion between the two positively charged cores.

vi. The fact that Fe(III)PPIX forms dimers and not higher aggregates in aqueous solution can be rationalised in terms of the structure of the model. Given that the axial HO^-/H_2O ligands are directed outwards, this would be expected to sterically hinder further association. Furthermore, the tendency for the axial ligands to hydrogen bond to solvent water molecules in the bulk environment would be expected to be more energetically favourable that forcing the hydrophilic faces to interact with one another. The crystal structure of $Fe(OEP)(H_2O)]ClO_4$[253] indeed provides evidence for this hypothesis: included water molecules as well as the two perchlorate counter ions form an extended hydrogen-bonded network between the axial water ligands of neighbouring $Fe(OEP)(H_2O)$ dimers.

vii. The existence of broadened signals as far downfield as 60 ppm in the high-field ^{1}H NMR spectrum, is consistent with the presence of a paramagnetic Fe(III) centre.

viii. Magnetic susceptibility measurements for the aqueous Fe(III)PPIX dimer (μ = 4.21) are consistent with an admixed S= 3/2, 5/2 spin state. This result does not contradict the conclusion arrived at from the ^{1}H NMR spectrum of the same species (which is shown to be consistent with a high-spin species). In fact, in the case that the axial ligand field strength is weak (e.g. H_2O/HO^-), large zero-field splittings are observed for high-spin Fe(III) porphyrins, thus resulting in the admixed state.[267] Magnetic moments reported previously for related $\pi - \pi$ (or stacked) dimers are also in agreement. Cheng et al.[253] reported the temperature dependence of the effective magnetic moment of $Fe(OEP)(H_2O)]ClO_4$ and showed that the data fitted to a modified admixed intermediate-spin (S = 3/2, 5/2) Maltempo model[268] in which antiferromagnetic exchange had to be assumed between two neighbouring iron atoms within the $\pi - \pi$ dimer.[269] The exchange coupling constant, *J*, for two weakly interacting Fe(III) centres was determined as –1.0 cm^{-1}.[253] At 300 K, Cheng et al. recorded an effective magnetic moment of ~ 4.8.[253] The value determined in this work suggests that the degree of antiferromagnetic exchange may be greater than in the case of $Fe(OEP)(H_2O)]ClO_4$. By contrast, for diferric complexes containing an oxo bridge (Fe–O–Fe) where antiferromagnetic coupling is expected to be strong, *J* values are of the order of -70 cm^{-1},[270] providing further support that the aqueous Fe(III)PPIX dimer is not a μ-oxo dimer.

ix. MD/SA calculations, both at high temperature using restraints[254] and unrestrained at low temperature, converge on a structure in which the two Fe(III)PPIX molecules interact in a $\pi - \pi$ manner, with the axial water ligands directed outwards in the majority of cases. The simulated structures also show that the two porphyrins are likely to be laterally shifted relative to one another. Of the 50 lowest-energy structures obtained at high temperature, the majority exhibited a lateral shift in the range 2.5 – 3.0 Å. This is considerably less than the lateral shift of 3.39 Å reported for $Fe(OEP)(H_2O)]ClO_4$,[253] which supports the previous suggestion that the

degree of antiferromagnetic coupling may be greater in the aqueous Fe(III)PPIX dimer.

The larger sample set of calculations performed at high temperature shows that there are several different families of energetically-favourable structures, suggesting that the Fe(III)PPIX dimer is dynamic and not fixed in any single preferred conformation. This is consistent with previously observed behaviour of porphyrins, which are able to interchange between conformations close in energy, namely domed, ruffled or saddled conformations.[271] Such conformations have been observed in the solid state as well: haemin[255] shows evidence of a domed conformation (Figure 4.13 A) while the porphyrin is slightly ruffled in $Fe(OEP)(H_2O)]ClO_4$ (Figure 4.13 B).[253]

It has been shown previously[48] and confirmed in the present study that the μ-oxo dimer of Fe(III)PPIX can be induced by the addition of a small amount of an organic base (e.g. 10% (v/v) pyridine) to alkaline solution. Furthermore, it has previously been observed that the same effect occurs in the presence of high salt concentrations. Hence the conditions of 1.2 M NaCl (pH 11) under which Blauer and Zvilichovsky[37] detected large aggregates of 45 – 50 molecules (Chapter 1.5.1) are consistent with those required for μ-oxo dimer formation. The presence of higher aggregates would be likely as a result of π-stacking between the unligated, hydrophobic faces.

A thorough investigation and understanding of the speciation of Fe(III)PPIX in aqueous solution is of direct importance for understanding the mechanism by which haemozoin forms. The contention that Fe(III)PPIX exists as a μ-oxo dimer, and yet is able to convert to haemozoin/β-haematin, is reliant on an equilibrium between the dimer and monomeric Fe(III)PPIX.[167,272] Dorn et al.[272] suggested that a lipid environment could accelerate the detoxification of Fe(III)PPIX by shifting the equilibrium in favour of the monomeric form. Based on the findings presented in this chapter, Egan et al.[73] assumed in their investigation of the mechanism of haemozoin formation at the lipid/water interface that Fe(III)PPIX exists in aqueous solution as a $\pi - \pi$ (or stacked) dimer. In order to form the haemozoin dimer, the $\pi - \pi$ (or stacked) dimer would not need to split into monomers as would be

necessary in the case of the μ-oxo dimer. Figure 4.16 is a schematic of the steps that would be necessary. Essentially, all that would be required for the haemozoin dimer (**3**) to form would be a simple change in the lateral shifts of the two porphyrins (**1**) and for each of the propionate side chains to adopt a suitable conformation in order to achieve coordination to the Fe(III) centre of its partner molecule (**2**). Thus the model developed in this chapter provides a clearer understanding of how the Fe(III)PPIX dimer is able to convert to the haemozoin dimer.

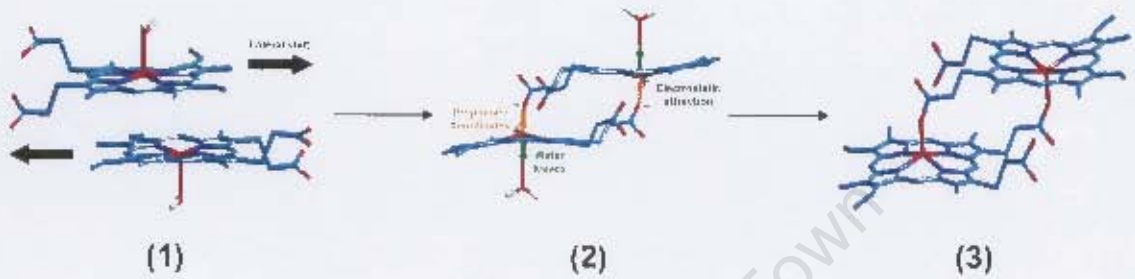

Figure 4.16 A schematic representation of the changes required of the $\pi - \pi$ (or stacked) dimer (**1**) in order to form the haemozoin dimer (**3**). A change in the lateral shift of **1** would align the propionate group of one Fe(III)PPIX molecule with the Fe(III) centre of its partner (**2**). Once in this precursor state, charge-assisted coordination of the propionate group to Fe(III), and the loss of axial water from the outer face, would result in the formation of **3**.

4.5 CONCLUSIONS

From the extensive evidence provided in this work, performed using several different physical techniques, the conclusion of Brown et al.[41] that aqueous Fe(III)PPIX exists as a dimer, has been confirmed. Furthermore, it has been shown that higher aggregates of Fe(III)PPIX are unlikely. This work has overturned the long-held view that aqueous Fe(III)PPIX (haematin) is a μ-oxo dimer. Rather, a new model in which two Fe(III)PPIX molecules interact in a $\pi - \pi$ (or stacked) manner with their axial ligands directed outwards is proposed. Reiterating the words of Ridley and co-workers,[273] "the structure and stability of the haematin μ-oxo dimer precludes its incorporation into haemozoin, as the iron co-ordination sites are blocked." The $\pi - \pi$ dimer provides a facile pathway to rationalise how aqueous Fe(III)PPIX may be incorporated into haemozoin.

5. THE ORIENTED NUCLEATION OF β-HAEMATIN AT THE MMG/WATER INTERFACE

5.1 INTRODUCTION

Pisciotta and Sullivan[87] have described the lipid/water interface as oily and suggest that in such a hydrophobic environment, the loss of the axial water ligand (present at acid pH) is promoted, leaving the Fe(III) centre free for coordination by the propionate group of the adjacent porphyrin. In 2006, Egan et al. proposed a model to explain the formation of β-haematin at the lipid/water interface.[73] Through the use of molecular dynamics simulations they showed that Fe(III)PPIX, demonstrated to be a $\pi - \pi$ (or stacked) dimer in the current work, converts rapidly to a haemozoin precursor in vacuum, which to some extent mimics the low dielectric medium of a lipid environment.

That crystalline monolayers of amphiphilic molecules are able to induce the oriented nucleation of molecular crystals as a result of structural complementarity between the head groups of the monolayer and the functional groups projecting from the parallel surface of the crystal is well established.[88] Previously it has been observed that the growth of synthetic β-haematin crystals takes place from what appears to be a common nucleation point,[98] which is consistent with biomineralisation.[73] Thus the question of how haemozoin crystals nucleate is of central importance and the ability of a crystalline monolayer of lipid molecules at the lipid/water interface to induce the nucleation and orientation of β-haematin through epitaxis is of great interest.

Pisciotta et al.[74] determined that haemozoin isolated from the lipid nanospheres present in the digestive food vacuole was predominantly surrounded by monopalmitic and monostearic glycerols (MPG and MSG respectively). In an earlier study that investigated the efficacy of eleven different lipids in promoting β-haematin at the lipid/water interface,[73] *rac*-glycerol 1-myristate (MMG) was determined to be one of the more efficient. MMG is a structural analogue of MPG and MSG, differing only in the length of its hydrocarbon chain, and was used as a model lipid throughout the current investigations. It is suspected that its hydrophilic

head group, which contains two hydroxyl (-OH) groups, may be involved in the induced nucleation of β-haematin via functional group complementarity with Fe(III)PPIX.

5.2 METHODS

This section describes the details of methods used specifically in the investigation of β-haematin formation at a MMG/water interface. The materials used have been previously listed in Table 3.1.

5.2.1 Preparation of β-Haematin from Acetate Solution

The synthesis and characterisation of β-haematin from acetate solution has been described previously.[61] β-haematin formed according to this methodology was used in the current work as a reference in order to compare the product obtained at the MMG/water interface.

5.2.1.1 Sample Preparation

12.9 M Acetate Buffer, pH 5.0

25.0 ml was prepared by dissolving sodium acetate trihydrate (28.1005 g, 207 mmol) in glacial acetic acid (6.64 ml, 116 mmol) in an incubated (60°C) beaker with continual stirring. Through combination of the correct amounts of sodium acetate trihydrate and glacial acetic acid, this solution attains the desired pH and volume without the need to be made to volume with water.

5.2.1.2 Experimental Procedures

Haemin (15.0 g, 23.0 μmol) was dissolved in 3.0 ml of 0.1 M NaOH in a thermostatted (60°C) glass titration cell. 0.3 ml of 1 M HCl was added followed by 1.74 ml of the 12.9 M acetate buffer. The reaction mixture was stirred rapidly for 60 minutes after which the reaction was stopped by the addition of chilled water. The product was collected by filtration using 0.25 μm cellulose nitrate discs and

typically dried in a desicator over phosphorus pentoxide for up to 48 hours before further analysis.

The product collected from acetate solution after a 60 minute period of incubation was characterised by ATR-IR and Raman spectroscopy.

5.2.2 Preparation of β-Haematin at the MMG/Water Interface

5.2.2.1 Sample Preparation

50.0 mM Citrate Buffer, pH 4.8

Citric acid monohydrate (10.5070 g, 50.0 mmol) was dissolved in 900 ml distilled water. The pH was adjusted to 4.8 by the addition of sodium hydroxide (NaOH), either in concentrated solution form, or as a solid (calculated concentration of 3.68 g/dm^3, 92 mM). The solution was made up to a final volume of 1000 ml.

1:9 Acetone:Methanol (v/v) Solution

1 ml of acetone was mixed together with 9 ml of methanol in a glass vial.

Lipid Solution

2.5 mg MMG (Figure 5.1) was dissolved in 5.0 ml of the 1:9 acetone:methanol solution giving a concentration of 0.5 mg/ml. This solution was stored in a glass vial below 0°C.

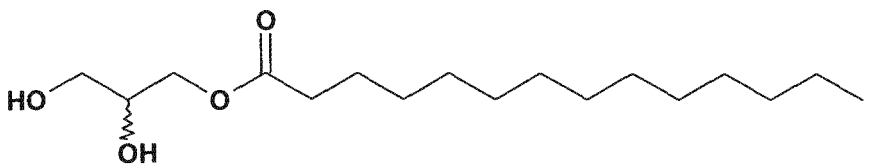

Figure 5.1 The chemical structure of *rac*-glycerol 1-myristate (MMG).

Fe(III)PPIX Solution

2.0 mg haematin was dissolved in 1.2 ml of 0.1 M NaOH in a 10 ml glass vial. After complete dissolution of the solid, 1.8 ml of the 1:9 acetone:methanol solution was added and the new solution was thoroughly mixed to give a final concentration of 0.67 mg/ml. This solution was prepared fresh for each individual experiment.

5:45:50 Pyridine:Water:Acetone (v/v) Solution

To 10.0 ml 0.2 M HEPES buffer pH 7.5, 5.0 ml pyridine and 50.0 ml acetone were added and thoroughly mixed together. The solution was made to volume in a 100.0 ml volumetric flask with distilled water. Volumes correspond to a mole ratio of 1:17.9:5.5 pyridine:water:acetone.

5.2.2.2 Experimental Procedures

All experiments were carried out in Schott Duran crystallising dishes with an internal diameter of 9 cm. For the purposes of incubation, these glass vessels were partially immersed into a water bath set at 38°C to ensure that the working temperature of the experiment remained close to 37°C at all times. A large watch glass was used as a lid for each vessel.

Firstly, 50.0 ml of citrate buffer was measured into each glass vessel and pre-incubated at 37°C while lipid and Fe(III)PPIX solutions were prepared. On average this process took 15 – 20 minutes.

The interface was prepared in two ways. One method, used in initial experiments, involved spreading of 1.0 ml of lipid solution over the surface of the citrate buffer before 0.5 ml (0.33 mg) of Fe(III)PPIX solution was added drop-wise to the pre-incubated interface using a syringe with a needle diameter of 0.5 mm. The precursor (Fe(III)PPIX) could not be introduced from the subphase below the surface active layer due to the fact that it readily precipitates under pH conditions less than 6. Later, a modified method relied on premixing 1.0 ml of lipid solution with 0.5 ml of Fe(III)PPIX solution. This "premix" was then spread drop-wise over the surface of the citrate buffer using a syringe as before. In both cases, once Fe(III)PPIX had been delivered to the interface, the experiment was left to incubate for 30 minutes.

At the end of the incubation period the surface was agitated, releasing the product into the bulk medium. The total volume (51.5 ml) was transferred to an 85 ml Nalgene centrifuge tube and centrifuged at 10,000 rpm for 10 minutes. The supernatant was discarded and the pellet kept for further analysis. 1.0 ml of the

pyridine:water:acetone solution (pH 7.5) was added to "wash" the pellet. 5% pyridine at pH 7.5 selectively dissolves unreacted haematin in the presence of β-haematin, while 50% acetone proved useful in dissolving any co-pelleted lipid. After a second centrifugation, the remaining product (pellet) was typically dried in a desicator over phosphorus pentoxide for up to 48 hours before further analysis.

FT-IR and Raman spectroscopy were used to characterise the products collected from the interface after a 30 min period of incubation.

5.2.3 Nucleation and Orientation of β-Haematin at the MMG/Water Interface

5.2.3.1 The Beamline and Experimental Station

Hamburger Synchrotronstrahlungslabor (HASYLAB) at Deutches Elektronensynchrotron (DESY) is home to numerous synchrotron beamlines available for scientific research involving photons. The experimental station at beamline BW1 includes a liquid surface diffractometer, which is designed for X-ray Reflectivity (XR) and Grazing Incidence X-ray Diffraction (GIXD) measurements from films at liquid surfaces. The instrument arrangement is shown below (Figure 5.2).

5.2.3.2 Sample Preparation

The calculations detailed in this section are for an experimental surface area in the trough of 240 cm^2. This is 3.8 times larger than the surface area of a single crystallising dish. Fresh citrate buffer (50.0 mM, pH 4.8) was prepared daily.

BW1 Fe(III)PPIX Solution

5.0 mg haematin was dissolved in 0.6 ml of 0.1 M NaOH in a 2 ml plastic Eppendorf tube. After complete dissolution of the solid, 0.9 ml of the 1:9 acetone:methanol solution was added and the new solution was thoroughly mixed to give a final concentration of 3.3 mg/ml. This solution was prepared fresh for each individual experiment.

The positive meniscus of the liquid inside the trough is maintained through surface tension and contact with the Teflon edges. Higher concentrations of Fe(III)PPIX stock solutions were used in these experiments compared to those carried out routinely in the crystallising dishes to ensure that minimal volumes were added to the trough in order to avoid spillage.

BW1 Lipid Solution

0.95 mg MMG was dissolved in 0.5 ml of the 1:9 acetone:methanol solution giving a concentration of 1.9 mg/ml.

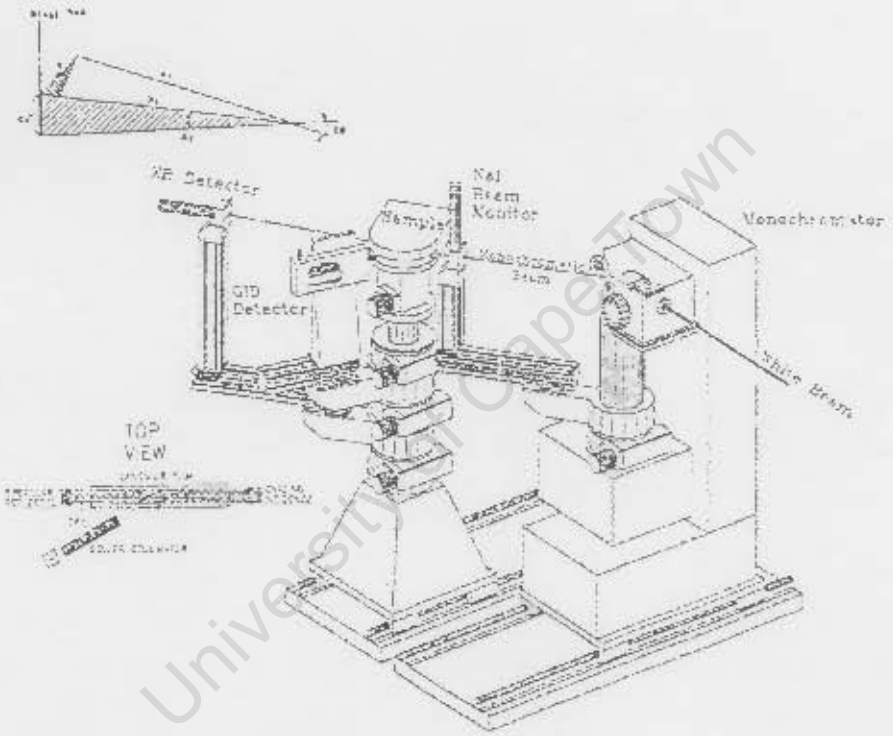

Figure 5.2 The instrument arrangement at BW1, HASYLAB, DESY. Starting from the right hand side, a white beam exiting the storage ring enters a helium filled chamber housing a beryllium crystal monochromator. Passing through the monochromator, the beam is deflected downwards so that it makes an angle of incidence with the horizontal liquid surface of the sample of ≤ 10°. The NaI beam monitor enables counting of the signal intensity prior to it reaching the sample trough. Two detectors may be moved into place depending on the nature of the measurement: either the XR detector or the GIXD position sensitive detector (labelled GID detector). Reproduced from reference 274.

5.2.3.3 Experimental Procedures

The arrangement inside the experimental chamber is shown in the schematic diagram below (Figure 5.3).

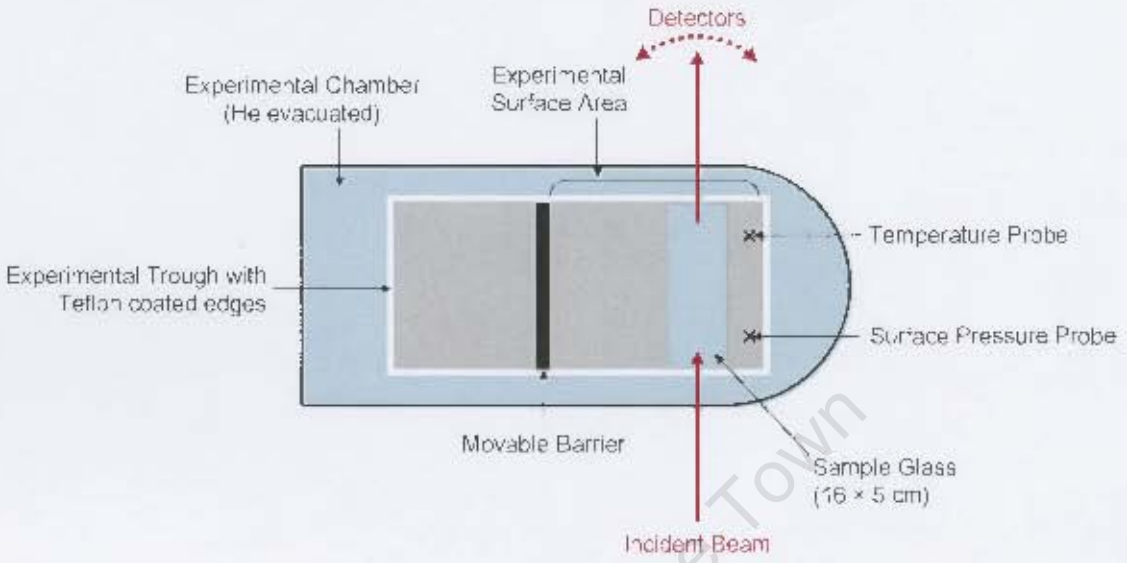

Figure 5.3 Schematic top view of the experimental chamber at the Liquid Surface Diffractometer at beamline BW1, HASYLAB.

Typically the trough was filled with buffer (~ 250 ml) while the experimental chamber was warmed to 37°C. The sample was introduced immediately after preparation, and primarily over the sample glass to maximise the chances of product falling within the incident X-ray footprint. Once Fe(III)PPIX had been delivered to the MMG/water interface, the system was left for a 30 minute incubation period. For the purpose of data collection, the system was cooled to 20°C and the experimental chamber was flushed with helium to reduce X-ray background scattering. The alignment of the water level relative to the incident beam was checked before any measurements were undertaken.

Experiments were conducted during eight-hour beam shifts. The details of several experiments designed to provide insight into the possible mechanism of β-haematin formation are described below.

Control Experiments

Fe(III)PPIX only: 0.76 ml of BW1 Fe(III)PPIX solution was premixed with 0.5 ml of the 1:9 acetone:methanol solution in place of the lipid solution. The mixture was added to the surface of the citrate buffer drop-wise with a syringe.

Lipid only: 0.5 ml of BW1 lipid solution was premixed with 0.76 ml of the 1:9 acetone:methanol solution in place of the haematin solution. The mixture was added to the surface of the citrate buffer drop-wise with a syringe. It is estimated from equation set 5.1 that approximately 16 layers of close-packed lipid molecules could, in principle, be formed from the amount of MMG used:

The total number of MMG molecules (N_{total}) is given by equation 5.1a:

$$N_{total} = n \times A \qquad (5.1a)$$

$$= \left(\frac{0.95 \times 10^{-3}\ \text{g}}{303\ \text{gmol}^{-1}} \right) \times \left(6.0223 \times 10^{23}\right)$$

$$= 1.8882 \times 10^{18}\ \text{molecules}$$

The surface area of the trough (SA_{trough}) used in the experiments was 240 cm^2, which is equivalent to 2.4 × 10^{18} $Å^2$. The surface area of a single MMG molecule (SA_{MMG}) can be calculated from GIXD data (see section 5.3.3.1). Assuming a hexagonal or close-packed arrangement, SA_{MMG} was found to be 20.3 $Å^2$. Therefore, the number of MMG molecules per single layer (N_{layer}) is given by equation 5.1b:

$$N_{layer} = \frac{SA_{trough}}{SA_{MMG}} \qquad (5.1b)$$

$$= \frac{2.4 \times 10^{18}}{20.3} = 1.182 \times 10^{17}\ \text{molecules}$$

The number of theoretical layers, L, is thus readily calculated according to equation 5.1c:

$$L = \frac{N_{total}}{N_{layer}} \qquad (5.1c)$$

$$= \frac{1.8882 \times 10^{18}}{1.182 \times 10^{17}} = 15.9\ \text{theoretical layers}$$

The Effectiveness of Near-Monolayer Coverage of MMG

0.1 ml (0.19 mg) of BW1 lipid solution was premixed with 0.076 ml (0.25 mg) of BW1 Fe(III)PPIX solution and the mixture was added to the surface of the citrate buffer, drop-wise with a syringe. It is estimated that approximately 3 layers of close-packed lipid molecules could, in principle, be formed from the amount of MMG used. If the amount of lipid was reduced below this limiting value, it was observed that the Fe(III)PPIX did not remain at the surface but rather precipitated into the aqueous buffer. Incubation for 30 minutes at 37°C was allowed before measurements were taken.

The Effectiveness of Premixing

In the first case, 0.5 ml (0.95 mg) of BW1 lipid solution was premixed with 0.76 ml (2.53 mg) of BW1 Fe(III)PPIX solution and the mixture was added to the surface of the citrate buffer drop-wise with a syringe. In the second case, 0.5 ml of BW1 lipid solution was first layered on to the surface of the citrate buffer after which 0.76 ml of BW1 Fe(III)PPIX solution was added to the surface. In both cases, it is estimated that approximately 16 layers of close-packed lipid molecules could, in principle, be formed from the amount of MMG used. Incubation for 30 minutes at 37°C was allowed before measurements were taken.

5.2.3.4 Measurement Procedures

Incident monochromatic X-rays of wavelength 1.304 Å were used in these experiments and the sample was manipulated to the correct height using motorised elevators. For GIXD measurements: with an incident angle $\alpha_i < 0.85\ \alpha_c$, where α_c is the critical angle for total external reflection, the position sensitive detector (PSD) was scanned over a $2\theta_{xy}$ range where $2\theta_{xy}$ is the angle between the projections of the incident and diffracted beams in the horizontal plane (refer to Chapter 2.6.4.3 for a detailed description). Bragg peaks were obtained by integrating over the whole q_z window of the detector. For a particular q_{xy} value, the intensity could be simultaneously measured over all q_z to yield Bragg rods. For XR measurements: the incident angle was varied in the range $0.5\ \alpha_c \leq \alpha_i \leq 30\ \alpha_c$ and the reflected beam measured by the X-ray reflectivity detector.

5.2.3.5 Characterisation of the Products

Following GIXD and XR measurements, the products were collected into glass vials and transported back to South Africa for further analysis. Samples were analysed by FT-IR spectroscopy and Scanning Electron Microscopy (SEM).

5.2.4 The Role of –OH Groups in Nucleating β-Haematin

Docosane, $CH_3(CH_2)_{20}CH_3$, and methyl laurate, (CH_3)-O-C(=O)-$(CH_2)_{10}CH_3$, (Figure 5.4) lack –OH groups and were therefore proposed as good substitutes for MMG in order to probe the role of the terminal –OH groups in nucleating β-haematin.

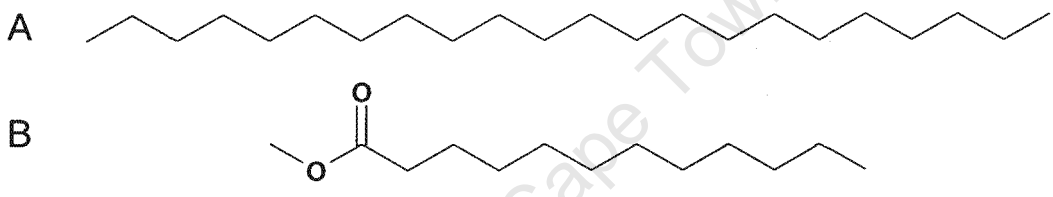

Figure 5.4 The chemical structures of (A) docosane and (B) methyl laurate.

5.2.4.1 Sample Preparation

Docosane Solution

A 1.9 mg/ml stock solution was prepared by dissolving 1.9 mg docosane in 1.0 ml of a solution containing 1:3:6 acetone:chloroform:methanol (v/v).

Methyl Laurate Solution

A 2.61 mg/ml stock solution was prepared to volume in a 1.0 ml volumetric flask by dissolving 3 µl of neat methyl laurate (0.869 g/ml) in 1:9 acetone:methanol solution.

Fe(III)PPIX Solution

2.0 mg haematin was dissolved in 1.2 ml of 0.1 M NaOH in a 10 ml glass vial. After complete dissolution of the solid, 1.8 ml of the 1:9 acetone:methanol solution was added and the new solution was thoroughly mixed to give a final concentration of 0.67 mg/ml. This solution was prepared fresh for each individual experiment.

5.2.4.2 Experimental Procedures

These experiments were carried out in Schott Duran crystallising dishes with an internal diameter of 9 cm, which were treated as before (5.2.2.2 Experimental Procedures). 50.0 ml of citrate buffer was measured into each glass vessel and pre-incubated at 37°C while docosane, methyl laurate and Fe(III)PPIX solutions were prepared. On average this process took 15 – 20 minutes.

Docosane and methyl laurate are largely insoluble in aqueous medium and the solvent system used to dissolve docosane showed a tendency to precipitate Fe(III)PPIX at high concentrations. Thus it was reasoned that premixing either of the solutions with the Fe(III)PPIX/NaOH solution would not produce a sensible result and therefore, the interface was prepared according to earlier methodology where no premixing with the Fe(III)PPIX solution was carried out. Firstly, the interface was prepared by adding either docosane (0.13 ml, 0.25 mg) or methyl laurate (0.10 ml, 0.26 mg) solutions drop-wise over the surface of the citrate buffer. Subsequently, 0.5 ml (0.33 mg) of Fe(III)PPIX solution was added drop-wise to the pre-incubated interface using a syringe with a needle diameter of 0.5 mm. Once Fe(III)PPIX had been delivered to the interface, the experiments were left to incubate for 30 minutes. Control experiments in the presence and absence of MMG were carried out at the same time.

At the end of the incubation period the surface was agitated as before to release the product into the bulk medium. The total volume (~ 50.5 ml) was transferred to an 85 ml Nalgene centrifuge tube and centrifuged at 10,000 rpm for 10 minutes. The supernatant was discarded and the pellet kept for further analysis. 1.0 ml of the pyridine:water:acetone solution (pH 7.5) was added to "wash" the pellet as before. In the case of methyl laurate, the supernatant remaining after a second centrifugation was subsequently diluted (40:1960 µl) and the absorbance measured at 405 nm to quantify the unreacted haematin. The remaining pellet from docosane and methyl laurate experiments was analysed in nujol by FT-IR.

5.3 RESULTS

5.3.1 Preparation of β-Haematin from Acetate Solution

As discussed before, the synthesis and characterisation of β-haematin from acetate solution has been well documented.[61] The synthesis was repeated in the current work in order to obtain a reference sample against which β-haematin formed under different conditions could be compared. Furthermore, while the product obtained from acetate solution had been previously characterised by FT-IR and SEM, both the ATR-IR and Raman spectra of this species have not been reported.

The normalised ATR-IR spectra of the starting material (haemin) and the products collected after 5 and 60 minutes incubation are shown (Figure 5.5 A). The product collected after 5 minutes is most likely haematin (H_2O–Fe(III)PPIX). The vertical dotted lines at 1662 and 1208 cm^{-1} indicate the characteristic marker bands of β-haematin in the product obtained after 60 minutes. These have previously been assigned as the C=O and C–O stretching frequencies respectively, of the coordinated propionate group. These peaks are absent in the spectrum of the starting material and appear only as weak bands in the second derivative spectrum (Figure 5.5 B) of the product obtained after 5 min. The second derivative spectrum allows weak peaks to be distinguished more clearly from noise and emphasises the striking difference between haematin and β-haematin. The spectra of all three materials have in common the band appearing at ~ 1710 cm^{-1}. In the case of β-haematin this has been assigned as the C=O stretching frequency of the free propionic acid group. Of note is that the peaks in the spectrum of β-haematin are sharper than those of haemin. This has been attributed to a reduction in the extent of hydrogen bonding in the case of β-haematin.[53]

5.3 RESULTS

5.3.1 Preparation of β-Haematin from Acetate Solution

As discussed before, the synthesis and characterisation of β-haematin from acetate solution has been well documented.[61] The synthesis was repeated in the current work in order to obtain a reference sample against which β-haematin formed under different conditions could be compared. Furthermore, while the product obtained from acetate solution had been previously characterised by FT-IR and SEM, both the ATR-IR and Raman spectra of this species have not been reported.

The normalised ATR-IR spectra of the starting material (haemin) and the products collected after 5 and 60 minutes incubation are shown (Figure 5.5 A). The product collected after 5 minutes is most likely haematin (H_2O–Fe(III)PPIX). The vertical dotted lines at 1662 and 1208 cm^{-1} indicate the characteristic marker bands of β-haematin in the product obtained after 60 minutes. These have previously been assigned as the C=O and C–O stretching frequencies respectively, of the coordinated propionate group. These peaks are absent in the spectrum of the starting material and appear only as weak bands in the second derivative spectrum (Figure 5.5 B) of the product obtained after 5 min. The second derivative spectrum allows weak peaks to be distinguished more clearly from noise and emphasises the striking difference between haematin and β-haematin. The spectra of all three materials have in common the band appearing at ~ 1710 cm^{-1}. In the case of β-haematin this has been assigned as the C=O stretching frequency of the free propionic acid group. Of note is that the peaks in the spectrum of β-haematin are sharper than those of haemin. This has been attributed to a reduction in the extent of hydrogen bonding in the case of β-haematin.[53]

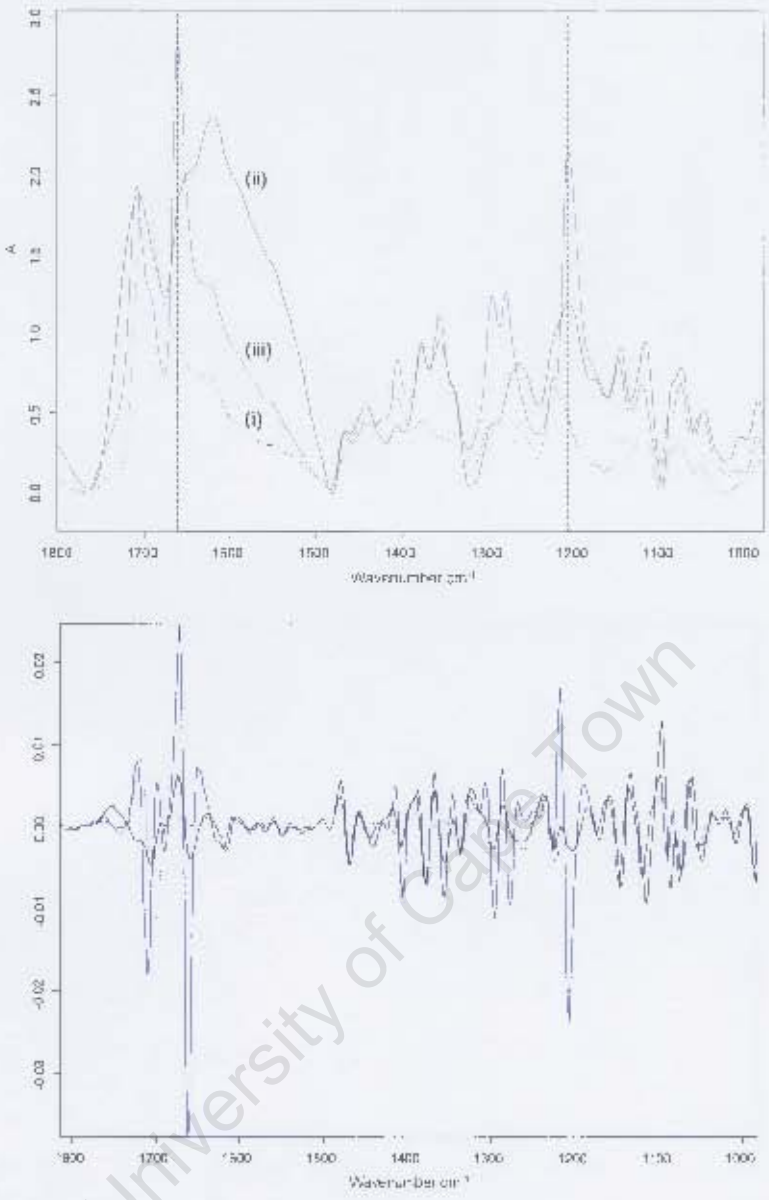

Figure 5.5 (A) The normalised ATR-IR spectra of (i) haemin (grey dashed line), (ii) the product collected after 5 min reaction time (black solid line) and (iii) β-haematin (blue solid line) formed from acetate solution. The vertical dotted lines at 1662 and 1208 cm^{-1} in the spectrum of the latter product indicate the characteristic marker bands of β-haematin. (B) The second derivative spectra of the same reaction products emphasising the striking difference between haematin and β-haematin.

The average Raman spectrum of the product formed from acetate solution, collected using a laser excitation wavelength of 785 nm, confirms that it is indeed β-haematin (Figure 5.6). The profile of bands is very similar to that previously reported for β-haematin and haemozoin (refer to Figure 2.8).[214,218] The assignments have been presented in Chapter 2.4.3.

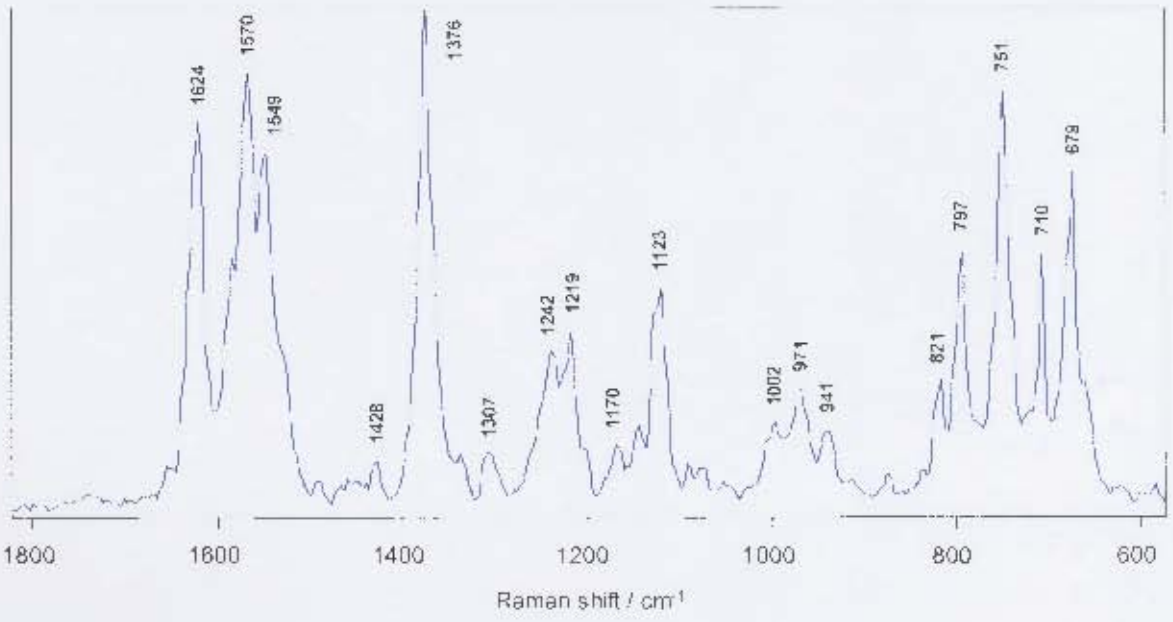

Figure 5.6 The average Raman spectrum of β-haematin formed from acetate solution.

5.3.2 Preparation of β-Haematin at the MMG/Water Interface

A detailed investigation of the formation of β-haematin at the pentanol/water, octanol/water and lipid/water interfaces has been previously reported.[73,98] However, it was necessary in the present study to prepare and characterise β-haematin obtained at the MMG/water interface to ensure reproducibility before proceeding to synchrotron work on the nucleation process. Unique opportunities to investigate the system using Raman spectroscopy and synchrotron radiation required a thorough understanding of the original system in order to reproducibly obtain the product outside of the Egan laboratory where previous work had been conducted.

Thus, the product recovered from the MMG/water interface was analysed using several different methods in order to confirm that it was indeed β-haematin. Figure 5.7 shows the FT-IR and Raman spectra of the product collected directly from the interface. Marker bands and band profiles in the IR and Raman spectra respectively are characteristic of β-haematin, as described above.

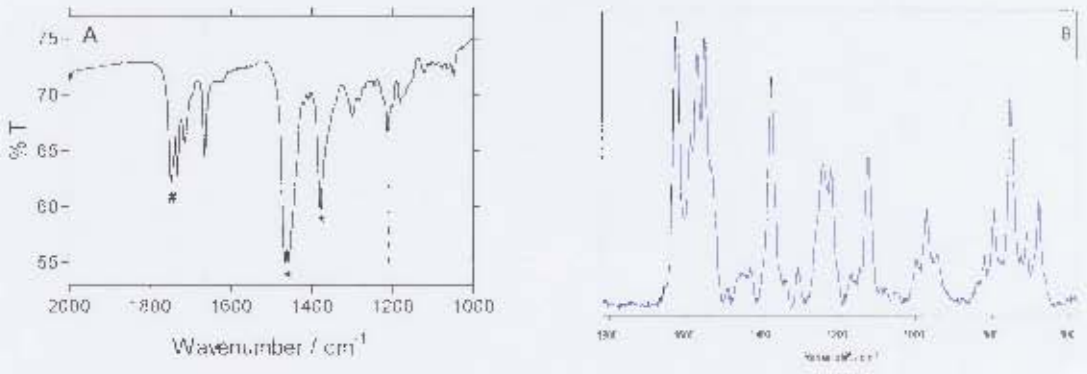

Figure 5.7 The FT-IR (A) and Raman (B) spectra of the product recovered from the interface. In (A), asterisks indicate nujol peaks while # indicates the lipid (MMG) C=O stretch.

5.3.3 Nucleation and Orientation of β-Haematin at the MMG/Water Interface

In order to probe the role of MMG in the induced oriented nucleation of β-haematin, a series of crystallisation experiments based on those performed routinely in crystallisation dishes and reported previously[73] were carried out *in situ* in a Langmuir trough. Grazing incidence X-ray diffraction (GIXD) and X-ray reflectivity (XR) data were recorded of the material at the liquid surface.

5.3.3.1 Control Experiments

In order to confirm that a lipid/water interface is important for the formation of β-haematin crystals, independent control experiments were performed (i) in the absence of lipid and (ii) in the absence of Fe(III)PPIX.

When β-haematin crystallisation was attempted in the absence of lipid, the GIXD measurements yielded only two peaks (q_{hor} = 0.58 and 1.64 $Å^{-1}$) that were inconsistent with β-haematin and were thus attributed to an unknown phase. XR as a technique provides information regarding crystal planes that are parallel to the surface and data are typically shown in the form of R/R_F as a function of q_{vert}, where R is the measured reflectivity and R_F is the Fresnel reflectivity of a perfect reflecting water surface.[94] The XR curve of material formed in the absence of lipid (Figure 5.8 A) exhibits a minimum at a q_{vert} value of 0.55 $Å^{-1}$ and shows no indication of Bragg peaks belonging to β-haematin beyond this point. The FT-IR

spectrum (Figure 5.8 B) of the same sample that was analysed using the liquid surface diffractometer reflects a broad peak at ~ 1594 cm^{-1} but no peaks at 1660 and 1210 cm^{-1}. The broad peak at ~ 1594 cm-1 has been previously observed in samples of haematin. SEM images (Figure 5.8 C and D) show a relatively smooth surface with no evidence of β-haematin crystals. Thus, the independent data suggest that the unknown phase is most likely an unknown phase of haematin.

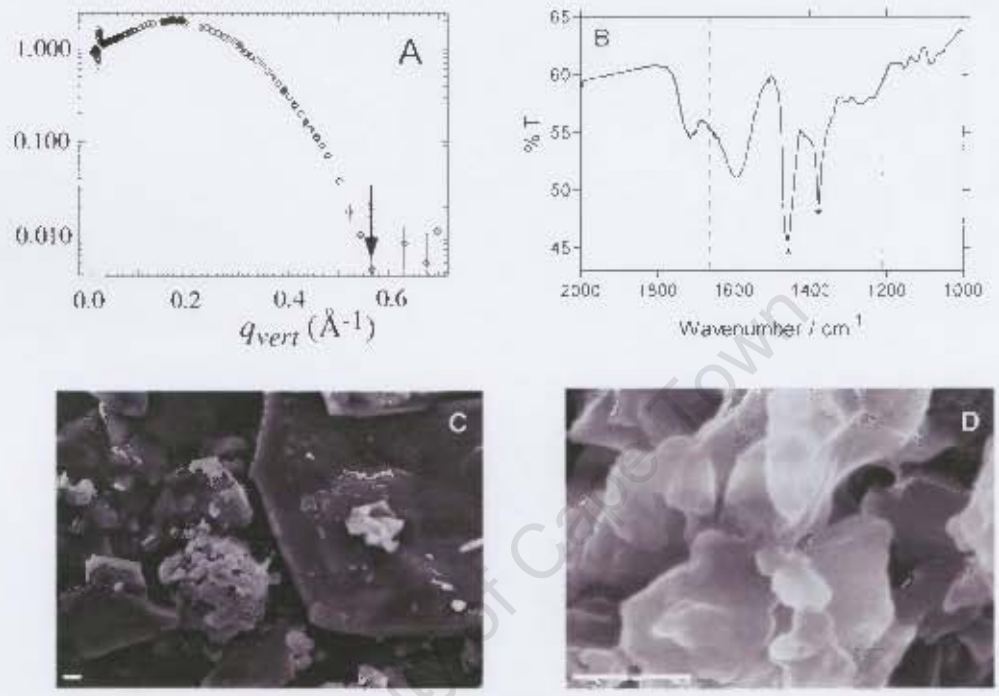

Figure 5.8 (A) The XR curve for material formed in the absence of lipid shows no evidence of Bragg peaks belonging to β-haematin. (B) The FT-IR spectrum does not exhibit characteristic β-haematin stretches at ~ 1660 and 1210 cm^{-1}. As before, asterisks in the FT-IR spectrum indicate nujol peaks. (C) An SEM image of the same material confirms the presence of only haematin. (D) A higher resolution SEM image of (C) confirming the absence of β-haematin crystals. The white scale bars in (C) and (D) correspond to lengths of 1 μm.

In the absence of Fe(III)PPIX, the same concentration of lipid that was used to crystallise β-haematin gave rise to a crystalline monolayer of MMG molecules. In order to deduce the unit cell dimensions and molecular orientation of the MMG molecules in the monolayer, it is necessary to first describe the theory underlying GIXD analysis.[94] The analysis of GIXD data in simple cases treats the lipid molecules as freely rotating alkane chains with cylindrical symmetry. The molecules may then pack in one of three cell types namely hexagonal ($a = b$, $\gamma =$

120°), distorted hexagonal/centred rectangular ($a = b$, $\gamma \neq 120°$) and oblique ($a \neq b$, $\gamma \neq 120°$) (Figure 5.9 A). Molecules packed in a hexagonal arrangement are aligned directly perpendicular to the surface of the monolayer, while molecules packed in the distorted hexagonal and oblique arrangements are tilted. Furthermore, Langmuir monolayers are regarded as powders as opposed to single crystals and thus the observed diffraction pattern consists of coinciding Bragg rods ((hk;q_{vert}) and (-h-k; q_{vert})). The hexagonal cell has three equivalent d-spacings: d_{hk} = d_{10}, d_{01} and $d_{1\text{-}1}$ (Figure 5.9 A i). These three reflections will appear as a single Bragg peak in the GIXD pattern (Figure 5.9 B), with its corresponding Bragg rod (Figure 5.9 C) reaching maximum intensity at the horizon, q_{vert} (or q_z) = 0 $Å^{-1}$. The distorted hexagonal cell gives rise to two Bragg peaks in the GIXD pattern, corresponding to the combined (10)/(01) and (1-1) reflections. The three reflections are resolved in the case of the oblique cell, giving rise to three independent Bragg peaks in the GIXD spectrum.

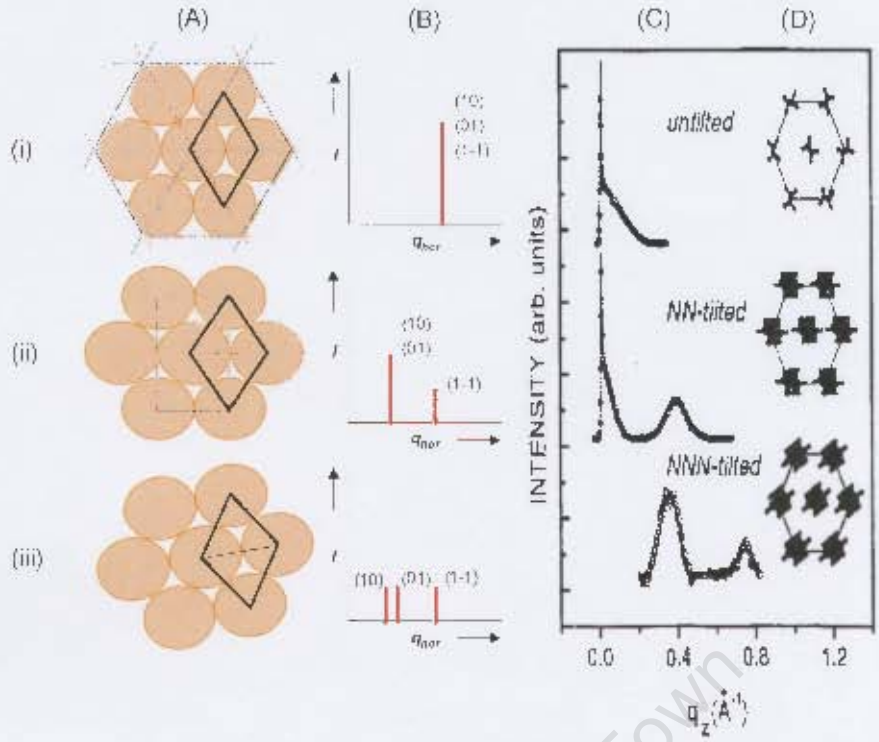

Figure 5.9 (A) Schematic views of the molecular packing in (i) hexagonal, (ii) distorted hexagonal and (iii) oblique unit cells. The sets of planes giving rise to the three equivalent d-spacings are indicated as dashed red, blue and green lines in (i). (B) The GIXD patterns ($I(q_{hor})$) observed for each unit cell type together with the Miller indices for each reflection. (C) The corresponding Bragg rods integrated over q_z. (D) The corresponding tilt directions observed for each unit cell. NN and NNN indicate that chains are tilted in the direction of their nearest neighbour and next-nearest neighbour respectively. Reproduced from reference 94.

Returning to the GIXD pattern returned by the monolayer of MMG molecules, a single, sharp Bragg peak (Figure 5.10 A) centred at q_{hor} = 1.5 Å^{-1} is immediately reminiscent of the hexagonal cell type. This deduction is confirmed by the corresponding Bragg rod (Figure 5.10 B), which shows that the integrated intensity is maximum at q_{vert} = 0 Å^{-1}. Thus it is concluded that the hydrocarbon chains of the MMG molecules in these experiments are oriented directly perpendicular to the monolayer surface, with no evidence of tilting.

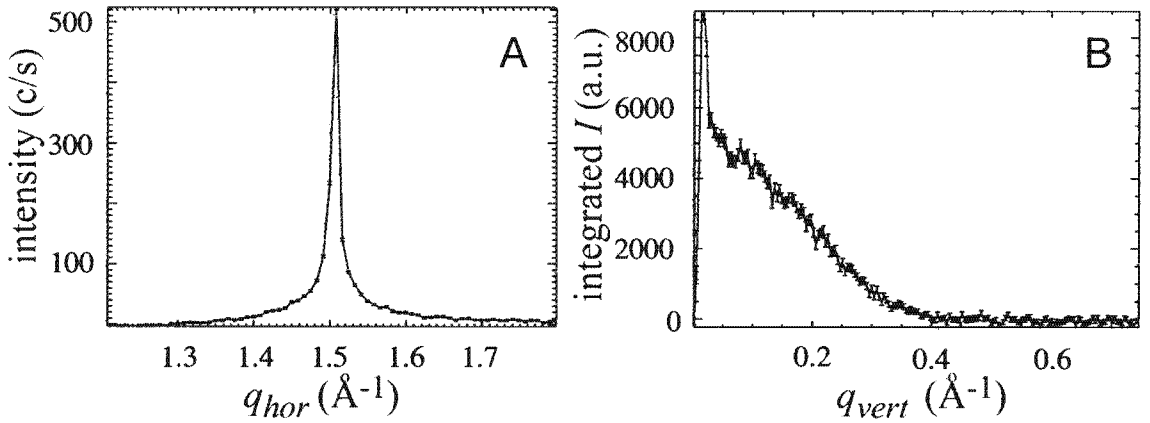

Figure 5.10 The GIXD pattern $I(q_{hor})$, measured from a monolayer of MMG molecules. The single Bragg peak (A) and corresponding Bragg rod with maximum intensity at q_{vert} = 0 Å^{-1} (B) confirm a hexagonal arrangement of molecules.

The position of the Bragg peak (q_{hor} = 1.5 Å^{-1}) corresponds to unit cell dimensions of a = b = 4.84 Å, where a = d/sin60° and d = $2\pi/q_{hor}$. Thus a single molecule with a cross-sectional area of 20.3 Å^2 (absin120°) occupies each unit cell. The full-width-at-half-maximum (FWHM) of the Bragg rod measured by GIXD (Figure 5.10 B) corresponds to a value of 14.2 Å according to equation 2.10. The XR curve (Figure 5.11) is typical for a monolayer consisting of lipid molecules with a single hydrocarbon chain. The first minimum occurs at q_{vert} = 0.28 Å^{-1} and corresponds to a domain size (film thickness) of 22.5 Å ($2\pi/q_{vert}$). The different results may be rationalised as follows: GIXD measures the crystalline part of the monolayer corresponding to only the hydrocarbon chain, whereas XR measures a whole MMG monolayer, inclusive of the hydrocarbon chain and the polar head group. The concentration of lipid delivered to the surface of the citrate buffer was sufficient in principle to pack approximately 16 layers. Thus it is apparent that only the top layer crystallised to form a monolayer. Possible interpretations of this observation are reserved for the discussion.

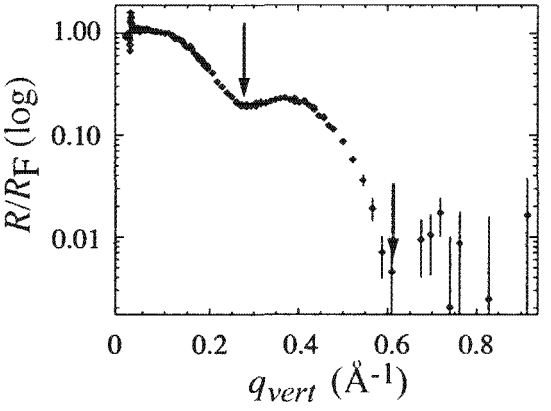

Figure 5.11 The XR curve measured from the solution of lipid spread over the surface of citrate buffer. The first minimum position (left most arrow) corresponds to a film thickness of 22.5 Å, suggesting that only a monolayer is crystalline.

5.3.3.2 The Effectiveness of Near-Monolayer Coverage of MMG

The effectiveness of near-monolayer coverage of MMG to nucleate and promote β-haematin formation was investigated. An estimated quantity of lipid sufficient for 3 layers of close-packed lipid molecules was pre-determined to be able to induce β-haematin formation (Figure 5.12). In this case, the experiment was repeated several times in order to collect a sufficient total amount of material. Reducing the quantity to that sufficient for only 1.5 layers did not produce β-haematin in good yield. However, when the quantity needed for 3 layers was used in the Langmuir trough (a once-off experiment), the concentration of Fe(III)PPIX added to the interface was insufficient to be detected by the X-rays.

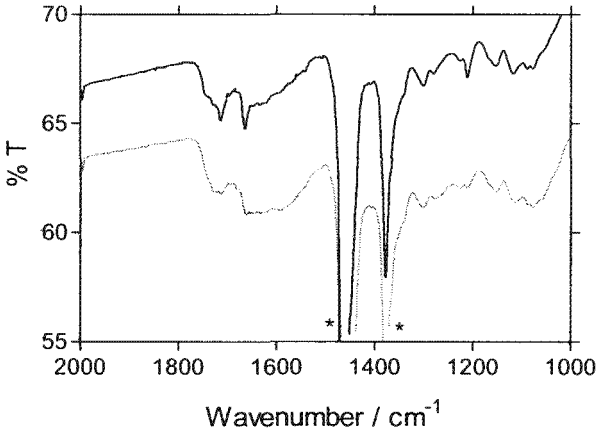

Figure 5.12 The FT-IR spectrum of β-haematin formed at the MMG/water interface, where the concentration of lipid was estimated to be sufficient to produce 3 layers of close packed lipid molecules (black solid line). The solid grey line indicates that 1.5 layers of lipid molecules are insufficient to promote significant β-haematin formation. Asterisks indicate nujol peaks.

5.3.3.3 The Effectiveness of Premixing

The analysis of the GIXD patterns for three independent experiments carried out using a subphase of 50.0 mM citrate buffer, pH 4.8 and sufficient lipid for about 16 layers (Figure 5.13 A – C) indicates that there were two crystalline phases present *in situ*. Three distinct Bragg peaks, albeit weak, correspond to the (001), (020) and (011) reflections of β-haematin, while Bragg peaks corresponding to the (031) and (131) reflections appear as a shoulder to a much more intense peak centred at 1.64 $Å^{-1}$. The latter peak, as well as a second intense peak centred at 0.59 $Å^{-1}$, are not consistent with β-haematin but rather correspond to the same "unknown phase" of haematin observed in the absence of lipid.

The five assigned reflections account for five of the eight most intense Bragg peaks in the calculated diffraction pattern of three-dimensional haemozoin/β-haematin crystals (Figure 5.14).[57] GIXD as a technique provides information regarding the crystal planes that are normal to the surface. The notable absence of the normally very intense (100) Bragg peak strongly implies therefore, that β-haematin crystals observed *in situ* near the air/liquid interface are oriented with this face parallel to the surface.

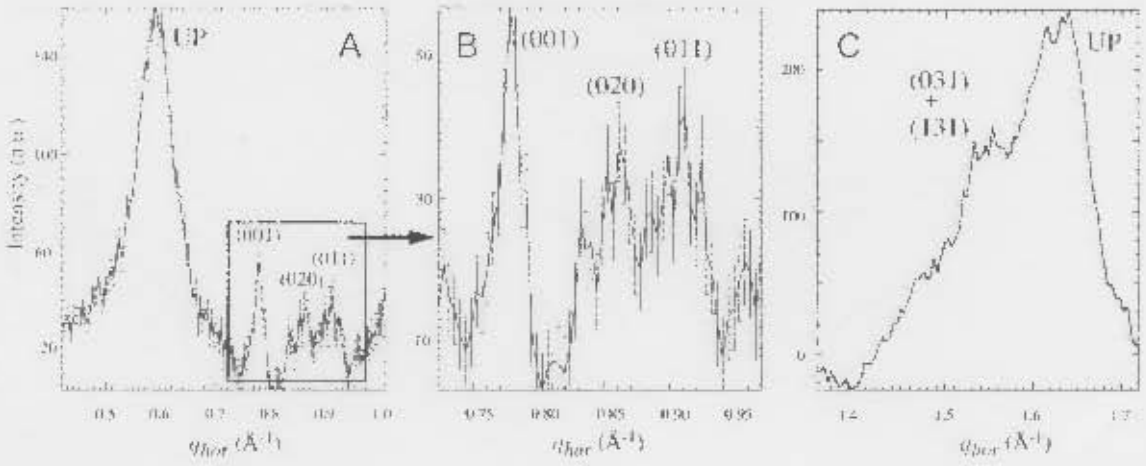

Figure 5.13 The GIXD pattern $I(q_{hor})$, where q_{hor} is the horizontal component of the scattering vector q, measured from an experiment in which a premixed solution of lipid and Fe(III)PPIX was added to the surface of citrate buffer (pH 4.8). The pattern in (B) is an expansion of the q_{hor} range indicated in (A). The Bragg peaks arising from β-haematin crystals are labeled (hkl). A second unknown phase (UP) of haematin is responsible for the same two intense Bragg peaks seen in the absence of lipid.

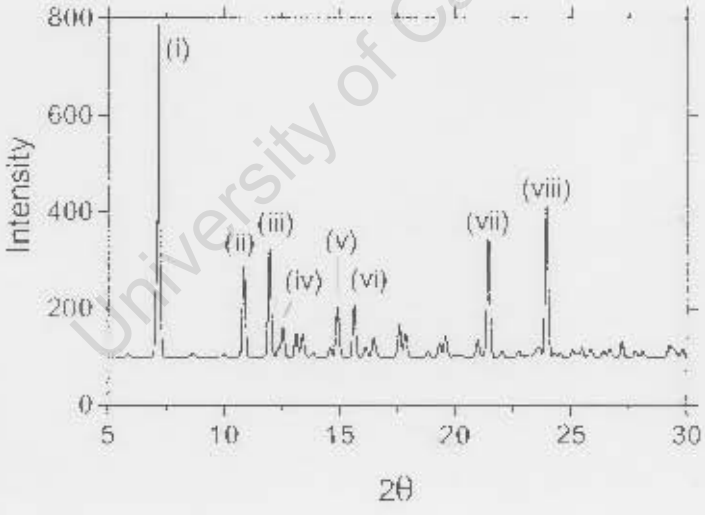

Figure 5.14 The calculated x-ray diffraction pattern of haemozoin/β-haematin is presented for comparison. The most prominent peaks are: i. (100), ii. (001), iii. (020), iv. (011), v. (120), vi. (111), vii. (031) and viii. (131). Reproduced based on data from reference 57.

From the unit cell dimensions of β-haematin originally determined by Pagola and co-workers,[57] the expected positions of q_{hor} and q_{vert}, the horizontal and vertical components respectively of the scattering vector can be calculated. Assuming that β-haematin crystals are oriented on their (hkl = 100) face, it is necessary to first re-orientate the original unit cell (Figure 5.15) such that (hkl) indices transform to

(h'k'l') = (klh). In two-dimensional crystal systems there is assumed to be little periodicity in the *c* direction. In GIXD therefore, only (h'k' = kl) indices are relevant, and correspond to crystal planes that do not lie parallel to the surface. For the five reflections observed in the GIXD pattern, the d-spacings together with the calculated and observed values of q_{hor} and q_{vert} are presented in Table 5.1.

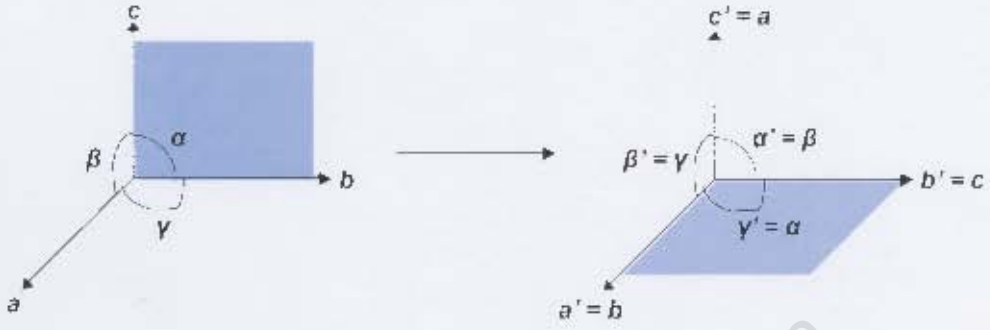

Figure 5.15 Schematic of the β-haematin unit cell transformation, assuming that crystals lie with their *bc* (100) face (blue) parallel to the liquid surface.

Table 5.1 The calculated and observed positions of q_{hor} and q_{vert} according to the unit cell geometry and dimensions of β-haematin crystals

(hkl)*	d-SPACING / Å	$q_{hor(CALC)}$ / Å^{-1}	$q_{vert(CALC)}$ / Å^{-1}	$q_{hor(OBS)}$ / Å^{-1}	$q_{vert(OBS)}$ / Å^{-1}
(**001**)	7.98	0.782	0.094	0.778	~0
(**020**)	7.27	0.856	0.123	0.861	~0
(**011**)	6.94	0.892	0.155	0.910	~0
(**031**)	4.11	1.51	0.275	1.55	~0.4
(**131**)	3.71	1.51	0.799	1.51	~0.8

* The relevant (h'k' = kl) Miller indices are indicated in bold font.

The average domain size of the β-haematin crystals in the *bc* plane, parallel to the liquid surface, can be estimated from the FWHM of the Bragg peaks according to equation 2.10. The average value from the (001), (020) and (011) reflections yields approximately 250 Å. The domain size perpendicular to the *bc* plane can be estimated from the FWHM of the Bragg rods. The average value is approximately 20 Å or two lattice spacings along *a* (Figure 5.16). It must be emphasised that this value is an indication of the mosaic block thickness along *a* and does not correspond to the actual thickness of the β-haematin crystals.

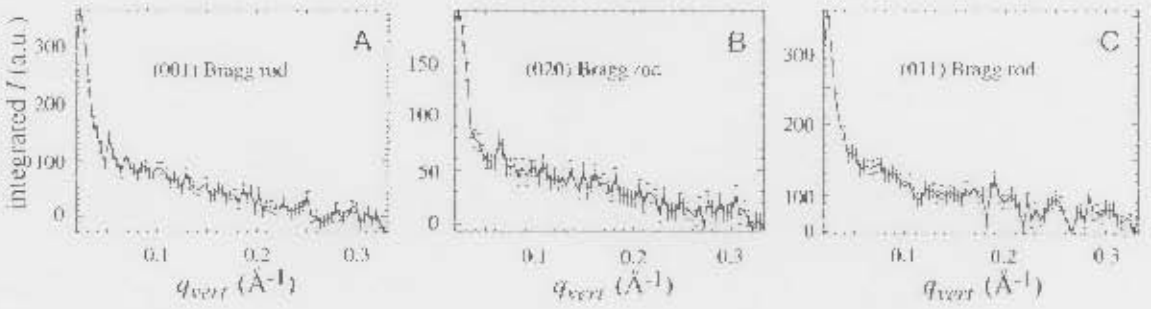

Figure 5.16 The integrated Bragg rods corresponding to the (A) (001), (B) (020) and (C) (011) Bragg peaks.

Independent XR measurements performed on the same samples substantiate the GIXD results. According to the crystal structure of β-haematin, the calculated value of q_{vert} for the (100) reflection is 0.524 Å^{-1}. XR measurements at different positions on two different samples yielded a broad (100) Bragg peak in the range 0.52 – 0.57 Å^{-1}. The minimum position in the XR curves corresponds to a q_{vert} value of 0.45 Å^{-1}, which contrasts the value of 0.55 Å^{-1} obtained for the "unknown phase" of haematin. As before, the crystal domain size can be obtained from the FWHM of the (100) Bragg peak. In this case the value ranged from 35 – 50 Å. By contrast to GIXD measurements, in which crystals that do not necessarily lie perfectly perpendicular to the surface may also contribute, XR measurements are perfectly selective for planes that are parallel to the surface. Thus, this value is probably more reliable than the ~ 20 Å value determined from GIXD measurements.

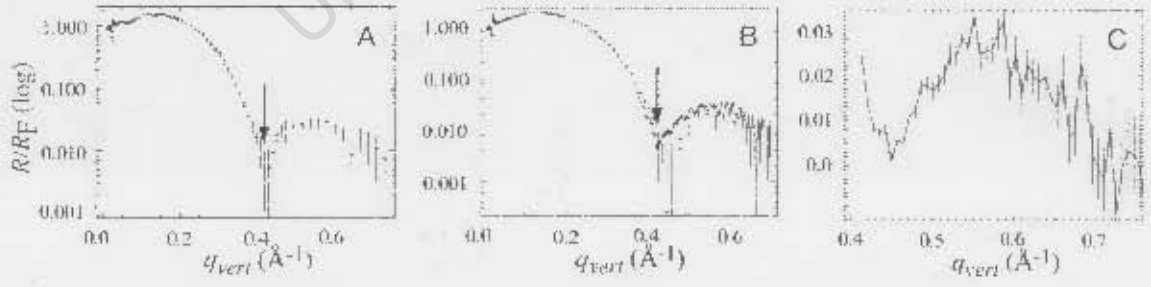

Figure 5.17 (A) and (B) The XR curves measured from two independent samples of β-haematin. The broad (100) Bragg peak, centred at approximately 0.55 Å^{-1} (expanded in (C)), indicates that the crystals are oriented with their (100) face parallel to the liquid surface.

In order to independently confirm the formation of β-haematin crystals, the same samples that were measured using the liquid-surface diffractometer were

transported in glass vials to UCT for further analysis. The FT-IR spectrum (Figure 5.18 A) of the product shows the characteristic stretches of β-haematin at ~ 1660 and 1210 cm^{-1}. The SEM image (Figure 5.18 B) of the crystals confirms that the product has an identical morphology to haemozoin crystals. The crystals exhibit the typical habit (habitual shape and form) that has been observed[57,99] and calculated.[97] Furthermore, the crystals are 1 – 2 microns in length, larger than synthetic β-haematin crystals formed in acidic medium at high temperatures[63,96] and of a similar size to both natural haemozoin crystals and those obtained under anhydrous conditions.[96]

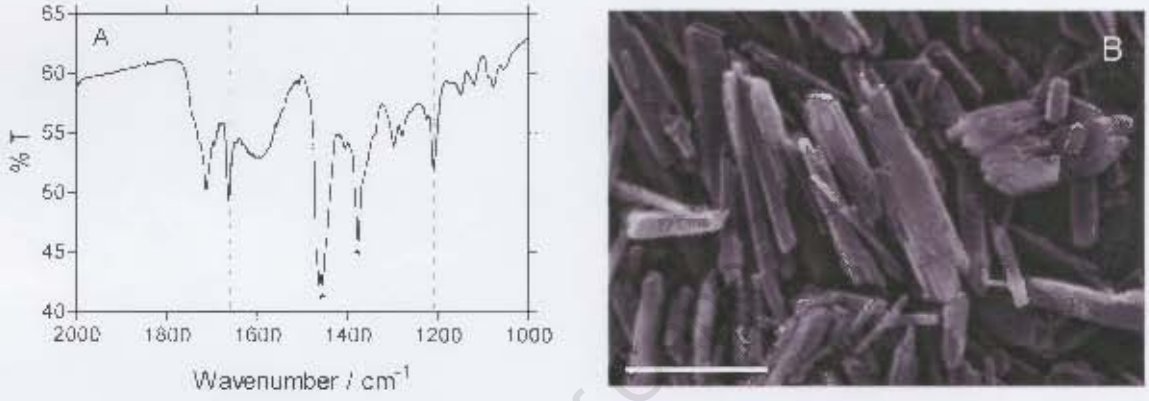

Figure 5.18 (A) The FT-IR spectrum of the β-haematin sample recovered from the Langmuir trough at BW1. Nujol peaks are indicated by asterisks. (B) An SEM image of the same material. GIXD and XR measurements reported here were recorded on this particular sample. The white scale bar corresponds to a length of 1 μm.

As a final note regarding the effectiveness of premixing, experiments in which lipid and haematin solutions were introduced separately did not yield β-haematin crystals when using the liquid-surface diffractometer. However, observations of Fe(III)PPIX introduced atop a perfect monolayer indicate that this is almost certainly an artefact of using the Langmuir trough as β-haematin has been recovered from experiments carried out in crystallisation dishes with no premixing.

5.3.4 The Role of –OH Groups in Nucleating β-Haematin

Subsequent to the studies carried out using the liquid-surface diffractometer, the abilities of docosane and methyl laurate, molecules that lack –OH groups, to nucleate and promote β-haematin formation were investigated. As evidenced by

the FT-IR spectra (Figure 5.19) of the products formed in the presence of docosane and methyl laurate, docosane appears incapable of nucleating and promoting the formation of β-haematin, while methyl laurate is able to promote the formation of β-haematin. The efficiency of MMG and methyl laurate to promote the formation of β-haematin was quantified using a pyridine assay previously described.[132] At the end of the reaction, a solution of 5% (v/v) aqueous pyridine was used to selectively solubilise unreacted Fe(III)PPIX. Presented in terms of the percentage of β-haematin formed (Figure 5.20), MMG appears 1.8 times more efficient in nucleating and promoting the formation of β-haematin.

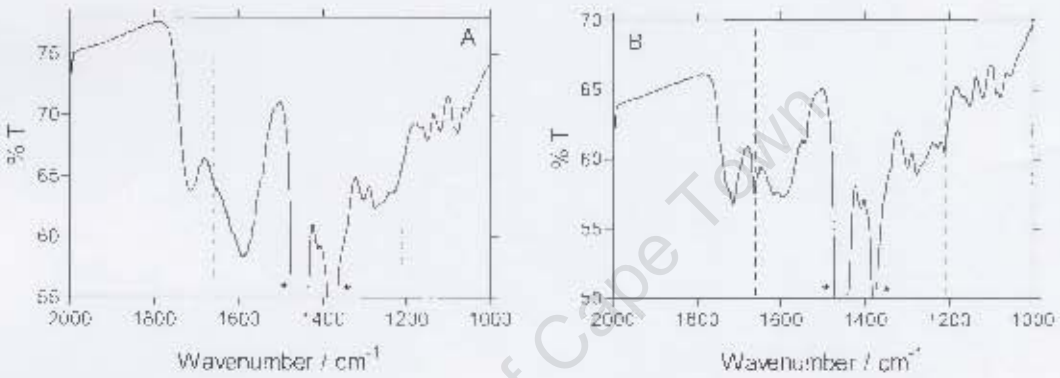

Figure 5.19 The ability of molecules that lack –OH groups to nucleate and promote β-haematin formation. The FT-IR spectra of the products formed in the presence of (A) docosane and (B) methyl laurate. The characteristic stretches of β-haematin (1660 and 1210 cm^{-1}) are absent from the product collected from the docosane/water interface, while present in the product collected from the methyl laurate/water interface.

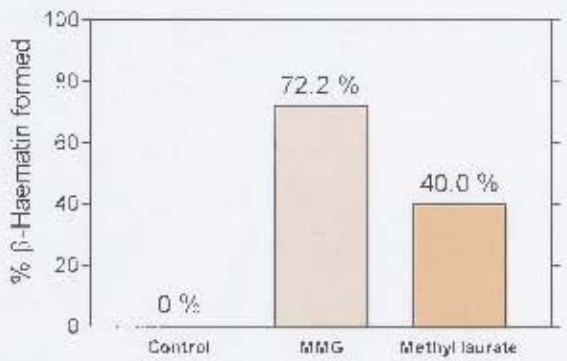

Figure 5.20 The conversion of Fe(III)PPIX to β-haematin is promoted 1.8 times more efficiently in the presence of MMG compared to methyl laurate.

5.4 Discussion

By comparison to β-haematin formed from acetate solution, the product recovered from the MMG/water interface after 30 minutes incubation was confirmed, using FT-IR and Raman spectroscopy, to be β-haematin. The GIXD analysis of the product formed in the absence of MMG corroborates the conclusion of previous work[73,98] that a lipid/water interface is critical in the formation of β-haematin. Two intense Bragg peaks were identified in the GIXD pattern of the product obtained from aqueous medium alone and attributed to an unknown phase (UP). Based on the broad IR signal and the SEM images of the same sample, it is suggested that the unknown phase is in fact an ordered form of haematin.

In the absence of Fe(III)PPIX, both GIXD and XR measurements indicate that a single monolayer of MMG molecules crystallises at the air/water interface. Furthermore, the molecules adopt a hexagonal unit cell and are aligned perpendicular to the surface. However, according to the calculated surface area per molecule, sufficient MMG solution was added to form approximately 16 layers. Two possibilities have been considered in order to account for this discrepancy. In the first case (Figure 5.21 A), crystalline monolayers form at both the air/water and MMG/water (where water is actually the citrate buffer solution) interfaces, while the intermediate "layer" is a disordered MMG/water phase in which the lipid molecules are oriented randomly with respect to one another. It is unlikely that XR measurements would be able to detect the second monolayer, thus accounting for a single monolayer at the air/water interface while the rest of the material appears to have the same electron density as water. An alternative and more likely hypothesis is that a single monolayer of MMG molecules crystallises at the air/water interface, while the remaining lipid solution forms lipid droplets or micelles, which being dispersed in the aqueous solution give rise to an electron density that can not be distinguished from that of water (Figure 5.21 B).

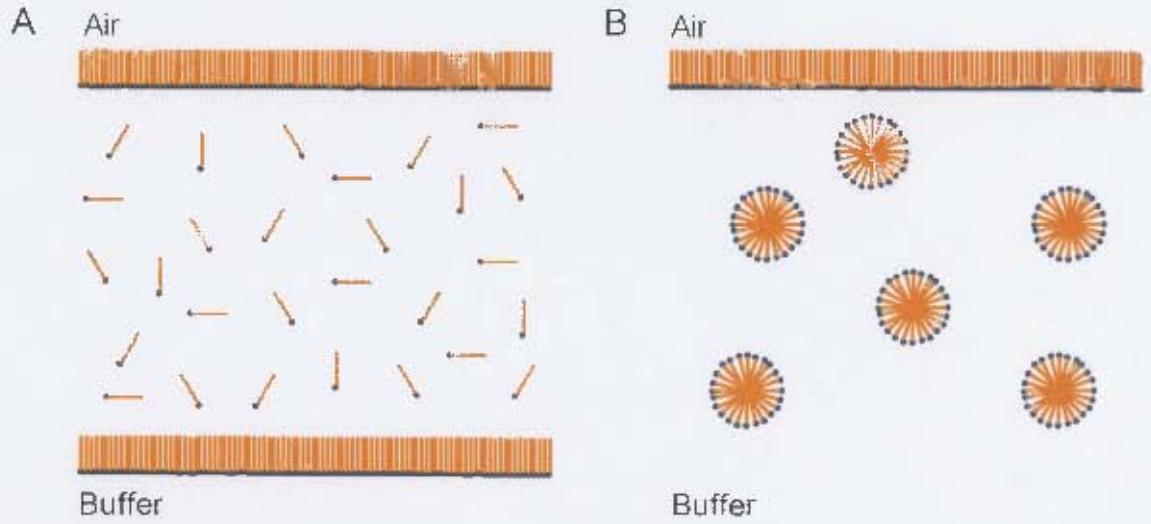

Figure 5.21 Schematic representations of the possible arrangements of lipid molecules. (A) Crystalline monolayers form at both the air/water and MMG/water interfaces, while the intermediate "layer" is a disordered MMG/water phase in which the lipid molecules are oriented randomly with respect to one another. (B) A single crystalline monolayer of MMG molecules exists at the air/water interface while the remaining lipid solution forms lipid droplets or micelles that are dispersed in the aqueous medium.

While the details concerning the nucleation of haemozoin *in vivo* are not definitive, the results of the current work regarding the orientation and nucleation of β-haematin at the MMG/water interface provide valuable insight into this process. The results of an extensive GIXD and XR investigation of the product obtained after a premixed solution of lipid and Fe(III)PPIX was delivered to and incubated (30 minutes) at the MMG/water interface (37°C, pH 4.8) in the first instance confirm the presence of β-haematin crystals. Bragg peaks corresponding to the (001), (020), (011), (031) and (131) reflections were detected in the GIXD pattern, albeit weak. By nature of the technique, it is inferred that the sets of "planes" in the two-dimensional crystal lattice that give rise to these reflections are either directly perpendicular or obliquely oriented relative to the air-liquid surface. The absence of the (100) Bragg peak from the measured GIXD pattern implies that the crystals float on this face, such that it is parallel to the liquid surface. XR data provide a measure of the depth of the crystalline material that gives rise to an electron density different to water, and yielding a Bragg peak corresponding to the (100) reflection, provide complementary evidence that the β-haematin crystals float on this face.

Experimental observations at the liquid-surface diffractometer indicated that the formation of β-haematin crystals was not uniform over the entire surface area. Furthermore, disparity exists between the weak diffraction peaks observed in the GIXD pattern and the well formed, micron-sized crystals observed by SEM. Taking into account the earlier discussions regarding the tentative arrangement of MMG molecules into lipid droplets or micelles, these results may be rationalised as follows. It is likely that GIXD and XR measurements were able to detect only the β-haematin that nucleated at the surface monolayer, thus explaining the weak intensity of the diffraction signals. The majority of β-haematin crystals, including those observed by SEM that were indistinguishable in size and morphology from haemozoin, were most likely formed at the surface of lipid droplets well below the liquid surface, rendering them undetected by either GIXD or XR.

The theoretical growth morphology of haemozoin crystals has been described[97] in terms of the unit cell axes of the crystal structure of β-haematin (refer to 1.6.4.2 Haemozoin Crystal Morphology).[57] The slow growing (100) and (010) faces are dominant in the crystal habit, while the fastest growing (011) and (001) faces are developed to a lesser extent. The growth rate of a particular face is dependent to some extent of the physical characteristics of the face. Those faces that are highly corrugated are typically the fastest growing as the addition of new β-haematin dimers would be akin to a docking process as opposed to one of nucleation each time against a smooth (slow growing) face. Thus the observation that the horizontal (parallel to the water surface) crystal domain size is 5 – 7 times greater than the vertical (perpendicular to the water surface) domain size is expected given that the slow growing and therefore smooth (100) face is parallel to the surface.

Based on the experimental observations that the β-haematin crystals are oriented on their (100) face at the interface, and that the growth rate is fastest parallel to the surface, Figure 5.22 serves as a visual interpretation of the molecular arrangement. The growth rate of β-haematin crystals is expected to be fastest along the *c* axis given that the (001) face is highly corrugated (refer to Figure 1.29).[99]

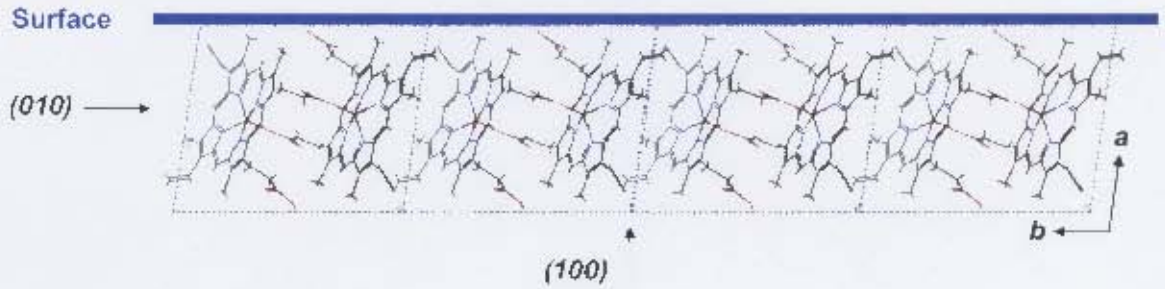

Figure 5.22 The arrangement of β-haematin dimers at the interface viewed down the *c* axis. The (100) crystal face is parallel to the surface, while the fastest growing, corrugated (001) face is in the plane of the page.

As seen in the diagram above, when the (100) crystal face is parallel to the surface, the propionic acid groups of the β-haematin dimers are exposed. Porphyrin methyl and vinyl peripheral groups are exposed to a lesser degree. Crystal nucleation at the lipid/water interface, assuming epitaxial-type molecular complementarity, is therefore expected to be based on interactions between the porphyrin propionic acid groups and the –OH groups and oxygen lone pairs of the MMG lipid molecules. This work extends the model of haemozoin formation across the lipid/water interface proposed by Egan and co-workers[73] as it provides insight into the specific role of the lipid molecules. It is evident therefore, that molecules that do not possess complementary –OH groups, such as docosane and methyl laurate, would not be able to promote β-haematin formation via the (100) face. It is a possibility that methyl laurate is able to nucleate β-haematin via the (010) face, which exposes porphyrin methyl and vinyl groups, although this was not investigated in this work.

5.5 CONCLUSIONS

This study on the oriented nucleation of β-haematin at the MMG/water interface has provided interesting insight into the possible nucleation of haemozoin crystals in a lipid environment. While interpretations remain speculative, it has been unequivocally demonstrated that β-haematin floats at the surface on its (100) face, and that growth in a direction perpendicular to the surface is slowest. This is in agreement with the theoretical growth morphology[97] of haemozoin/β-haematin, which has shown that the (100) face is significantly expressed in the crystal habit. Nucleation and epitaxial growth, via complementarity between the lipid head –OH groups and the exposed surface carboxylic acid groups of β-haematin, is offered as a plausible explanation for these observations.

6. THE INTERACTION OF ANTIMALARIALS WITH FE(III)PPIX AND THE INHIBITION OF β-HAEMATIN FORMATION

6.1 INTRODUCTION

The research and development of new antimalarial drugs is a growing priority given the weight that the malaria burden has on the world's population, and which is amplified by increasing parasitic resistance towards many of the commonly prescribed chemotherapeutic agents.[25]

In order to realise this goal, one of two major routes towards finding new compounds that are antimalarially active may be pursued.[25] The first is to screen combinatorial and natural product libraries for activity against a validated drug target. According to this approach, neither the molecular structure nor the original intended use of the compounds is of importance. The second approach is the structure-based design of novel compounds, and is reliant on prior knowledge of the pharmacophore.

It has been shown that mutations in the malaria parasite's food vacuole membrane transport proteins underlie their resistance to quinoline and related antimalarials,[182,183,185,188] which leave the formation of haemozoin as a parasite-specific, and thus valuable drug target. Rationalisation of both the mechanism of haemozoin formation and its inhibition requires in the first instance, a correct interpretation of the structure of Fe(III)PPIX in aqueous solution. Assuming the model of a $\pi - \pi$ (or stacked) dimer, quinoline drugs may (i) insert themselves between the two Fe(III)PPIX molecules,[142] (ii) split the dimer to form 1:1 complexes with monomeric Fe(III)PPIX,[123] (iii) interact with the ligated faces of Fe(III)PPIX[163] or (iv) stabilise an alternative structure of Fe(III)PPIX, the μ-oxo dimer.[38,159,167,275] Alternatively, it has been suggested that quinoline drugs may interact with the surface of haemozoin crystals either directly[57,97] or as a Fe(III)PPIX–quinoline complex.[122,137]

The rational design of new antimalarials necessitates an understanding of the drug target and how drugs interact with the target. However, the details of the structural

features of the pharmacophore target complex are not known in this case. In the case that quinoline compounds split the $\pi - \pi$ dimer to form 1:1 complexes with monomeric Fe(III)PPIX, the question remains why certain compounds inhibit haemozoin formation and are active, where as others are inactive.

6.2 METHODS

This section describes the details of methods used specifically in the investigation of Fe(III)PPIX–antimalarial complexes and the inhibition of β-haematin at the MMG/water interface. The materials used have been previously listed in Table 3.1.

6.2.1 Inhibition of β-Haematin Formation at the MMG/Water Interface

6.2.1.1 Sample Preparation

0.05 mM Drug Solutions Containing 50.0 mM Citrate, pH 4.8

Citric acid monohydrate (5.2535 g, 25.0 mmol) was dissolved in 400 ml distilled water together with the appropriate mass of antimalarial drug (Table 6.1). The pH was adjusted to 4.8 by the addition of concentrated sodium hydroxide (NaOH), after which the solution was made up to a final volume of 500 ml.

Table 6.1 Quantities of antimalarial salts required for the preparation of 0.05 mM solutions (V = 500 ml) containing 50.0 mM citrate, pH 4.8

COMPOUND	MOLECULAR MASS / $gmol^{-1}$	MASS / g
Chloroquine diphosphate (CQ)	515.9	0.0129
Quinine sulphate dihydrate (QN)	782.9 (391.45)*	0.0098
Quinidine sulphate dihydrate (QD)	782.9 (391.45)*	0.0098
Amodiaquine dihydrochloride dihydrate (AQ)	464.8	0.0116
Quinacrine dihydrochloride (QC)	472.9	0.0118
Pyronaridine phosphate (PN)	616.06 (518.06)#	0.0130

* The value in brackets is the actual mass used given these compounds are hemisulphate salts.

The mass required to prepare a 0.05 mM stock solution was originally calculated using the molecular mass of the free base as shown in brackets. All subsequent data presented have been corrected for the actual molecular mass of the phosphate salt.

1:9 Acetone:Methanol (v/v) Solution

1 ml of acetone was mixed together with 9 ml of methanol in a glass vial.

Lipid Solution

3.0 mg MMG was dissolved in 3.0 ml of the 1:9 acetone:methanol solution giving a concentration of 1.0 mg/ml. This solution was stored in a glass vial below 0°C.

Fe(III)PPIX Solution

2.0 mg haematin was dissolved in 1.2 ml of 0.1 M NaOH in a 10 ml glass vial. After complete dissolution of the solid, 1.8 ml of the 1:9 acetone:methanol solution was added and the new solution was thoroughly mixed to give a final concentration of 0.67 mg/ml. This solution was prepared fresh for each individual experiment.

5:45:50 Pyridine:Water:Acetone (v/v) Solution

To 10.0 ml 0.2 M HEPES buffer pH 7.5, 5.0 ml pyridine and 50.0 ml acetone were added and thoroughly mixed together. The solution was made to volume in a 100.0 ml volumetric flask with distilled water. Volumes correspond to a mole ratio of 1:17.9:5.5 pyridine:water:acetone.

6.2.1.2 Experimental Procedures

All experiments were carried out in Schott Duran crystallising dishes with an internal diameter of 9 cm. For the purposes of incubation, these glass vessels were partially immersed into a water bath set at 38°C to ensure that the working temperature of the experiment remained close to 37°C at all times. A large watch glass was used as a lid for each vessel.

Serial dilutions of the respective drug-containing citrate buffer were prepared using a 50.0 ± 1.0 ml measuring cylinder. This was deemed accurate enough for the purposes of the investigations. Regular (drug free) citrate buffer (50.0 mM, pH 4.8) was used to make up dilute solutions to volume. Each glass vessel was pre-incubated to 37°C while lipid and Fe(III)PPIX solutions were prepared. On average this process took 15 – 20 minutes.

The interface was prepared according to earlier methodology where no premixing of the lipid and Fe(III)PPIX solutions was carried out. It was reasoned that the drugs would partition into the lipid layer during the period of equilibration prior to the addition of Fe(III)PPIX. Firstly, 0.5 ml of lipid solution was added drop-wise over the surface of the citrate buffer. Subsequently 0.5 ml (0.33 mg) of Fe(III)PPIX solution was added drop-wise to the pre-incubated interface using a syringe with a needle diameter of 0.5 mm. Once Fe(III)PPIX had been delivered to the interface, the experiment was left to incubate for 30 minutes.

At the end of the incubation period the interface was agitated as before (Chapter 5) to release the product into the bulk medium. The total volume (51.0 ml) was transferred to an 85 ml Nalgene centrifuge tube and centrifuged at 10,000 rpm for 10 minutes. The supernatant was discarded and the pellet kept for further analysis. 1.0 ml of the pyridine:water:acetone solution (pH 7.5) was added to "wash" the pellet as before (Chapter 5). The supernatant remaining after a second centrifugation was subsequently diluted (40:1960 µl) and the absorbance measured at 405 nm to quantify the unreacted haematin. The absorbance values were plotted as a function of drug concentration and fitted to a simple exponential equation. The drug concentration at 50 % absorbance change is a measure of the IC_{50}, the drug concentration required to inhibit 50 % β-haematin formation.

In some cases, the product obtained after the first centrifugation (of the total 51.0 ml) was characterised directly by IR, while in others it was lifted directly from the interface onto a glass microscope slide and analysed by Raman spectroscopy. Both procedures were performed in order to compare the product to Fe(III)PPIX alone and β-haematin. Principle Components Analysis (PCA, Chapter 2.5) was used to explore the variability between Raman spectra recorded of β-haematin, Fe(III)PPIX and its complexes with CQ and QN.

6.2.2 The Crystal Structure of Fe(III)PPIX–Halofantrine

6.2.2.1 Crystallisation of Fe(III)PPIX–Hf

Owing to its insolubility in water, 0.7 mg halofantrine hydrochloride, Hf.HCl (1.3 μmol), was dissolved in 0.5 ml of methanol. This solution was premixed with 0.5 ml of lipid solution and the mixture was spread on to the surface of 50.0 ml of regular (drug-free) citrate buffer, pH 4.8. The mass of 0.7 mg Hf.HCl was calculated as if the final drug concentration of 0.026 mM were in the total 50.0 ml volume. This system was allowed to equilibrate to 37°C before 0.5 ml of the haematin solution was added drop-wise to the interface. The system was incubated for 30 minutes after which all material was centrifuged as before. The supernatant was discarded and the pellet was washed with 1.0 ml of the pyridine:water:acetone solution. The centrifuge tube was sealed and allowed to stand upright for several days before being laid on its side. Small crystals were observed on the side of the tube after 10 days. A single crystal of dimensions 0.02 mm × 0.06 mm × 0.12 mm was selected for X-ray diffraction.

6.2.2.2 Crystal Structure Analysis

Data collection was performed on a Nonius Kappa-CCD four-circle diffractometer using monochromatic MoK_α radiation of wavelength 0.71073 Å. Standard φ and ω scans were performed and an area detector was used to collect the reflections. Accurate cell parameters were determined by least-squares analysis of the reflection data. *COLLECT*[276] software was used in the process.

The structure was solved by direct methods using SHELXS-97, a program for the solution of crystal structures.[277,278] Determination of the space group symmetry was facilitated by X-PREP,[279] while refinement of the structure was achieved using SHELXL-97.[277,278] X-SEED,[257] a graphical interface for these programmes, was used for further investigation of the crystal structure and packing arrangements. All non-hydrogen atoms were treated anisotropically. Unless otherwise stated, all hydrogen atoms were placed in geometrically calculated positions and refined as riding atoms with C–H = 0.95 – 0.99 Å and $U_{iso}(H) = 1.2U_{eq}(C)$ ($1.5U_{eq}(C)$ for

methyl groups). The H atoms attached to N5 (H5N), O4 (H4) and the water molecule O1W (H1W and H2W) were located in the difference map and refined independently with their own displacement parameters. In the case of the included water molecule, the H1W–O1W–H2W bond angle was restrained to ensure a sensible final geometry.

The crystallographic data has been lodged at the Cambridge Crystallographic Data Centre[256] as file CCDC_659633. This data can be accessed free of charge via <www.ccdc.cam.ac.uk/data_request.cif>.

6.2.3 The Association of Halofantrine and Quinidine with Fe(III)PPIX in Acetonitrile

6.2.3.1 Sample Preparation

Haemin Solutions:

Solutions of Fe(III)PPIX were prepared by vortexing haemin (1 – 3 mg) in acetonitrile, made to volume in a 5.0 ml volumetric flask. Given the sparing solubility of haemin in this solvent, 2 ml aliquots of the mixture were centrifuged to remove undissolved particles.

Halofantrine and Quinidine Solutions:

The free bases of Hf and QD were prepared by precipitation from aqueous methanol and aqueous solutions of their salts respectively, using concentrated NaOH. The free base of QD was easily filtered and washed thoroughly with distilled water prior to being dried in a dessicator. The free base of Hf was extremely sticky. Agglomerates of compound were collected from solution and washed extensively prior to being dried in a dessicator.

Stock solutions (2.3 and 2.2 mM) of the free bases of Hf and QD respectively were prepared by dissolving the appropriate solid in 2.0 ml each of acetonitrile.

6.2.3.2 Experimental Procedures

The supernatant obtained after the centrifugation of the haemin/acetonitrile solutions was used directly in the cuvette. The concentration of dissolved Fe(III)PPIX was estimated from the Soret absorbance to be approximately 12 μM. Spectrophotometric titrations of Fe(III)PPIX were performed by the addition of 2 × 5.0 μl followed by 4 × 10.0 μl aliquots of drug stock solution in each case. The UV-vis spectra of the solutions were recorded between 300 – 800 nm after each addition. The final concentration of drug in the cuvette was approximately 58 μM. Further additions of drug did not alter the final spectrum obtained in each case.

6.2.4 Computational Investigation of Structures of Complexes of *Cinchona* Alkaloids with Fe(III)PPIX

The HYPERCHEM suite of packages[231] was used for all modelling studies. A force field previously developed for Fe(III) porphyrins by Marques and co-workers[246-248] was used with the addition of new parameters for the Fe(III)–alkoxide bond.

6.2.4.1 Force Field Parameterisation

In order to investigate a molecule using a particular force field, each atom within the molecule is assigned an atom name and type. The most frequently used atom types in the Marques force field are described in Table 6.2. The porphyrin core is labelled according to its respective atom types in Figure 6.1 A and standard numbering scheme in Figure 6.1 B. All other atoms were assigned numbers in order after the porphyrin core.

Table 6.2 Frequently used atom types and their description

ATOM TYPE	DESCRIPTION	ATOM TYPE	DESCRIPTION
CA	Porphyrin carbon, directly bonded to NA or NB	O2	Alcohol oxygen
CB	Porphyrin carbon, bonded to CA	NA	Porphyrin, $(NA)R_3$
CM	Porphyrin meso carbon	NB	Porphyrin, $=(NB)R_2$
C4	Tetrahedral carbon	N3	sp^3 nitrogen cation
CO	Carbonyl carbon	H	Hydrogen (e.g. C–H)
FE3	Iron(III)	HN	Amine hydrogen

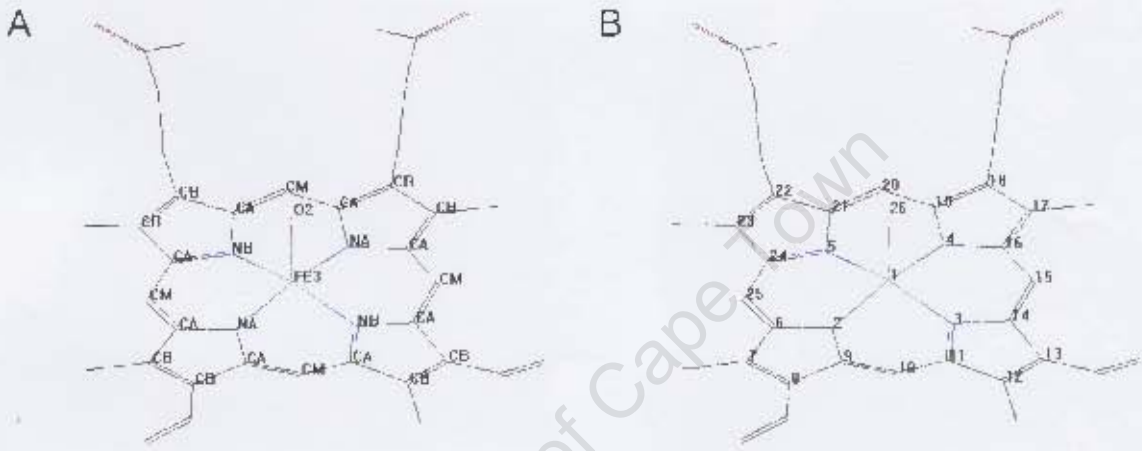

Figure 6.1 Standard atom types (A) and numbering scheme (B) applied to the porphyrin core. Hydrogen atoms have been removed for clarity.

A model of the Fe(III)PPIX–Hf complex was built and missing parameters were identified by means of a single point (SP) calculation. Parameters for the organic molecule, halofantrine, were available from Allinger's original force field[280] and were directly imported. Parameters for torsion angles involving FE3 were modified[281] (single atom type substitutions) relative to the closest matched parameter available from Allinger's force field. Torsion parameters have only weak force constants and furthermore, single atom type substitutions were not considered serious given that the geometry around FE3 would be restrained during modelling (see 6.2.4.2). A subsequent force field parameterisation was undertaken to determine the appropriate values for parameters for which no values existed, namely the FE3–O2 bond and the FE3–O2–C4 bond angle.

The Cambridge Structural Database (CSD)[256] was subsequently surveyed for five-coordinate Fe(III)–alkoxide complexes. Five molecules that were structurally similar to the Fe(III)PPIX–Hf structure were selected (Table 6.3) together with the Fe(III)PPIX–Hf complex from the current work.

Table 6.3 Compounds selected from the CSD for use in the structural survey

CSD REF CODE	CHEMICAL NAME	REFERENCE
FEWQON	5,15-(O, O'-(2-methyl-2'-hydroxy-3,3'-diamido biphenyl)-diphenyl)porphyrin – methoxy-iron(III) dichloromethane solvate	262
MFMPOR	Methoxy iron(III) mesoporphyrin-IX-dimethyl ester	262
MPORFE10	Meso-tetraphenylporphinato-methoxy-iron(III)	263
NADKOS	1,2,4,5-tetrakis-2'-O-phenyleneoxy)ethoxy)benzene-α,β,γ,δ porphyrin)methoxo-iron methanol solvate	263
SILKUT	Methoxy-octaethylporphinato-iron(III)	264

All atoms were assigned atom types and numbered according to the standard scheme. The average strain-free porphyrin geometry (bond lengths, bond angles and dihedrals) of the six crystal structures was used as a reference in the development of the force field. At the same time, a model of the Fe(III)PPIX–Hf complex was built and geometry optimised using the existing force field. The resulting geometry was compared to the average values obtained from the structural survey of the related crystal structures. The force field is considered correct if the absolute difference between the crystal structure averages and the values returned by the force field agree within certain tolerance limits. These are 0.015 Å for bond lengths, 1.5° for bond angles and 4° for torsion angles.[248] In the case that the absolute difference between the crystal structure averages and the model was greater than these tolerance limits, modifications to the force field parameters were made. Several iterations were made until the absolute differences were all within the tolerance limits. The results of the final iteration are given in Table 6.4 and the final bond length and angle parameters are reported in Table 6.5.

Table 6.4 Final averages, together with standard deviations (SDEV), obtained for bond lengths (Å) and bond angles (°) of the porphyrin core for the original crystal structures and the modelled structures of the same complexes. The absolute differences between the crystal averages and the model averages are shown

		Fe-O	Fe-N	Fe-O-C	N-Fe-O	N-Fe-N (*cis*)	N-Fe-N (*trans*)
Crystal	Average	1.843	2.070	126.136	102.762	87.202	154.465
	SDEV	0.017	0.011	2.018	1.974	0.610	1.270
Absolute Difference: |Crystal – Model|		0.003	0.010	0.122	0.462	0.198	0.933
Model	Average	1.846	2.080	126.258	102.300	87.400	155.398
	SDEV	0.002	0.007	0.689	0.439	0.524	0.714

Table 6.5 Final values of new parameters used in force field

Parameter	Equilibrium Value	K
FE3—O2 bond	1.843 Å	2.00 mdyne/Å
FE3–O2—C4 angle	126.1 °	1.00 mdyne/Å/radian^2 *

* While the equilibrium value is entered in degrees, the force field includes an internal unit conversion to radians, thus accounting for the given units.

Each compound has eight dihedrals of the type CA–N–FE3–O2 and sixteen dihedral angles of the type CA–N–FE3–N. In the latter case, these may take on large positive, large negative, small positive and small negative values, depending on the relationship between the two nitrogen atoms (cis or trans) as well as the direction in which atoms are reached (clockwise or anti-clockwise). In order to obtain averages, a deconvolution process was undertaken. For the six reference compounds, values for all 48 dihedrals of the type CA–N–FE3–O2 and all 96 dihedrals of the type CA–N–FE3–N respectively were sorted into ascending order. This grouped large positive, large negative, small positive and small negative values together and from these groups, the average of each group was used. The absolute difference between the crystal averages and the model averages was determined as before (Table 6.6).

Table 6.6 Final averages obtained for the dihedral angles of the porphyrin core for the original crystal structures and the modelled structures of the same complexes. The absolute differences between the crystal averages and the model averages are reported

		CA–NA–FE–NB / °	CA–N–FE–O / °
CRYSTAL	Group 1	-174.414	-82.092
	Group 2	-20.384	82.080
	Group 3	20.514	
	Group 4	174.591	
ABSOLUTE DIFFERENCE: |CRYSTAL – MODEL|	Group 1	1.375	0.342
	Group 2	0.232	0.204
	Group 3	0.005	
	Group 4	1.371	
MODEL	Group 1	-175.789	-81.750
	Group 2	-20.152	81.876
	Group 3	20.519	
	Group 4	175.962	

6.2.4.2 The Use of Restraints

The MM2 coding used in HYPERCHEM,[231] MM+, is not a faithful reproduction of Allinger's original code.[280] In particular, the way in which MM+ handles atoms (A) with a coordination number greater than four is of concern.[284] In MM2, such atoms are treated as any other atom and structural parameters involving them can be entered e.g. bond angles: X–A–X and dihedrals: X–X–A–X. In the case of the coordination number being greater than four, such as an Fe(III) porphyrin, MM+ uses a "points on the sphere" model in which bond angles and dihedrals of the type X–A–X and X–X–A–X respectively are ignored. The force field uses 1,3 van der Waals interactions to model the coordination sphere of A. This has proved an unsuccessful model and the way to overcome this is to specify certain restraints.[284]

The values of the restraints used in these calculations were taken from the structural parameters survey and are the average values of the six structures used in the force field parameterisation. The values are tabulated in Table 6.7.

Table 6.7 Restraints used to model the five-coordinate Fe(III) centre

NAME	FREQUENCY	VALUE / °	K / mdyne/Å/radian^2
NA—FE3—O2	2	102.8	156
NB—FE3—O2	2	102.8	156
NA—FE3—NB	4	87.2	47
NA—FE3—NA	1	154.5	12
NB—FE3—NB	1	154.5	12
CA—NA—FE3—O2	4	± 82.1	10
CA—NB—FE3—O2	4	± 82.1	10
CA—NA—FE3—NB	8	± 20.5 and ± 174.5	20
CA—NB—FE3—NA	8	± 20.5 and ± 174.5	20

6.2.4.3 Modelling the Complexes of the *Cinchona* Alkaloids with Fe(III)PPIX

The complexes of the *Cinchona* alkaloids quinine (QN), quinidine (QD), 9-epiquinine (eQN) and 9-epiquinidine (eQD) with Fe(III)PPIX were built and these initial structures were geometry optimised using the modified force field. Based on the crystal structure of Fe(III)PPIX–Hf, the quinuclidine nitrogen atom was protonated. Under the acidic conditions *in vivo* (digestive food vacuole) or *in vitro*, it is expected that one of the propionate side chains would exist in the protonated propionic acid form, as was determined in the crystal structure of Fe(III)PPIX–Hf. However, as it was not known which side chain should remain as the propionic acid, both were deprotonated and each one investigated independently. Molecular Dynamics (MD) simulations were performed on each initial structure in order to determine the minimum energy conformation. A trajectory of 100 ps run time was performed at 1000 K for each structure during which time 1000 snapshots (1 per every 0.1 ps) of the molecule were collected and stored, including the velocities at each point. Every tenth snapshot (i.e. that taken every 1 ps) was selected, with subsequent Simulated Annealing (SA) (cooled from 1000 K to 0 K) over a 20 ps time period followed by geometry optimisation. The details are summarised in Figure 6.2.

Owing to the flexibility of halofantrine's alkyl side chain, the Fe(III)PPIX–Hf complex could not be used in the computational study. By contrast, the overall flexibility of each Fe(III)PPIX–alkaloid complex is reduced because of the bulky, rigid quinuclidine ring. Rotation about two bonds, namely Fe(III)"–O10 and C8–C9

(Figure 6.3), is expected to contribute most significantly to the overall energy surface of the complex. These two dihedral angles were defined as φ and ψ respectively. Of the one hundred structures annealed, the minimum energy structure for each of the four complexes was selected as a starting conformation for further analysis. This involved calculation of the energy surfaces as a result of rotation of φ and ψ relative to each other through 360° in 30° increments.

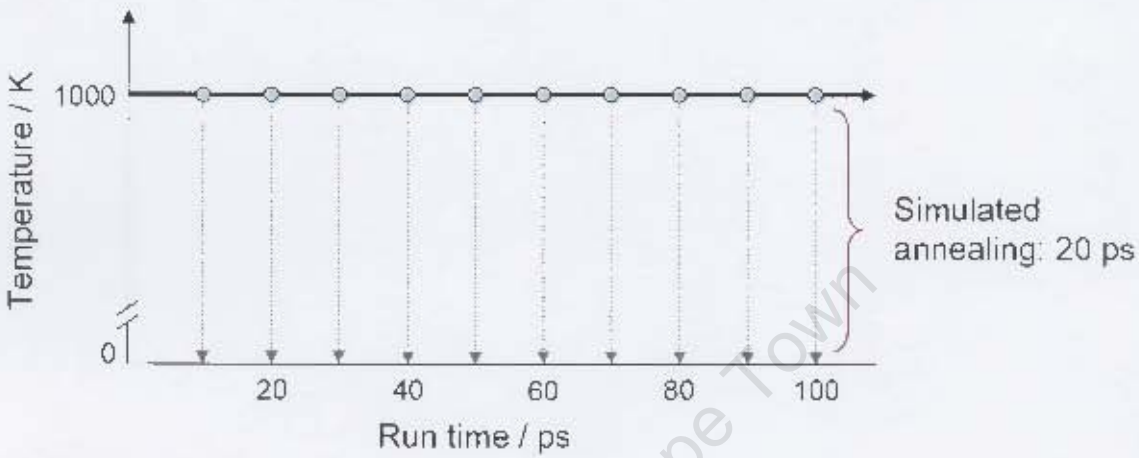

Figure 6.2 Summary of the conditions used for MD/SA simulations. Every tenth snapshot that was annealed (mint green circle) is indicated along the simulation trajectory (→). The cooling effect of simulated annealing is also indicated (vertical grey arrows).

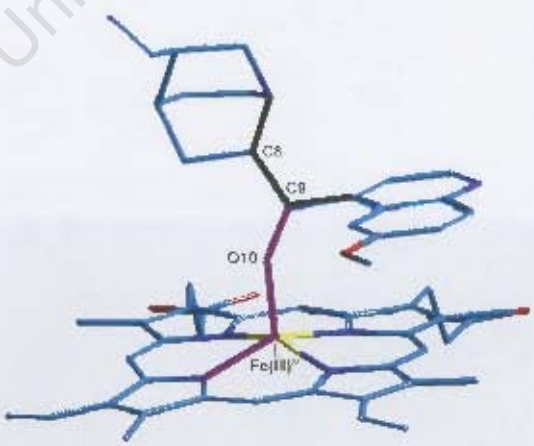

Figure 6.3 Model structure of a Fe(III)PPIX–alkaloid complex showing the two dihedral angles about which most free rotation is expected. Solid purple lines indicate φ and solid grey lines indicate ψ. Atom colour coding: cyan – C, yellow – Fe, blue – N and red – O.

As described in the Results and Discussion (Chapter 6.3 and 6.4), we suspect that an intramolecular, charge-assisted, hydrogen bond between the quinuclidine $N–H^+$ group and the propionate COO^- group is important in determining the biological activity of the four *Cinchona* alkaloids under investigation. However, hydrogen bonding could not be directly incorporated in the simulation, as it is not treated adequately in Allinger's original force field. The approach adopted in these studies was therefore to calculate the difference in strain energy between the conformation required for the formation of an intramolecular, charge-assisted, hydrogen bond and that of the lowest energy structure for each complex. The differences in strain energy (ΔE) can be considered as the energy penalty required to achieve the conformation required for the formation of the hydrogen bond in each complex. Since the four alkaloid compounds differ only in their stereochemistry about C8 and C9, a direct comparison of energies is possible.

In order to achieve a conformation suitable for the formation of the intramolecular hydrogen bond, rotation of φ and ψ as well as a change in conformation of the propionate group is necessary. Since either propionate group could be involved, ΔE was calculated for both cases and the lower value chosen. A dummy bond was included between the quinuclidine $N–H^+$ group (donor) and the propionate COO^- group (acceptor). The length was restrained to 1.882 Å, the average for hydrogen bonds of this type.[285] A very large force constant of 100,000 mdyne/Å was used to ensure the dummy bond retained its set length during geometry optimisation. No restraints were imposed on the hydrogen bond angle. The dummy bond was subsequently removed and a second geometry optimisation performed. The difference in energy between this new conformation and the minimum energy conformation (ΔE) was then calculated for each complex.

6.3 RESULTS

6.3.1 Inhibition of β-Haematin Formation at the MMG/Water Interface

To date, the β-haematin inhibitory activities of antimalarial drugs have been investigated under conditions that deviate from the biological conditions expected in the malaria parasite's digestive food vacuole.[61,68,125,132] Given the recent evidence that lipids are involved in the formation of haemozoin[74] and β-haematin,[73] the inhibitory activities of several aqueous-soluble antimalarial drugs were investigated at the MMG/water interface.

6.3.1.1 Qualitative Investigation of the Inhibition of β-Haematin Formation

The resultant Fe(III)PPIX–CQ and –QN complexes were characterised by resonance Raman spectroscopy (Figure 6.4) in order to confirm that β-haematin formation had indeed been inhibited. The Raman spectra were collected using an excitation wavelength of 785 nm, which is able to excite the Fe(III)PPIX chromophore. Bands belonging to CQ and QN were not detected using this wavelength as neither compound exhibits an electronic transition near 785 nm. Thus the average Raman spectra of Fe(III)PPIX, β-haematin and the Fe(III)PPIX–CQ and –QN complexes, normalised to ν_{10} (~ 1622 cm^{-1}), appear very similar. However, upon closer inspection it is observed that the intensities and Raman shifts of many bands differ between species. Of particular interest are the A_{1g} modes at 679, 796, 1378 and 1569 cm^{-1} and the B_{1g} modes at 754 and 1551 cm^{-1} (Figure 6.4), which have been previously assigned (Table 2.1). Most are either pyrrole in-plane stretches (e.g. $C_\beta C_\beta$), pyrrole in-plane breathing modes or pyrrole deformation modes. Significant intensity differences have been previously observed for these bands between spectra of haemozoin from control and CQ-treated *P. falciparum* infected cells when exciting with near-IR radiation (e.g. 785 nm).[286] The authors used these differences to indirectly investigate the interactions between the Fe(III)PPIX chromophore and antimalarial drugs such as CQ.

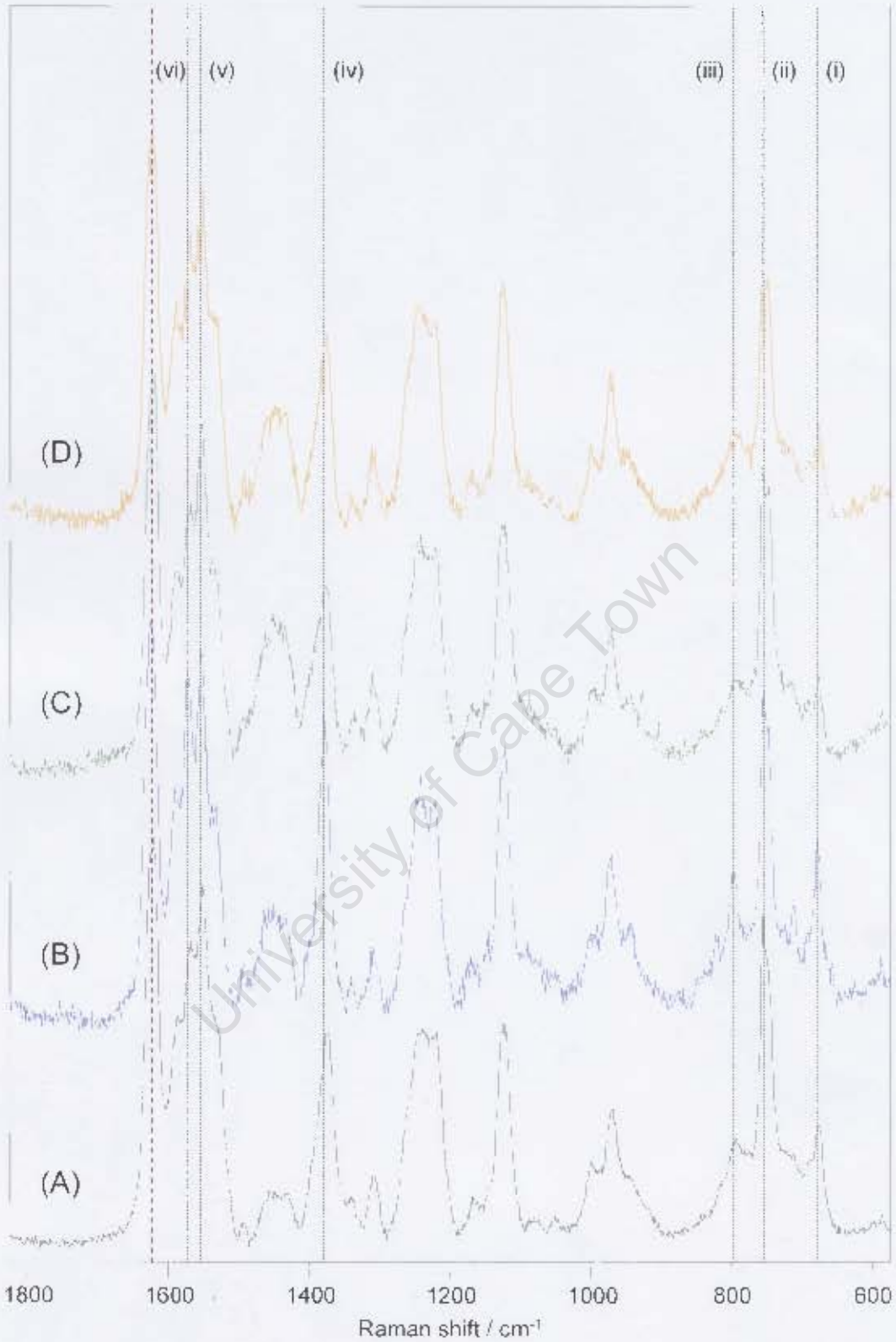

Figure 6.4 The average Raman spectra of (A) Fe(III)PPIX, (B) β-haematin, and the complexes of Fe(III)PPIX with (C) CQ and (D) QN. A laser excitation wavelength of 785 nm was used to collect the spectra. All spectra were normalised to ν_{10} (indicated by the purple dashed line at ~ 1622 cm^{-1}). Dashed black lines indicate the A_{1g} modes (i) 679, (iii) 796, (iv) 1378 and (vi) 1569 cm^{-1} and the B_{1g} modes (ii) 754 and (v) 1551 cm^{-1}.

The changes in intensity of the six modes relative to ν_{10} are more readily appreciated from the bar graph shown in Figure 6.5. Significant reductions of the bands at 679, 796 and 1378 cm^{-1} are observed for Fe(III)PPIX and its complexes with CQ and QN relative to β-haematin. While the bands at 754, 1551 and 1569 cm^{-1} do show decreases relative to β-haematin, they are not as pronounced. The intensity differences between bands in the spectrum of pure Fe(III)PPIX and those in the spectra of drug-affected Fe(III)PPIX are not as marked. The band appearing at approximately 1378 cm^{-1} (ν_4) has been labelled as the electron density marker band and changes in its intensity have been taken as an indicator of the relative intensity of $\pi - \pi$ interactions between antimalarial drugs and the porphyrin.[198,286] A more detailed explanation of this phenomenon is reserved for the discussion (section 6.4).

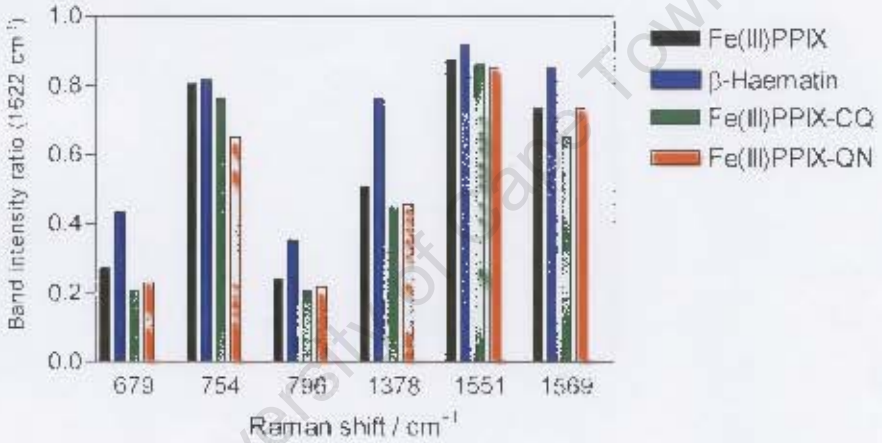

Figure 6.5 The relative intensities (normalised to ν_{10} at ~ 1622 cm^{-1}) of the A_{1g} (679, 796, 1378 and 1569 cm^{-1}) and B_{1g} (754 and 1551 cm^{-1}) modes for Fe(III)PPIX (black bars), β-haematin (blue bars), the Fe(III)PPIX–CQ complex (green bars) and the Fe(III)PPIX–QN complex (orange bars).

Principle Components Analysis (PCA, described in Chapter 2.5) is a multivariate statistical method that is useful for extracting descriptors that give rise to variance between two sample sets.[219] Raman spectra (785 nm) of Fe(III)PPIX–CQ (symbol **c**) and Fe(III)PPIX–QN (symbol **q**) were compared to Fe(III)PPIX (symbol **0**) in Figure 6.6 A and B respectively and to β-haematin (symbol **b**) in Figure 6.6 C and D respectively in order to determine which porphyrin bands account most for the variation between the different species. In the initial PCA analyses carried out for each pair of sample sets (**0** vs. **c**; **0** vs. **q**; **b** vs. **c** and **b** vs. **q**), some separation between the two groups was observed, although the explained variance along

PC1 was relatively low (60, 51, 24 and 15% respectively). The corresponding loadings plots for PC1 in each case, arrived at after a second-derivative calculation was applied to the data, are shown in the left column of Figure 6.6. Strong loadings are associated with A_{1g} modes at approximately 676, 797, 1380, 1572 cm^{-1} and the B_{1g} modes at approximately 750 and 1624 cm^{-1} in the analyses of **b** vs. **c** and **b** vs. **q**, and are indicated by purple in Figure 6.6. In the analyses of **0** vs. **c** and **0** vs. **q**, strong loadings (indicated by yellow in Figure 6.6) are associated with four of the same modes. However, the A_{1g} modes at 797 and 1572 cm^{-1} exhibit weaker loadings while an additional B_{1g} mode at approximately 1547 cm^{-1} shows strong loadings. These most extreme variables along PC1, which fall outside the dashed lines in each loadings plot in Figure 6.6, were subsequently selected as the basis for recalculation of the PCA. The resultant scores plots are shown in the right column of Figure 6.6. In each case there is clear separation of the sample sets being compared. The explained variances along PC1 are **0** vs. **c** (80%), **0** vs. **q** (78%), **b** vs. **c** (72%) and **b** vs. **q** (63%), representing increases compared to the initial calculation of 20, 27, 48 and 48% respectively. Thus the bands with strong loadings described above are implicated as significant contributors to variance between any two sample sets, confirming the earlier analysis based on peak intensity.

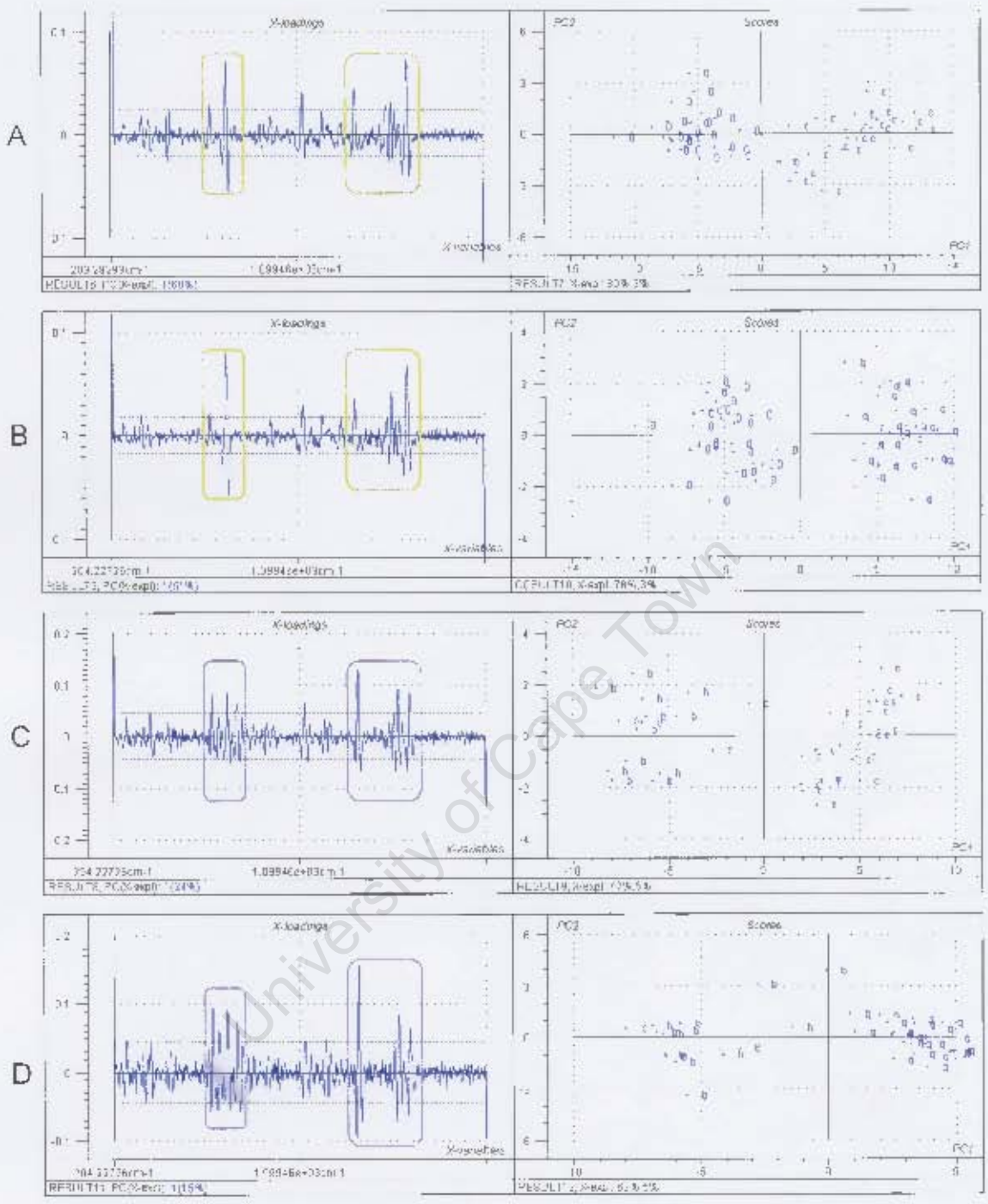

Figure 6.6 PCA results showing second derivative loadings plots of PC1 (left) and scores plots of PC1 versus PC2 (right) taken from the loadings plot along PC1 of the extreme variables (outside of the dashed lines). Raman spectra (785 nm) of Fe(III)PPIX–CQ (symbol **c**) and Fe(III)PPIX–QN (symbol **q**) were compared to Fe(III)PPIX (symbol **0**) in A and B respectively and to β-haematin (symbol **b**) in C and D respectively. Positive and negative loadings correspond to negative and positive locations in the respective scores plots.

In a PCA analysis, positive loadings correspond to objects that have negative values in the scores plot, while negative loadings correspond to objects that have a positive value in the scores plot. In each PCA analysis performed (**0** vs. **c**, **0** vs. **q**, **b** vs. **c** and **b** vs. **q**), the control sets of spectra (either **0** or **b**) appear as negative scores and therefore correspond to positive loadings. The positions of the bands indicated by the strongest positive loadings in all analyses reflect only small wavenumber shifts compared to their characteristic positions in the average spectra of β-haematin and Fe(III)PPIX (Tables 6.8 and 6.9). Frosch and co-workers[156] have reported that small wavenumber shifts in the range 2 – 3 cm^{-1} indicate non-covalent interactions between Fe(III)PPIX and drug in the electronic ground state. Hence the fact that all shifts in this work are in the range 0 – 4 cm^{-1} suggests that non-covalent interactions (e.g. π – π stacking) are the sole contributors to the association of CQ and QN with either β-haematin or Fe(III)PPIX.

Table 6.8 The positions of bands (cm^{-1}) in the average Raman spectra of Fe(III)PPIX (0) and β-haematin (b) that contribute significantly to the PCA analyses

ASSIGNMENT	SYMMETRY	0	b
ν_7	A_{1g}	676	679
ν_{15}	B_{1g}	755	754
ν_6	A_{1g}	794	796
ν_{22}	A_{2g}	1123	1121
ν_4	A_{1g}	1373	1378
ν_{11}	B_{1g}	1549	1551
ν_2	A_{1g}	1567	1569
ν_{10}	B_{1g}	1620	1624

Table 6.9 Raman shifts (cm^{-1}) for bands appearing as strong positive loadings in the PCA relative to their positions in the average spectra of β-haematin (b) and Fe(III)PPIX (0)

0 vs. c	SHIFT	0 vs. q	SHIFT
676	0	676	0
753	2	754	1
1122	1	1122	1
1371	2	1371	2
1547	2	1546	3
1624	-4	1621	-1

b vs. c	SHIFT	b vs. q	SHIFT
678	1	679	0
750	4	750	4
797	-1	797	-1
1122	-1	1124	-3
1379	-1	1380	-2
1571	-2	1572	-3
1627	-3	1627	-3

1. The numbers in the coloured boxes indicate the positions of the Fe(III)PPIX (**0**, top) and β-haematin (**b**, bottom) peaks in the loadings plots.

6.3.1.2 Quantitative Investigation of the Inhibition of β-Haematin Formation

The selective solubilising properties of 5% (v/v) aqueous pyridine, which have been previously described,[132] were exploited in order to quantitate the inhibitory activities of several antimalarial drugs. In each case, the UV-vis absorbance of the resultant bispyridyl-Fe(III)PPIX complex formed by reaction of pyridine with Fe(III)PPIX that had not been converted to β-haematin, was measured (405 nm) as a function of drug concentration and fitted to a simple exponential equation. The concentration at 50 % absorbance is a measure of the concentration required to inhibit 50% β-haematin formation (IC_{50}). Representative curves for each drug are shown in Figure 6.7, while the observed IC_{50} data are summarised in Table 6.10. On average, the initial absorbance of the bispyridyl-Fe(III)PPIX complex in the absence of drug is close to 0.55, while the absorbance of the complex in the presence of the highest concentration of drug is about 1.0. While the data suggest that the reaction proceeds to as little as 45 % conversion in the absence of drug, it is possible that light scattering from microscopic β-haematin crystals or lipid

molecules may have contributed to the high initial readings. Furthermore, that the method chosen to investigate the inhibition of β-haematin formation at the interface (i.e. no premixing) may not be as efficient as when Fe(III)PPIX and lipid are introduced premixed cannot be ruled out. As a means of validating the MMG/water interface system considered in the current work as a method to investigate the inhibitory activities of antimalarial compounds, the observed IC_{50} data were correlated to the biological activities determined against the chloroquine-susceptible 3D7 *P. falciparum* isolate (Figure 6.8).[125] When the data for all six drugs investigated are included, there is a reasonable correlation (r^2 = 0.80, P = 0.0162) with the biological data. When data for CQ is excluded the correlation improves to r^2 = 0.98.

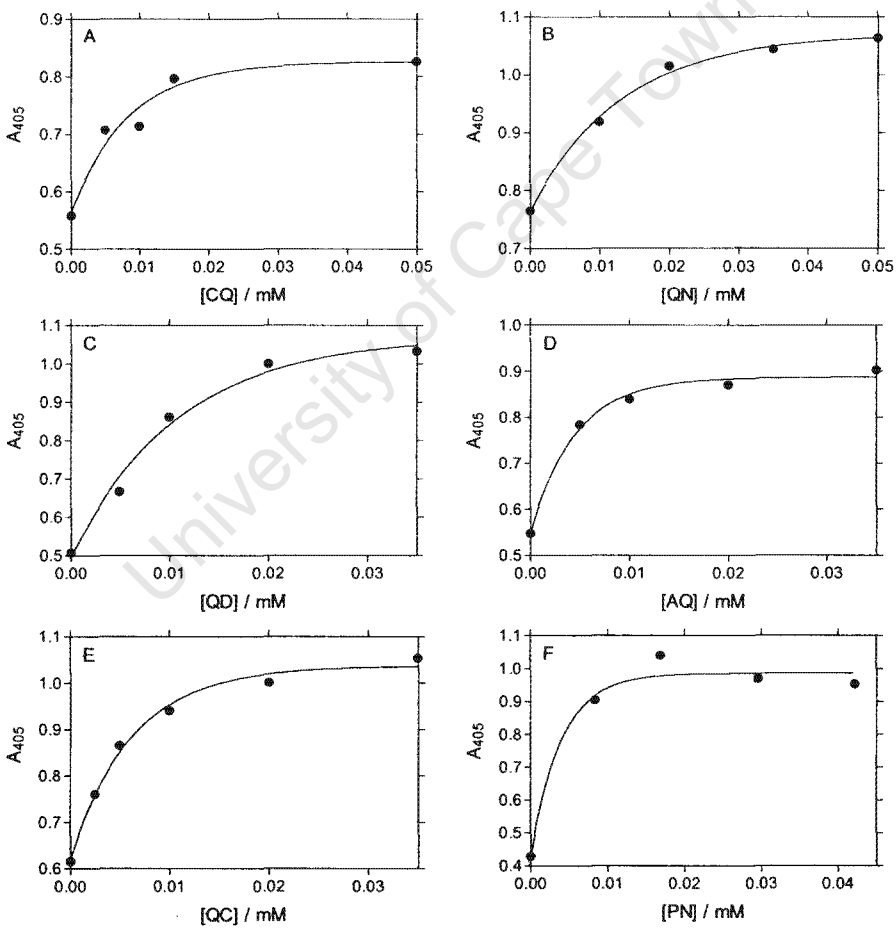

Figure 6.7 The variation in the absorbance of bispyridyl-Fe(III)PPIX complex (405 nm) formed by reaction of pyridine with Fe(III)PPIX that had not been converted to β-haematin as a function of antimalarial concentration for (A) chloroquine (CQ), (B) quinine (QN), (C) quinidine (QD), (D) amodiaquine (AQ), (E) quinacrine (QC) and (F) pyronaridine (PN). In each case, the solid line is the best fit of the data to a simple exponential equation in order to determine the IC_{50} for each drug.

Table 6.10 IC_{50} data obtained for the inhibition of β-haematin at the lipid/water interface (LWI)

ANTIMALARIAL COMPOUND	OBSERVED IC_{50} / μM*
Chloroquine (CQ)	7.3 ± 0.7
Quinine (QN)	9.0 ± 0.8
Quinidine (QD)	6.8 ± 0.8
Amodiaquine (AQ)	3.0 ± 0.3
Quinacrine (QC)	4.0 ± 0.2
Pyronaridine (PN)	2.7 ± 0.6

* Mean ± standard error of the mean for at least three independent measurements.

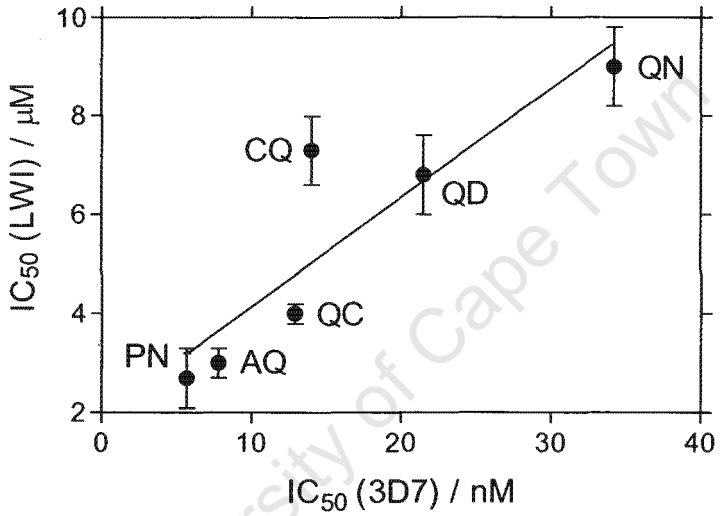

Figure 6.8 The correlation (r^2 = 0.80; P = 0.0162) between the inhibitory activities of antimalarial drugs at the lipid/water interface (IC_{50} (LWI)) and their biological activity (IC_{50} (3D7)).[125]

6.3.2 The Crystal Structure of Fe(III)PPIX–Halofantrine

The crystal structure of the Fe(III)PPIX–halofantrine complex determined in this work is the first example of a complex between Fe(III)PPIX and an antimalarial drug. Halofantrine is in fact a phenanthrene methanol compound, although it bears much structural resemblance to related quinoline methanol compounds.

Structural analysis revealed that the Fe(III)PPIX–Hf complex crystallises in the triclinic centrosymmetric space group $P\bar{1}$, indicating a primitive lattice type. The unit cell was found to contain two molecules at (x,y,z) and (-x,-y,-z). The atom

labelling scheme of the asymmetric unit is shown (Figure 6.9). The crystal and structure refinement parameters are summarised in Table 6.11.

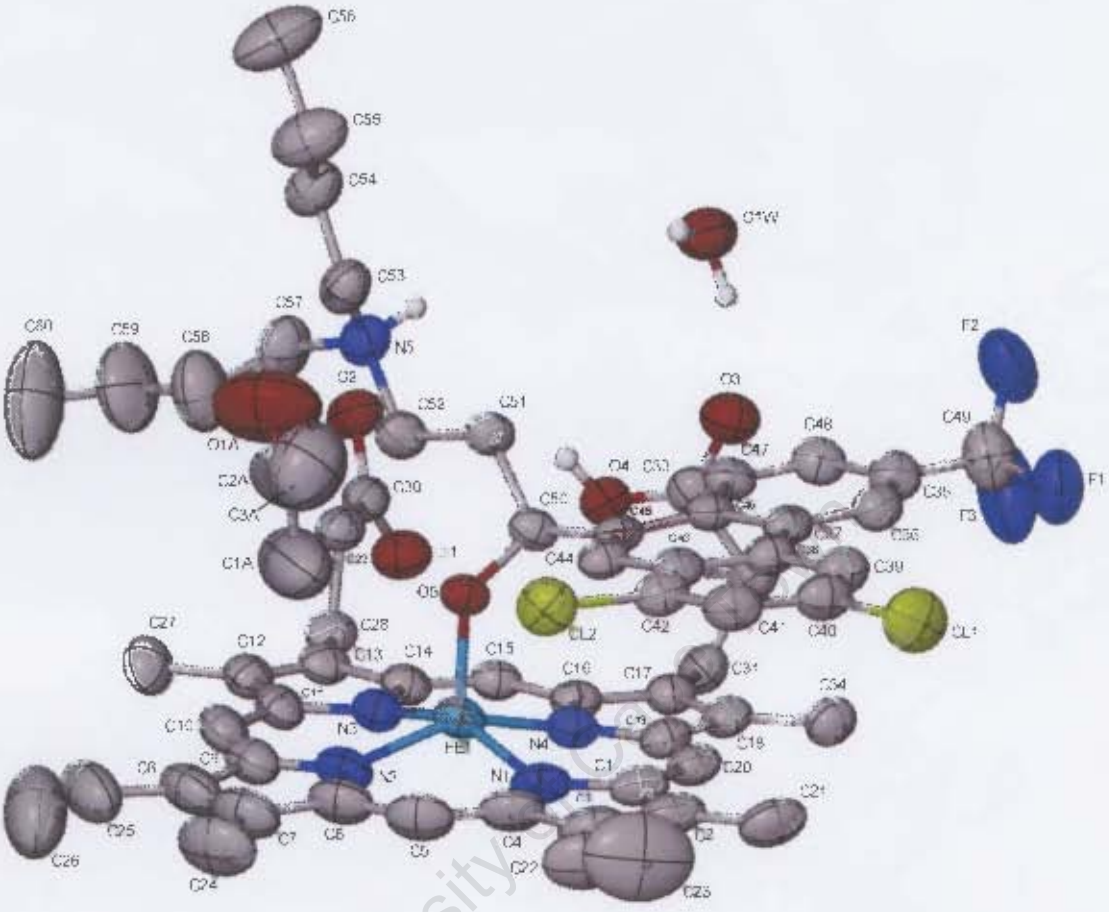

Figure 6.9 The atom labelling scheme of the asymmetric unit of the Fe(III)PPIX-halofantrine complex. Thermal ellipsoids are drawn at 50% and illustrate significant disorder in the vinyl groups of Fe(III)PPIX, the butyl chain termini of halofantrine and the included molecule of acetone. Atom colour coding: grey – C, cyan – Fe, dark blue – N, red – O, yellow – Cl and light blue – F.

Table 6.11 Crystal and structure refinement parameters for Fe(III)PPIX–Hf

PARAMETER	VALUE
Molecular formula	$C_{60}H_{60}Cl_2F_3FeN_5O_5$, C_3H_6O, H_2O
Molecular mass / g mol^{-1}	1191.98
Lattice type, Space group	Triclinic, $P\ \bar{1}$
a, b, c / Å	10.3410(3), 15.1939(5), 19.7077(8)
α, β, γ / °	84.7060(10), 74.9230(10), 73.007(3)
Volume / Å^3	2858.91(18)
Z	2
Calculated density (D_x) / g cm^{-3}	1.385
Temperature / K	113
MoK_α / Å, μ(MoK_α) / mm^{-1}	0.71073, 0.426
F(000)	1250
Crystal size / mm	0.02 × 0.06 × 0.12
θ / °	2.54 – 25.46
h, k, l	-12 → 11, -18 → 18, -23 → 23
Reflections: total, independent	40172, 10464
Reflections ($I > 2\sigma(I)$)	5019
Parameters	750
S	1.020
$R[F^2 > 2\sigma(F^2)]$	0.0790
$wR(F^2)$, $w = 1 / [\sigma^2(F_o^2) + (0.1461P)^2 + 2.2934P]$ where $P = (F_o^2+2F_c^2) / 3$	0.1858
$\Delta\rho$ excursions / eÅ^{-3}	0.616, -0.484

The crystal of the Fe(III)PPIX–Hf complex reveals several important structural features regarding the interaction of the antimalarial drug with its receptor, Fe(III)PPIX. In addition to the envisaged π-stacking of the phenanthrene ring of Hf over the porphyrin, Hf is seen to coordinate to the Fe(III) centre of Fe(III)PPIX via its hydroxyl group. The Fe–O bond length (1.840(4) Å) is consistent with the coordination of an alkoxide (1.816 – 1.867 Å)[262-264,282,283] rather than an alcohol (2.113 – 2.160 Å).[287,288] Intermolecular hydrogen bonding occurs between the protonated terminal nitrogen atom of halofantrine (N5–H5N$^+$) and the propionate group (C30(O2)O1$^-$) of a neighbouring Fe(III)PPIX molecule. A second hydrogen bond, involving the carbonyl oxygen atom (O2) of this same propionate group and the propionic acid group (C33(O3)O4–H4) of the adjacent Fe(III)PPIX molecule, is also present. Further hydrogen bonding within the crystal involves the solvent water molecules. Figure 6.10 shows the various hydrogen bonds in the crystal

packing diagram while specific details of the hydrogen bond geometries are reported in Table 6.12. Included acetone molecules do not contribute to the hydrogen bonding network, but exist in channels as shown in Figure 6.11.

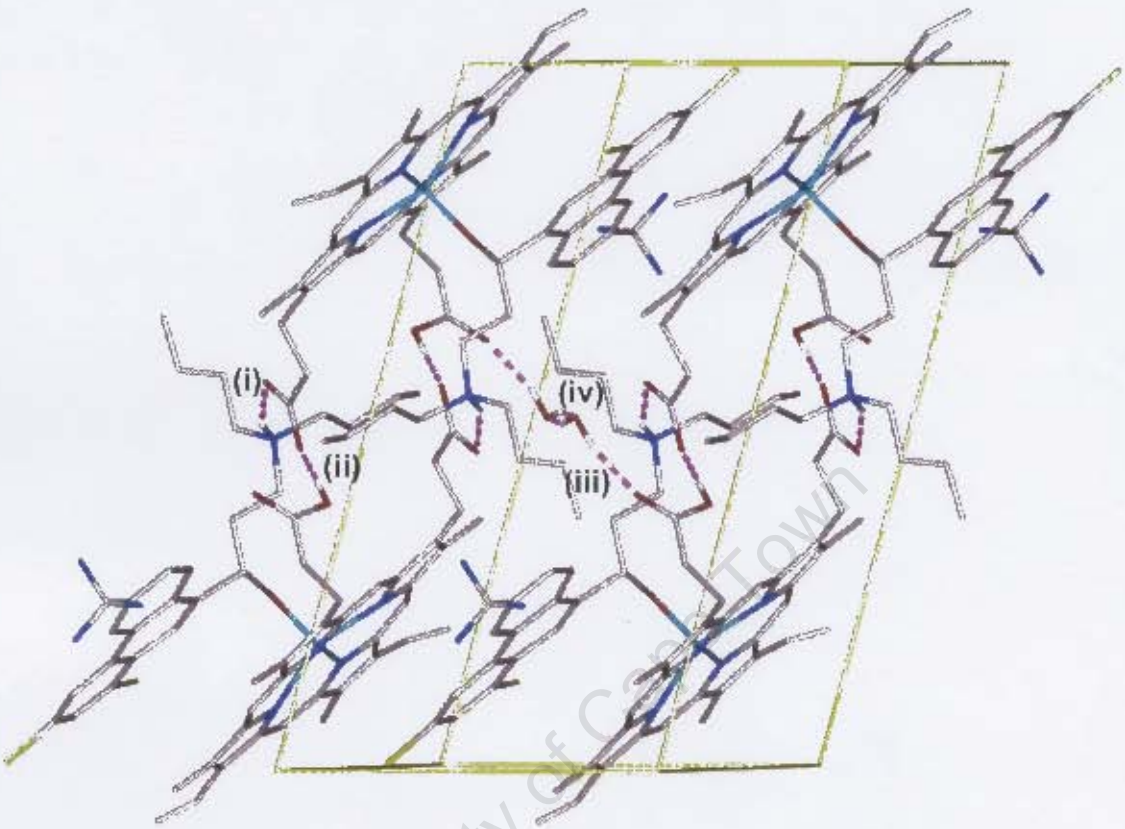

Figure 6.10 The crystal packing of Fe(III)PPIX–halofantrine as viewed from the *ac* face. Hydrogen bonds (pink dashed lines) contributing significantly to the overall packing are (i) N5–H5N···O1, (ii) O4–H4···O2, (iii) O1W–H1W···O3 and (iv) O1W–H2W···O1W. Acetone molecules, which do not contribute to the hydrogen bonding network, have been removed for clarity.

Table 6.12 Hydrogen bond geometry in Fe(III)PPIX–Hf

D–H···A	D–H (Å)	H···A (Å)	D···A (Å)	D–H···A (°)
N5–H5N···O1[a]	0.9900(11)	1.79(3)	2.710(6)	153(5)
O4–H4···O2[a]	0.93(7)	1.52(8)	2.449(6)	177(7)
O1W–H1W···O3	0.954(10)	1.85(2)	2.784(6)	165(7)
O1W–H2W···O1W[b]	0.953(10)	2.50(3)	3.413(11)	161(7)

Symmetry code: [a] 2 – x, -y, 1 – z; [b] 1 – x, -y, 1 – z

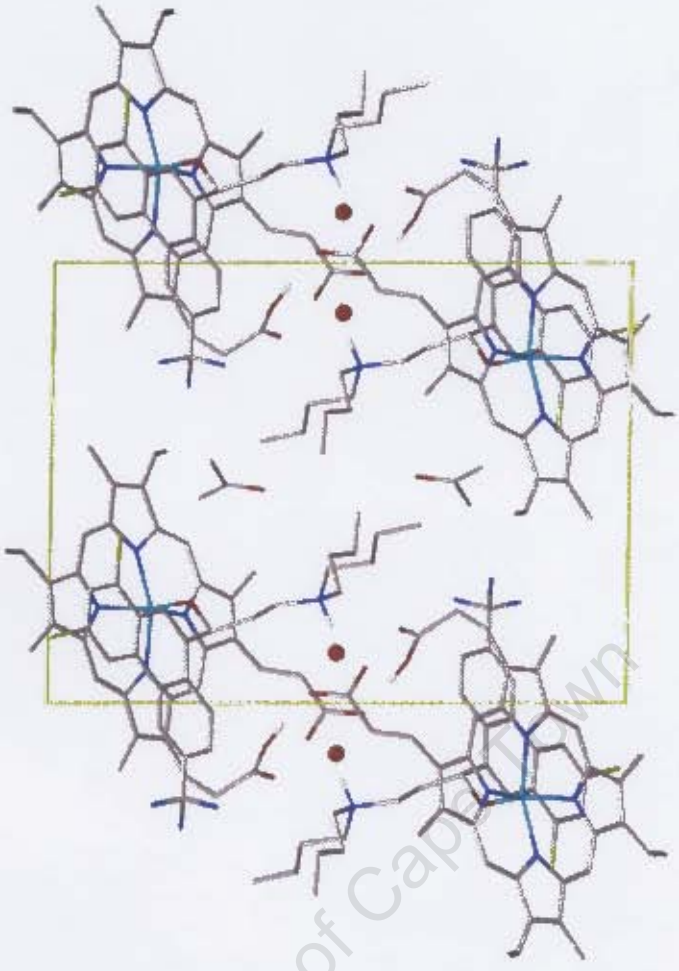

Figure 6.11 The crystal packing of Fe(III)PPIX–halofantrine viewed along the *a* axis, illustrating the centrosymmetric relationship between molecules. Water molecules are represented as red spheres. Included molecules of acetone are shown in channels which run parallel to the stacked columns of Fe(III)PPIX–Hf complexes. Intermolecular hydrogen bonds have been omitted for clarity.

6.3.3 The Association of Halofantrine and Quinidine with Fe(III)PPIX in Acetonitrile

The *Cinchona* alkaloids quinine (QN), quinidine (QD), 9-epiquine (eQN) and 9-epiquinidine (eQD) differ only in their relative stereochemistry at two chiral centres (C8 and C9) and thus present a unique opportunity to investigate the relationship between structure and activity. As has been discussed previously (Chapter 1.7), QN and QD are active against malaria parasites while their epimers (eQN and eQD) are inactive.

In the current work, all attempts to crystallise Fe(III)PPIX complexes of the *Cinchona* alkaloids were unsuccessful. QN and its stereoisomers are however structurally related to Hf, the former compounds being described as quinoline methanols compared to Hf, which is a phenanthrene methanol compound. On the basis of structural similarities it was conjectured that the alkaloids may coordinate to the Fe(III) centre of Fe(III)PPIX in a similar manner to Hf. Indeed, the observed changes in the UV-vis spectrum of Fe(III)PPIX in acetonitrile upon titration with solutions of the free base of both Hf and QD are strikingly similar (Figure 6.12). The appearance of isosbestic points in the spectrum obtained with QD indicates that only two species are present in solution. These are most likely Fe(III)PPIX and the Fe(III)PPIX–QD complex.

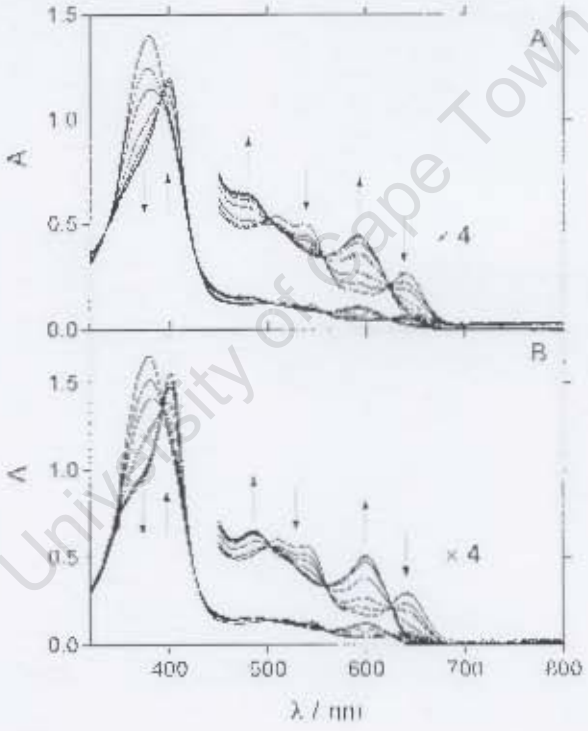

Figure 6.12 The changes in the UV-vis spectrum of Fe(III)PPIX in acetonitrile (A) upon coordination of the free base of halofantrine and (B) upon association with QD free base in acetonitrile. The conditions for the spectrophotometric titrations are: [Fe(III)PPIX] ≈ 12 μM. Individual spectra in each case correspond to 2 × 5.0 μl and 4 × 10.0 μl additions of 2.3 and 2.2 mM stock solutions of halofantrine and QD respectively.

6.3.4 Computational Investigation of Structures of Complexes of *Cinchona* Alkaloids with Fe(III)PPIX

Taking into consideration the similar changes effected in the UV-vis spectrum of Fe(III)PPIX upon addition of QD as compared to Hf, it seems likely that the Fe(III)PPIX–alkaloid complexes are analogous in structure to the Fe(III)PPIX–Hf complex. Thus the four Fe(III)PPIX–alkaloid complexes were modelled using molecular mechanics.

Initially, the four complexes were built and their minimum energy conformations found following molecular dynamics simulations (Figure 6.13 A). The rigid nature of the bicyclic quinuclidine side chain of the alkaloids reduces conformational freedom when the alkaloids are coordinated to the Fe(III) porphyrin. Apart from the porphyrin (methyls, vinyls and propionates) and alkaloid (methoxy and vinyl) peripheral groups, only two torsion angles were identified as being significantly flexible. These are N2"–Fe(III)"–O10–C9 (φ) and C4'–C9–C8–N1 (ψ). Whilst maintaining all other torsional angles essentially constant, φ and ψ were rotated relative to one another in order to investigate the strain energy surface for each complex (Figure 6.14).

In the crystal structure of Fe(III)PPIX–Hf, the hydrogen bonding potential of the complex was satisfied by *inter*molecular interactions with neighbouring complexes and included water molecules. In aqueous solution it is expected that solvent water molecules would satisfy this same potential. In solution in a lipid environment however, where haemozoin formation is most likely to occur,[73,74] the hydrogen bonding potential of the complex can only be satisfied through the formation of *intra*molecular hydrogen bonds. In the same way that the terminal nitrogen atom in the hydrocarbon chain of halofantrine was protonated in the crystal structure of Fe(III)PPIX–Hf, so the nitrogen atom in the quinuclidine side chain of the alkaloids is likely to exist in a protonated (positively charged) state ($N–H^+$). Furthermore, the porphyrin is expected to have one negatively charged propionate group (COO^-), as was the case in the crystal structure. Such features lend themselves to the likely formation of an intramolecular, charge-assisted hydrogen bond. The force field used for these investigations is not able to model hydrogen bonding directly. Thus

the approach was to compare the strain energies of the conformations required for the formation of the intramolecular, charge-assisted hydrogen bond (Figure 6.13 B) to the minimum energy conformations in each case.

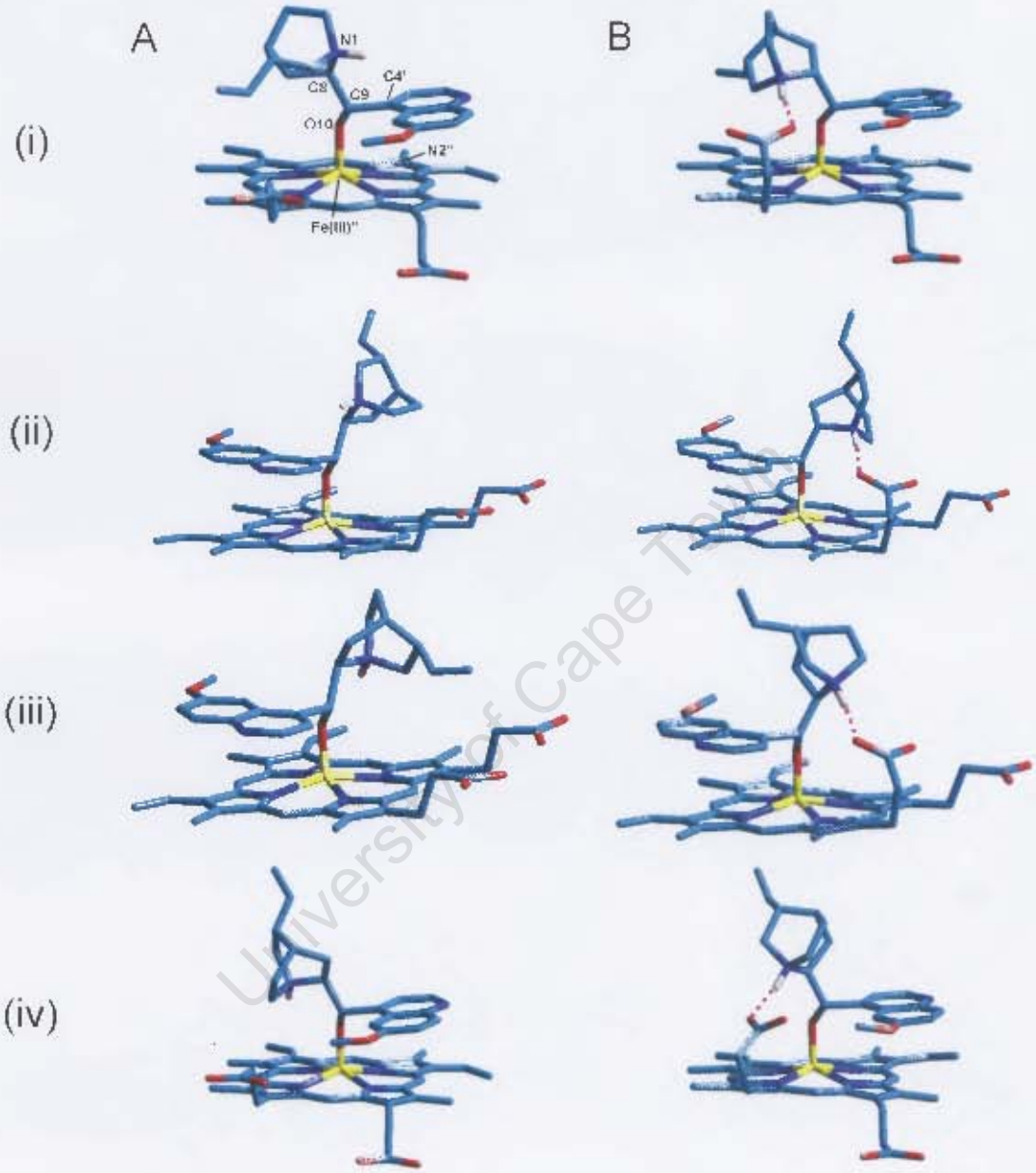

Figure 6.13 (A) Models of the lowest energy conformations of Fe(III)PPIX complexes with (i) quinidine (QD), (ii) quinine (QN), (iii) 9-epiquinidine (eQD) and (iv) 9-epiquinine (eQN). (B) The strained conformations required for the formation of an intramolecular, charge-assisted hydrogen bond (pink dashed line). The numbering scheme relevant for the identification of φ and ψ is shown in A (i). Atom colour coding: cyan – C, yellow – Fe, blue – N and red – O.

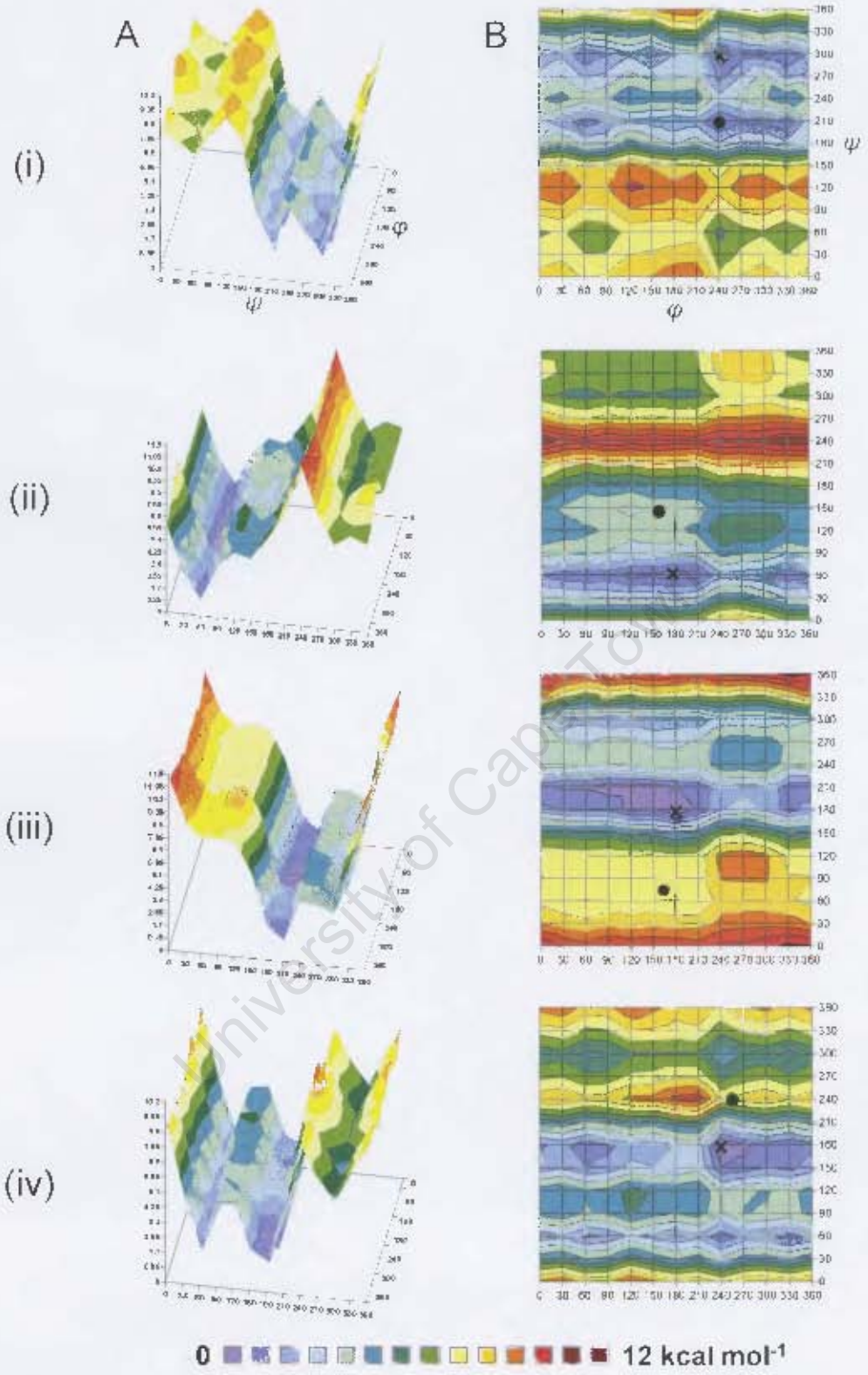

Figure 6.14 Relative strain energy surfaces (A) and contour plots (B) for rotation about the torsion angles φ and ψ in the complexes of Fe(III)PPIX (i) –QD, (ii) –QN, (iii) –eQD and (iv) –eQN. The position of the minimum energy conformation (×) and that required for the formation of the intramolecular, charge-assisted hydrogen bond (•) are indicated on the contour plots.

As can be seen from the energy surfaces above, the conformations required for the formation of an intramolecular, charge-assisted hydrogen bond are close to local energy minima in the case of Fe(III)PPIX–QD and –QN, while close to energy maxima in the case of Fe(III)PPIX–eQD and –eQN. The difference in energy (ΔE) between the minimum energy conformation and the conformation required for the formation of the intramolecular, charge-assisted hydrogen bond was determined in each case (Table 6.13).

Table 6.13 The energy penalty (ΔE) for the formation of an intramolecular, charge-assisted hydrogen bond in the Fe(III)PPIX–alkaloid complexes

ALKALOID	QD	QN	EQD	EQN
E(strained)	35.691345	37.904392	40.787464	44.347370
E(minimum)	31.489590	31.849438	30.602007	33.084751
ΔE / kcal mol^{-1}	4.202	6.055	10.185	11.263

Interestingly, the differences in strain energy show a linear correlation with the biological activity[121] (Figure 6.15) and parallel the inverse of the β-haematin inhibitory activities[128] of the four *Cinchona* alkaloids.

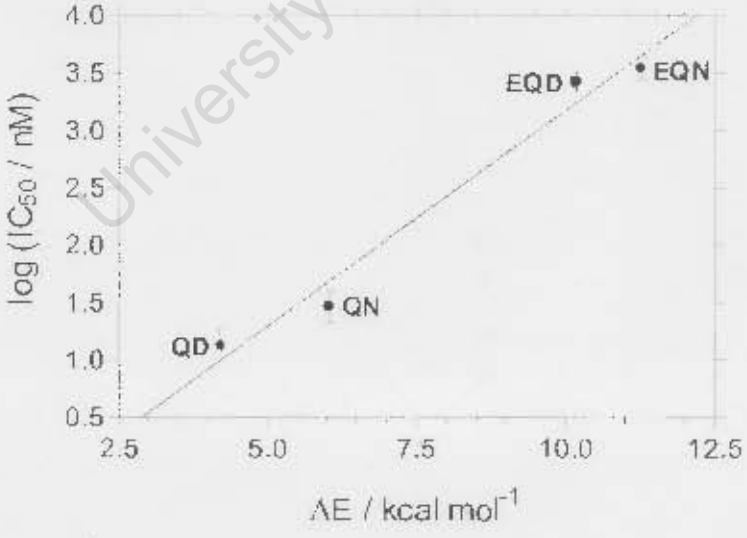

Figure 6.15 The correlation between the strain energy penalty (ΔE) for the formation of an intramolecular, charge-assisted hydrogen bond and the biological activities[127] of the four *Cinchona* alkaloids.

6.4 DISCUSSION

The lipid/water interface model was initially developed in order to probe the mechanism of β-haematin formation, as a means of understanding the role of lipids in the formation of haemozoin *in vivo*. Expanding the scope of this model, the β-haematin inhibitory activities of various antimalarial compounds were investigated in this work under conditions that mimic the biological environment where haemozoin is formed. While the outcome of the inhibition study at the lipid/water interface cannot directly explain the mechanism of inhibition, the results do correlate with biological activity and seem to attest to the role of lipids in the process.

The Raman spectra demonstrate that in the presence of antimalarial compounds, the product obtained at the lipid(MMG)/water interface is not β-haematin. The intensity profile of certain A_{1g} and B_{1g} modes in the spectra of Fe(III)PPIX and its complexes with CQ and QN relative to β-haematin has been observed previously.[286] In 2004, Wood et al.[218] proposed an exciton theory to explain the significant enhancement of certain vibrational modes in haemozoin/ β-haematin that were not expected to give rise to resonance enhancement upon excitation at near infrared wavelengths. It was based on the supposition that electronic energy in the form of an exciton could propagate through aggregated haemozoin/β-haematin in a z-polarised (perpendicular to the porphyrin plane) direction giving rise to Aggregated Enhanced Raman Scattering (AERS).[289] The reduced intensity of certain bands, particularly of ν_{10}, the electron density marker band (1376 cm^{-1}), in the presence of antimalarial drugs has been explained on the basis of these molecules acting as "molecular spacers" that interrupt the propagation of the exciton.[286] The extent of reduction has been taken to be an indicator of the relative intensity of $\pi - \pi$ interactions between the drugs and the porphyrin. An interesting observation is that for the four A_{1g} and two B_{1g} modes investigated, the intensity profiles of the bands belonging to Fe(III)PPIX–CQ and Fe(III)PPIX–QN are similar to that of Fe(III)PPIX, while quite distinct from β-haematin. This may provide further indirect evidence in favour of the $\pi - \pi$ (or stacked) model of Fe(III)PPIX dimerisation as opposed to one containing a covalent linkage (i.e. a μ-oxo dimer).

The influence of $\pi - \pi$ interactions is further supported by the results of the PCA analysis. As indicated by the scores plot in each case, there is clear separation of the drug-affected material from either of the controls (Fe(III)PPIX, **0**, or β-haematin, **b**) along PC1. The strong positive loadings indicate bands belonging to the controls, and in all cases reflect small wavenumber shifts (0 – 4 cm^{-1}) compared to their characteristic positions in the average spectra of Fe(III)PPIX and β-haematin. Wavenumber shifts of 2 – 3 cm^{-1} are indicative of non-covalent (probably $\pi - \pi$) interactions. Indeed, the results of a polarisation-resolved resonance Raman investigation of the interactions between Fe(III)PPIX and CQ have confirmed such behaviour.[156] This result at first appears contradictory to the computational work reported in this chapter in which coordination of the Fe(III) centre by the hydroxyl oxygen atom is assumed in the Fe(II)PPIX complexes of the *Cinchona* alkaloids. However, it is reasonable to assume that wavenumber shifts of a similar magnitude would be obtained if coordination of the Fe(III) centre took place via the hydroxyl group of an aryl methanol antimalarial compound. Such coordination would alter the coordination sphere of the Fe(III) centre only slightly, given that the axial H_2O/HO^- ligand would be displaced in favour of coordination via the very similar hydroxyl (alkoxide) oxygen atom of the drug. Thus only $\pi - \pi$ interactions between the porphyrin and the aromatic ring system of the drug molecule would be the main distinction between the free molecule and the Fe(III)PPIX–drug complex. Since the profiles of drug-affected material compared to both Fe(III)PPIX and β-haematin exhibit these small wavenumber shifts, the PCA results determined in this work can not be used to conclusively establish the target of the antimalarial drugs CQ and QN and hence their mode of action.

The IC_{50} data obtained for the inhibition of β-haematin at the MMG/water interface exhibit a reasonable correlation to previously determined biological activities against malaria parasites,[125] albeit there are large associated errors with individual data points. The methodology adopted in the current work allowed for a period of equilibration prior to the introduction of Fe(III)PPIX to the lipid/water interface. It was reasoned that this time should allow drug molecules to partition into the lipid layer. However, antimalarial drugs accumulate in the digestive food vacuole via pH trapping to different degrees.[101] The results may have been further complicated owing to difficulties experienced in solubilising the Fe(III)PPIX–drug complexes in

some instances as well as obtaining the MMG/water interface reproducibly in each experiment. Halofantrine (Hf), a particularly insoluble compound, has for example, given rise to inconsistent results in the past, some authors reporting very strong activity[132] while others have reported extremely weak activity.[125] Given its insolubility in aqueous solution, Hf was not included in the inhibition study reported in this work. However, its insolubility properties were likely exploited in obtaining the crystal structure of its complex with Fe(III)PPIX. The amount of Hf present during the incubation had been calculated according to the total volume of the system. However, assuming that the drug was concentrated in the lipid layer, the amount present represents a ratio of 2.5 equivalents relative to Fe(III)PPIX. The presence of a large excess of Hf has been shown to cause false negative readings when assayed using 5% (v/v) aqueous pyridine owing to low solubility of its Fe(III)PPIX complex.[132] Based on the Fe–O coordination observed in the crystal structure, it is possible that the Fe(III)PPIX–drug complex is no longer soluble in the aqueous pyridine solution. This is offered as a plausible explanation for the difficulties experienced in solubilising some Fe(III)PPIX–drug complexes at high drug concentrations.

The crystal structure of the Fe(III)PPIX–Hf complex obtained in this work is the first example of its kind. It demonstrates several features that have been matters of speculation in the past:

i. The drug is complexed to monomeric Fe(III)PPIX and not a μ-oxo dimer as some have suggested.[38,162,167] This lends further support to the earlier evidence in this work that Fe(III)PPIX does not form a μ-oxo dimer in aqueous solution, but rather a $\pi - \pi$ dimer. This is probably split apart by the drug in order to form a 1:1 Fe(III)PPIX complex.
ii. The iron porphyrin is five-coordinate.
iii. Halofantrine, an example of an aryl methanol antimalarial, coordinates to the Fe(III) centre of the porphyrin as has been suggested for the QN complex of Fe(III)PPIX by several authors,[142,144,158] rather than associating with Fe(III)PPIX exclusively through intermolecular $\pi - \pi$ interactions.
iv. The experimentally observed Fe(III)–O bond length (1.840(4) Å) indicates conclusively that the alcohol functional group of Hf is deprotonated,

resulting in an alkoxide species. This has been suggested previously in the case of QN.[144,158] When not complexed to Fe(III)PPIX, the pK_a of the alcohol functional group is expected to be similar to that of benzyl alcohol (approximately 14.3[290]), and thus the presence of an alkoxide at the acidic pH of the digestive food vacuole (*in vivo*) does not at first seem likely. However, in support of the existence of the alkoxide is the fact that the crystal was not obtained under strongly basic conditions. Indeed, the complex is neutral in the crystal structure: the quinuclidine tertiary amino group is protonated while one propionic acid group is protonated and the other not. Thus, the interpretation of this observation is that the pK_a of the alkoxide is depressed below that of the propionic acid group (probably approximately 5 – 6 in free Fe(III)PPIX[291]) upon coordination to the metal centre.

While the crystal structure of Fe(III)PPIX–Hf is unable to unequivocally predict analogous behaviour for antimalarial compounds that do not possess an alcohol functional group, it may certainly provide a model for the interaction of other aryl methanol antimalarials with Fe(III)PPIX, as has been assumed for the *Cinchona* alkaloids in this work. The strikingly similar spectroscopic changes observed for Fe(III)PPIX in acetonitrile, upon titration with both the free bases of Hf and QD, provide support for this contention. Acetonitrile provides a relevant model for the non-aqueous, aprotic environment of a lipid body, where it seems likely that haemozoin formation takes place.[74] Whilst antimalarial drugs in the digestive food vacuole of the malaria parasite accumulate in their protonated form due to pH trapping,[176] it is likely that the drug would enter the lipid body in a neutral, unprotonated state.

As previously indicated, the *Cinchona* alkaloids (QN, QD, eQN and eQD) differ only in their relative stereochemistry at C8 and C9, and owing to their distinctly different β-haematin inhibitory activities thus present a unique opportunity to investigate the relationship between structure and activity. Previous work has recognised the differences in the conformation of the alkaloids themselves[121,168] and the orientation of the N1–H^+ dipoles in models of their coordination complexes with Fe(III)PPIX.[128] While Warhurst et al. suggested that coordination takes place

via the alkoxide,[128] some authors have suggested different ligand binding modes, for example via the quinoline nitrogen atom.[169] To date however, no results have offered a compelling explanation for the markedly different activities of the four alkaloids.

The molecular mechanics investigation of the four Fe(III)PPIX–alkaloid complexes carried out in this work led to the determination of the energy penalty required for each complex to achieve a conformation in which an intramolecular, charge-assisted hydrogen bond can form between the protonated quinuclidine amine and the porphyrin propionate group. As has been shown, the energy penalties show a linear correlation with the biological activities of the four *Cinchona* alkaloids.

The possible role of the intramolecular, charge-assisted hydrogen bond in promoting the activity of QD and QN compared to their epimers can be rationalised in terms of a proposed mechanism of haemozoin formation at the lipid/water interface.[73] The magnitude of the association constants for the formation of complexes between Fe(III)PPIX and the *Cinchona* alkaloids in 40% (v/v) aqueous DMSO[123,126,151] suggests that both the active and the inactive alkaloids are able to form complexes with Fe(III)PPIX in solution, from which one can conclude that while association with Fe(III)PPIX is necessary, it is not sufficient to inhibit haemozoin/β-haematin formation.[123,127] Given the evidence that Fe(III)PPIX molecules form aggregates with the Fe(III)PPIX–QN complex in aqueous solution,[124] and the evidence in support of an Fe(III)PPIX $\pi - \pi$ dimer, it can be assumed that the complexes probably exist as $\pi - \pi$ dimers as shown (Scheme 6.1, **1** and **5**). Water molecules in the bulk environment satisfy the hydrogen bonding potential of the protonated quinuclidine amine and porphyrin propionate groups. Upon entering a lipid environment, the complexes of the inactive alkaloids are able to proceed to the formation of the haemozoin precursor as normal (**2**). Given the large energy penalty for the formation of an intramolecular, charge-assisted hydrogen bond, the propionate groups are expected to remain free to coordinate Fe(III), at which point the alkaloids would be displaced from their axial positions (**3**). Thus haemozoin formation is expected to proceed as normal (**4**) in the presence of the inactive alkaloids eQD and eQN. In the case of the Fe(III)PPIX complexes of the active alkaloids, QD and QN, the likelihood of formation of an

intramolecular, charge-assisted hydrogen bond is greater given the smaller energy penalty. Thus it is rationalised that the formation of the intramolecular, charge-assisted hydrogen bond stabilises the Fe(III)PPIX–alkaloid complex (**6**), either making the propionate groups unavailable for haemozoin precursor formation or preventing Fe(III)PPIX incorporation into haemozoin so that haemozoin formation is inhibited. An early study by Warhurst corroborates the differing behaviour of the active and inactive alkaloids in a non-aqueous, hydrophobic environment.[157] By monitoring changes in the visible spectrum of Cl-Fe(III)PPIX (haemin) in benzene, he showed that QN interacts and forms a complex with the porphyrin, while eQN is unable to do so, in contrast to the aqueous environment where both form almost equally strong complexes.

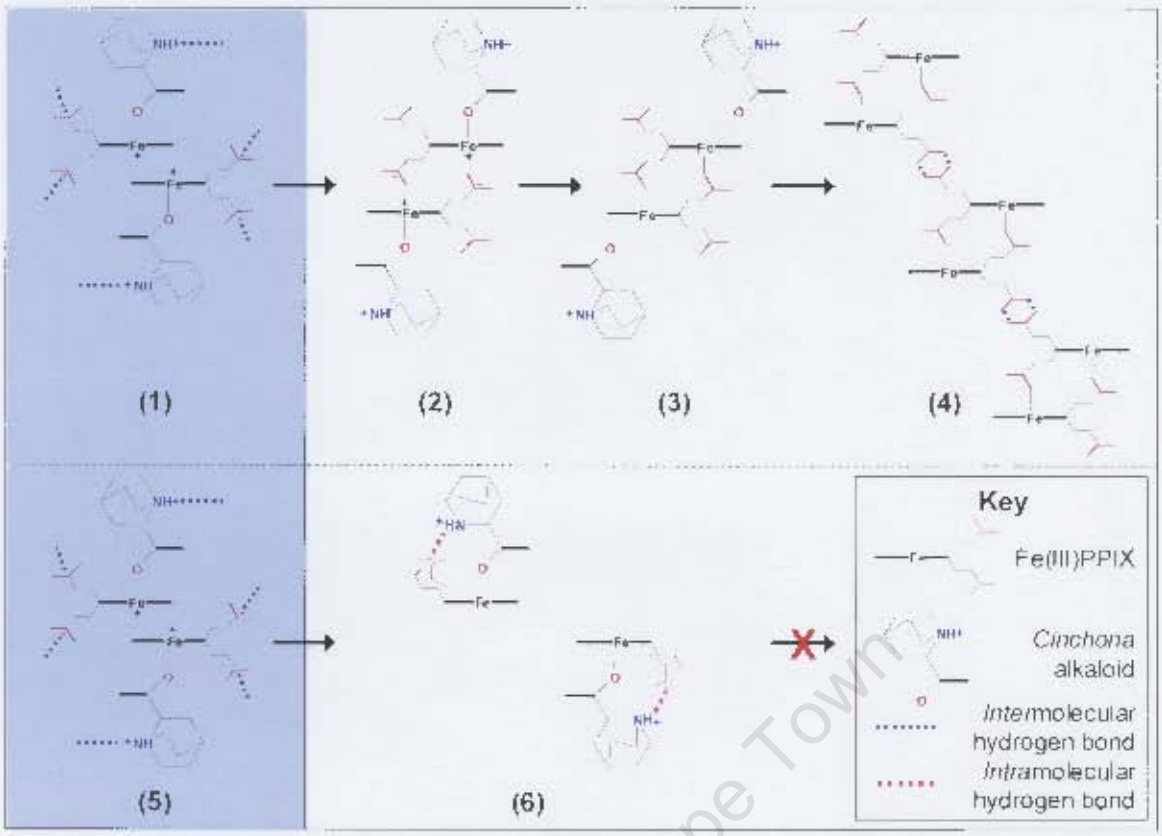

Scheme 6.1 The proposed mechanism of haemozoin inhibition by the *Cinchona* alkaloids. The various stages represent (**1**) the Fe(III)PPIX complexes of the *inactive* alkaloids, 9-epiquinidine and 9-epiquinine in aqueous solution, (**2**) the haemozoin precursor dimer with inactive alkaloids as axial ligands, (**3**) the haemozoin dimer, (**4**) haemozoin crystal assembly, (**5**) the Fe(III)PPIX complexes of the *active* alkaloids, quinidine and quinine in aqueous solution and (**6**) the Fe(III)PPIX complexes of the *active* alkaloids in a lipid environment, stabilised by an intramolecular, charge-assisted hydrogen bond.

6.5 CONCLUSION

On the basis of a lipid environment having been identified as important for the formation of haemozoin/β-haematin, drug inhibition of this process is more than likely to take place in the same non-aqueous, hydrophobic environment.[87] The crystal structure of the Fe(III)PPIX-halofantrine complex has revealed insight into the structural binding mode of this class of antimalarial drug. The application of these features to the Fe(III)PPIX complexes of the *Cinchona* alkaloids, which were modelled on the basis that they would occur in a lipid environment, has lead to the determination of a new model that is able, for the first time, to explain the relative activities of the four alkaloids. The three-point mode of interaction involves (i) coordination of the hydroxyl (alkoxide) group of the drug to the Fe(III) centre of the porphyrin, (ii) π-stacking between the drug and porphyrin planar aromatic ring systems and (iii) intramolecular, charge-assisted hydrogen bonding between the drug ($N–H^+$) and the porphyrin propionate group (COO^-). Charge-assistance is well known to augment the directing effects of strong hydrogen bonds, and is a common tool in the hands of the crystal engineer.[292] In the same way, exploitation of the three-point model determined in this work may indeed provide a novel pathway for the rational design of antimalarial compounds. The advantage of this model is that aromatic rings other than the quinoline nucleus could be incorporated, thus increasing the chemical diversity of chemotherapeutic agents.

7. OVERALL CONCLUSIONS AND FUTURE WORK

7.1 OVERALL CONCLUSIONS

Malaria infection is characterised by the appearance of crystals of malaria pigment (haemozoin) within parasitised erythrocytes. This pigment is the metabolic by-product of haemoglobin degradation during which toxic quantities of Fe(III)PPIX are released into the aqueous environment inside the digestive food vacuole. The mechanism by which Fe(III)PPIX is incorporated into haemozoin relies on a correct structural interpretation of the speciation of Fe(III)PPIX in solution. While several studies have claimed that Fe(III)PPIX exists in aqueous solution as large aggregates,[36,37,39,40] a careful study by Brown et al.[41] demonstrated that this species is in fact only a dimer. The authors maintained that Fe(III)PPIX is present as a μ-oxo dimer in which two high-spin Fe(III) porphyrins are covalently bonded via an Fe–O–Fe linkage. While this interpretation became popularly cited, it fails to provide a rational explanation of how Fe(III)PPIX might proceed to haemozoin formation, as the Fe(III) coordination sites are not available. While some authors have proposed that the μ-oxo dimer exists in equilibrium with monomeric Fe(III)PPIX which is readily incorporated into haemozoin,[167,272] it is difficult then to relate this to the mechanism of its formation. In the current study, owing to improved instrument sensitivity and the development of non-linear least squares fitting algorithms in the intervening years, a reinvestigation of the data presented by Brown and co-workers was undertaken. The spectrophotometric results obtained are supported by diffusion measurements and confirm that Fe(III)PPIX indeed exists in aqueous solution as a dimer. However, subsequent spectroscopic and magnetic susceptibility studies do not support the contention that Fe(III)PPIX is present as a μ-oxo dimer. Rather, a new model of dimerisation is presented in which two high-spin Fe(III) porphyrins interact in a back-to-back manner through $\pi - \pi$ stacking and have their axial H_2O/HO^- ligands directed outwards. The formation of the haemozoin bicyclic dimer from the Fe(III)PPIX $\pi - \pi$ dimer requires only a lateral shift of the two porphyrins followed by coordination of the propionate groups to the neighbouring Fe(III) centre and subsequent release of the axial H_2O/HO^- ligands from the opposite face of the porphyrin.

Two studies have recently implicated the aqueous/lipid interface region as important in the formation of haemozoin and its synthetic counterpart β-haematin.[73,74] However, neither has been able to explain the role of the lipid molecules in the mechanism of crystallisation. The biomineralisation of haemozoin infers the need for a site of nucleation. In the present study, grazing incidence X-ray diffraction and X-ray reflectivity measurements were undertaken using a liquid surface diffractometer in order to investigate the possible role of the hydrophilic head groups of lipid molecules in nucleating and orientating β-haematin at the lipid/water interface. Experiments performed in the absence of an interface did not yield β-haematin, thus corroborating the importance of the interface. In the presence of the lipid, which on its own forms an ordered monolayer at the water surface, β-haematin formation was confirmed by the presence of characteristic diffraction peaks, albeit weak. Specifically, the data indicate that β-haematin crystals float on their (100) face at the surface. The molecular consequence of this arrangement is that the carboxylic acid moieties of surface propionic acid groups are exposed at the surface. Molecular complementarity between these groups and the lipid head groups (hydroxyl moieties and oxygen lone pairs) is most likely responsible for nucleating and orienting the β-haematin crystals in the manner observed. Thus crystallisation appears to be a form of epitaxial growth. The present study confirmed the importance of the lipid hydroxyl groups by investigating two molecules that do not possess these. Docosane, a straight chain hydrocarbon, did not promote β-haematin formation, while methyl laurate, which does express a polar ester moiety at the interface, did produce β-haematin but in smaller yield. While the results of the current study are not conclusive in their entirety, they do provide the first tangible insight into the specific role of the lipid/water interface in promoting haemozoin nucleation and orientation.

The large majority of 4-aminoquinoline and aryl methanol antimalarial drugs are believed to target the process of haemozoin formation, either through interaction with Fe(III)PPIX prior to its incorporation into the growing crystal[61,124,125] or with the crystal itself.[97,122] The implication of haemozoin formation taking place in the so-called "oily" environment of the lipid/water interface is that drug activity is likely to take place in the same non-aqueous environment.[87] This necessarily shifts investigations of these processes away from pure aqueous chemistry. The current

work explored the inhibition of β-haematin formation at the lipid/water interface. Experimentally determined drug IC_{50} data were found to correlate with reported biological activity against malaria parasites. However, the relationship between the structure of target–drug complexes and drug activity has not been definitively established from previous inhibition studies. Analysis of the changes in intensity and Raman shifts (as determined by PCA) of key porphyrin signals in the Raman spectra of products recovered directly from the interface suggests that $\pi - \pi$ stacking is important in the interactions between drug molecules and the biological target, either Fe(III)PPIX or β-haematin. However, the crystal structure of the Fe(III)PPIX–halofantrine complex determined in this work has provided more detailed insight into the mode of interaction in the target–drug complex. The target in this case is Fe(III)PPIX, negating the suggestion that drugs only interact directly with haemozoin crystals. While $\pi - \pi$ stacking evidently contributes to complex formation, coordination of the monomeric porphyrin Fe(III) centre by halofantrine via its hydroxyl (alkoxide) moiety appears pivotal. Furthermore, the formation of a drug complex with monomeric Fe(III)PPIX is easily explained from the $\pi - \pi$ model of Fe(III)PPIX dimerisation and not the μ-oxo dimer. Finally, key *inter*molecular hydrogen bonding interactions occurring between the positively charged (protonated) terminal amine of halofantrine and the negatively charged propionate group of Fe(III)PPIX stabilise the solid phase crystalline structure. However, the formation of haemozoin crystals takes place in solution, not the solid state, where drug molecules will not be in close contact with one another. Thus it is suggested that the hydrogen bonding potential of the protonated terminal amine and propionate groups is likely to actually be satisfied by charge-assisted *intra*- as opposed to *inter*molecular hydrogen bonding. Based on such a model, the results of a computational investigation of the complexes formed between Fe(III)PPIX and the *Cinchona* alkaloids (quinine, quinidine, 9-epiquinine and 9-epiquinidine), in which this three-point model of target–drug interaction was further assessed, indicate that drug activity is directly correlated with the ability of complexes to adopt conformations in which the formation of a charge-assisted *intra*molecular hydrogen bond is possible.

Overall, the work of this thesis project has contributed a correct structural characterisation of ferrihaem (Fe(III)PPIX) in aqueous solution. The $\pi - \pi$ dimer of

Fe(III)PPIX is able to account for the formation of haemozoin crystals at the lipid/water interface and its inhibition by aryl methanol antimalarial drugs, neither of which are easily rationalised when starting from a μ-oxo dimer. The structure of Fe(III)PPIX–halofantrine and modelling of the analogous Fe(III)PPIX–*Cinchona* alkaloid complexes suggest that the interaction of arylmethanol antimalarials with Fe(III)PPIX involves an unexpected three-point interaction, namely $\pi - \pi$ stacking, coordination to the metal centre and hydrogen bonding to the haem propionate group. This model may open the way to the rational design of novel non-quinoline haemozoin-inhibiting antimalarials. The main conclusions reached in this thesis are summarised in Scheme 7.1 below.

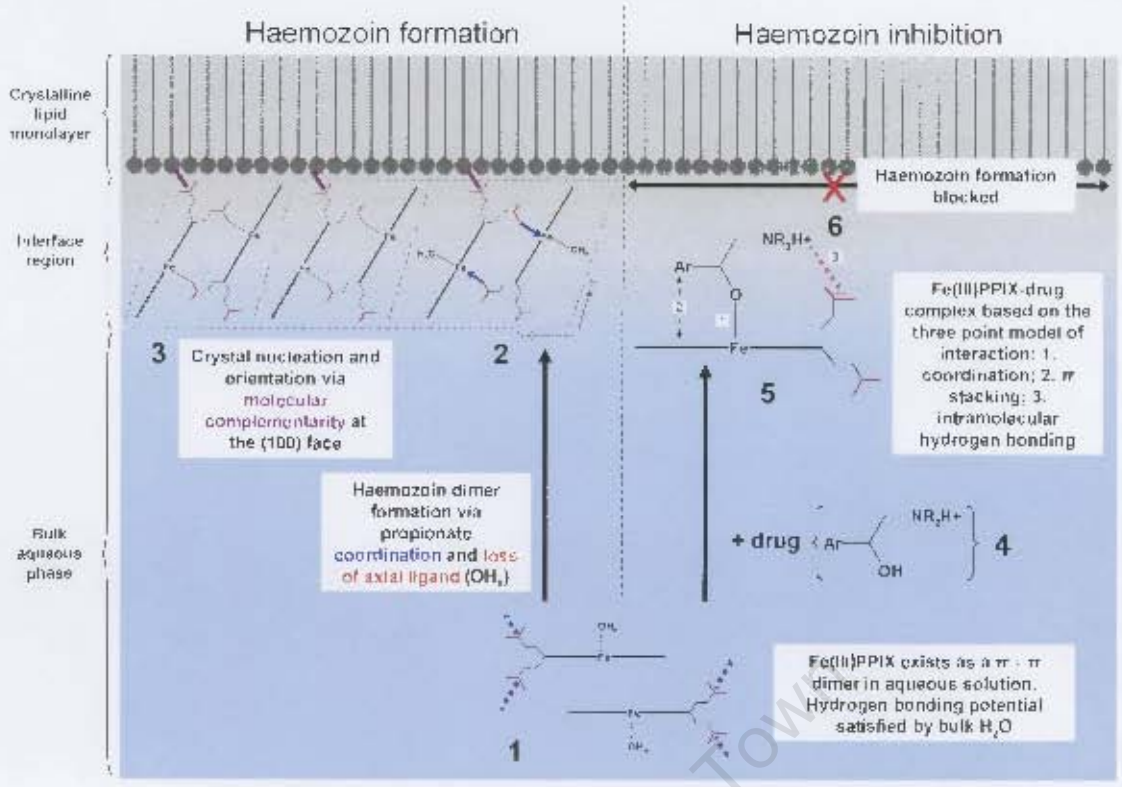

Scheme 7.1 The proposed formation and inhibition by aryl methanol antimalarial drugs of haemozoin at the lipid/water interface. In the bulk aqueous phase, Fe(III)PPIX is believed to exist as a $\pi - \pi$ dimer (**1**) in which the hydrogen bonding potential is satisfied by H_2O molecules. Depending on pH, the axial ligand (OH_n) can exist as water (OH_2, n = 2) or hydroxyl (OH, n = 1). In the absence of drug, movement of Fe(III)PPIX into the interface region favours the formation of the haemozoin dimer (**2**) via propionate coordination (blue arrows) and loss of the axial H_2O/HO ligands (orange bonds). Crystal nucleation and orientation (**3**) occurs via molecular complementarity (purple) between lipid hydroxyl and haemozoin surface propionic acid groups. In the presence of an aryl methanol antimalarial drug (**4**), which is able to interact with Fe(III)PPIX according to the determined three-point model (**5**), haemozoin formation is inhibited (**6**).

7.2 FUTURE WORK

The results of the work presented in Chapter 4 regarding the speciation of Fe(III)PPIX in aqueous solution have overturned the widely accepted view that Fe(III)PPIX is present as a μ-oxo dimer under these conditions. However, while this current study has shown that Fe(III)PPIX exists rather as a $\pi - \pi$ dimer, further investigations are required in order to understand the conditions under which Fe(III)PPIX forms a μ-oxo dimer. The following studies are proposed:

i. In light of the green μ-oxo dimer precipitate obtained by Brown et al.[44] from basified DMSO, it would be useful to perform a thorough and systematic UV-vis spectroscopic investigation of the ability of different solvents, both protic and aprotic, to induce μ-oxo dimer formation. In addition, magnetic susceptibility measurements could be used to confirm the speciation of Fe(III)PPIX.

ii. Based on the observation by Blauer and Zvilichovsky[37] of a green complex of Fe(III)PPIX in 1.2 M NaCl, investigation of the effects of high ionic strength on the speciation of Fe(III)PPIX in solution. Furthermore, given that these authors proposed aggregates of between 45 – 50 molecules, diffusion measurements would be complementary.

According to the evidence presented in Chapter 5, β-haematin crystals are nucleated at the MMG/water interface via their (100) face as a result of molecular complementarity between the lipid –OH groups and β-haematin surface propionic acid groups. Supporting studies performed at the methyl laurate/water interface indicate that β-haematin crystals do form, however in lower yield. In order to explore the role of molecular complementarity in directing the orientation of β-haematin crystals, the following studies are proposed:

iii. To investigate the orientating effects of MPG and MSG, the two lipid molecules that have been isolated in association with native haemozoin crystals from *P. falciparum*.[74]

iv. To investigate the ability of lipid-type analogues, but which lack the proposed essential –OH groups, to nucleate β-haematin, and to perform grazing incidence X-ray diffraction and X-ray reflectivity measurements of β-haematin formed at an interface created using such molecules in order to determine whether the preferred orientation differs from the (100) face.

Based on the crystal structure of the Fe(III)PPIX–halofantrine complex, a three-point model of drug–target interaction was proposed in Chapter 6 for aryl methanol antimalarial drugs. Theoretical calculations of the analogous complexes formed with the *Cinchona* alkaloids were further presented as a means of validating this model. The ability of a charge-assisted intramolecular hydrogen bond to form

between the protonated terminal amine of the drug side chain and the deprotonated porphyrin propionate was considered important for an active compound. In order to verify these speculations, the following studies are proposed:

v. To continue ongoing experimental efforts to crystallise the Fe(III)PPIX complexes of the *Cinchona* alkaloids in order to verify whether coordination takes place in an analogous manner to halofantrine.

vi. To investigate experimental methods that would be sensitive enough to distinguish an *intra*molecular hydrogen bond in such complexes. It would be preferable that such investigations be carried out in solution as opposed to the solid phase in order to decrease the likelihood of *inter*molecular hydrogen bonding as observed in the crystal structure of Fe(III)PPIX–Hf. Resonance Raman spectroscopy has been used previously to determine hydrogen bonding in solution-phase bilirubin/lipid complexes[293] and between imidazoles and (octaethylporphinato)iron(III)[294] for example, suggesting that this may be a suitable method.

vii. To synthesise novel molecules designed according to the three-point model of interaction and test their antimalarial activity against *P. falciparum* as well as their ability to inhibit β-haematin formation.

8. REFERENCES

(1) Sherman, I. W. In *Malaria: Parasite biology, pathogenesis and protection*; Sherman, I. W., Ed.; ASM Press: Washington D.C., **1998**.

(2) Bruce-Chwatt, L. J. In *Malaria. Principles and practice of malariology*; Wernsdorfer, W., McGregor, I., Eds.; Churchill Livingstone: Edinburgh, **1988**; Vol. 1.

(3) Lancisi, G. M. *De noxiis paludum effluvius eorumque remediis*; Salvioni, J M: Rome, **1717**.

(4) Laveran, C. L. A. *A newly discovered parasite in the blood of patients suffering from malaria. Parasitic etiology of attacks of malaria*; Cornell University Press: Ithaca, New Yorc, **1978**.

(5) Ross, R. *Br. Med. J.* **1897**, *ii*, 1736-1788.

(6) World Health Organisation, World Malaria Report,; www.rbm.who.int/wmr 2005.html, accessed on 23/01/08.

(7) Sachs, J.; Malaney, P. *Nature* **2002**, *415*, 680-685.

(8) Nchinda, T. C. *Emerg. Infect. Dis.* **1998**, *4*, 398-403.

(9) Novartis, Malaria and Health; www.malariaandhealth.com/professional/the _disease/02_worldsmost.htm, accessed on 10/07/2008.

(10) Rosenthal, P. J.; Miller, L. H. In *Antimalarial chemotherapy: Mechanisms of action, resistance, and new directions in drug discovery*; Rosenthal, P. J., Ed.; Humana Press: New Jersey, **2001**.

(11) Lycett, G. J.; Kafatos, F. C. *Nature* **2002**, *417*, 387-388.

(12) Egan, T. J. *Drug Des. Rev.-Online* **2004**, *1*, 93-110.

(13) Bannister, L. H.; Hopkins, J. M.; Fowler, R. E.; Krishna, S.; Mitchell, G. H. *Parasitol. Today* **2000**, *16*, 427-433.

(14) Loria, P.; Miller, S.; Foley, M.; Tilley, L. *Biochem. J.* **1999**, *339*, 363-370.

(15) Egan, T. J.; Combrink, J. M.; Egan, J.; Hearne, G. R.; Marques, H. M.; Ntenteni, S.; Sewell, B. T.; Smith, P. J.; Taylor, D.; van Schalkwyk, D. A.; Walden, J. C. *Biochem. J.* **2002**, *365*, 343-347.

(16) Yayon, A.; Timberg, R.; Friedman, S.; Ginsburg, H. *J. Protozool.* **1984**, *31*, 367-372.

(17) Yayon, A.; Cabantchik, Z. I.; Ginsburg, H. *EMBO J.* **1984**, *3*, 2695-2700.

(18) Krogstad, D. J.; Schlesinger, P. H.; Gluzman, I. Y. *J. Cell Biol.* **1985**, *101*, 2302-2309.

(19) Geary, T. G.; Divo, A. D.; Jensen, J. B.; Zangwill, M.; Ginsburg, H. *Biochem. Pharmacol.* **1990**, *40*, 685-691.

(20) Hayward, R.; Saliba, K. J.; Kirk, K. *J. Cell Sci.* **2006**, *119*, 1016-1025.

(21) Eggleson, K. K.; Duffin, K. L.; Goldberg, D. E. *J. Biol. Chem.* **1999**, *274*, 32411-32417.

(22) Banerjee, R.; Liu, J.; Beatty, W.; Pelosof, L.; Klemba, M.; Goldberg, D. E. *Proc. Natl. Acad. Sci. USA* **2002**, *99*, 990-995.

(23) Rosenthal, P. J.; McKerrow, J. H.; Aikawa, M.; Nagasawa, H.; Leech, J. H. *J. Clin. Invest.* **1988**, *82*, 1560-1566.

(24) Goldberg, D. E.; Slater, A. F. G.; Cerami, A.; Henderson, G. B. *Proc. Natl. Acad. Sci. USA* **1990**, *87*, 2931-2935.

(25) Olliaro, P. L.; Yuthavong, Y. *Pharmacol. Ther.* **1999**, *81*, 91-110.

(26) Liu, J.; Istvan, E. S.; Gluzman, I. Y.; Gross, J.; Goldberg, D. E. *Proc. Natl. Acad. Sci. USA* **2006**, *103*, 8840-8845.

(27) Krugliak, M.; Zhang, J.; Ginsburg, H. *Mol. Biochem. Parasitol.* **2002**, *119*, 249-256.

(28) Jackson, K. E.; Klonis, N.; Ferguson, D. J. P.; Adisa, A.; Dogovski, C.; Tilley, L. *Mol. Microbiol.* **2004**, *54*, 109-122.

(29) Lew, V. L.; Tiffert, T.; Ginsburg, H. *Blood* **2003**, *101*, 4189-4194.

(30) Chou, A. C.; Fitch, C. D. *J. Clin. Invest.* **1980**, *66*, 856-858.

(31) Sugioka, Y.; Suzuki, M. *Biochim. Biophys. Acta* **1991**, *1074*, 19-24.

(32) Brown, W. *J. Exp. Med.* **1911**, *13*, 290-299.

(33) Hänscheid, T.; Egan, T. J.; Grobusch, M. P. *The Lancet* **2007**, *7*, 675-685.

(34) Ziele, K.; Reuter, F. *Z. Physiol. Chem.* **1933**, *221*, 101.

(35) Haurowitz, F. *Z. Physiol. Chem.* **1938**, *254*, 266.

(36) Shack, J.; Clark, W. M. *J. Biol. Chem.* **1947**, *171*, 143-187.

(37) Blauer, G.; Zvilichovsky, B. *Arch. Biochem. Biophys.* **1968**, *127*, 749-755.

(38) Moreau, S.; Perly, B.; Biguet, J. *Biochimie* **1982**, *64*, 1015-1025.

(39) Srinivas, V.; Rao, C. M. *Biochem. Int.* **1990**, *21*, 849-855.

(40) Kuzelova, K.; Mrhalova, M.; Hrkal, Z. *Biochim. Biophys. Acta* **1997**, *1336*, 497-501.

(41) Brown, S. B.; Dean, T. C.; Jones, P. *Biochem. J.* **1970**, *117*, 733-739.

(42) Inada, Y.; Shibata, K. *Biochem. Biophys. Res. Commun.* **1962**, *9*, 323-327.

(43) Brown, S. B.; Lantzke, I. R. *Biochem. J.* **1969**, *115*, 279-285.

(44) Brown, S. B.; Jones, P.; Lantzke, I. R. *Nature* **1969**, *223*, 960-961.

(45) Hewkin, D. J.; Griffith, W. P. *J. Chem. Soc.* **1966**, *A*, 472-475.

(46) Cheng, L.; Lee, J.; Powell, D. R.; Richter-Addo, G. B. *Acta Cryst.* **2004**, *E60*, m1340-m1342.

(47) Fleischer, E. B.; Srivastava, T. S. *J. Am. Chem. Soc.* **1969**, *91*, 2403-2405.

(48) O'Keeffe, D. H.; Barlow, C. H.; Smythe, G. A.; Fuchsman, W. H.; Moss, T. H.; Lilienthal, H. R.; Caughey, W. S. *Bioinorg. Chem.* **1975**, *5*, 125-147.

(49) Yamada, K. A.; Sherman, I. W. *Expt. Parasitol.* **1979**, *48*, 61-74.

(50) Ashong, J. O.; Blench, I. P.; Warhurst, D. C. *Trans. R. Soc. Trop. Med. Hyg.* **1989**, *83*, 167-172.

(51) Fitch, C. D.; Kanjananggulpan, P. *J. Biol. Chem.* **1987**, *262*, 15552-15555.

(52) Brémard, C.; Girerd, J. J.; Kowalewski, P.; Merlin, J. C.; Moreau, S. *Appl. Spectrosc.* **1993**, *47*, 1837-1842.

(53) Slater, A. F. G.; Swiggard, W. J.; Orton, B. R.; Flitter, W. D.; Goldberg, D. E.; Cerami, A.; Henderson, G. B. *Proc. Natl. Acad. Sci. USA* **1991**, *88*, 325-329.

(54) Bohle, D. S.; Debrunner, P.; Jordan, P. A.; Madsen, S. K.; Schulz, C. E. *J. Am. Chem. Soc.* **1998**, *120*, 8255-8256.

(55) Hamsik, A. *Z Physiol Chem* **1936**, *241*, 156-167.

(56) Bohle, D. S.; Dinnebier, R. E.; Madsen, S. K.; Stephens, P. W. *J. Biol. Chem.* **1997**, *272*, 713-716.

(57) Pagola, S.; Stephens, P. W.; Bohle, D. S.; Kosar, A. D.; Madsen, S. K. *Nature* **2000**, *404*, 307-310.

(58) Bohle, D. S.; Helms, J. B. *Biochem. Biophys. Res. Commun.* **1993**, *193*, 504-508.

(59) Blauer, G.; Akkawi, M. *Arch. Biochem. Biophys.* **2002**, *398*, 7-11.

(60) Huy, N. T.; Maeda, A.; Uyen, D. T.; Trang, D. T. X.; Sasai, M.; Shiona, T.; Oida, T.; Harada, S.; Kamei, K. *Acta Trop.* **2007**, *101*, 130-138.

(61) Egan, T. J.; Ross, D. C.; Adams, P. A. *FEBS Lett.* **1994**, *352*, 54-57.

(62) Egan, T. J.; Tshivase, M. G. *Dalton Trans.* **2006**, 5024-5032.

(63) Egan, T. J.; Mavuso, W. W.; Ncokazi, K. K. *Biochemistry* **2001**, *40*, 204-213.

(64) Ziegler, J.; Chang, R. T.; Wright, D. W. *J. Am. Chem. Soc.* **1999**, *121*, 2395-2400.

(65) Hempelmann, E.; Egan, T. J. *Trends Parasitol.* **2002**, *18*, 11.

(66) Slater, A. F. G.; Cerami, A. *Nature* **1992**, *355*, 167-169.

(67) Chou, A. C.; Fitch, C. D. *Life Sci.* **1992**, *51*, 2073-2078.

(68) Dorn, A.; Stoffel, R.; Matile, H.; Bubendorf, A.; Ridley, R. G. *Nature* **1995**, *374*, 269-271.

(69) Pandey, A. V.; Tekwani, B. L. *FEBS Lett.* **1996**, *393*, 189-192.

(70) Sullivan, D. J. J.; Gluzman, I. Y.; Goldberg, D. E. *Science* **1996**, *271*, 219-222.

(71) Jani, D.; Nagarkatti, R.; Beatty, W.; Angel, R.; Slebodnick, C.; Andersen, J.; Kumar, S.; Rathore, D. *PLoS Pathog.* **2008**, *4*, e1000053.

(72) Coppens, I.; Vielemayer, O. *Int. J. Parasitol.* **2005**, *35*, 597-615.

(73) Egan, T. J.; Chen, J. Y.-J.; de Villiers, K. A.; Mabotha, T. E.; Naidoo, K. J.; Ncokazi, K. K.; Langford, S. J.; McNaughton, D.; Pandiancherri, S.; Wood, B. R. *FEBS Lett.* **2006**, *580*, 5105-5110.

(74) Pisciotta, J. M.; Coppens, I.; Tripathi, A. K.; Scholl, P. F.; Shuman, J.; Bajad, S.; Shulaev, V.; Sullivan, D. J. J. *Biochem. J.* **2007**, *402*, 197-204.

(75) Pandey, A. V.; Babbarwal, V. K.; Okoyeh, J. N.; Joshi, R. M.; Puri, S. K.; Singh, R. L.; Chauhan, V. S. *Biochem. Biophys. Res. Commun.* **2003**, *308*, 736-743.

(76) Wellems, T. E.; Howard, R. J. *Proc. Natl. Acad. Sci. USA* **1986**, *83*, 6065-6069.

(77) Pandey, A. V.; Joshi, R. M.; Tekwani, B. L.; Singh, R. L.; Chauhan, V. S. *Mol. Biochem. Parasitol.* **1997**, *90*, 281-287.

(78) Papalexis, V.; Siomos, M.-A.; Campanale, N.; Guo, X.-G.; Kocak, G.; Foley, M.; Tilley, L. *Mol. Biochem. Parasitol.* **2001**, *115*, 77-86.

(79) Sullivan, D. J. J. *Int. J. Parasitol.* **2002**, *32*, 1645-1653.

(80) Healy, G. R.; Ruebush, T. K. *Am. J. Clin. Pathol.* **1980**, *73*, 107-109.

(81) Egan, T. J. *Mol. Biochem. Parasitol.* **2008**, *157*, 127-136.

(82) Bendrat, K.; Berger, B. J.; Cerami, A. *Nature* **1995**, *378*, 138.

(83) Ridley, R. G.; Dorn, A.; Matile, H.; Kansy, M. *Nature* **1995**, *378*, 138-139.

(84) Fitch, C. D.; Cai, G.-z.; Chen, Y.-F.; Shoemaker, J. D. *Biochim. Biophys. Acta* **1999**, *1454*, 31-37.

(85) Fitch, C. D.; Cai, G.-z.; Shoemaker, J. D. *Biochim. Biophys. Acta* **2000**, *1535*, 45-49.

(86) Oliveira, M. F.; Kycia, S. W.; Gomez, A.; Kosar, A. J.; Bohle, D. S.; Hempelmann, E.; Menezes, D.; Vannier-Santos, M. A.; Oliveira, P. L.; Ferreira, S. T. *FEBS Lett.* **2005**, *579*, 6010-6016.

(87) Pisciotta, J. M.; Sullivan, D. J. J. *Parasitol. Int.* **2008**, *57*, 89-96.

(88) Weissbuch, I.; Lahav, M.; Leiserowitz, L. *Cryst. Growth Des.* **2003**, *3*, 125-150.

(89) Langmuir, I. *J. Am. Chem. Soc.* **1917**, *39*, 1848-1906.

(90) Lafont, S.; Rapaport, H.; Somjen, G. J.; Renault, A.; Howes, P. B.; Kjaer, K.; Als-Nielsen, J.; Leiserowitz, L.; Lahav, M. *J. Phys. Chem. B* **1998**, *102*, 761-765.

(91) Konikoff, F. M.; Chung, D. S.; Donovan, J. M.; Small, D. M.; Carey, M. C. *J. Clin. Invest.* **1992**, *90*, 1155-1160.

(92) Fairland, F. A.; Sharbaugh, D. M.; Talham, D. R.; Gower, L. B. *Langmuir* **2007**, *23*, 1988-1994.

(93) Jacquemain, D.; Grayer Wolf, S.; Leveiller, F.; Lahav, M.; Leiserowitz, L.; Deutsch, M.; Kjaer, K.; Als-Nielsen, J. *J. Am. Chem. Soc.* **1990**, *112*, 7724-7736.

(94) Jacquemain, D.; Wolf, S. G.; Leveiller, F.; Deutsch, M.; Kjaer, K.; Als-Nielsen, J.; Lahav, M.; Leiserowitz, L. *Angew. Chem. Int. Ed.* **1992**, *31*, 130-152.

(95) Hartman, P.; Perdok, W. G. *Acta Cryst.* **1955**, *8*, 49-52.

(96) Bohle, D. S.; Kosar, A. D.; Stephens, P. W. *Acta Cryst.* **2002**, *D58*, 1752-1756.

(97) Buller, R.; Peterson, M. L.; Almarsson, Ö.; Leiserowitz, L. *Cryst. Growth Des.* **2002**, *2*, 553-562.

(98) Mabotha, T. E., PhD Thesis: *Haemozoin formation, effects of chloroquine on iron distribution in Plasmodium falcipaum and the correlation of thermodynamic and structural factors with 4-aminoquinoline activity*, University of Cape Town, **2007**.

(99) Solomonov, I.; Osipova, M.; Feldman, Y.; Baehtz, C.; Kjaer, K.; Robinson, I. K.; Webster, G. T.; McNaughton, D.; Wood, B. R.; Weissbuch, I.; Leiserowitz, L. *J. Am. Chem. Soc.* **2007**, *129*, 2615-2627.

(100) Meshnick, S. R. In *Malaria: Parasite biology, pathogenesis, and protection*; Sherman, I. W., Ed.; ASM Press: Washington D.C., **1998**.

(101) Foley, M.; Tilley, L. *Pharmacol. Ther.* **1998**, *79*, 55-87.

(102) Cohen, S. N.; Yielding, K. L. *J. Biol. Chem.* **1965**, *240*, 3123-3131.

(103) Cohen, S. N.; Yielding, K. L. *Proc. Natl. Acad. Sci. USA* **1965**, *54*, 521-527.

(104) Gluzman, I. Y.; Schlesinger, P. H.; Krogstad, D. J. *Antimicrob. Agents Chemother.* **1987**, *31*, 32-36.

(105) Schlesinger, P. H.; Krogstad, D. J.; Herwaldt, B. L. *Antimicrob. Agents Chemother.* **1988**, *32*, 793-798.

(106) Chou, A. C.; Chevli, R.; Fitch, C. D. *Biochemistry* **1980**, *19*, 1543-1549.

(107) Winstanley, P. A.; Breckenridge, A. M. *Ann. Trop. Med. Parasitol.* **1987**, *81*, 619-627.

(108) Slater, A. F. G. *Pharmacol. Ther.* **1993**, *57*, 203-235.

(109) Macomber, P. B.; Sprinz, H.; Tousimis, A. J. *Nature* **1967**, *214*, 937-939.

(110) Warhurst, D. C.; Hockley, D. J. *Nature* **1967**, *214*, 935-936.

(111) Saliba, K. J.; Folb, P. I.; Smith, P. J. *Biochem. Pharmacol.* **1998**, *56*, 313-320.

(112) Homewood, C. A.; Warhurst, D. C.; Peters, W.; Baggaley, V. C. *Nature* **1972**, *235*, 50-52.

(113) Rosenthal, P. J.; McKerrow, J. H.; Rasnick, D.; Leech, J. H. D. *Mol. Biochem. Parasitol.* **1989**, *35*, 177-183.

(114) Silva, A. M.; Lee, A. Y.; Gulnik, S. V.; Maier, P.; Collins, J.; Bhat, T. N.; Collins, P. J.; Cachau, R. E.; Luker, K. E.; Gluzman, I. Y.; Francis, S. E.; Oksman, A.; Goldberg, D. E.; Erickson, J. W. *Proc. Natl. Acad. Sci. USA* **1996**, *93*, 10034-10039.

(115) Ginsburg, H.; Nissani, E.; Krugliak, M. *Biochem. Pharmacol.* **1989**, *38*, 2645-2654.

(116) Fitch, C. D.; Yunis, N. G.; Chevli, R.; Gonzalez, Y. *J. Clin. Invest.* **1974**, *54*, 24-33.

(117) Krugliak, M.; Ginsburg, H. *Life Sci.* **1991**, *49*, 1213-1219.

(118) Mungthin, M.; Bray, P. G.; Ridley, R. G.; Ward, S. A. *Antimicrob. Agents Chemother.* **1998**, *42*, 2973-2977.

(119) Webster, R. V.; Craig, J. C.; Shyamala, V.; Kirby, G. C.; Warhurst, D. C. *Biochem. Pharmacol.* **1991**, *42S*, S225-S227.

(120) Egan, T. J. *TARGETS* **2003**, *2*, 115-124.

(121) Karle, J. M.; Karle, I. L.; Gerena, L.; Milhous, W. K. *Antimicrob. Agents Chemother.* **1992**, *36*, 1538-1544.

(122) Sullivan, D. J. J.; Gluzman, I. Y.; Russel, D. G.; Goldberg, D. E. *Proc. Natl. Acad. Sci. USA* **1996**, *93*, 11865-11870.

(123) Egan, T. J.; Mavuso, W. W.; Ross, D. C.; Marques, H. M. *J. Inorg. Biochem.* **1997**, *68*, 137-145.

(124) Dorn, A.; Vippagunta, S. R.; Matile, H.; Jaquet, C.; Vennerstrom, J. L.; Ridley, R. G. *Biochem. Pharmacol.* **1998**, *55*, 727-736.

(125) Hawley, S. R.; Bray, P. G.; Mungthin, M.; Atkinson, J. D.; O'Neill, P. M.; Ward, S. A. *Antimicrob. Agents Chemother.* **1998**, *42*, 682-686.

(126) Egan, T. J.; Hempelmann, E.; Mavuso, W. W. *J. Inorg. Biochem.* **1999**, *73*, 101-107.

(127) Egan, T. J.; Hunter, R.; Kaschula, C. H.; Marques, H. M.; Misplon, A.; Walden, J. *J. Med. Chem.* **2000**, *43*, 283-291.

(128) Warhurst, D. C.; Craig, J. C.; Adagu, I. S.; Meyer, D. J.; Lee, S. Y. *Malar. J.* **2003**, *2*.

(129) Miller, L. H.; Neva, F. A.; Gill, F. *Ann. Intern. Med.* **1978**, *88*, 200-202.

(130) Chong, C. R.; Sullivan, D. J. J. *Biochem. Pharmacol.* **2003**, *66*, 2201-2212.

(131) Egan, T. J.; Ncokazi, K. K. *J. Inorg. Biochem.* **2005**, *99*, 1532-1539.

(132) Ncokazi, K. K.; Egan, T. J. *Anal. Biochem.* **2005**, *338*, 306-319.

(133) Famin, O.; Ginsburg, H. *Biochem. Pharmacol.* **2002**, *63*, 393-398.

(134) Jacobs, G. H.; Milhous, M.; Wilbur, K.; Rabbege, J. R. *Am. J. Trop. Med. Hyg.* **1987**, *36*, 9-14.

(135) Olliaro, P. L.; Castelli, F.; Caligaris, S.; Druilhe, P.; Carosi, G. *Microbiologica* **1989**, *12*, 15-28.

(136) Bray, P. G.; Ward, S. A.; O'Neill, P. M. *Curr. Top. Microbiol. Immunol.* **2005**, *295(Malaria)*, 3-38.

(137) Sullivan, D. J. J.; Matile, H.; Ridley, R. G.; Goldberg, D. E. *J. Biol. Chem.* **1998**, *273*, 31103-31107.

(138) Marques, H. M. *Inorg. Chim. Acta* **1991**, *190*, 291-295.

(139) Marques, H. M.; Munro, O. Q.; Crawcour, M. L. *Inorg. Chim. Acta* **1992**, *196*, 221-229.

(140) Cohen, S. N.; Phifer, K. O.; Yielding, K. L. *Nature* **1964**, *202*, 805-806.

(141) Graf, W.; Pommerening, K.; Scheler, W. *Acta Biol. Med. Ger.* **1971**, *26*, 895-909.

(142) Constantinidis, I.; Satterlee, J. D. *J. Am. Chem. Soc.* **1988**, *110*, 927-932.

(143) Constantinidis, I.; Satterlee, J. D. *J. Am. Chem. Soc.* **1988**, *110*, 4391-4395.

(144) Marques, H. M.; Voster, K.; Egan, T. J. *J. Inorg. Biochem.* **1996**, *64*, 7-23.

(145) Satterlee, J. D.; Shelnutt, J. A. *J. Phys. Chem.* **1984**, *88*, 5487-5492.

(146) Lantzke, I. R.; Watts, D. W. *J. Am. Chem. Soc.* **1967**, *89*, 815-821.

(147) Davies, T. H. *J. Biol. Chem.* **1940**, *135*, 597-622.

(148) Collier, G. S.; Pratt, J. M.; De Wet, C. R.; Tshabalala, C. F. *Biochem. J.* **1979**, *179*, 281-289.

(149) Kaschula, C. H.; Egan, T. J.; Hunter, R.; Basilico, N.; Parapini, S.; Taramelli, D.; Pasini, E.; Monti, D. *J. Med. Chem.* **2002**, *45*, 3531-3539.

(150) Egan, T. J.; Ncokazi, K. K. *J. Inorg. Biochem.* **2004**, *98*, 144-152.

(151) Mavuso, W. W., PhD Thesis: *Synthetic haemozoin: Characterisation, mechanism of formation from haematin and the effect of antimalarial drugs*, University of Cape Town, **2001**.

(152) Lukas, B.; Miller, J. R.; Silver, J.; Wilson, M. T.; Morrison, I. E. G. *J. Chem. Soc., Dalton Trans.* **1982**, 1035-1040.

(153) Adams, P. A.; Berman, P. A. M.; Egan, T. J.; Marsh, P. J.; Silver, J. *J. Inorg. Biochem.* **1996**, *63*, 69-77.

(154) Shelnutt, J. A. *J. Am. Chem. Soc.* **1981**, *103*, 4275-4277.

(155) Shelnutt, J. A. *J. Am. Chem. Soc.* **1983**, *105*, 774-778.

(156) Frosch, T.; Küstner, B.; Schlücker, S.; Szeghalmi, A.; Schmitt, M.; Kiefer, W.; Popp, J. *J. Raman Spectr.* **2004**, *35*, 819-821.

(157) Warhurst, D. C. *Biochem. Pharmacol.* **1981**, *30*, 3323-3327.

(158) Behere, D. V.; Goff, H. M. *J. Am. Chem. Soc.* **1984**, *106*, 4945-4950.

(159) Moreau, S.; Perly, B.; Chachaty, C.; Deleuze, C. *Biochim. Biophys. Acta* **1985**, *840*, 107-116.

(160) Hunter, C. A.; Sanders, J. K. M. *J. Am. Chem. Soc.* **1990**, *112*, 5525-5534.

(161) O'Neill, P. M.; Willock, D. J.; Hawley, S. R.; Bray, P. G.; Storr, R. C.; Ward, S. A.; Park, B. K. *J. Med. Chem.* **1997**, *40*, 437-448.

(162) Leed, A.; DuBay, K.; Ursos, L. M. B.; Sears, D.; de Dios, A. C.; Roepe, P. D. *Biochemistry* **2002**, *41*, 10245-10255.

(163) Dascombe, M. J.; Drew, M. G. B.; Morris, H.; Wilairat, P.; Auparakkitanon, S.; Moule, W. A.; Alizadeh-Shekalgourbi, S.; Evans, P. G.; Lloyd, M.; Dyas, A. M.; Carr, P.; Ismail, F. M. D. *J. Med. Chem.* **2005**, *48*, 5423-5436.

(164) de Dios, A. C.; Tycko, R.; Ursos, L. M. B.; Roepe, P. D. *J. Phys. Chem. A* **2003**, *107*, 5821-5825.

(165) Egan, T. J. *J. Inorg. Biochem.* **2006**, *100*, 916-926.

(166) Vippagunta, S. R.; Dorn, A.; Matile, H.; Bhattacharjee, A., K; Karle, J. M.; Ellis, W., Y; Ridley, R. G.; Vennerstrom, J. L. *J. Med. Chem.* **1999**, *42*, 4630-4639.

(167) Portela, C.; Afonso, C. M. M.; Pinto, M. M. M.; Ramos, M. J. *Bioorg. Med. Chem.* **2004**, *12*, 3313-3321.

(168) Oleksyn, B. J.; Suszko-Purzycka, A.; Dive, G.; Lamotte-Brasseur, J. *J. Pharm. Sci.* **1991**, *81*, 122-127.

(169) da Silva, T. H. Á.; de Oliveira, M. T.; dos Santos, H. F.; de Oliveira, A. B.; de Almeida, W. B. *Quim Nova* **2005**, *28*, 244-249.

(170) Orjih, A. U.; Banyal, H. S.; Chevli, R.; Fitch, C. D. *Science* **1981**, *214*, 667-669.

(171) Sugioka, Y.; Suzuki, M.; Sugioka, K.; Nakano, M. *FEBS Lett.* **1987**, *223*, 251-254.

(172) Campanale, N.; Nickel, C.; Daubenberger, C. A.; Wehlan, D. A.; Gorman, J. J.; Klonis, N.; Becker, K.; Tilley, L. *J. Biol. Chem.* **2003**, *278*, 27354-27361.

(173) Hoppe, H. C.; van Schalkwyk, D. A.; Wiehart, U. I. M.; Meredith, S. A.; Egan, J.; Weber, B. W. *Antimicrob. Agents Chemother.* **2004**, *48*, 2370-2378.

(174) Fitch, C. D.; Russel, N. V. *Antimicrob. Agents Chemother.* **2006**, *50*, 2415-2419.

(175) Fitch, C. D. *Antimicrob. Agents Chemother.* **1973**, *3*, 545-548.

(176) Yayon, A.; Cabantchik, Z. I.; Ginsburg, H. *Proc. Natl. Acad. Sci. USA* **1985**, *82*, 2784-2788.

(177) Bennett, T. N.; Kosar, A. J.; Ursos, L. M. B.; Dzekunov, S. M.; Singh, S. A. B.; Fidock, D. A.; Roepe, P. D. *Mol. Biochem. Parasitol.* **2004**, *133*, 99-114.

(178) Bray, P. G.; Saliba, K. J.; Davies, J. D.; Spiller, D. G.; White, M. R. H.; Kirk, K.; Ward, S. A. *Mol. Biochem. Parasitol.* **2002**, *119*, 301-304.

(179) Sanchez, C. P.; Wünsch, S.; Lanzer, M. *J. Biol. Chem.* **1997**, *272*, 2652-2658.

(180) Bray, P. G.; Mungthin, M.; Ridley, R. G.; Ward, S. A. *Mol. Pharmacol.* **1998**, *54*, 170-179.

(181) Krogstad, D. J.; Schlesinger, P. H.; Herwaldt, B. L. *Antimicrob. Agents Chemother.* **1988**, *32*, 799-801.

(182) Sanchez, C. P.; Stein, W. D.; Lanzer, M. *Trends Parasitol.* **2007**, *23*, 332-339.

(183) Wellems, T. E.; Walker-Jonah, A.; Panton, L. J. *Proc. Natl. Acad. Sci. USA* **1991**, *88*, 3382-3386.

(184) Fidock, D. A.; Nomura, T.; Talley, A. K.; Cooper, R. A.; Dzekunov, S. M.; Ferdig, M. T.; Ursos, L. M. B.; Sidhu, A. B. S.; Naude, B.; Deitsch, K. W.; Su, X.-Z.; Wootton, J. C.; Roepe, P. D.; Wellems, T. E. *Mol. Cell* **2000**, *6*, 861-871.

(185) Warhurst, D. C. *Curr. Sci.* **2007**, *92*, 1556-1560.

(186) Pradines, B.; Pages, J.-M.; Barbe, J. *Curr. Drug Targets, Infect. Disord.* **2005**, *5*, 411-431.

(187) Cowman, A. F.; Karcz, S.; Galatis, D.; Culvenor, J. G. *J. Cell Biol.* **1991**, *113*, 1033-1042.

(188) Jiang, H.; Joy, D. A.; Furuya, T.; Su, X.-z. *J. Postgrad. Med.* **2006**, *52*, 271-276.

(189) Cowman, A. F.; Galatis, D.; Thompson, J. K. *Proc. Natl. Acad. Sci. USA* **1994**, *91*, 1143-1147.

(190) Egan, T. J.; Kaschula, C. H. *Curr. Opin. Infect. Dis.* **2007**, *20*, 598-604.

(191) De, D.; Krogstad, F. M.; Cogswell, F. B.; Krogstad, D. J. *Am. J. Trop. Med. Hyg.* **1996**, *55*, 579-583.

(192) Ridley, R. G.; Hofheinz, W.; Matile, H.; Jaquet, C.; Dorn, A.; Masciadri, R.; Jolidon, S.; Richter, W. F.; Guenzi, A.; Girometta, M. A.; Urwyler, H.; Huber, W.; Thaithong, S.; Peters, W. *Antimicrob. Agents Chemother.* **1996**, *40*, 1846-1854.

(193) Stocks, P. A.; Raynes, K. J.; Bray, P. G.; Park, B. K.; O'Neill, P. M.; Ward, S. A. *J. Med. Chem.* **2002**, *45*, 4975-4983.

(194) Biot, C.; Glorian, G.; Maciejewski, L. A.; Brocard, J. S. *J. Med. Chem.* **1997**, *40*, 3715-3718.

(195) Tait, G. H. In *Porphyrins and related compounds*; Goodwin, T. W., Ed.; Academic Press: London, **1968**.

(196) Gouterman, M. *J. Chem. Phys.* **1959**, *30*, 1139-1161.

(197) Gouterman, M. In *The Porphyrins*; Dolphin, D., Ed.; Academic Press: New York, **1968**; Vol. 3.

(198) Wood, B. R.; McNaughton, D. *Expert Rev. Proteomics* **2006**, *3*, 525-544.

(199) Williams, D. H.; Fleming, I. *Spectroscopic methods in organic chemistry*; Fifth ed.; McGraw-Hill: London, **1995**.

(200) Munro, O. Q.; Marques, H. M. *Inorg. Chem.* **1996**, *35*, 3768-3779.

(201) Rhodes, W.; Chase, M. *Rev. Mod. Phys.* **1967**, *39*, 348-361.

(202) Smith, W. E.; Dent, G. In *Modern Raman spectroscopy - A practical approach*; John Wiley and Sons, **2005**, Chapter 1, 1-21.

(203) Michelson-Morley Experiment; http://scienceworld.wolfram.com/physics /Michelson-MorleyExperiment.html, accessed on 12/08/2008.

(204) Northwestern University, Keck Interdisciplinary Surface Science Centre-NUANCE; www.nuance.northwestern.edu/keckii/ftir2.asp, accessed on 10/07/2008.

(205) Born, M.; Wolf, E. *Principles of Optics. Electromagnetic theory of propagation, interference and diffraction of light*; Seventh (expanded) edition ed.; Cambridge University Press: London, **1999**.

(206) Smith, W. E.; Dent, G. In *Modern Raman spectroscopy - A practical approach*; John Wiley and Sons, **2005**, Chapter 4, 94-112.

(207) Notingher, I.; Hench, L. L. *Expert Rev. Med. Devices* **2006**, *3*, 215-234.

(208) Tang, J.; Albrecht, A. C. *J. Chem. Phys.* **1968**, *49*, 1144-1154.

(209) Spiro, T. G.; Li, X.-Y. In *Biological applications of Raman spectroscopy*; Spiro, T. G., Ed.; Wiley and Sons: New York, **1988**.

(210) Spiro, T. G.; Strekas, T. C. *J. Am. Chem. Soc.* **1974**, *96*, 338-345.

(211) Abe, M.; Kitagawa, T.; Kyogoku, K. *J. Chem. Phys.* **1978**, *69*, 4526-4534.

(212) Yamamoto, T.; Palmer, G.; Gill, D.; Salmeen, I. T.; Rimai, L. *J. Biol. Chem.* **1973**, *248*, 5211-5213.

(213) Ong, C. W.; Shen, Z. X.; Ang, K. K. H.; Kara, U. A. K.; Tang, S. H. *Appl. Spectrosc.* **1999**, *53*, 1097-1101.

(214) Wood, B. R.; Langford, S. J.; Cooke, B. M.; Glenister, F. K.; Lim, J.; McNaughton, D. *FEBS Lett.* **2003**, *554*, 247-252.

(215) Bohle, D. S.; Conklin, B. J.; Cox, D.; Madsen, S. K.; Paulson, S.; Stephens, P. W.; Yee, G. T. *Am. Chem. Soc. Symp. Ser.* **1994**, *572*, 497-515.

(216) Hu, S.; Smith, K. M.; Spiro, T. G. *J. Am. Chem. Soc.* **1996**, *118*, 12638-12646.

(217) Frosch, T.; Koncarevic, S.; Zedler, L.; Schmitt, M.; Schenzel, K.; Becker, K.; Popp, J. *J. Phys. Chem. B* **2007**, *111*, 11047-11056.

(218) Wood, B. R.; Langford, S. J.; Cooke, B. M.; Lim, J.; Glenister, F. K.; Duriska, M.; Unthank, J. K.; McNaughton, D. *J. Am. Chem. Soc.* **2004**, *126*, 9233-9239.

(219) Davis, A. M. In *Medicinal Chemistry. Principles and practice*; King, F. D., Ed.; Royal Society of Chemistry: Cambridge, **1994**.

(220) Shlens, J. Report: *A tutorial on principle component analysis*, Salk Institute for Biological Studies, **2005**.

(221) Palmer, M.; Botany Department, Oklahoma State University; www.ordination.okstate.edu/PCA.htm, accessed on 10/07/2008.

(222) Principle Components Analysis; www.cnx.org/content/m11461/latest/pca.jpg, accessed 10/07/2008.

(223) Azároff, L. In *Elements of X-Ray Crystallography*; McGraw-Hill, **1968**.

(224) Kuzmenko, I.; Rapaport, H.; Kjaer, K.; Als-Nielsen, J.; Weissbuch, I.; Lahav, M.; Leiserowitz, L. *Chem. Rev.* **2001**, *101*, 1659-1696.

(225) Marra, W. C.; Eisenberger, P.; Cho, A. Y. *J. Appl. Phys.* **1979**, *50*, 6927-6933.

(226) Kjaer, K.; Als-Nielsen, J.; Helm, C. A.; Tippman-Krayer, P.; Möhwald, H. *J. Phys. Chem.* **1989**, *93*, 3200-3206.

(227) Vineyard, G. H. *Phys. Rev. B: Condens. Matter* **1982**, *26*, 4146-4159.

(228) Kjaer, K.; Als-Nielsen, J.; Helm, C. A.; Tippman-Krayer, P.; Möhwald, H. *Thin Solid Films* **1988**, *159*, 17-28.

(229) FIT; v 1.08; University of the Witwatersrand, Department of Chemistry: Johannesburg.

(230) GraphPad Prism; v 3.0; GraphPad Software, Inc.: San Diego.

(231) HYPERCHEM; v 7.5; Hypercube, Inc.: Gainesville, Florida.

(232) OPUS; v 6.0; Bruker Optic, GmbH, 1997-2006.

(233) The Unscrambler; v 9.2; CAMO Process AC.

(234) Endnote; Windows v 4.0; ISI ResearchSoft: Berkeley.

(235) Jeney, V.; Balla, J.; Yachie, A.; Varga, Z.; Vercellotti, G. M.; Eaton, J. W.; Balla, G. *Blood* **2002**, *100*, 879-887.

(236) Larsson, S. C.; Adami, H.-O.; Giovannucci, E.; Wolk, A. *J. Natl. Cancer Inst.* **2005**, *97*, 232-233.

(237) Pierre, F.; Peiro, G.; Taché, S.; Cross, A. J.; Bingham, S. A.; Gasc, N.; Gottardi, G.; Corpet, D. E.; Guéraud, F. *Cancer Epidemiol. Biomarkers Prev.* **2006**, *15*, 2274-2279.

(238) Fitch, C. D.; Chevli, R.; Banyal, H. S.; Phillips, G.; Pfaller, M. A.; Krogstad, D. J. *Antimicrob. Agents Chemother.* **1982**, *21*, 819-822.

(239) Kumar, S.; Bandyopadhyay, U. *Toxicol. Lett.* **2005**, *157*, 175-188.

(240) Linder, P. W.; Nassimbeni, L. R.; Polson, A.; Rodgers, A. L. *J. Chem. Educ.* **1976**, *53*, 330-332.

(241) Evans, D. F. *J. Chem. Soc.* **1959**, 2003-2005.

(242) Crawford, T. H.; Swanson, J. *J. Chem. Educ.* **1971**, *48*, 382-386.

(243) Schubert, E. M. *J. Chem. Educ.* **1992**, *69*, 62.

(244) De Buysser, K.; Herman, G. G.; Bruneel, E.; Hoste, S.; Van Driessche, I. *Chem. Phys.* **2005**, *315*, 286-292.

(245) *CRC Handbook of Chemistry and Physics*; CRC: Boca Raton, 1980-1981.

(246) Munro, O. Q.; Bradley, J. C.; Hancock, R. D.; Marques, H. M.; Marsicano, F.; Wade, P. W. *J. Am. Chem. Soc.* **1992**, *114*, 7218-7230.

(247) Munro, O. Q.; Marques, H. M.; Debrunner, P. G.; Mohanrao, K.; Scheidt, W. R. *J. Am. Chem. Soc.* **1995**, *117*, 935-954.

(248) Marques, H. M.; Munro, O. Q.; Grimmer, N. E.; Levendis, D. C.; Marsicano, F.; Pattrick, G.; Markoulides, T. *J. Chem. Soc., Faraday Trans.* **1995**, *91*, 1741-1749.

(249) Christian, G. *Analytical Chemistry*; Wiley: New York, **1994**.

(250) Atkins, P. W. *Physical Chemistry*; Fifth ed.; Oxford University Press: Oxford, **1994**.

(251) Gustafson, K. E.; Dickhut, R. M. *J. Chem. Eng. Data* **1994**, *39*, 281-285.

(252) Budd, D. L.; La Mar, G. N.; Langry, K. C.; Smith, K. M.; Nayyir-Mazhir, R. *J. Am. Chem. Soc.* **1979**, *101*, 6091-6096.

(253) Cheng, B.; Safo, M. K.; Orosz, R. D.; Reed, C. A.; Debrunner, P. G.; Scheidt, W. R. *Inorg. Chem.* **1994**, *33*, 1319-1324.

(254) de Villiers, K. A.; Kaschula, C. H.; Egan, T. J.; Marques, H. M. *J. Biol. Inorg. Chem.* **2007**, *12*, 101-117.

(255) Koenig, D. F. *Acta Cryst.* **1965**, *18*, 663-673.

(256) Cambridge Structural Database; V S26; Cambridge Crystallographic Data Centre: Cambridge, 2004.

(257) Barbour, L. J. *J. Supramol. Chem.* **2003**, *1*, 189-191.

(258) Cowgill, R. W.; Clark, W. M. *J. Biol. Chem.* **1952**, *198*, 33-61.

(259) Brown, S. B.; Hatzikonstantinou, H.; Herries, D. G. *International Journal of Biochemistry* **1980**, *12*, 701-707.

(260) Brown, S. B.; Jones, P.; Prudhoe, K.; Suggett, A. *Nature* **1968**, *219*, 605-606.

(261) Oumous, H.; Lecomte, C.; Protas, J.; Cocolios, P.; Guilard, R. *Polyhedron* **1984**, *3*, 651-659.

(262) Hoard, J. L.; Hamor, M. J.; Hamor, T. A.; Caughey, W. S. *J. Am. Chem. Soc.* **1965**, *87*, 2312-2319.

(263) Lecomte, C.; Chadwick, D. L.; Coppens, P.; Stevens, E. D. *Inorg. Chem.* **1983**, *22*, 2982-2992.

(264) Hatano, K.; Uno, T. *Bull. Chem. Soc. Jpn.* **1990**, *63*, 1825-1827.

(265) Scolaro, L. M.; Castriciano, M.; Romeo, A.; Patanè, S.; Cefalì, E.; Allegrini, M. *J. Phys. Chem. B* **2002**, *106*, 2453-2459.

(266) Ma, J. C.; Dougherty, D. A. *Chem. Rev.* **1997**, *97*, 1303-1324.

(267) Munro, O. Q.; de Wet, M.; Pollak, H.; van Wyk, J.; Marques, H. M. *J. Chem. Soc., Faraday Trans.* **1998**, *94*, 1743-1752.

(268) Maltempo, M. M. *J. Chem. Phys.* **1974**, *61*, 2540-2547.

(269) Gupta, G. P.; Lang, G.; Scheidt, W. R.; Geiger, D. K.; Reed, C. A. *J. Chem. Phys.* **1986**, *85*, 5212-5220.

(270) Davydov, R. M.; Ménage, S.; Fontecave, M.; Gräslund, A.; Ehrenberg, A. *J. Biol. Inorg. Chem.* **1997**, *2*, 242-255.

(271) Shelnutt, J. A. In *The Porphyrin Handbook*; Kadish, K. M., Smith, K. M., Guilard, R., Eds.; Academic: San Diego, **2000**; Vol. 7.

(272) Dorn, A.; Vippagunta, S. R.; Matile, H.; Bubendorf, A.; Vennerstrom, J. L.; Ridley, R. G. *Biochem. Pharmacol.* **1998**, *55*, 737-747.

(273) Ridley, R. G.; Dorn, A.; Vippagunta, S. R.; Vennerstrom, J. L. *Ann. Trop. Med. Parasitol.* **1997**, *91*, 559-566.

(274) HASYLAB, DESY; http://hasylab.desy.de/facilities/doris_iii/beamlines/ BW1/ index_eng.html, accessed on 22/06/2008.

(275) Vippagunta, S. R.; Dorn, A.; Ridley, R. G.; Vennerstrom, J. L. *Biochim. Biophys. Acta* **2000**, *1475*, 133-140.

(276) Nonius, B. V.; Nonius: Delft, The Netherlands, **1998**.

(277) Sheldrick, G. M. Göttingen, Germany, 1997.

(278) Sheldrick, G. M. *Acta Cryst.* **2008**, *A64*, 112-122.

(279) XPREP; v 5.1/NT; Bruker Analytical X-ray Systems, 1997.

(280) Allinger, N. L. *J. Am. Chem. Soc.* **1977**, *99*, 8127-8134.

(281) Marques, H. M., Private Communication: Force field parameterisation in Hyperchem, 2006.

(282) Prévot, L.; Jaquinod, L.; Fischer, J.; Weiss, R. *Inorg. Chim. Acta* **1998**, *283*, 98-104.

(283) Johnson, M. R.; Seok, W. K.; Ma, W.; Slebodnick, C.; Wilcoxen, K. M.; Ibers, J. A. *J. Org. Chem.* **1996**, *61*, 3298-3303.

(284) Marques, H. M., Private Communication to Mabotha T. E.: Getting started in Hyperchem, 2004.

(285) Pimentel, W. H.; McClellan, A. L. In *The Hydrogen Bond*; W H Freeman: San Francisco, **1960**.

(286) Webster, G. T.; Tilley, L.; Deed, S.; McNaughton, D.; Wood, B. R. *FEBS Lett.* **2008**, *582*, 1087-1092.

(287) Einstein, F. W. B.; Willis, A. C. *Inorg. Chem.* **1978**, *17*, 3040-3045.

(288) Gans, P.; Buisson, G.; Duee, E.; Regnard, J. R.; Marchon, J. C. *J. Chem. Soc., Chem. Commun.* **1979**, 393-395.

(289) Akins, D. L. *J. Phys. Chem.* **1986**, *90*, 1530-1534.

(290) Andrés, G. O.; de Rossi, R. H. *ARKIVOC* **2003**, 127-138.

(291) Marques, H. M. *Inorg. Chem.* **1990**, *29*, 1597-1599.

(292) Braga, D.; Maini, L.; Grepioni, F.; De Cian, A.; Félix, O.; Fischer, J.; Hosseini, M. W. *New J. Chem.* **2000**, *24*, 547-553.

(293) Yang, B.; Morris, M. D.; Xie, M.; Lightner, D. A. *Biochemistry* **1991**, *30*, 688-694.

(294) Uno, T.; Hatano, K.; Nawa, T.; Nakamura, K.; Nishimura, Y.; Arata, Y. *Inorg. Chem.* **1991**, *30*, 4322-4327.